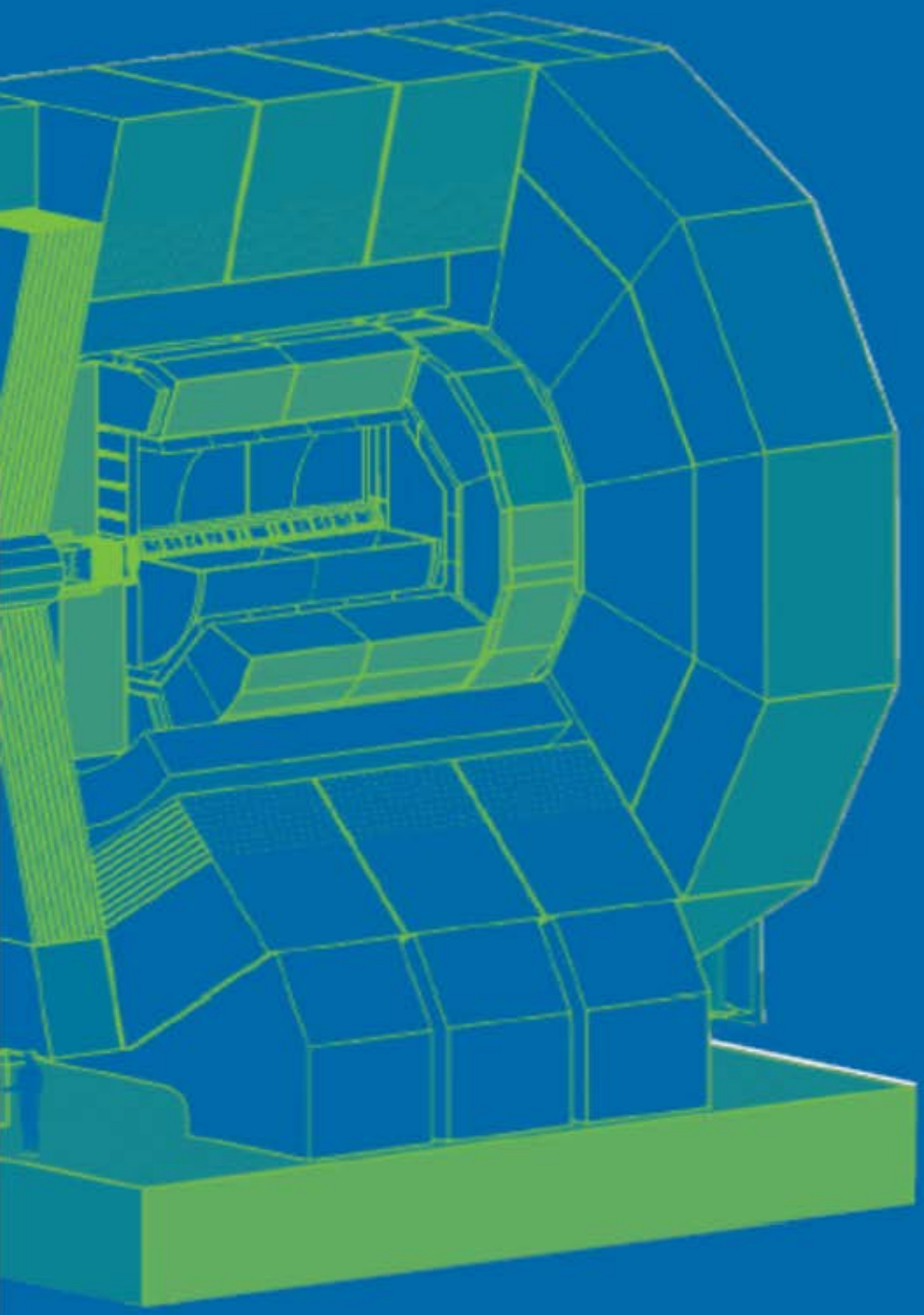

The International Large Detector

Letter of Intent

by the
ILD Concept Group
February 2010

DESY 2009-87
FERMILAB-PUB-09-682-E
KEK Report 2009-6

International Large Detector

Letter Of Intent

The ILD concept group

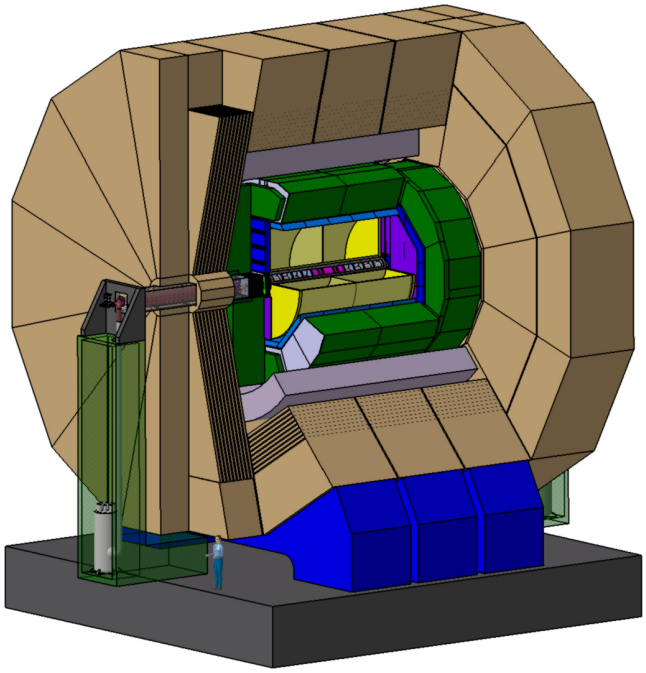

February 2010

LIST OF SIGNATORIES

SIGNATORIES

Holger Stoeck
University of Sydney, Falkiner High Energy Physics Group, School of Physics, A28, Sydney, NSW 2006, Australia

Thomas Bergauer, Marko Dragicevic, Helmut Eberl, Sebastian Frank, Elena Ginina, Stephan Haensel, Hana Hlucha, Wolfgang Kiesenhofer, Manfred Krammer, Winfried A. Mitaroff, Fabian Moser, Meinhard Regler, Manfred Valentan, Wolfgang Waltenberger
Österreichische Akademie der Wissenschaften, Institut für Hochenergiephysik, Nikolsdorfergasse 18, A-1050 Vienna, Austria

Konstantin Afanaciev, Vladimir Drugakov, Igor Emeliantchik, Alexandr Ignatenko, Nikolai Shumeiko
National Scientific & Educational Centre of Particle & High Energy Physics (NCPHEP), Belarusian State University, M.Bogdanovich street 153, 220040 Minsk, Belarus

Martin Grunewald
University of Ghent, Department of Subatomic and Radiation Physics, Proeftuinstraat 86, 9000 Gent, Belgium

Alain Bellerive, Madhu S. Dixit[1]
Carleton University, Department of Physics, 1125 Colonel By Drive, Ottawa, Ontario, Canada K1S 5B6

François Corriveau
McGill University, Department of Physics, Ernest Rutherford Physics Bldg., 3600 University Street, Montreal, Quebec, H3A 2T8 Canada

Mauricio Barbi
University of Regina, Department of Physics, Regina, Saskatchewan, S4S 0A2 Canada

Jason M Abernathy, Dean Karlen[1]
University of Victoria, Department of Physics and Astronomy, P.O.Box 3055 Stn Csc, Victoria, BC V8W 3P6, Canada

Jean-Pierre Martin
Université de Montréal, Département de Physique, Groupe de Physique des Particules, C.P. 6128, Succ. Centre-ville, Montréal, Qc H3C 3J7, Canada

Li Bo, Shaomin Chen, Zhi Deng, Yuanning Gao, Fanfan Jing, Yu-Ping Kuang, Yulan Li, Bo Li, Ting Li, Bo Liu, Wenbin Qian, Junping Tian[3], Yi Wang, Zhenwei Yang, Qian Yue, Yanxi Zhang, Baojun Zheng, Liang Zhong, Xianglei Zhu
Center for High Energy Physics (TUHEP), Tsinghua University, Beijing, China 100084

Jin Min Yang
Institute of Theoretical Physics, Chinese Academy of Sciences, P.O.Box 2735, Beijing, China 100080

Chunxu Yu
Nankai University, Department of Physics, Tianjin, China 300071

Cunfeng Feng, Xingtao Huang, Zuotang Liang, Meng Wang, Xueyao Zhang, Chengguang Zhu
Shandong University, 27 Shanda Nanlu, Jinan, China 250100

Hongfang Chen, Liang Han, Ge Jing, Wengan Ma, Ming Shao, Kezhu Song, Qun Wang, Xiaoliang Wang, Zizong Xu, Wenbiao Yan, Renyou Zhang, Ziping Zhang, Jiawei Zhao, Zhengguo Zhao, Yongzhao Zhou
University of Science and Technology of China, Department of Modern Physics (DMP), Jin Zhai Road 96, Hefei, China 230026

Zdenek Dolezal, Zbynek Drasal, Peter Kodys, Peter Kvasnicka, Jan Scheirich, Josef Zacek
Charles University, Institute of Particle & Nuclear Physics, Faculty of Mathematics and Physics, V Holesovickach 2, CZ-18000 Prague 8, Czech Republic

Jaroslav Cvach, Michal Marcisovsky, Stanislav Nemecek, Ivo Polak, Pavel Ruzicka, Petr Sicho, Jan Smolík, Vaclav Vrba, Jaroslav Zalesak
Institute of Physics, ASCR, Academy of Science of the Czech Republic, Division of Elementary Particle Physics, Na Slovance 2, CZ-18221 Prague 8, Czech Republic

Mogens Dam, Peter H Hansen, Stefania Xella
Niels Bohr Institute (NBI), University of Copenhagen, Blegdamsvej 17, DK-2100 Copenhagen, Denmark

Risto Orava[4]
University of Helsinki, Department of Physical Sciences, P.O. Box 64 (Vaino Auerin katu 11), FIN-00014, Helsinki, Finland

David Attie, Marc Besancon, Paul Colas, Eric Delagnes, Nicolas Fourches, Giomataris Ioannis, Francois Kircher, Pierre Lutz[5], Christophe Royon, Maxim Titov
CEA Saclay, IRFU, F-91191 Gif-sur-Yvette, France

Jerome Baudot[6], Auguste Besson[6], Andrea Brogna[6], Gilles Claus[6], Claude Colledani[6], Rita De Masi, Andrei Dorokhov[6], Guy Doziere[6], Abdelkader Himmi[6], Christine Hu-Guo[6], Marc Imhoff[6], Frederic Morel[6], Isabelle Valin[6], Yorgos Voutsinas, Marc Winter
Institut Pluridisciplinaire Hubert Curien, 23 Rue du Loess - BP28, 67037 Strasbourg Cedex 2, France

Helenka Przysiezniak[2]
Laboratoire d'Annecy-le-Vieux de Physique des Particules (LAPP), Chemin du Bellevue, BP 110, F-74941 Annecy-le-Vieux Cedex, France

Bernard Bouquet, Stephane L.C. Callier, Patrick Cornebise, Olivier Dadoun, Christophe De La Taille, Philippe Doublet, Frédéric Dulucq, Michele Faucci Giannelli[22], Julien L Fleury, Matthieu Joré, Hengne Li, Gisele Martin-Chassard, Roman Poeschl, Ludovic Raux, Francois Richard, Nathalie Seguin-Moreau, Dirk Zerwas, Zhiqing Zhang, Fabian Zomer
Laboratoire de l'Accélérateur Linéaire (LAL), Université Paris-Sud 11, Bâtiment 200, 91898 Orsay, France

Cristina Carloganu, Pascal Gay, Philippe Gris
Laboratoire de Physique Corpusculaire de Clermont-Ferrand (LPC), Université Blaise Pascal, I.N.2.P.3./C.N.R.S., 24 avenue des Landais, 63177 Aubière Cedex, France

Alexandre Charpy, Catalin Ciobanu, Wilfrid Da Silva, Guillaume Daubard, Jacques David, Christophe Evrard, Jean-Francois Genat[24], Jean Francois Huppert, Didier Imbault, Frédéric Kapusta, Dhellot Marc, Ghislain Patrick, Thanh Hung Pham, Philippe Repain, Aurore Savoy-Navarro, Rachid Sefri
Laboratoire de Physique Nucléaire et des Hautes Energies (LPNHE), Université Pierre et Marie Curie, IN2P3/CNRS, Tour 43, RdC, 4, Place Jussieu, 75252, Paris-Cedex 05, France

Joël Bouvier, Daniel Dzahini, Laurent Gallin-Martel, Julien Giraud, Denis Grondin, Jean-Yves Hostachy, Sabine Kraml, Kaloyan Krastev, Eric Lagorio, Laurent Morin, Fatah-Ellah Rarbi, Christophe Vescovi, Mahfoud Yamouni
Laboratoire de Physique Subatomique et de Cosmologie (LPSC), Université Joseph Fourier (Grenoble 1), CNRS/IN2P3, Institut Polytechnique de Grenoble, 53 rue des Martyrs, F-38026 Grenoble Cedex, France

Marc Anduze, Khaled Belkadhi, Vincent Boudry, Jean-Claude Brient, Catherine Clerc, Rémi Cornat, David Decotigny, Mickael Frotin, Franck Gastaldi, Daniel T D Jeans, Antoine Mathieu, Paulo Mora De Freitas, Gabriel Musat, Marcel Reinhard, Manqi Ruan, Jean-Charles Vanel, Henri L Videau
Laboratoire Leprince-Ringuet (LLR), École polytechnique – CNRS/IN2P3, Route de Saclay, F-91128 Palaiseau Cedex, France

Jean-Charles Fontaine
Université de Haute Alsace Mulhouse-Colmar, Groupe de Recherche en Physique des Hautes Energies (GRPHE), 61 rue Albert Camus, 68093 Mulhouse Cedex, France

Marc Bedjidian, Christophe Combaret, Gérald Grenier, Robert Kieffer, Imad Laktineh, Patrice Lebrun, Nick Lumb, Hervé Mathez, Kieffer Robert, Muriel Vander Donckt
Université de Lyon, F-69622, Lyon, France ; Université Lyon 1, Villeurbanne ; CNRS/IN2P3, Institut de Physique Nucléaire de Lyon

Uwe Renz, Markus Schumacher
Albert-Ludwigs Universität Freiburg, Physikalisches Institut, Hermann-Herder Str. 3, D-79104 Freiburg, Germany

Ringo Sebastian Schmidt[9]
Brandenburg University of Technology, Postfach 101344, D-03013 Cottbus, Germany

Hartwig Albrecht, Steve J. Aplin, Jochen Bürger, Christoph Bartels[12], Philip Bechtle, Jeannine Beck, Moritz Beckmann[11], Ties Behnke, C. Mikael U. Berggren, Karsten Buesser, Stefano Caiazza[12], Alan J. Campbell, Sandra Christen[12], Dörte David, Klaus Dehmelt, Ralf Diener, Guenter Eckerlin, Wolfgang Ehrenfeld, Eckhard Elsen, Jan Engels, Riccardo Fabbri, Manfred Fleischer, Frank Gaede, Erika Garutti, Andreas Gellrich, Ingrid-Maria Gregor, Tobias Haas, Lea Hallermann[12], Anthony Hartin, Martin Harz, Isa Heinze[12], Christian Helebrant[12], Daniela Käfer, Claus Kleinwort, U. Koetz, Volker Korbel, Dirk Krücker, Bernward Krause, Kirsten Kschioneck, Jan Kuhlmann, Frank Lehner, Diana Linzmaier, Jenny List, Angela Isabela Lucaci-Timoce, Benjamin Lutz[12], Ivan Marchesini[12], Cornelius Martens, Niels Meyer, Norbert Meyners, Joachim Mnich, Sergey Morozov[12], Carsten Niebuhr, Alexander Petrov, Volker Prahl, Alexei Raspereza, Philipp Roloff[12], Christoph Rosemann, K. Peter Schüler, Peter Schade, Joern Schaffran, Sebastian Schmitt, Uwe Schneekloth, Felix Sefkow, Klaus Sinram, Blanka Sobloher[12], Richard Stromhagen, Robert Volkenborn, Nanda Wattimena, Katarzyna Wichmann, Wolfram Zeuner[20]
Deutsches Elektronen-Synchrotron DESY, A Research Centre of the Helmholtz Association, Notkestrasse 85, 22607 Hamburg, Germany (Hamburg site)

Matthias Bergholz[7], Johannes Bluemlein, Maria Elena Castro Carballo, Hans Henschel, Hanna Kluge, Wolfgang Lange, Wolfgang Lohmann, Klaus Moenig, Martin Ohlerich, Sabine Riemann, Tord Riemann, André Sailer, Andreas Schälicke, Heinz Juergen Schreiber, Sergej Schuwalow, Andriy Ushakov
Deutsches Elektronen-Synchrotron DESY, A Research Centre of the Helmholtz Association, Platanenallee 6, 15738 Zeuthen, Germany (Zeuthen site)

Ariane Frey, Carsten Hensel, Arnulf Quadt
Georg-August-Universität Göttingen, II. Physikalisches Institut, Friedrich-Hund-Platz 1, 37077 Göttingen, Germany

Ralph Dollan
Humboldt Universität zu Berlin, Fachbereich Physik, Institut für Elementarteilchenphysik, Newtonstr. 15, D-12489 Berlin, Germany

Wim De Boer[20], Robert Rossmanith
Institut für Experimentelle Kernphysik, KIT,Universität Karlsruhe (TH), Wolfgang-Gaede-Str. 1, Postfach 6980, 76128 Karlsruhe

Stefan Tapprogge
Johannes Gutenberg Universität Mainz, Institut für Physik, 55099 Mainz, Germany

Otmar Biebel, Ralf Hertenberger, Raimund Ströhmer
Ludwig-Maximilians-Universität München, Fakultät für Physik, Am Coulombwall 1, D - 85748 Garching, Germany

Ladislav Andricek, Allen Caldwell, Xun Chen, Christian M Kiesling, Shaojun Lu[10], Andreas Moll[10], Hans-Günther Moser, Bob Olivier, Katja Seidel[10], Ronald Dean Settles, Frank Simon[10], Christian Soldner, Lars Weuste
Max-Planck-Institut für Physik (Werner-Heisenberg-Institut), Föhringer Ring 6, 80805 München, Germany

Werner Bernreuther, Tatsiana Klimkovich, Hans-Ulrich Martyn[8], Stefan Roth
Rheinisch-Westfälische Technische Hochschule (RWTH), Physikalisches Institut, Physikzentrum, Sommerfeldstrasse 14, D-52056 Aachen, Germany

Deepak Kar, Michael Kobel, Wolfgang F. Mader, Xavier Prudent, Rainer Schwierz, Dominik Stockinger, Arno Straessner
Technische Universität Dresden, Institut für Kern- und Teilchenphysik, D-01069 Dresden, Germany

Nils Feege[8], Andreas Imhof, Benno List, Oliver Wendt[8]
University of Hamburg, Physics Department, Institut für Experimentalphysik, Luruper Chaussee 149, 22761 Hamburg, Germany

Alexander Kaplan[8], Hans-Christian Schultz-Coulon
University of Heidelberg, Kirchhoff Institute of Physics, Albert Überle Strasse 3-5, DE-69120 Heidelberg, Germany

Michal Czakon[13], Malgorzata Worek[13], Christian Zeitnitz
University of Wuppertal, Gaußstraße 20, D-42119 Wuppertal, Germany

Ian Brock, Klaus Desch, Jochen Kaminski, Martin Killenberg, Thorsten Krautscheid, Adrian Vogel, Norbert Wermes, Peter Wienemann
Universität Bonn, Physikalisches Institut, Nußallee 12, 53115 Bonn, Germany

Alexander Kaukher, Oliver Schäfer
Universität Rostock, Fachbereich Physik, Universitätsplatz 3, D-18051 Rostock, Germany

Peter Buchholz, Ivor Fleck, Bakul Gaur, Marcus Niechciol
Universität Siegen, Fachbereich für Physik, Emmy Noether Campus, Walter-Flex-Str.3, D-57068 Siegen, Germany

Csaba Hajdu, Dezso Horvath
Hungarian Academy of Sciences, KFKI Research Institute for Particle and Nuclear Physics, P.O. Box 49, H-1525 Budapest, Hungary

Bipul Bhuyan
Indian Institute of Technology, Guwahati, Guwahati, Assam 781039, India

Sudeb Bhattacharya, Nayana Majumdar, Supratik Mukhopadhyay, Sandip Sarkar
Saha Institute of Nuclear Physics, 1/AF Bidhan Nagar, Kolkata 700064, India

Atul Gurtu, Gobinda Majumder
Tata Institute of Fundamental Research, School of Natural Sciences, Homi Bhabha Rd., Mumbai 400005, India

B. C. Choudhary
University of Delhi, Department of Physics and Astrophysics, Delhi 110007, India

Manas Maity
Visva-Bharati University, Department of Physics, Santiniketan 731235, India

Halina Abramowicz, Ronen Ingbir, Aharon Levy, Iftach Sadeh
Tel-Aviv University, School of Physics and Astronomy, Ramat Aviv, Tel Aviv 69978, Israel

Antonio Bulgheroni
Istituto Nazionale di Fisica Nucleare (INFN), Sezione di Milano, Via Celoria 16, I-20133 Milano, Italy

Lodovico Ratti, Valerio Re
Istituto Nazionale di Fisica Nucleare (INFN), Sezione di Pavia, Via Bassi 6, I-27100 Pavia, Italy

Simonetta Gentile
Istituto Nazionale di Fisica Nucleare (INFN), Sezione di Roma, c/o Dipartimento di Fisica - Università degli Studi di Roma "La Sapienza", P.le Aldo Moro 2, I-00185 Roma, Italy

Diego Gamba, Giuseppe Giraudo, Paolo Mereu
Istituto Nazionale di Fisica Nucleare (INFN), Sezione di Torino, c/o Universitá di Torino, facoltá di Fisica, via P Giuria 1, 10125 Torino, Italy

Alessandro Calcaterra, Marcello Piccolo
Laboratori Nazionali di Frascati, via E. Fermi, 40, C.P. 13, I-00044 Frascati, Italy

Massimo Caccia[15], Chiara Cappellini[15]
Università dell'Insubria in Como, Dipartimento di Scienze CC.FF.MM., via Vallegio 11, I-22100 Como, Italy

Takuo Yoshida
Fukui University, Department of Physics, 3-9-1 Bunkyo, Fukui-shi, Fukui 910-8507, Japan

Yasuo Arai, Hirofumi Fujii, Keisuke Fujii, Junpei Fujimoto, Yowichi Fujita, Takanori Hara, Tomiyoshi Haruyama, Takeo Higuchi, Katsumasa Ikematsu, Yukiko Ikemoto, Eiji Inoue, Hideo Itoh, Go Iwai, Nobu Katayama, Masanori Kawai, Makoto Kobayashi, Hideyo Kodama, Takashi Kohriki, Yoshinari Kondou, Akihiro Maki, Yasuhiro Makida, Takeshi Matsuda[8], Satoshi Mihara, Akiya Miyamoto, Takeshi Murakami, Isamu Nakamura, Kazuo Nakayoshi, Shohei Nishida, Mitsuaki Nozaki, Nobuchika Okada, Tsunehiko Omori, Masatoshi Saito, Toshiya Sanami, Hiroshi Sendai, Shoichi Shimazaki, Yusuke Suetsugu, Yasuhiro Sugimoto, Kazutaka Sumisawa, Shuji Tanaka, Manobu Tanaka, Ken-Ichi Tanaka, Toshiaki Tauchi, Kazuya Tauchi, Katsuo Tokushuku, Toru Tsuboyama, Junji Urakawa, Yutaka Ushiroda, Hiroshi Yamaoka, M. Yamauchi, Yoshiji Yasu, Tamaki Yoshioka
High Energy Accelerator Research Organization, KEK, 1-1 Oho, Tsukuba, Ibaraki 305-0801, Japan

Tohru Takahashi
Hiroshima University, Department of Physics, 1-3-1 Kagamiyama, Higashi-Hiroshima, Hiroshima 739-8526, Japan

Masaki Asano
Institute for Cosmic Ray Research, University of Tokyo, 5-1-5 Kashiwa-no-Ha, Kashiwa, Chiba 277-8582, Japan

Toshiyuki Iwamoto, Yoshio Kamiya, Hiroyuki Matsunaga, Toshinori Mori, Wataru Ootani, Taikan Suehara, Tomohiko Tanabe, Satoru Yamashita
International Center for Elementary Particle Physics, University of Tokyo, Hongo 7-3-1, Bunkyo District, Tokyo 113-0033, Japan

Hirokazu Ikeda
Japan Aerospace Exploration Agency, Sagamihara Campus, 3-1-1 Yoshinodai, Sagamihara, Kanagawa 220-8510 , Japan

Yukihiro Kato
Kinki University, Department of Physics, 3-4-1 Kowakae, Higashi-Osaka, Osaka 577-8502, Japan

Akimasa Ishikawa, Kiyotomo Kawagoe, Takashi Matsushita, Hiroshi Takeda, Satoru Uozumi, Yuji Yamazaki
Kobe University, Department of Physics, 1-1 Rokkodai-cho, Nada-ku, Kobe, Hyogo 657-8501, Japan

Takashi Watanabe
Kogakuin University, Department of Physics, Shinjuku Campus, 1-24-2 Nishi-Shinjuku, Shinjuku-ku, Tokyo 163-8677, Japan

Fumiyoshi Kajino
Konan University, Department of Physics, Okamoto 8-9-1, Higashinada, Kobe 658-8501, Japan

Takahiro Fusayasu
Nagasaki Institute of Applied Science, 536 Abamachi, Nagasaki-Shi, Nagasaki 851-0193, Japan

Takashi Mori
Nagoya University, High Energy Physics Lab., Div. of Particle and Astrophysical Sciences, Furo-cho, Chikusa-ku, Nagoya, Aichi 464-8602, Japan

Takeo Kawasaki, Hitoshi Miyata, Minori Watanabe
Niigata University, Department of Physics, Ikarashi, Niigata 950-218, Japan

Hiroaki Ono
Nippon Dental University School of Life Dentistry at Niigata, 1-8 Hamaura-cho, Chuo-ku, Niigata 951-1500, Japan

Eiichi Nakano
Osaka City University, Department of Physics, Faculty of Science, 3-3-138 Sugimoto, Sumiyoshi-ku, Osaka 558-8585, Japan

Hirotoshi Kuroiwa, Kenichi Nakashima, Akira Sugiyama, Shiro Suzuki, Hiroshi Yamaguchi
Saga University, Department of Physics, 1 Honjo-machi, Saga-shi, Saga 840-8502, Japan

Yoji Hasegawa, Yasuhiro Ide, Katsushige Kotera, Miho Nishiyama, Takayuki Sakuma, Tohru Takeshita, Shunsuke Tozuka, Koji Yanagida
Shinshu University, 3-1-1, Asahi, Matsumoto, Nagano 390-8621, Japan

Masaya Iwabuchi, Ryo Yonamine
Sokendai, The Graduate University for Advanced Studies, Shonan Village, Hayama, Kanagawa 240-0193, Japan

Kazurayama Hironori, Yasuyuki Horii, Kennosuke Itagaki, Kazutoshi Ito, Yusuke Kamai, Eriko Kato, Tomonori Kusano, Tadashi Nagamine, Yoshimasa Ono, Yoshiyuki Onuki, Tomoyuki Sanuki, Rei Sasaki, Yutaro Sato, Fumihiko Suekane, Yosuke Takubo, Akira Yamaguchi, Hitoshi Yamamoto, Kohei Yoshida
Tohoku University, Department of Physics, Aoba District, Sendai, Miyagi 980-8578, Japan

Osamu Nitoh
Tokyo University of Agriculture Technology, Department of Applied Physics, Naka-machi, Koganei, Tokyo 183-8488, Japan

Toshinori Abe, Hiroki Kawahara, Sachio Komamiya
University of Tokyo, Department of Physics, 7-3-1 Hongo, Bunkyo District, Tokyo 113-0033, Japan

Toshinori Ikuno, Shinhong Kim, Yuji Sudo
University of Tsukuba, Institute of Physics, 1-1-1 Ten'nodai, Tsukuba, Ibaraki 305-8571, Japan

Donghee Kim, Guinyun Kim, Hyunok Kim, Hong Joo Kim, Hwanbae Park
Center for High Energy Physics (CHEP) / Kyungpook National University, 1370 Sankyuk-dong, Buk-gu, Daegu 702-701, Korea

Eun-Joo Kim
Chonbuk National University, Division of Science Education, Jeonju 561-756, Korea (South)

Jik Lee, Jiwoo Nam, Shinwoo Nam, Il Hung Park, Jongmann Yang
Ewha Womans University, 11-1 Daehyun-Dong, Seodaemun-Gu, Seoul, 120-750, Korea

Byunggu Cheon
Hanyang University, Department of Physics, Seoul 133-791, Korea

Suyong Choi, Intae Yu
Sungkyunkwan University (SKKU), Natural Science Campus 300, Physics Research Division, Chunchun-dong, Jangan-gu, Suwon, Kyunggi-do 440-746, Korea

Choong Sun Kim
Yonsei University, Department of Physics, 134 Sinchon-dong, Sudaemoon-gu, Seoul 120-749, Korea

Nicolo De Groot[16], Sijbrand De Jong[16], Frank Filthaut[16]
Institute for Mathematics, Astrophysics and Particle Physics (IMAPP), P.O. Box 9010, 6500 GL Nijmegen, Netherlands

Stan Bentvelsen, Auke Colijn[16], Paul De Jong, Olga Igonkina, Peter Martin Kluit, Els Koffeman[16], Frank Linde, Marcel Merk[17], Antonio Pellegrino, Jan Timmermans[8], Harry Van Der Graaf, Marcel Vreeswijk
Nikhef, National Institute for Subatomic Physics, P.O. Box 41882, 1009 DB Amsterdam, Netherlands

Gerhard Raven[16]
Vrije Universiteit, Department of Physics, Faculty of Sciences, De Boelelaan 1081, 1081 HV Amsterdam, Netherlands

Gerald Eigen, Per Osland
University of Bergen, Institute of Physics, Allegaten 55, N-5007 Bergen, Norway

Sameen Ahmed Khan
Salalah College of Technology (SCOT), Engineering Department, Post Box No. 608, Postal Code 211, Salalah, Sultanate of Oman

Editha P. Jacosalem
MSU-Iligan Institute of Technology, Department of Physics, Andres Bonifacio Avenue, 9200 Iligan City, Phillipines

Marek Idzik, Danuta Kisielewska, Krzysztof Swientek
AGH University of Science and Technology, Akademia Gorniczo-Hutnicza im. Stanislawa Staszica w Krakowie, Al. Mickiewicza 30 PL-30-059 Cracow, Poland

Marek Adamus
Andrzej Soltan Institute for Nuclear Studies, High Energy Physics Department, P-6, Ul. Hoza 69, PL-00 681 Warsaw, Poland

Witold Daniluk, Eryk Kielar, Tadeusz Lesiak, Krzysztof Oliwa, Bogdan Pawlik, Wojciech Wierba, Leszek Zawiejski
The Henryk Niewodniczanski Institute of Nuclear Physics, Polish Academy of Sciences (IFJ PAN), ul. Radzikowskiego 152, PL-31342 Cracow, Poland

Pawel Luzniak
University of Lodz, Faculty of Physics and Applied Informatics, Pomorska 149/153, PL-90-236 Lodz, Poland

Jacek Ciborowski[18], Grzegorz Grzelak, Lukasz Maczewski[18], Piotr Niezurawski, Aleksander Filip Zarnecki
University of Warsaw, Institute of Experimental Physics, Ul. Hoza 69, PL-00 681 Warsaw, Poland

Janusz Rosiek
University of Warsaw, Institute of Theoretical Physics, Ul. Hoza 69, PL-00 681 Warsaw, Poland

Cornelia Coca, Mihai-Octavian Dima, Laurentiu Alexandru Dumitru, Marius Ciprian Orlandea, Eliza Teodorescu
National Institute of Physics and Nuclear Engineering "Horia Hulubei" (IFIN-HH), Str. Atomistilor no. 407, P.O. Box MG-6, R-76900 Bucharest - Magurele, Romania

Aura Rosca[19]
West University of Timisoara, Faculty of Physics, Bd. V. Parvan 4, 300223 Timisoara, Romania

A. Bondar, A.F. Buzulutskov, L.I. Shechtman, Valery I. Telnov
Budker Institute for Nuclear Physics (BINP), 630090 Novosibirsk, Russia

Marina Chadeeva, Mikhail Danilov, Vasily Morgunov[8], Vladimir Rusinov, Evgueny I. Tarkovsky
Institute of Theoretical and Experimetal Physics, B. Cheremushkinskawa, 25, RU-117259, Moscow, Russia

Alexander Olchevski
Joint Institute for Nuclear Research (JINR), Joliot-Curie 6, 141980, Dubna, Moscow Region, Russia

Eduard Boos, Leonid Gladilin, Mikhail M. Merkin
Lomonosov Moscow State University, Skobeltsyn Institute of Nuclear Physics (MSU SINP), 1(2), Leninskie gory, GSP-1, Moscow 119991, Russia

Boris A. Dolgoshein, Elena Popova
Moscow Engineering Physics Institute (MEPhI), Dept. of Physics, 31, Kashirskoye shosse, 115409 Moscow, Russia

Nicola D'Ascenzo[8], Valery Galkin, Alexei Galkin, Dmitri Ossetski, Dmitri Ryzhikov, Valeri Saveliev
Obninsk State Technical University for Nuclear Engineering (IATE), Obninsk, Russia

Ivanka Bozovic-Jelisavcic, Stevan Jokic, Tatjana Jovin, Judita Mamuzic, Mihajlo Mudrinic, Mila Pandurovic, Ivan Smiljanic
VINCA Institute of Nuclear Sciences, Laboratory of Physics, PO Box 522, YU-11001 Belgrade, Serbia and Montenegro

Jozef Ferencei
Institute of Experimental Physics, Slovak Academy of Sciences, Watsonova 47, SK-04001 Kosice, Slovakia

Enrique Calvo Alamillo, Mary-Cruz Fouz, Jesus Puerta-Pelayo
Centro de Investigaciones Energéticas, Medioambientales y Tecnológicas, CIEMAT, Avenida Complutense 22, E-28040 Madrid, Spain

Juan Pablo Balbuena, Daniela Bassignana, Celeste Fleta, Manuel Lozano, Giulio Pellegrini, Miguel Ullán
Centro Nacional de Microelectrónica (CNM), Instituto de Microelectrónica de Barcelona (IMB), Campus UAB, 08193 Cerdanyola del Vallès (Bellaterra), Barcelona, Spain

Carmen Alabau Pons, Markus Ball, Angeles Faus-Golfe, Juan Fuster, Carlos Lacasta Llácer, Carlos Mariñas, Marcel Vos
Instituto de Fisica Corpuscular (IFIC), Centro Mixto CSIC-UVEG, Edificio Investigacion Paterna, Apartado 22085, 46071 Valencia, Spain

Jordi Duarte Campderrós, Marcos Fernandez Garcia, Francisco Javier González Sánchez, Richard Jaramillo Echeverría, Amparo Lopez Virto, Celso Martinez Rivero, David Moya, Alberto Ruiz-Jimeno, Ivan Vila
Instituto de Fisica de Cantabria, (IFCA, CSIC-UC), Facultad de Ciencias, Avda. Los Castros s/n, 39005 Santander, Spain

Bernardo Adeva, Abraham Gallas, Carmen Iglesias Escudero, Juan J. Saborido, Pablo Vazquez Regueiro
Instituto Galego de Fisica de Altas Enerxias (IGFAE,USC) Facultad de Fisica, Campus Sur E-15782 Santiago de Compostela, Spain

Juan Antonio Aguilar-Saavedra, Nuno Castro
Universidad de Granada, Departamento de Física Teórica y del Cosmos, Campus de Fuentenueva, E-18071 Granada, Spain

Thorsten Lux, Cristobal Padilla, Imma Riu
Universitat Autònoma de Barcelona, Institut de Fisica d'Altes Energies (IFAE), Campus UAB, Edifici Cn, E-08193 Bellaterra, Barcelona, Spain

Jordi Riera-Babures, Xavier Vilasis-Cardona
Universitat Ramon Llull, La Salle, C/ Quatre Camins 2, 08022 Barcelona, Spain

Angel Dieguez, Lluis Garrido Beltran
University de Barcelona, Facultat de Física, Av. Diagonal, 647, Barcelona 08028, Spain

Vincent Hedberg, Leif Jonsson, Bjorn Lundberg, Ulf Mjornmark, Anders Oskarsson, Lennart Osterman, Evert Stenlund
Lunds Universitet, Fysiska Institutionen, Avdelningen för Experimentell Högenergifysik, Box 118, 221 00 Lund, Sweden

Michael Campbell, Albert De Roeck, Konrad Elsener, Andrea Gaddi, Hubert Gerwig, Christian Grefe[14], Michael Hauschild, Lucie Linssen, Xavier Llopart Cudie, Luciano Musa, Dieter Schlatter, Peter Speckmayer
CERN, CH-1211 Genève 23, Switzerland

Günther Dissertori, Gerard Faber, Alain Hervé, Nebojsa Smiljkovic
ETH Zürich, Institute for Particle Physics (IPP), Schafmattstrasse 20, CH-8093 Zürich, Switzerland

Hideyuki Nakazawa
National Central University, High Energy Group, Department of Physics, Chung-li, Taiwan 32001

Paoti Chang, Wei-Shu Hou, Koji Ueno, Min-Zu Wang
National Taiwan University, Physics Department, Taipei, Taiwan 106

Gudrid A. Moortgat-Pick[21]
Durham University, Department of Physics, Ogen Center for Fundamental Physics, South Rd., Durham DH1 3LE, UK

James Ballin
Imperial College, Blackett Laboratory, Department of Physics, Prince Consort Road, London, SW7 2BW, UK

Andre Sopczak
Lancaster University, Physics Department, Lancaster LA1 4YB, UK

Grahame Blair, Veronique Boisvert
Royal Holloway, University of London (RHUL), Department of Physics, Egham, Surrey TW20 0EX, UK

Chris Damerell, Kristian Harder
STFC Rutherford Appleton Laboratory, Chilton, Didcot, Oxon OX11 0QX, UK

Derek J. Attree, Valeria Bartsch, Filimon Gournaris, Alexey Lyapin, David J. Miller, Martin Postranecky, Matthew Warren, Matthew Wing
University College of London (UCL), High Energy Physics Group, Physics and Astronomy Department, Gower Street, London WC1E 6BT, UK

Owen Miller, Nigel K. Watson, John A. Wilson
University of Birmingham, School of Physics and Astronomy, Particle Physics Group, Edgbaston, Birmingham B15 2TT, UK

Joel Goldstein
University of Bristol, H. H. Wills Physics Lab, Tyndall Ave., Bristol BS8 1TL, UK

Bart Hommels, John Marshall, Georgios Mavromanolakis[25], Mark Thomson, David R Ward

University of Cambridge, Cavendish Laboratory, J J Thomson Avenue, Cambridge CB3 0HE, UK

Victoria J Martin, Hajrah Tabassam, Roberval Walsh
University of Edinburgh, School of Physics, James Clerk Maxwell Building, The King's Buildings, Mayfield Road, Edinburgh EH9 3JZ, UK

Richard Bates, Craig Buttar, Tony Doyle, Lars Eklund, Val O'Shea, Chris Parkes, Aidan Robson
University of Glasgow, Department of Physics & Astronomy, University Avenue, Glasgow G12 8QQ, Scotland, UK

Tim Greenshaw
University of Liverpool, Department of Physics, Oliver Lodge Lab, Oxford St., Liverpool L69 7ZE, UK

David Bailey, Roger Barlow[21]
University of Manchester, School of Physics and Astronomy, Schuster Lab, Manchester M13 9PL, UK

Brian Foster
University of Oxford, Particle Physics Department, Denys Wilkinson Bldg., Keble Road, Oxford OX1 3RH England, UK

Stefano Moretti[23]
University of Southampton, School of Physics and Astronomy, Highfield, Southampton S017 1BJ, England, UK

Jose Repond
Argonne National Laboratory (ANL), 9700 S. Cass Avenue, Argonne, IL 60439, USA

John Butler
Boston University, Department of Physics, 590 Commonwealth Avenue, Boston, MA 02215, USA

Lawrence Gibbons, J. Ritchie Patterson, Daniel Peterson
Cornell University, Laboratory for Elementary-Particle Physics (LEPP), Ithaca, NY 14853, USA

Marco Verzocchi
Fermi National Accelerator Laboratory (FNAL), P.O.Box 500, Batavia, IL 60510-0500, USA

Rick J. Van Kooten
Indiana University, Department of Physics, Swain Hall West 117, 727 E. 3rd St., Bloomington, IN 47405-7105, USA

Z.D. Greenwood, Lee Sawyer, Markus Wobisch
Louisiana Tech University, Department of Physics, Ruston, LA 71272, USA

Dhiman Chakraborty, David Hedin, Guilherme Lima, Vishnu Zutshi
Northern Illinois University, Department of Physics, DeKalb, Illinois 60115-2825, USA

Qing He, Kirk T Mcdonald
Princeton University, Department of Physics, P.O. Box 708, Princeton, NJ 08542-0708, USA

Bruce A. Schumm
University of California Santa Cruz, Institute for Particle Physics, 1156 High Street, Santa Cruz, CA 95064, USA

Burak Bilki, Ed Norbeck, Yasar Onel
University of Iowa, Department of Physics and Astronomy, 203 Van Allen Hall, Iowa City, IA 52242-1479, USA

Jadranka Sekaric, Brian Van Doren, Graham W. Wilson
University of Kansas, Department of Physics and Astronomy, Malott Hall, 1251 Wescoe Hall Drive, Room 1082, Lawrence, KS 66045-7582, USA

Haijun Yang
University of Michigan, Department of Physics, 500 E. University Ave., Ann Arbor, MI 48109-1120, USA

Giovanni Bonvicini
Wayne State University, Department of Physics, Detroit, MI 48202, USA

[1] also at TRIUMF, 4004 Wesbrook Mall, Vancouver, BC V6T 2A3, Canada

[2] also at Université de Montréal, Département de Physique, Groupe de Physique des Particules, C.P. 6128, Succ. Centre-ville, Montréal, Qc H3C 3J7, Canada

[3] also at Institute of High Energy Physics - IHEP, Chinese Academy of Sciences, P.O. Box 918, Beijing, China 100049

[4] also at Helsinki Institute of Physics (HIP), P.O. Box 64, FIN-00014 University of Helsinki, Finland

[5] also at Laboratoire de l'Accélérateur Linéaire (LAL), Université Paris-Sud 11, Bâtiment 200, 91898 Orsay, France

[6] also at Université de Strasbourg, UFR de Sciences Physiques, 3-5 Rue de l'Université, F-67084 Strasbourg Cedex, France

[7] also at Brandenburg University of Technology, Postfach 101344, D-03013 Cottbus, Germany

[8] also at Deutsches Elektronen-Synchrotron DESY, A Research Centre of the Helmholtz Association, Notkestrasse 85, 22607 Hamburg, Germany (Hamburg site)

[9] also at Deutsches Elektronen-Synchrotron DESY, A Research Centre of the Helmholtz Association, Platanenallee 6, 15738 Zeuthen, Germany (Zeuthen site)

[10] also at Excellence Cluster Universe, Technische Universität München, Boltzmannstr. 2, 85748 Garching, Germany

[11] also at Gottfried Wilhelm Leibniz Universität Hannover, Fakultät für Mathematik und Physik, Appelstraße 2, 30167 Hannover, Germany

[12] also at University of Hamburg, Physics Department, Institut für Experimentalphysik, Luruper Chaussee 149, 22761 Hamburg, Germany

[13] also at University of Wuppertal, Gaußstraße 20, D-42119 Wuppertal, Germany

[14] also at Universität Bonn, Physikalisches Institut, Nußallee 12, 53115 Bonn, Germany

[15] also at Istituto Nazionale di Fisica Nucleare (INFN), Sezione di Milano, Via Celoria 16, I-20133 Milano, Italy

[16] also at Nikhef, National Institute for Subatomic Physics, P.O. Box 41882, 1009 DB Amsterdam, Netherlands

[17] also at Vrije Universiteit, Department of Physics, Faculty of Sciences, De Boelelaan 1081, 1081 HV Amsterdam, Netherlands

[18] also at University of Lodz, Faculty of Physics and Applied Informatics, Pomorska 149/153, PL-90-236 Lodz, Poland

[19] also at National Institute of Physics and Nuclear Engineering "Horia Hulubei" (IFIN-HH), Str. Atomistilor no. 407, P.O. Box MG-6, R-76900 Bucharest - Magurele, Romania

[20] also at CERN, CH-1211 Genève 23, Switzerland

[21] also at Cockcroft Institute, Daresbury, Warrington WA4 4AD, UK

[22] also at Royal Holloway, University of London (RHUL), Department of Physics, Egham, Surrey TW20 0EX, UK

[23] also at STFC Rutherford Appleton Laboratory, Chilton, Didcot, Oxon OX11 0QX, UK

[24] also at Enrico Fermi Institute, University of Chicago, 5640 S. Ellis Avenue, RI-183, Chicago, IL 60637, USA

[25] also at Fermi National Accelerator Laboratory (FNAL), P.O.Box 500, Batavia, IL 60510-0500, USA

CONTENTS

1 Introduction **1**
1.1 ILD Philosophy . . . 1
1.2 Basic Layout of ILD . . . 2
1.3 Performance Requirements . . . 3
1.4 Overview of the ILD Letter of Intent . . . 4

2 Detector Optimisation **5**
2.1 Simulation Tools and Detector Parameters . . . 5
2.1.1 GLD Software: JSF . . . 6
2.1.2 LDC Software: Mokka and Marlin . . . 7
2.2 Detector Optimisation for Particle Flow . . . 8
2.2.1 Particle Flow Optimisation Methodology . . . 9
2.2.2 HCAL Depth . . . 9
2.2.3 Magnetic Field versus Detector Radius . . . 10
2.2.4 Detector Aspect Ratio . . . 12
2.2.5 ECAL and HCAL Granularity . . . 13
2.2.6 ECAL and HCAL detector technology . . . 13
2.3 Background Considerations . . . 14
2.4 Detector Optimisation for Tracking . . . 15
2.4.1 Momentum Resolution . . . 15
2.4.2 Impact Parameter Resolution . . . 16
2.4.3 Conclusions . . . 17
2.5 Flavour Tagging . . . 18
2.6 Physics Performance . . . 19
2.6.1 Higgs Recoil Mass . . . 19
2.6.2 Tau pairs . . . 20
2.6.3 Chargino and neutralino production . . . 21
2.7 Conclusions . . . 22
2.8 Choice of ILD Parameters . . . 24

3 Physics Performance **25**
3.1 Software for ILD Performance Studies . . . 25
3.2 ILD Detector Performance . . . 27
3.2.1 ILD Tracking Performance . . . 27
3.2.2 Background Studies . . . 29
3.2.3 ILD Flavour Tagging Performance . . . 34

3.2.4 ILD Particle Flow Performance . . . 36
3.3 Physics Performance . . . 37
3.3.1 Higgs Boson mass . . . 37
3.3.2 Higgs Boson Branching Fractions . . . 41
3.3.3 Tau-pairs . . . 43
3.3.4 Chargino and Neutralino Production . . . 44
3.3.5 Top production . . . 47
3.3.6 Strong EWSB . . . 49
3.3.7 Lepton production in SPS1a' . . . 49
3.3.8 Photon Final States . . . 52
3.4 Other Studies . . . 53
3.4.1 Measurement of Beam Polarisation from WW production . . . 53
3.4.2 Heavy Gauge Boson Production in Littlest Higgs Model . . . 53
3.4.3 ZHH Production . . . 54
3.5 Conclusions . . . 54
3.5.1 Detector Performance . . . 54
3.5.2 Physics Performance . . . 55

4 The ILD Sub-Detector Systems 57
4.1 Vertex Detector . . . 57
4.1.1 Physics Driven Requirements and Running Constraints . . . 58
4.1.2 Global Design Aspects . . . 59
4.1.3 Pixel Technology and System Integration Studies . . . 61
4.1.4 Outlook . . . 62
4.2 Silicon Tracking . . . 63
4.2.1 Baseline Design of the Silicon Trackers . . . 63
4.2.2 Performances of the Silicon tracking system . . . 64
4.2.3 Calibration Procedures . . . 67
4.2.4 Silicon Tracker Material Budget . . . 67
4.2.5 Baseline construction and Integration of Silicon components . . . 68
4.2.6 R&D needs and prospects for Silicon tracking . . . 68
4.3 The Time Projection Chamber . . . 69
4.3.1 Motivation . . . 69
4.3.2 Design . . . 70
4.3.3 R&D Effort for the LCTPC . . . 75
4.4 The Calorimeter System . . . 77
4.4.1 Introduction to calorimeters . . . 77
4.4.2 General Layout . . . 77
4.4.3 The Electromagnetic Calorimeter . . . 77
4.4.4 The Hadronic Calorimeter . . . 85
4.4.5 Calorimeter Readout System . . . 93
4.4.6 Status and future R&D plans . . . 95
4.5 Forward Detectors . . . 95
4.5.1 The Design of the Very Forward Region . . . 96
4.5.2 LumiCal . . . 97
4.5.3 BeamCal . . . 98
4.5.4 The Pair Monitor . . . 100

4.5.5 GamCal . . . 100
4.5.6 LHCal . . . 100
4.5.7 Priority R&D topics . . . 101
4.6 Coil and Return Yoke . . . 101
4.6.1 Physics Requirements . . . 101
4.6.2 Magnet Design . . . 102
4.6.3 Magnetic Field . . . 104
4.6.4 Technical Aspects . . . 104
4.7 Muon Detector . . . 104
4.7.1 Conceptual Design . . . 105
4.7.2 Performance . . . 105
4.7.3 Outlook . . . 106
4.8 Calibration and Alignment . . . 107
4.8.1 Tracking System Calibration and Alignment . . . 108
4.8.2 Calorimeter Calibration and Alignment . . . 113
4.8.3 Conclusions . . . 117

5 Data Acquisition and Computing 119
5.1 DAQ Concept . . . 119
5.2 Front end electronics . . . 122
5.3 Detector Control and Monitoring . . . 122
5.4 Data Processing . . . 122
5.4.1 Event Building and Prompt Reconstruction . . . 122
5.4.2 Offline computing . . . 123
5.5 Software . . . 123
5.6 Outlook and R&D . . . 124

6 Detector Integration
Machine Detector Interface 125
6.1 Mechanical Concept . . . 125
6.2 Detector Assembly and Opening . . . 126
6.3 Civil facilities and services . . . 127
6.3.1 Detector Services . . . 127
6.3.2 Surface Assembly Hall . . . 128
6.3.3 Underground Experiment Hall . . . 128
6.4 Push-pull Operations . . . 129
6.4.1 Moving the ILD Detector . . . 131
6.4.2 Shielding . . . 132
6.4.3 Alignment and Calibration . . . 132
6.5 R&D Plans: Detector Integration . . . 132
6.6 The Interaction Region . . . 133
6.6.1 The Beampipe . . . 133
6.6.2 Support of the Final Focus Magnets . . . 135
6.7 Machine-Induced Backgrounds . . . 136
6.7.1 Background Uncertainties . . . 136
6.7.2 Provisions for the Low-P Beam Parameters . . . 137
6.8 Measurement of Energy and Polarisation . . . 138
6.9 R&D Plans: Machine Detector Interface . . . 138

7 Costing **139**
7.1 Methodology of Costing 139
7.2 ILD Work Breakdown Structure 140
7.3 ILD Current Cost Evaluation 140
7.4 Cost Scaling Laws with Detector Parameters 141
7.5 Conclusion 144

8 The ILD group **145**

9 R&D Plan **147**

10 Conclusions **151**

LIST of FIGURES

1.2-1 View of the ILD detector concept. 3

2.2-1 Jet energy resolution versus number of HCAL layers. 10
2.2-2 Dependence of jet energy resolution on B-field and ECAL inner radius. . . . 11
2.2-3 Jet energy resolution in the endcap region. 12
2.2-4 Jet energy resolution vs ECAL and HCAL segmentation. 13
2.3-5 Track density of pair background. 15
2.4-6 Transverse momentum resolution versus momentum. 16
2.4-7 Impact parameter resolution. 17
2.5-8 Flavour tagging comparison. 18
2.6-9 Reconstructed Higgs recoil mass. 19
2.6-10 $\tau \to \pi\nu$ selection 21
2.6-11 W and Z mass and energy distributions. 22

3.1-1 The ILD00 detector. 26
3.2-2 Numbers of hits and Material budget of the ILD tracking system. 27
3.2-3 Tracking performance. 28
3.2-4 Track finding efficiency. 29
3.2-5 TPC hits with 150 BXs background. 30
3.2-6 TPC hits with background after micro-curler removal. 31
3.2-7 Reconstructed TPC tracks in the presence of background. 31
3.2-8 Background tracks in the Silicon detectors. 33
3.2-9 Tracking Efficiency with Background. 34
3.2-10 Higgs recoil mass distribution with background effects 35
3.2-11 ILD flavour tagging performance. 35
3.2-12 ILD jet energy resolution versus $\cos\theta$. 37
3.3-13 Higgs recoil mass. 38
3.3-14 Higgs recoil mass with Bremsstrahlung. 39
3.3-15 Generated and reconstructed Higgs recoil mass. 40
3.3-16 Flavour tagging in $\mathrm{ZH} \to \ell^+\ell^- X$. 42
3.3-17 $\mathrm{H} \to \mathrm{c\bar{c}}$ from $\mathrm{ZH} \to \mathrm{q\bar{q}}X$ and $\mathrm{ZH} \to \nu\bar{\nu}X$. 43
3.3-18 $\tau \to \pi\nu$ selection. 44
3.3-19 Chargino/neutralino selection and mass fits. 46
3.3-20 Top quark mass. 47
3.3-21 Top quark forward-backward asymmetry. 48
3.3-22 $\nu_e\bar{\nu}_e$WW and $\nu_e\bar{\nu}_e$ZZ mass distributions. 49
3.3-23 Smuon event selection. 51

3.3-24 Stau selection. 52

4.1-1 Vertex detector geometries for the two design options. 60
4.2-2 Schematic view of the tracking system and of the SI tracking components. . 65
4.2-3 Transverse momentum resolution vs p_T. 66
4.3-4 Occupancy in the TPC 72
4.3-5 R&D Results from Large Prototype and Small Prototype Studies 75
4.3-6 Design ideas for a thin TPC endcap 76
4.4-7 Global layout of the ECAL (left) and layout of one module (right). 78
4.4-8 Reconstructed vs true energy for photons in di-jets. 79
4.4-9 Reconstructed tau masses vs ECAL cell size. 79
4.4-10 Influence of material in front of the ECAL. 80
4.4-11 Si sensors for the ECAL. 82
4.4-12 Layout of scitillator strips. 83
4.4-13 Layout of the MPPC, micro-strip line and readout chip on the FPC board. 84
4.4-14 Calibration systen for the ScECAL. 84
4.4-15 HCAL layout 1, view of the test beam experiment. 86
4.4-16 Design 2 layout of the HCAL (left) and layout of one module (right). 87
4.4-17 Details of AHCAL module design. 88
4.4-18 AHCAL physics prototype layer (left), event display (right). 90
4.4-19 Linearity and resolution for AHCAL. 90
4.4-20 Longitudinal shower profile, test beam data and simulations. 91
4.4-21 Single gap GRPC scheme 91
4.4-22 Mini-DHCAL prototype. 92
4.5-23 The very forward region of ILD. 96
4.5-24 The Si-W LumiCal. 98
4.5-25 Prototype silicon sensor for LumiCal. 98
4.5-26 Prototypes of readout chips. 98
4.5-27 One half of BeamCal. 99
4.5-28 Distribution of energy deposited by pairs in BeamCal. 99
4.5-29 A GaAs prototype detector for BeamCal. 100
4.5-30 Pair Monitor 100
4.6-31 ILD magnet cross section. 102
4.6-32 Stray fields and endcap deformation. 103
4.7-33 Strip response and efficiency. 106
4.7-34 Muon identification efficiency. 106
4.7-35 Correcting for energy leakage in the calorimeter. 107
4.8-36 Infra-red laser beam traversing silicon sensors. 110
4.8-37 AMS results on the reconstruction of laser signals in silicon strip detectors. 111
4.8-38 Required luminosity for in-situ calorimeter calibration. 116
4.8-39 Comparison of measured energy resolution for different test beam locations. 116

5.1-1 General layout of the DAQ system 120

6.1-1 The ILD detector. 125
6.2-2 Detector opening procedures. 127
6.3-3 Cryogenics block diagram. 129
6.3-4 Design study for the underground experimental hall. 130

6.4-5 ILD detector in the garage position and on the beam line. 131
6.6-6 Interaction region of the ILD detector: inner detectors. 133
6.6-7 Beam pipe geometry. 134
6.6-8 Beampipe buckling and vacuum profiles. 135
6.6-9 Support of the magnets in the detector. 135
6.7-10 Background hit densities on the inner silicon detectors. 138

7.4-1 Cost vs. transverse detector size. 142
7.4-2 Cost vs. longitudinal detector size. 143
7.4-3 Dependence of the cost with the number of layers in the ECal. 143
7.4-4 Cost vs number of layers in the HCAL. 143

8.0-1 Structure of the ILD group. 146

LIST OF FIGURES

LIST of TABLES

2.1-1 Detector parameters for the optimisation studies. 6
2.2-2 Jet energy resolution. 10
2.2-3 Relative jet energy resolutions. 12
2.6-4 Relative Higgs mass precision. 20
2.6-5 $\tau^{\pm} \to \pi^{\pm}\nu$ selection. 21
2.6-6 The efficiency for $\chi_1^{\pm}$ and χ_2^0 selection. 22

3.1-1 Simulated tracking point resolutions. 25
3.2-2 Vertex detector occupancy. 32
3.2-3 ILD jet energy resolution. 36
3.3-4 Expected statistical uncertainties on m_{H}. 39
3.3-5 Higgs branching ratio measurement. 43
3.3-6 Efficiency and purity of tau decay mode selections. 45
3.5-7 Summary of physics sensitivities. 55

4.1-1 Impact parameter resolution at ILD and other colliders. 59
4.1-2 Parameters of the VTX detector options. 60
4.2-3 The projected values of basic SIT, SET, FTD, and ETD characteristics. . . 65
4.2-4 Extrapolation precision (R-ϕ and z). 66
4.3-5 Goals for performance and design of the LCTPC 70
4.4-6 Photon identification in the ECAL vs cell size. 79
4.4-7 Interaction of pions in the different parts of the tracker region. 81
4.6-8 Main geometrical and electrical parameters 103
4.8-9 Details of the Silicon detectors. 110

5.1-1 Data Volume in MB per bunch train for the major ILD detector components 121

6.7-1 Background numbers for ILD. 137

7.3-1 Table of sub-system costs. 141

CHAPTER 1

Introduction

1.1 ILD PHILOSOPHY

The **I**nternational **L**arge **D**etector (ILD) is a concept for a detector at the International Linear Collider, ILC. The ILC will collide electrons and positrons at energies of initially 500 GeV, upgradeable to 1 TeV. The ILC has an ambitious physics program, which will extend and complement that of the Large Hadron Collider (LHC). The ILC physics case has been well documented, most recently in the ILC Reference Design Report, RDR [1]. A hallmark of physics at the ILC is precision. The clean initial state and the comparatively benign environment of a lepton collider are ideally suited to high precision measurements. To take full advantage of the physics potential of ILC places great demands on the detector performance. The design of ILD, which is based on the GLD [2] and the LDC [3] detector concepts, is driven by these requirements. Excellent calorimetry and tracking are combined to obtain the best possible overall event reconstruction, including the capability to reconstruct individual particles within jets for particle flow calorimetry. This requires excellent spatial resolution for all detector systems. A highly granular calorimeter system is combined with a central tracker which stresses redundancy and efficiency. In addition, efficient reconstruction of secondary vertices and excellent momentum resolution for charged particles are essential for an ILC detector. The interaction region of the ILC is designed to host two detectors, which can be moved into the beam position with a "push-pull" scheme. The mechanical design of ILD and the overall integration of subdetectors takes these operational conditions into account. The main features of ILD are outlined below.

The central component of the ILD tracker is a Time Projection Chamber (TPC) which provides up to 224 precise measurements along the track of a charged particle. This is supplemented by a system of Silicon (Si) based tracking detectors, which provide additional measurement points inside and outside of the TPC, and extend the angular coverage down to very small angles. A Si-pixel based vertex detector (VTX) enables long lived particles such as b- and c-hadrons to be reconstructed. This combination of tracking devices, which has a large degree of redundancy, results in high track reconstruction efficiencies, and unprecedented momentum resolution and vertex reconstruction capabilities. One of the most direct measures of detector performance at the ILC is the jet-energy resolution. Precise di-jet mass reconstruction and separation of hadronically decaying W and Z bosons are essential for many physics channels. The ultimate jet energy resolution is achieved when every particle in the event, charged and neutral, is measured with the best possible precision. Within the

paradigm of particle flow calorimetry, this goal is achieved by reconstructing charged particles in the tracker, photons in the electromagnetic calorimeter (ECAL), and neutral hadrons in the ECAL and hadronic calorimeter (HCAL). The ultimate performance is reached for perfect separation of charged-particle clusters from neutral particle clusters in the calorimeters. Thus, a highly granular calorimeter outside the tracker is the second key component of ILD. Sampling calorimeters with dense absorber material and fine grained readout are used. A tungsten absorber based electromagnetic calorimeter (ECAL) covers the first interaction length, followed by a somewhat coarser steel based sampling hadronic calorimeter (HCAL). Several ECAL and HCAL readout technologies are being pursued.

1.2 BASIC LAYOUT OF ILD

The proposed ILD concept is designed as a multi-purpose detector, which provides excellent precision in spatial and energy measurement over a large solid angle. It has the following components:

- A multi-layer pixel-vertex detector (VTX), with three super-layers each comprising two layers. To minimise the occupancy from background hits, the first super-layer is only half as long as the outer two. Whilst the underlying detector technology has not yet been decided, the VTX is optimised for excellent point resolution and minimum material thickness. A five layer geometry, VTX-SL, with the layers spaced at equal distances to the IP is investigated as an alternative. In either case the vertex detector has a purely barrel geometry.
- A system of strip and pixel detectors surrounding the VTX detector. In the barrel, two layers of Si strip detectors (SIT) are arranged to bridge the gap between the VTX and the TPC. In the forward region, a system of Si-pixel and Si-strip disks (FTD) provides low angle tracking coverage.
- A large volume time projection chamber (TPC) with up to 224 points per track. The TPC is optimised for excellent 3-dimensional point resolution and minimum material in the field cage and in the end-plate. It also provides $\mathrm{d}E/\mathrm{d}x$ based particle identification capabilities.
- A system of Si-strip detectors, one behind the end-plate of the TPC (ETD) and one in between the TPC and the ECAL (SET). These provide additional high precision space points which improve the tracking measurements and provide additional redundancy in the regions between the main tracking volume and the calorimeters.
- A highly segmented ECAL providing up to 30 samples in depth and small transverse cell size. Two technology options are considered; Si-W and scintillator-W.
- A highly segmented HCAL with up to 48 longitudinal samples and small transverse cell size. Two options are considered, both based on a Steel-absorber structure. One option uses scintillator tiles of $3 \times 3\,\mathrm{cm}^2$, which are read out with an analogue system. The second uses a gas-based readout which allows a $1 \times 1\,\mathrm{cm}^2$ cell geometry with a binary or semi-digital readout of each cell.
- A system of high precision, radiation hard, calorimetric detectors in the very forward region (LumiCAL, BCAL, LHCAL). These extend the calorimetric coverage to almost 4π, measure the luminosity, and monitor the quality of the colliding beams.
- A large volume superconducting coil surrounds the calorimeters, creating an axial B-field of nominally 3.5 Tesla.

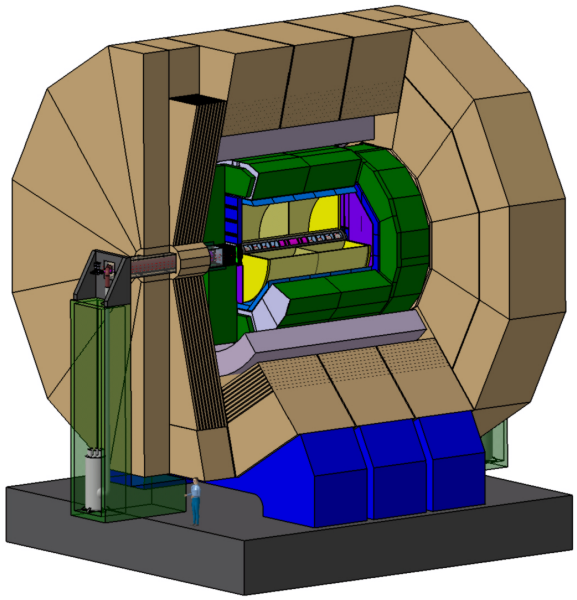

FIGURE 1.2-1. View of the ILD detector concept.

- An iron yoke, instrumented with scintillator strips or RPCs, returns the magnetic flux of the solenoid, and at the same time, serves as a muon filter, muon detector and tail catcher.
- A sophisticated data acquisition (DAQ) system which operates without an external trigger, to maximise the physics sensitivity.

Precision physics at the ILC requires that the beam parameters are known with great accuracy. The beam energy and the beam polarization will be measured in small dedicated experiments, which are shared by the two detectors present in the interaction region. These detectors will only be covered briefly in this document, more details may be found in a dedicated document. The luminosity of the interaction will be measured by the luminometers integrated in ILD. To enable the operation of the detector in a "push-pul" scenario, the complete detector is mounted on a movable platform, which can move sideways out of the beam to make space for the second detector in the interaction region. The platform ensures that the integrity and calibration of the detector is minimally disturbed during the moving process, making the re-commissioning of the detector after the "push-pull" operation easier. The ILD detector concept is shown graphically in Figure 1.2-1.

1.3 PERFORMANCE REQUIREMENTS

The requirements and resulting challenges for detectors at the ILC are described in the ILC RDR [4]. The ILC is designed to investigate in detail the mechanism of the electroweak symmetry breaking, and to search for and study new physics at energy scales up to 1 TeV. In addition, the collider will provide a wealth of information on Standard Model (SM) physics, for example top physics, heavy flavour physics, and physics of the Z and W bosons. The requirements for a detector are, therefore, that multi-jet final states, typical for many physics channels, can be reconstructed with high accuracy. The jet energy resolution should be sufficiently good that the hadronic decays of the W and Z can be separated. This translates

into a jet energy resolution of $\sigma_E/E \sim 3-4\%$ (equivalent to $30\%/\sqrt{E}$ at energies below 100 GeV). This requirement is one of the most challenging for ILD and has a large impact on the design of the calorimeters. It also impacts the way the tracking system is optimised. Nevertheless, the reconstruction of events with high precision benefits the ILD physics programme in several ways. A more precise detector will result in smaller systematic errors for many measurements, and thus will extend the ultimate physics reach of the ILC. In addition, a more precise detector implies that the luminosity delivered by the collider is used more efficiently, making it possible to reduce the overall running costs of the facility to reach a particular accuracy.

It is difficult to anticipate the full physics programme at a new facility before the physics of the energy regime where it will operate is known. A detector for the ILC therefore needs to be designed and optimised not only in view of a limited set of benchmark reactions, but also to be as versatile and as flexible as possible. Nevertheless the ILC community has defined a number of challenging benchmark physics reactions, which, to the best of our current knowledge, will form an important part of the physics programme at the ILC. The benchmark reactions stress the study of the Higgs boson and Supersymmetry (SUSY) as a model for a possible new physics scenario at the ILC. They also rely on excellent lepton and flavour tagging and probe the missing energy measurement capability of the detector. These reactions give only a flavour of the physics reach of the ILC.

1.4 OVERVIEW OF THE ILD LETTER OF INTENT

The signatories of this Letter of Intent are an international group of physicists with strong participation from Asia, Europe and the Americas. With this letter of intent the undersigned express their intention to develop further the ILD concept to a point where a concrete proposal can be made. However, at this stage, this does not represent a firm commitment either in terms of manpower or resources.

This document is organised as follows: Chapter 2 describes the studies used to optimise and define the main parameters of the ILD concept; Chapter 3 presents the performance of the ILD concept in terms of the low level detector response, such as momentum resolution, jet energy resolution, and flavour-tagging performance. It also describes a number of physics studies which demonstrate that the ILC concept is well optimised for physics at the ILC operating in the centre-of-mass energy range 200 GeV to 1 TeV; Chapter 4 describes the ILD subdetector systems in the context of the ongoing R&D programme; Chapter 6 describes the interface between ILD and the ILC; Chapter 7 discusses the current understanding of the likely cost of ILD; and finally, Chapters 8 and 9 describe the structure of the ILD group and the necessary R&D needed to realise this project.

CHAPTER 2

Detector Optimisation

The choice of the main parameters of the ILD, such as the magnetic field, B, and overall size, is motivated by extensive simulation studies based on variants of the GLD [2] and LDC [3] detector concepts. The main studies, described in the following sections, are of: i) the performance of particle flow calorimetry in terms of jet energy resolution; ii) the tracking performance for momentum resolution and impact parameter resolution; iii) the beam-related backgrounds and the impact of the choice of B; iv) the efficiency and purity of heavy flavour tagging; v) and the impact on physics performance in three benchmark processes.

Ideally the overall detector cost would feed directly into the optimisation of the ILD detector. However, because of the large uncertainties in the cost of raw materials and detector sensors, it is felt that the approach of optimising the detector performance for a fixed cost is not reliable at this stage. Hence, whilst cost is a consideration in defining the parameters of the ILD concept, the main criterion is to develop a detector concept optimised for physics at the ILC.

2.1 SIMULATION TOOLS AND DETECTOR PARAMETERS

The optimisation of the ILD concept was performed in parallel using the software tools developed by the GLD and the LDC groups. The detector models were simulated using a fairly detailed GEANT4 [5] simulation. A significant effort has been made to use a reasonable geometry for the subdetectors, including a description of dead regions and support structures, as described in in Section 3.1. The studies presented are based on full reconstruction of the simulated events without reference to the Monte Carlo (MC) truth information.

Six detector models were defined; three based on the GLD simulation (GLD, GLDPrime and GLD4LDC) and three based on the LDC simulation (LDC, LDCPrime, and LDC4GLD). The main parameters of the models are summarised in Table 2.1-1. The models represent different compromises between magnetic field and TPC outer radius. The software frameworks (JSF/Jupiter/Satellites and Mokka/Marlin) used to simulate and reconstruct the detector models are summarised below. The detector simulation was performed using GEANT4 (version 9.1 patch01) with the `LCPhysics` physics list [6].

Model Name		GLD	GLD′	GLD4LDC	LDC4GLD	LDC′	LDC	ILD
Simulator		Jupiter			Mokka			Mokka
B field (T)		3.0	3.5	4.0	3.0	3.5	4.0	3.5
Beampipe R_{min}		15.0	14.0	13.0	15.5	14.0	13.0	14.5
Vertex Detector	Geometry	cylindrical			ladders			ladders
	Layers	3 doublets			5			3 doublets
	R_{min}	17.5	16.0	15.0	16.5	15.0	14.0	16.0
Barrel SIT	Layers	4 cylinders			2 cylinders			2 cylinders
	Radii	90, 160, 230, 300			161.4, 270.1			165, 309
TPC drift region	R_{min}	437	435	371	371			395
	R_{max}	1978	1740	1520	1931	1733	1511	1739
	z_{max}	2600	2350	2160	2498	2248	2186	2247.5
TPC pad rows		256	217	196	260	227	190	224
ECAL barrel	R_{min}	2100	1850	1600	2020	1825	1610	1847.4
	Layers	33			20(thin)+9(thick)			20+9
	Total X_0	28.4			22.9			23.6
ECAL endcap z_{min}		2800	2250	2100	2700	2300	2550	2450
HCAL barrel	Layers	46	42	37	48			48
	R_{max}	3617	3260	2857	3554	3359	3144	3330
λ_I (ECAL+HCAL)		6.79	6.29	5.67	6.86			6.86

TABLE 2.1-1
Geometrical parameters of the baseline detector models used for the optimisation studies (GLD, GLDPrime, GLD4LDC, LDC4GLD, LDCPrime and LDC). Also shown are the corresponding parameters for the ILD baseline detector. Unless otherwise specified, values are shown in units of mm.

2.1.1 GLD Software: JSF

JSF [7] is a ROOT [8] based software framework for modular applications, such as event generation, fast and full simulation, event reconstruction and data analysis. The two main components are Jupiter [9] and Satellites [9]. Jupiter is a GEANT4 based detector simulation, designed to enable easy installation and modification of subdetector components. Satellites is a collection of event reconstruction modules in the JSF framework. Satellites includes smearing of hit points simulated by Jupiter, a "cheated" track finder using MC information to associate hits to tracks, a Kalman Filter based track fitter, and a cheated particle flow algorithm (PFA).

Jupiter reads a set of detector parameters at run time from a text file, which makes it easy to study different detector configurations. The geometry information is saved in an output ROOT file for use by event reconstruction. In the Jupiter detector simulation the vertex detector and intermediate silicon trackers are modelled as cylinders. The calorimeters have a 12-fold symmetry. The electromagnetic calorimeter consists of a sandwich structure comprising layers of 3 mm of tungsten absorber, 2 mm of scintillator, and a 1 mm air gap. The hadron calorimeter consists of layers comprising of 20 mm of iron absorber, 5 mm of

plastic scintillator, and a 1 mm air gap. For the purpose of simulation, the scintillator in both the ECAL and HCAL is segmented into $1 \times 1\,\mathrm{cm}^2$ readout tiles. Signals in these tiles can be combined at the time of reconstruction to simulate the strip readout structure of proposed system. In the version of the simulation used for the studies presented here, there is no gap between the ECAL and HCAL. Jupiter was executed as a module of the JSF and GEANT4 hits in each sensitive detector are saved in a ROOT file for subsequent study with the Satellites package or as an LCIO [10] file for reconstruction with MarlinReco [11].

The point resolution of the tracking chambers was implemented in the Satellites reconstruction. The GEANT4 hit points in the vertex detector (VTX) and intermediate silicon tracker (IT) were smeared with a Gaussian with the following resolutions. For the VTX, $\sigma_{r\phi}$ and σ_z were taken to be 2.8μm. For the barrel silicon tracker, a resolution of 10 μm was used for both $\sigma_{r\phi}$ and σ_z. The TPC space points were smeared by Gaussian resolutions, $\sigma_{r\phi}$ and σ_z, given by the following physically motivated form:

$$\begin{aligned} \sigma_{r\phi}^2/\mu\mathrm{m}^2 &= 50^2 + 900^2 \sin^2\phi + \left((25^2/22) \times (4/B)^2 \sin\theta\right) z; \\ \sigma_z^2/\mu\mathrm{m}^2 &= 400^2 + 80^2 \times z; \end{aligned}$$

where z is the drift length in cm, B is the magnetic field strength in Tesla, and θ and ϕ are the track angles with respect to the axes perpendicular to the readout plane and perpendicular to the pad rows, and the resolutions are given in μm. For the calorimeter hits, no additional smearing is applied at reconstruction time; the simulated energy deposits in the scintillator tiles are used directly.

The optimisation studies in the GLD framework use the Satellites reconstruction to investigate tracking performance and MarlinReco for other studies. The interoperability between the two software frameworks is provided by the LCIO data format, *e.g.* after simulating the detector response with the Jupiter program, MarlinReco and PandoraPFA [12] were used for the event reconstruction.

2.1.2 LDC Software: Mokka and Marlin

The software framework developed by the LDC concept is based on the LCIO persistency format and event data model. The detailed simulation of the detector response is performed by the GEANT4 based Mokka [13] application. The detailed subdetector geometries and component materials are stored in a MySQL database. The overall detector is then built from individual subdetectors, making it relatively straightforward to compare different technology choices. The corresponding `C++` code instantiating the subdetector geometry in memory is written such that the whole detector model can be scaled in length and radius; this feature proved invaluable in optimising the detector geometry. The GEAR [14] package provides access to these geometrical detector properties at the reconstruction and analysis level. The Mokka simulation of the different subdetectors is described in more detail in Section 3.1.

The Mokka generated events are processed in Marlin [15]. Marlin is a modular `C++` application framework which supports plug-in modules (called processors) which can be loaded at runtime. This plug-in-based design supports the distributed development of reconstruction algorithms and also allows comparison of different algorithms at runtime, *e.g.* it is possible to run two tracking algorithms producing parallel collections of reconstructed tracks.

Event reconstruction is performed with the MarlinReco [16] package. This consists of a set of modules for digitisation, track finding, track fitting, particle flow reconstruction, and flavour tagging. The hit smearing for the tracking detectors is implemented at the digitisation

stage using the same parameterisation as used for Satellites, except that resolutions for the intermediate silicon tracker (SIT) are taken to be $4\,\mu$m for $\sigma_{r\phi}$ and $50\,\mu$m for σ_z. The pattern recognition processors use Kalman Filter techniques and code developed for the LEP experiments. Tracks from standalone pattern recognition in the silicon trackers and in the TPC are combined and refitted, The resulting momentum resolution is discussed in Section 3.2.1. Reconstruction of the individual particles in the event is performed with the particle flow algorithm in the PandoraPFA [12] package, currently the best algorithm available. The LCFIVertex [17] package provides sophisticated code for vertex finding/fitting and for the identification of heavy flavour jets using a neural network approach. It also provides jet charge estimation. In addition to reconstruction algorithms, MarlinReco includes a set of analysis tools such as algorithms for jet finding and kinematic fitting. The RAVE toolkit [18], also available within Marlin, provides an alternative set of vertex reconstruction based on linear and non-linear estimators.

2.2 DETECTOR OPTIMISATION FOR PARTICLE FLOW

One of the main design considerations for a detector at the ILC is the ability to efficiently identify and distinguish $\mathrm{Z} \to \mathrm{q\bar{q}}$ and $\mathrm{W} \to \mathrm{q\bar{q}}$ decays. This imposes the requirement that the di-jet mass resolution should be comparable to the natural widths of the electroweak gauge bosons, $\sigma_m/m < 2.7\,\% \approx \Gamma_\mathrm{Z}/m_\mathrm{Z} \approx \Gamma_\mathrm{W}/m_\mathrm{W}$. In terms of jet energy resolution this requirement approximately corresponds to $\sigma_E/E < 3.8\,\%$. After accounting for the gauge boson widths, this results in a ~ 2.75 standard deviation separation of the W and Z mass peaks for di-jet events. Most of the interesting physics at the ILC, operating in the centre-of-mass range $\sqrt{s} = 0.5 - 1.0\,\mathrm{TeV}$, will consist of final states with four or more fermions and for processes near threshold, the gauge bosons will decay almost at rest. Hence the typical di-jet energies of interest will be in the range $80 - 350\,\mathrm{GeV}$. This sets the requirement on calorimetric performance of $\sigma_E/E \sim 30\,\%/\sqrt{E}$. It has been demonstrated that one way of reaching this goal is particle flow calorimetry[19]. Whilst, the separation of W and Z bosons defines the *minimum* requirement for the jet energy resolution, it should be remembered that di-jet invariant masses will be an important part of the event selection for many physics analyses; the jet energy resolution will affect the signal-to-background ratio in many analyses.

The ILD concept is based on the belief that particle flow calorimetry provides the best way of achieving the ILC jet energy goals. Particle flow reconstruction places strong requirements on the subdetector technologies and the overall detector design. Particle flow calorimetry requires efficient separation of photons and showers produced by neutral hadrons from showers produced by the interactions of charged hadrons. This implies high granularity calorimetry and that both the ECAL and HCAL lie inside the detector solenoid. For high energy jets, failures in the ability to efficiently separate energy deposits from different particles, the *confusion* term, will dominate the jet energy resolution. The physical separation of calorimetric energy deposits from different particles will be greater in a large detector, scaling as the inner radius of the ECAL, R, in the barrel region and the detector length, L, in the endcap region. There are also arguments favouring a high magnetic field, as this will tend to deflect charged particles away from the core of a jet. The scaling law here is less clear. The separation between a charged particle and an initially collinear neutral particle will scale as BR^2. However, there is no reason to believe that this will hold for a jet of (non-collinear) neutral and charged particles. The true dependence of particle flow on the overall detector parameters (B and R) has to be evaluated empirically.

2.2.1 Particle Flow Optimisation Methodology

The particle flow optimisation studies for ILD use the PandoraPFA algorithm[12] to reconstruct events for both the LDC and the GLD detector models. All studies are based on full reconstruction of the tracking and the calorimetric information. The starting point for the optimisation studies is the LDCPrime model with a 3.5 T magnetic field, an ECAL inner radius of 1825 mm and a 48 layer ($6\lambda_I$) HCAL. The ECAL and HCAL transverse segmentations are $5 \times 5\,\mathrm{mm}^2$ and $3 \times 3\,\mathrm{cm}^2$ respectively. The studies use variations of this model where (usually) a single parameter is changed and the dependence of jet energy resolution is determined as a function of this parameter. For each model variation, particle flow performance was evaluated using samples of approximately 10000 $\mathrm{Z} \rightarrow \mathrm{q\overline{q}}$ events (only light quarks, *i.e.* $q = u, d, s$) generated with the Z decaying at rest (no ISR or beamstrahlung) with $E_{\mathrm{Z}} = 91.2$, 200, 360, and 500 GeV. These jet energies are typical of those expected at the ILC for $\sqrt{s} = 0.5 - 1.0\,\mathrm{TeV}$. For each set of events, the rms_{90} of the total reconstructed energy distribution was determined, where rms_{90} is the root-mean-squared deviation from the mean in the smallest energy range containing 90 % of the reconstructed events.

2.2.2 HCAL Depth

Good particle flow calorimetry requires that both the ECAL and HCAL are within the detector solenoid. Consequently, in addition to the cost of the HCAL, the HCAL thickness impacts the cost of the overall detector through the radius of the superconducting solenoid. The thickness of the HCAL determines the average fraction of jet energy contained within the calorimeter system. The impact of the HCAL thickness on the particle flow performance is assessed by changing the number of HCAL layers in the LDCPrime model from 32 to 63. This corresponds to a variation of $4.0 - 7.9\,\lambda_I$ ($4.8 - 8.7\,\lambda_I$) in the HCAL (ECAL+HCAL).

The study of the optimal HCAL thickness depends on the possible use of the instrumented return yoke (the muon system) to correct for leakage of high energy showers out of the rear of the HCAL. The effectiveness of this approach is limited by the fact that, for much of the polar angle, the muon system is behind the relatively thick solenoid ($2\lambda_I$ in the Mokka simulation of the detector). Nevertheless, to assess the possible impact of using the muon detector as a "tail-catcher", the energy depositions in the muon detectors were included in the PandoraPFA reconstruction. Whilst the treatment could be improved upon, it provides an estimate of how much of the degradation in jet energy resolution due to leakage can be recovered in this way. The results are summarised in Figure 2.2-1 which shows the jet energy resolution obtained from PandoraPFA as a function of HCAL thickness. The effect of leakage is clearly visible, with about half of the degradation in resolution being recovered when including the muon detector information. For jet energies of 100 GeV or less, leakage is not a major contributor to the jet energy resolution provided the HCAL is approximately $4.7\lambda_I$ thick (38 layers). However, for $180-250$ GeV jets this is not sufficient; for leakage not to contribute significantly to the jet energy resolution at $\sqrt{s} = 1\,\mathrm{TeV}$, the results in Figure 2.2-1 suggest that the HCAL thickness should be between $5.5 - 6.0\lambda_I$ ($43 - 48$ layers). To allow for uncertainties in the simulation of the longitudinal development of hadronic showers, and to ensure the detector is appropriate for collisions at 1 TeV, a 48 layer HCAL was chosen for ILD. This was also used for the LDC-based models discussed below.

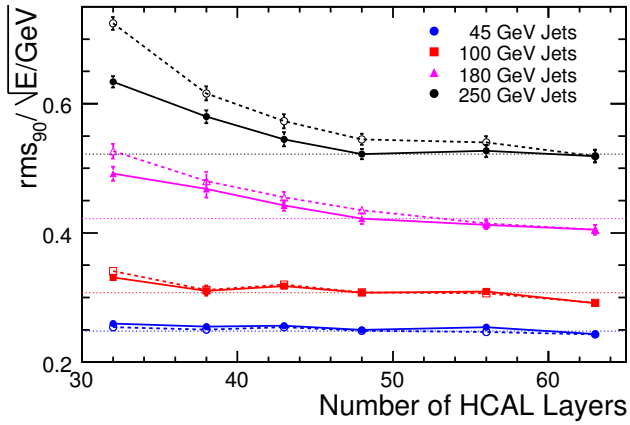

FIGURE 2.2-1. Jet energy resolutions (rms_{90}) for the LDCPrime detector model with different numbers of HCAL layers. Results are shown with (solid markers) and without (open markers) taking into account energy depositions in the muon detectors. All results are based on $\mathrm{Z} \rightarrow \mathrm{u\bar{u}}, \mathrm{d\bar{d}}, \mathrm{s\bar{s}}$ with generated polar angle in the barrel region of the detector, $|\cos\theta_{\mathrm{q\bar{q}}}| < 0.7$.

2.2.3 Magnetic Field versus Detector Radius

The dependence of particle flow performance on B and R is studied in the region of parameter space close to the LDCPrime model. The LDCPrime model assumes a magnetic field of 3.5 T and an ECAL inner radius of 1820 mm. A number of variations on these parameters were studied: i) variations of both B and R with four sets of parameters considered, "LDC-like" (B=4.0 T, R = 1600 mm), "GLD-like" (B=3.0 T, R = 2020 mm), "Small" (B=4.5 T, R = 1420 mm), and "SiD-like" (B=5.0 T, R = 1280 mm); i) variations in the ECAL inner radius from 1280 − 2020 mm with B = 3.5 T; and iii) variations in B from 2.5 − 4.5 T with R = 1825 mm. In total thirteen sets of parameters were considered spanning a wide range of B and R. In each case particle flow performance was evaluated for 45, 100, 180, and 250 GeV jets. Table 2.2-2 compares the jet energy resolutions for LDC, LDCPrime and LDC4GLD models. The differences between these models is small, $\sim 5\,\%$,. This is not surprising; the parameters of the LDC and GLD concepts on which these models are based were chosen such

Model			σ_E/E [%] versus E_{jet}			
Name	B/T	R/m	45 GeV	100 GeV	180 GeV	250 GeV
SiD-like	5.0	1.25	4.19 ± 0.06	3.72 ± 0.06	3.70 ± 0.07	3.94 ± 0.10
Small	4.5	1.42	3.90 ± 0.08	3.34 ± 0.07	3.54 ± 0.06	3.75 ± 0.08
LDC	4.0	1.60	3.82 ± 0.06	3.14 ± 0.06	3.26 ± 0.08	3.37 ± 0.07
LDCPrime	3.5	1.82	3.70 ± 0.06	3.07 ± 0.05	3.15 ± 0.07	3.30 ± 0.06
LDC4GLD	3.0	2.02	3.60 ± 0.05	2.97 ± 0.05	3.16 ± 0.06	3.32 ± 0.06

TABLE 2.2-2
Jet energy resolutions (rms_{90}) for different detector parameters. All results are based on $\mathrm{Z} \rightarrow \mathrm{u\bar{u}}, \mathrm{d\bar{d}}, \mathrm{s\bar{s}}$ events using scaled versions of the Mokka LDCPrime detector model. The results are quoted for the barrel region of the detector $|\cos\theta_{\mathrm{q\bar{q}}}| < 0.7$.

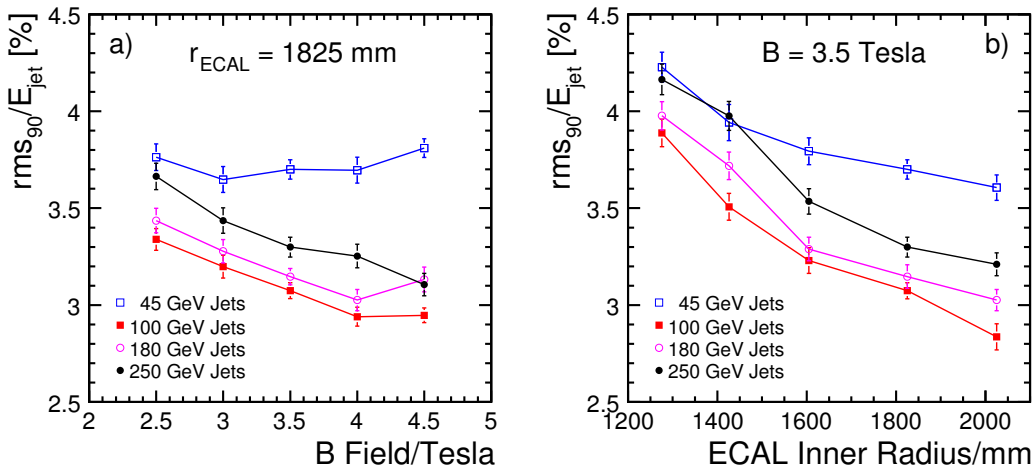

FIGURE 2.2-2. a) the dependence of the jet energy resolution (rms_{90}) on the magnetic field for a fixed ECAL inner radius (B=3.5 T corresponds to the LDCPrime model). b) the dependence of the jet energy resolution (rms_{90}) on the ECAL inner radius a fixed value of the magnetic field (R=1825 mm corresponds to the LDCPrime model).

that the smaller detector radius is compensated by a higher B. For the two smaller, higher B models listed in Table 2.2-2 degradations in performance are observed.

Figure 2.2-2 shows the dependence of the jet energy resolution ($\mathrm{rms}_{90}/\mathrm{E}_{\mathrm{jet}}$) on: a) magnetic field (fixed R) and b) ECAL inner radius (fixed B) for four different jet energies. For 45 GeV jets, the dependence of the jet energy resolution on B and R is weak; for these energies the intrinsic calorimetric energy resolutions, rather than the confusion term dominates. For higher jet energies, where the confusion term dominates, the jet energy resolution shows a stronger dependence on R than B.

The jet energy resolutions listed in Table 2.2-2 and those shown in Figure 2.2-2 are reasonably well described by the function:

$$\frac{\sigma_E}{E} = \frac{21}{\sqrt{E/\mathrm{GeV}}} \oplus 0.7 \oplus 0.004E \oplus 2.1 \left(\frac{R}{1825\,\mathrm{mm}}\right)^{-1.0} \left(\frac{B}{3.5\,\mathrm{T}}\right)^{-0.3} \left(\frac{E}{100\,\mathrm{GeV}}\right)^{0.3} \%.$$

This is the quadrature sum of four terms: i) the estimated contribution to the jet energy resolution from the intrinsic calorimetric resolution; ii) the contribution from imperfect track reconstruction, estimated by comparing the jet energy resolutions with those using tracks obtained from the MC information; iii) leakage, estimated by comparing the jet energy resolutions with those for an $8\,\lambda_I$ HCAL; and iv) the contribution from confusion obtained empirically from a fit to the data of Table 2.2-2 and Figure 2.2-2. In fitting the confusion term, a power-law $\kappa B^{\alpha} R^{\beta} E^{\gamma}$ provides a reasonable parameterisation of the data [1]. From the perspective of the optimisation of the detector, these studies show that for the particle flow calorimetry using the PandoraPFA algorithm, that the confusion term scales as approximately $B^{-0.3}R^{-1}$. For particle flow performance (with the PandoraPFA algorithm) the detector radius is more important than the magnetic field. This forms part of the motivation for the choice of a large detector radius for the ILD conceptual design. Table 2.2-3 lists the

[1] The majority of the data points lie within 2.5σ of the parameterisation, the only exception being the 45 GeV and 100 GeV jet energy resolutions for the "SiD-like" detector where the fit underestimates the resolution.

relative values of $B^{0.3}R$ and relative jet energy resolutions from the parameterisation above for the LDC, LDCPrime and LDC4GLD detector models. The main conclusion of this study is that, in terms of particle flow performance, the differences between the LDC, LDCPrime, and LDC4GLD detector models are at the level of $\pm 5\,\%$, with the larger models being slightly prefered.

Model			$B^{-0.3}R^{-1}$	Relative σ_E/E versus $E_{\rm jet}$			
Name	B/T	R/m	(relative)	45 GeV	100 GeV	180 GeV	250 GeV
LDC	4.0	1.60	1.08	1.02	1.04	1.05	1.06
LDC4GLD	3.0	2.02	0.95	0.99	0.97	0.96	0.96

TABLE 2.2-3
Expected jet energy resolutions (rms_{90}) of the LDC and LDC4GLD detector models relative to the LDCPrime resolution.

2.2.4 Detector Aspect Ratio

Although the cost of ILD will depend less strongly on length than on radius, it is, nevertheless, an important parameter in the detector optimisation. From the perspective of particle flow, the main effect will be on the performance of forward jets. For forward tracks, the importance of the B-field will be further diminished, and one might expect the confusion term to scale as L^{-1}, where L is the z-position of the endcap ECAL. Figure 2.2-3a shows the particle flow performance for jets in the endcap region ($0.80 < |\cos\theta_{\rm q\bar{q}}| < 0.95$). For particle flow reconstruction of forward jets it is beneficial to have the ECAL endcaps further from the interaction region. To maintain good jet energy resolution in the forward region of the detector the TPC drift length needs to be $\gtrsim 2000\,$mm.

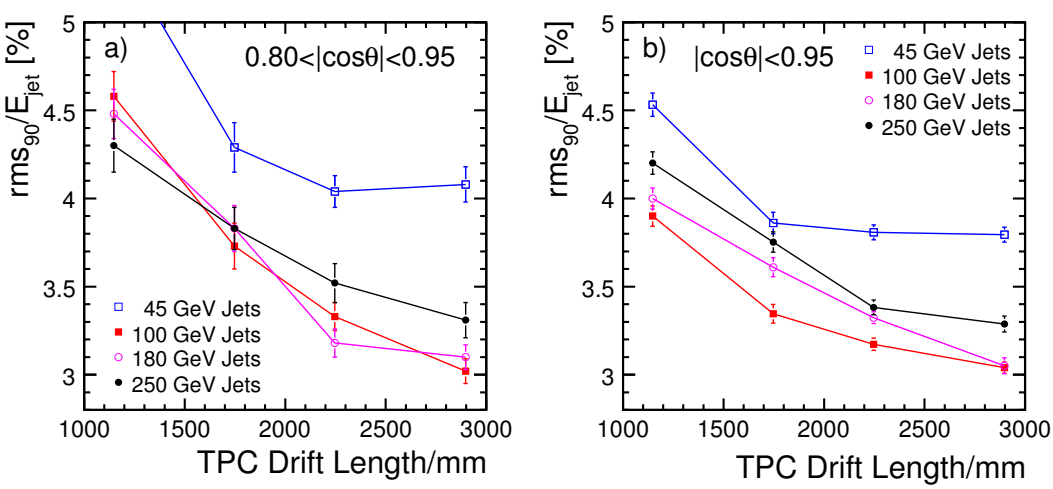

FIGURE 2.2-3. a) the dependence of the jet energy resolution in the "endcap" region ($0.80 < |\cos\theta_{\rm q\bar{q}}| < 0.95$) as a function of the TPC drift length in the LDCPrime model. b) the dependence of the jet energy resolution in the region ($|\cos\theta_{\rm q\bar{q}}| < 0.95$) as a function of the TPC drift length in the LDCPrime model.

Figure 2.2-3b shows the length dependence of the average jet energy resolution for jets with $|\cos\theta_{q\bar{q}}| < 0.95$. When considering all jets, the benefits to particle flow performance in going beyond a TPC drift length of 2200 mm are relatively small. From this study a TPC drift length of 2200 mm looks reasonable; the benefits of increasing the detector length are unlikely to justify the additional costs.

2.2.5 ECAL and HCAL Granularity

The dependence of particle flow performance on the transverse segmentation of the ECAL was studied using versions of the LDCPrime model with silicon pixel sizes of $5 \times 5\,\mathrm{mm}^2$, $10 \times 10\,\mathrm{mm}^2$, $20 \times 20\,\mathrm{mm}^2$, and $30 \times 30\,\mathrm{mm}^2$. The two main clustering parameters in the PandoraPFA algorithm were re-optimised for each ECAL granularity. The particle flow performance results are summarised in Figure 2.2-4a. For 45 GeV jets the dependence is relatively weak since the confusion term is not the dominant contribution to the resolution. For higher energy jets, a significant degradation in performance is observed with increasing pixel size. Within the context of the current reconstruction, the ECAL transverse segmentation has to be at least as fine as $10 \times 10\,\mathrm{mm}^2$ to meet the ILC jet energy requirement, $\sigma_E/E < 3.8\,\%$, for the jet energies relevant at $\sqrt{s} = 1\,\mathrm{TeV}$, with $5 \times 5\,\mathrm{mm}^2$ being preferred.

A similar study was performed for the HCAL using scintillator tile sizes of $1 \times 1\,\mathrm{cm}^2$, $3 \times 3\,\mathrm{cm}^2$, $5 \times 5\,\mathrm{cm}^2$, and $10 \times 10\,\mathrm{cm}^2$. The particle flow performance results are summarised in Figure 2.2-4b. From this study, it is concluded that the ILC jet energy resolution goals can be achieved with an HCAL transverse segmentation of $5 \times 5\,\mathrm{cm}^2$, although for higher energy jets there is a significant gain in going to $3 \times 3\,\mathrm{cm}^2$. There appears to be little motivation for $1 \times 1\,\mathrm{cm}^2$ over $3 \times 3\,\mathrm{cm}^2$ tiles.

2.2.6 ECAL and HCAL detector technology

The ILD concept incorporates two different technology options for both the ECAL and HCAL. The two ECAL technologies are: i) a Silicon-Tungsten (SiW) calorimeter where the baseline

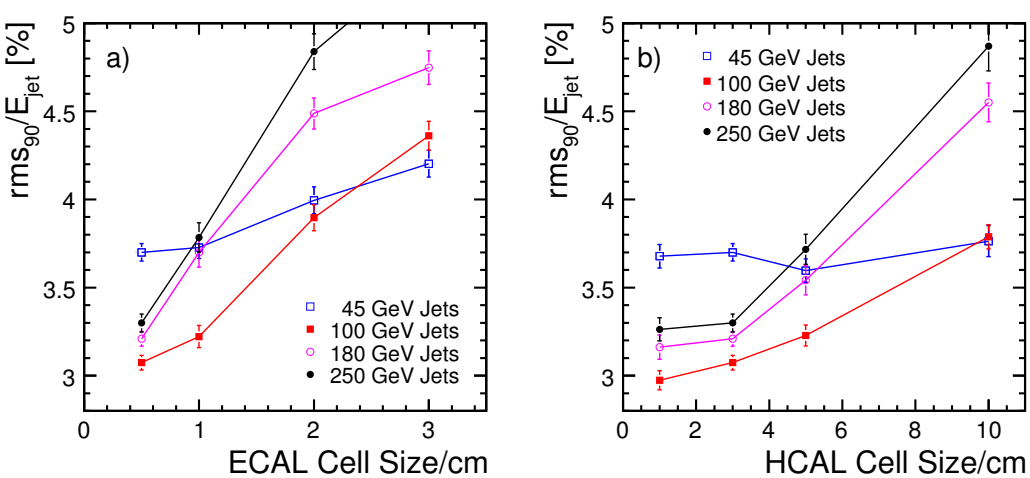

FIGURE 2.2-4. a) the dependence of the jet energy resolution (rms_{90}) on the ECAL transverse segmentation (Silicon pixel size) in the LDCPrime model. b) the dependence of the jet energy resolution (rms_{90}) on the HCAL transverse segmentation (scintillator tile size) in the LDCPrime model.

pixel size of $5 \times 5\,\mathrm{mm}^2$; and ii) a scintillator-Tungsten calorimeter where the $1 \times 4\,\mathrm{cm}^2$ scintillator strips in successive layers are perpendicular to each other with the aim of achieving a $1 \times 1\,\mathrm{cm}^2$ effective transverse granularity. The particle flow studies described above were obtained using the simulation of the SiW calorimeter. To extend these studies to the scintillator strip option requires additional step in the reconstruction, namely strip-based clustering. First studies[20] indicate that for 100 GeV jets the performance of the scintillator option with $1 \times 4\,\mathrm{cm}^2$ strips may approach that which would be obtained with a scintillator segmentation of $1 \times 1\,\mathrm{cm}^2$. However, at this stage, further work is needed to understand the limitations of the strip based ECAL for higher energy jets and whether it is possible to extend the approach to narrower strips to achieve an effective $5 \times 5\,\mathrm{mm}^2$ segmentation. The potential advantages of even finer segmentation, *e.g.* as provided by the MAPs-based ECAL, has yet to be studied in detail.

The two HCAL technologies under consideration are: i) an analogue steel-scintillator hadron calorimeter (AHCAL) with a tile size of $\sim 3 \times 3\,\mathrm{cm}^2$; and ii) a semi-digital calorimeter (DHCAL), *e.g.* using RPCs, with a readout pixel size of $1 \times 1\,\mathrm{cm}^2$ and a three level (2 bit per cell) readout. The particle flow studies described above used the AHCAL option. The particle flow performance of the semi-digital option is currently being studied in the context of the current PandoraPFA algorithm. Earlier studies (with the LDC detector model and a previous version of the PandoraPFA algorithm) found that the jet energy resolution for 100 GeV jets with a digital (single bit) readout was similar to that obtained with the AHCAL option. Further study is needed to establish the particle flow performance of the DHCAL option.

2.3 BACKGROUND CONSIDERATIONS

Beam-related backgrounds, and in particular e^+e^- pairs created by beam-beam interactions, are an essential input to the ILD design and optimisation. The e^+e^- pairs are produced at relatively low angles to the beam direction and spiral along the magnetic field lines parallel to the beam axis. As shown in Figure 2.3-5, the resulting pair-background tracks form a dense core with an approximately quadratic envelope. The radius of the dense core for a given value of z is roughly proportional to $\sqrt{B}$ [21]. The pair background determines the minimum radius of the beam pipe needed to avoid a large source of secondary background from electrons and positrons hitting the beam pipe. In turn, the radius of the beam pipe determines the radius of the innermost layer of the vertex detector, and consequently influences the impact parameter resolution for relatively low-momentum charged tracks. However, it has been shown [2], that if the magnetic field is $\gtrsim 3\,\mathrm{T}$, the required impact parameter resolution of $5\,\mu\mathrm{m} \oplus 10\,\mu\mathrm{m}/p(\mathrm{GeV})\sin^{3/2}\theta$ is achievable with a vertex detector layer thickness of $0.1 - 0.2\,\%\,X_0$/layer.

In terms of optimisation of ILD, the main effect of the pair background is to determine the inner radius of the vertex detector, which affects the impact parameter resolution and thus the flavour tagging performance. However, the difference between the radius of the core of the pair background between a 3T and a 4T magnetic field is only 15 %. In practice, the impact of the magnetic field on the inner radius of the vertex detector is less than this, as it is necessary to leave gaps between the dense core of the pair background and the beam pipe and between the beam pipe and the first layer of the vertex detector. These gaps are independent of the magnetic field, and when this is taken into account, the difference of inner radius of the vertex detector between a B-field of 3 T and 4 T is only $\sim 10\,\%$. The impact on the detector performance is discussed in the next two sections.

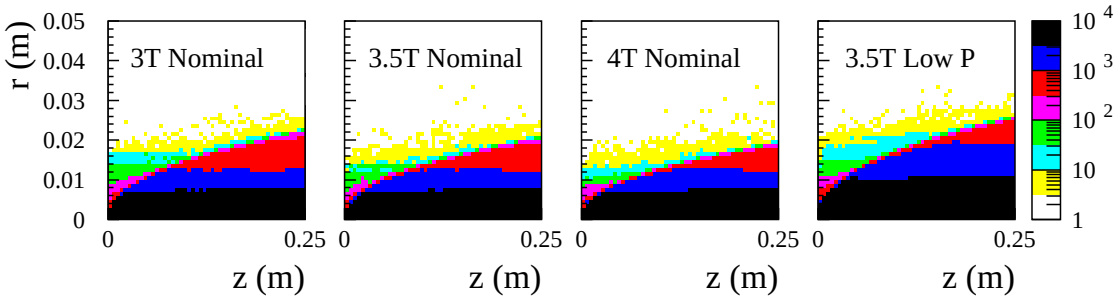

FIGURE 2.3-5. Track density of the e^+e^- pair background ($/\mathrm{cm}^{-2}/\mathrm{BX}$) with the nominal ILC beam parameters at $\sqrt{s} = 500\,\mathrm{GeV}$ for the detector magnetic field of 3 T, 3.5 T, and 4 T. Also shown is the background with the lowP option for the ILC beam parameters at $\sqrt{s} = 500\,\mathrm{GeV}$ with $B = 3.5\,\mathrm{T}$.

Finally, it is worth noting that the inner radius of the vertex detector for the lowP option of the ILC machine parameters is about 20% larger than that for the nominal option. Therefore, it can be concluded that the machine parameters have a larger impact on the inner radius of the vertex detector than the magnetic field of the detector.

2.4 DETECTOR OPTIMISATION FOR TRACKING

The tracking system of the ILD detector concept consists of a vertex detector (VTX) and a large volume TPC, complemented by additional Silicon tracking layers (FTD/SIT). In addition, in the LDC-based models, silicon tracking layers immediately outside the TPC are considered (ETD and SET). The dependence of the performance of the tracking system on the magnetic field and detector size was an important consideration in optimising the ILD. Considerations of momentum resolution favour a larger detector and higher magnetic field. As discussed above, a higher magnetic field also allows the first layer of the vertex detector to be closer to the interaction point (IP). The optimisation of the tracking system is, again, a balance between the magnetic field and detector radius. The parameter space spanning the LDC (smaller R, higher B-field) and GLD (larger R, lower B) concepts is investigated using the six detector models summarised in Table 2.1-1.

2.4.1 Momentum Resolution

Figure 2.4-6(a) shows the $1/p_\mathrm{T}$ resolution, as a function of p_T, for single muons in the GLD, GLDPrime and GLD4LDC models. The results were obtained using the Satellites Kalman Filter (Section 2.1.1). Figure 2.4-6(b) shows the relative $1/p_\mathrm{T}$ resolution compared to the average of three detector models at a particular value of p_T, plotted as a function of p_T. Above approximately 50 GeV, the resolution obtained with the GLD4LDC model is $\sim$5 % worse than the larger detector models due to the shorter lever arm of the TPC. For lower energy tracks the situation is reversed with the higher magnetic field resulting in the resolution for 4 T being $\sim$10 % better than for 3 T. Similar results were obtained with the LDC-based models using Mokka and MarlinReco (Section 2.1.2). The relative performance does not depend strongly on the angle. The differences in resolution for the range of B and R considered are small ($\lesssim 10\,\%$) compared to those arising from different layouts for the tracking system and the point resolutions of the components. For example, the use of hits in the silicon external

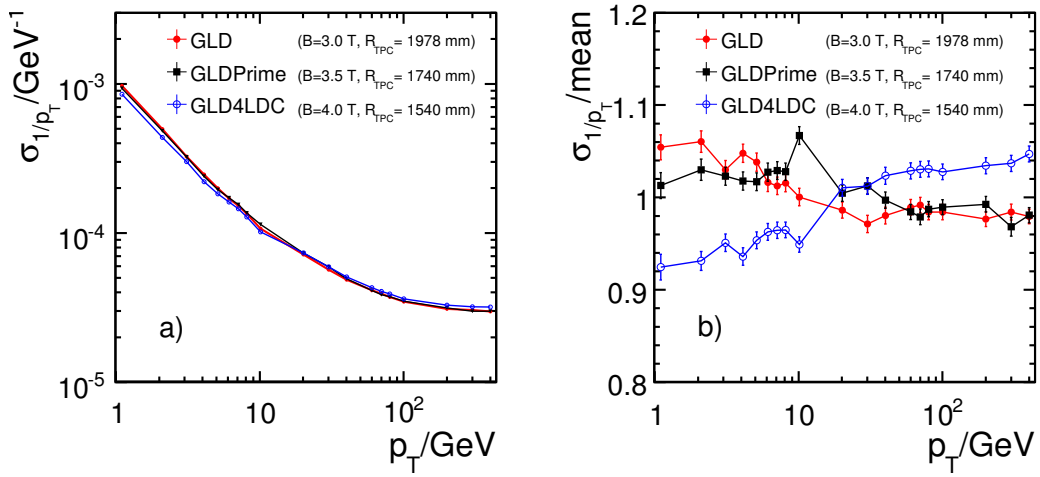

FIGURE 2.4-6. (a) $\sigma_{1/p_{\mathrm{T}}}$ for single muon tracks at 90° to the beam axis, as a function of transverse momentum, for the GLD, GLDPrime, and GLD4LDC models; and (b) the ratio of $\sigma_{1/p_{\mathrm{T}}}$ to the average of the three detector models as a function of transverse momentum. To avoid the TPC central membrane the generated muons were displaced from the IP by a few centimetres.

tracker (SET) outside the TPC in the LDCPrime model improves the momentum resolution by 15 % assuming an SET $r\phi$ hit resolution of $4\,\mu$m.

2.4.2 Impact Parameter Resolution

The impact parameter resolution, $\sigma_{r\phi}$, of the tracking system is an important input to the heavy flavour tagging capability of the detector. The most important detector considerations are the vertex detector design (point resolution and material budget) and the magnetic field which, as discussed in Section 2.3 affects the minimum distance of the first layer of the vertex detector from the interaction region, R_{min}. Figure 2.4-7a shows $\sigma_{r\phi}$ as a function of p_{T} for the GDC-based detector models. The GLD4LDC model has the best resolution, because the higher B-field allows the innermost layer of the vertex detector to be closer to the interaction point (IP). However the differences between the detector models considered, Figure 2.4-7b, are relatively small $\lesssim 5-10\,\%$.

Figure 2.4-7c shows the $\sigma_{r\phi}$ resolution for 1 GeV muons for the GLD-based detector models, plotted as a function of the track angle. Whilst the higher magnetic fields are favoured, the differences between the detector models are $\lesssim 15\,\%$. For higher energy tracks, where the effect of multiple Coulomb scattering is negligible, the differences between the models are even smaller. Although the variations in magnetic field and the corresponding inner radii of the vertex detector lead to relatively small differences in impact parameter resolution, different detector layouts have a more significant impact. Figure 2.4-7d compares the impact parameter resolution for the GLDPrime and LDCPrime detector models. The GLDPrime detector assumes a vertex detector consisting of six layers arranged in three closely spaced doublets (see Section 4.1.4), whereas the LDCPrime model assumes five equally spaced layers. The three double layer layout results in a significantly better impact parameter resolution for high momentum tracks because it gives two, rather than one, high precision measurements close to the IP.

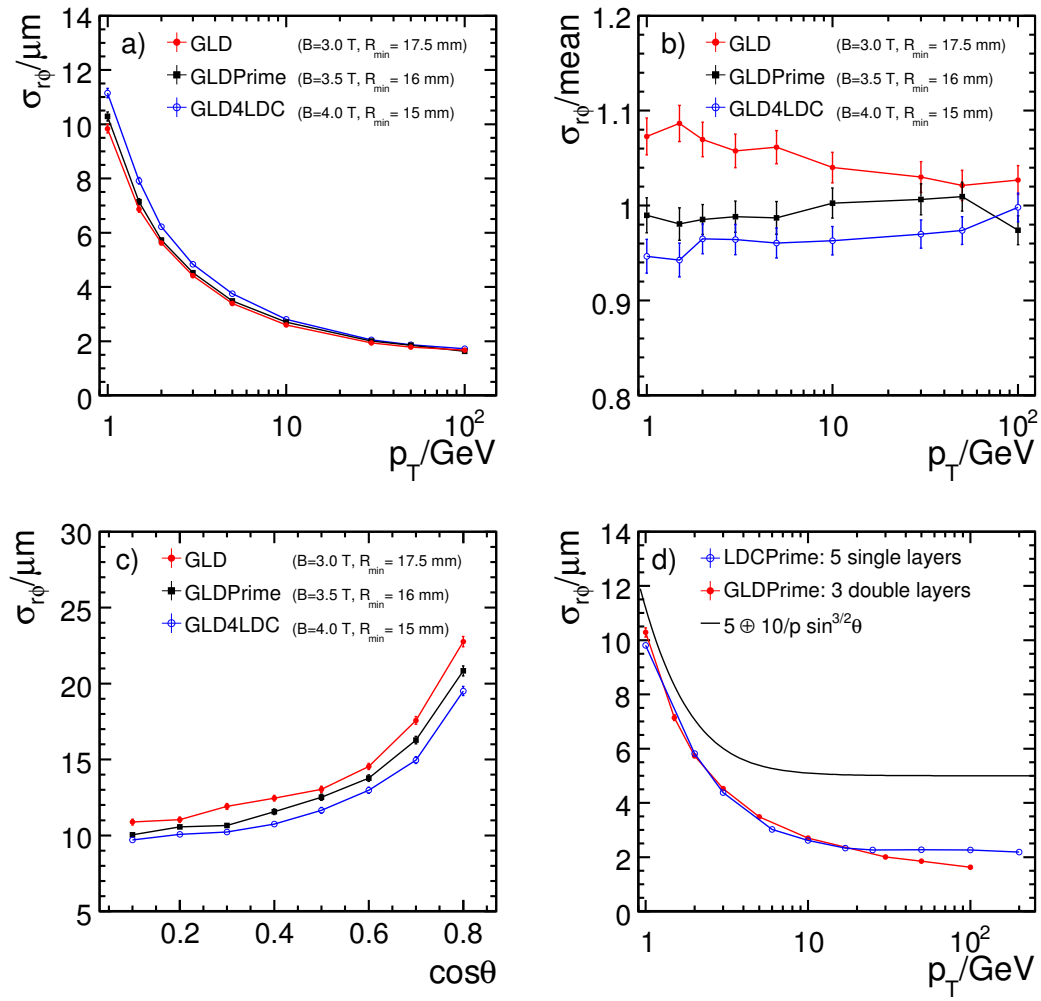

FIGURE 2.4-7. (a) $\sigma_{r\phi}$ as a function of p_{T} for GLD, GLDPrime, and GLD4LDC, and (b) the ratio of $\sigma_{r\phi}$ to the average of the three detector models. c) $\sigma_{r\phi}$ as a function of the track angle at the track energy of 1 GeV for GLD, GLDPrime, and GLD4LDC. d) the impact parameter resolution as a function of p_{T} for GLDPrime and LDCPrime. Also shown is the nominal ILC goal for impact parameter resolution.

2.4.3 Conclusions

For the range of B and R considered here, the differences in momentum resolution are $\lesssim 10\,\%$, with higher B-field preferred for low p_{T} tracks and a larger R preferred for high p_{T} tracks. The impact parameter resolution, $\sigma_{r\phi}$, is better for models with higher B as the first layer of the vertex detector can be placed closer to the IP. However, the differences in impact parameter resolution obtained with a 3 T and 4 T magnetic field are small, at most 15 % for low momentum tracks and $\lesssim 5\,\%$ for tracks above 2 GeV. It can be concluded that for the range of B and R spanned by the LDC and GLD detector concepts, the differences in impact parameter and momentum resolution are relatively small. It is also concluded that the tracking resolutions depend much more strongly on the subdetector technologies and tracking system layout than on the global parameters (B and R) of the detector.

2.5 FLAVOUR TAGGING

Heavy flavour tagging will be an essential tool in many physics analyses at the ILC. The flavour tagging performance depends primarily on the design of the vertex detector and, in particular, the impact parameter resolution. The flavour tagging performance is studied using MarlinReco for the full reconstruction of the simulated events and the sophisticated LCFIVertex package for heavy flavour tagging [22]. The LCFIVertex [17] flavour tagging uses three artificial neural networks (ANNs): i) a b-tag to discriminate b-quark jets from jets from charm and light quarks; ii) a c-tag to discriminate c-quark jets from b and light quark jets; and iii) a c/b-tag to discriminate between c-quark jets and b-quark jets. The ANNs use different sets of discriminant variables depending on whether either one, two, or more than two vertices are found in the jet. The ANN architecture is a multi-layer perceptron with $N = 8$ inputs, one hidden layer with $2N - 2$ nodes, and sigmoid activation functions. The weights were calculated using the back propagation conjugate gradient algorithm. Two of the most powerful inputs to the flavour tag are the joint likelihoods (in $r - \phi$ and in $r - z$) for all tracks in the jet to have originated from the primary vertex. The joint likelihoods depend on the respective $r - \phi$ and $r - z$ impact parameter significances of all the tracks in the jet. Consequently the impact parameter resolution of the vertex detector plays a central role in determining the flavour tagging performance. It was demonstrated in the previous section that the difference in $\sigma_{r\phi}$ in going from 3 T to 4 T is rather small. Consequently, one might expect the same to be true for flavour tagging performance.

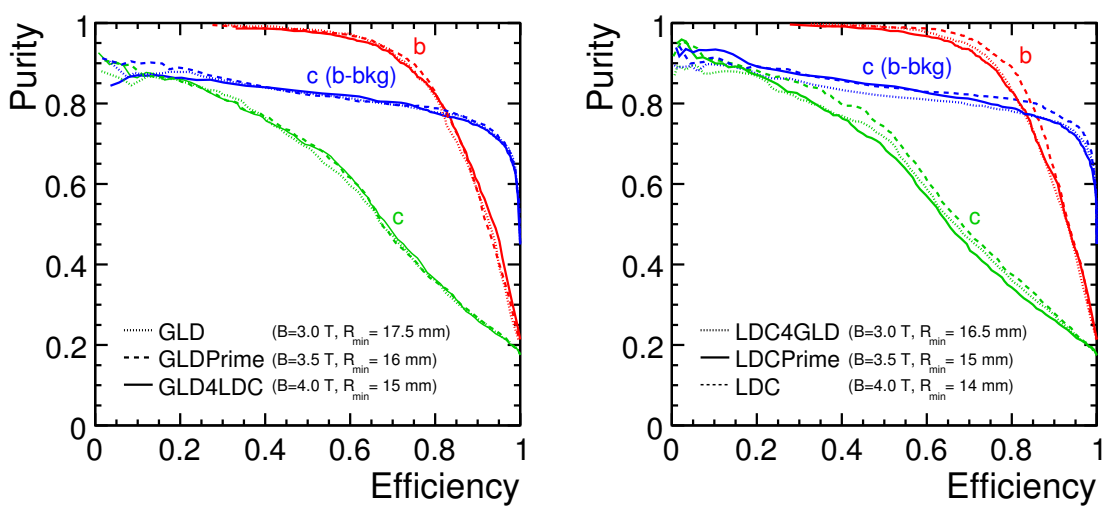

FIGURE 2.5-8. Flavour tagging performance for the (left) GLD-based and (right) LDC-based detector models.

The dependence of flavour tagging performance on the global detector parameters was investigated using the GLD- and LDC-based detector models. Separate ANNs were trained for each of the models. The samples used to evaluate the flavour tagging performance, which were generated with SM Z boson branching ratios, were independent of those used for the training. All the samples were generated at $\sqrt{s} = m_Z$. The results are shown in Figure 2.5-8. The observed differences in the flavour tagging performances between the GLD (LDC) models are $\lesssim 1\,\%$ ($\lesssim 4\,\%$). There is a preference for the 4.0 T configuration, in particular for

the b-tag at high efficiencies. However, the uncertainties on the efficiencies due to statistics and the ANN training procedure are $\sim 2\,\%$, and hence statistical significance of the observed differences are $\lesssim 2\sigma$. From this study it is concluded that the increased inner radius of the vertex detector when going from B=4 T to B=3 T, does not have a large impact on the flavour tagging performance of the detector.

2.6 PHYSICS PERFORMANCE

The previous sections of this chapter discuss the impact of the detector design on the low level measurements of jet energies, track momenta, impact parameters and flavour identification. Here the performance of the different detector models in Table 2.1-1 are compared for three physics analyses: the measurement of the Higgs mass, τ pair production and polarisation, and chargino/neutralino pair production.

2.6.1 Higgs Recoil Mass

One of the prime motivations for the unprecedented track momentum resolution at the ILC is the determination of the Higgs mass from the recoil mass distribution in $ZH \to \mu^+\mu^- X$ and $ZH \to \mathrm{e}^+\mathrm{e}^- X$ events. This sensitivities to this process if the LDC, LDCPrime and LDC4GLD detector models were compared. For this study only $\mathrm{e}^+\mathrm{e}^- \to ZZ \to \mathrm{e}^+\mathrm{e}^-/\mu^+\mu^- Z$ background was included. Figure 2.6-9 shows, for the LDCPrime model, the Higgs recoil mass distribution for selected events. To determine the Higgs mass and production cross section, the recoil mass distributions were fitted using a Gaussian for the peak region with an exponential component for the tails [23].

The results for the different detector models are summarised in Table 2.6-4. These numbers should not be compared with the physics sensitivity studies presented in Section 3.3.1 as only $\mathrm{e}^+\mathrm{e}^- \to ZZ \to \mathrm{e}^+\mathrm{e}^-/\mu^+\mu^- Z$ background is included and the events were generated with a different luminosity spectrum.

When interpreting the above results it is necessary to consider the relative importance of momentum resolution and the beam energy spread. For the assumed beam energy spread (a

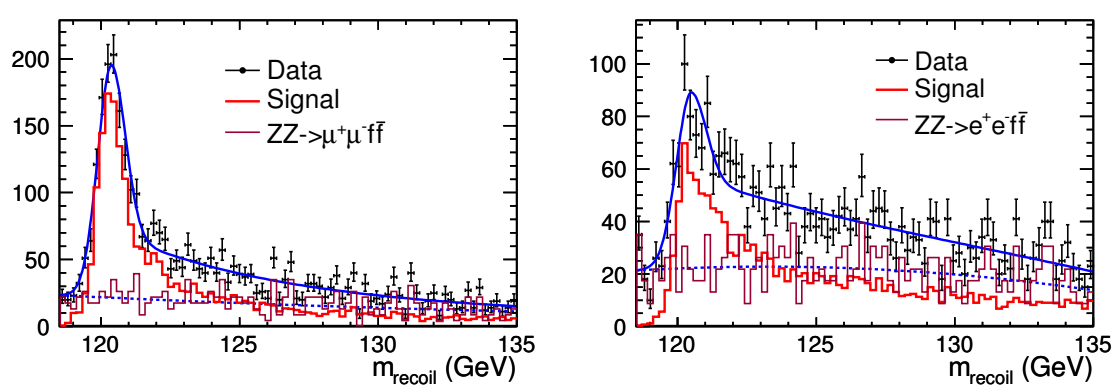

FIGURE 2.6-9. Distributions of the reconstructed Higgs recoil mass obtained with the LDCPrime model for (a) ZH $\to \mu^+\mu^- X$ and (b) ZH $\to \mathrm{e}^+\mathrm{e}^- X$. The events were generated with a top-hat beam energy distribution with a half width of 0.28% for the electron beam and 0.18% for the positron beam.

	$ZH \to \mu^+\mu^- X$		$ZH \to e^+e^- X$	
	$\Delta m_{\mathrm{recoil}}$	$\Delta\sigma$	$\Delta m_{\mathrm{recoil}}$	$\Delta\sigma$
LDCPrime	$23 \pm 0.4\,\mathrm{MeV}$	0.28 fb	$47 \pm 0.9\,\mathrm{MeV}$	0.49 fb
LDC	$23 \pm 0.4\,\mathrm{MeV}$	0.27 fb	$47 \pm 0.9\,\mathrm{MeV}$	0.52 fb

TABLE 2.6-4
The measurement precision of the Higgs recoil mass ($\Delta m_{\mathrm{recoil}}$) and cross section ($\Delta\sigma$) for ZH $\to \mu^+\mu^- X/\mathrm{e}^+\mathrm{e}^- X$. The events were generated with a top-hat beam energy distribution with a half width of 0.28% for the electron beam and 0.18% for the positron beam.

top-hat distribution with half-widths 0.28 % and 0.18 % for the electron and positron beams respectively), the event-by-event recoil mass resolution in the peak region is $\sim 400\,\mathrm{MeV}$, which this includes contributions from the beam energy spread and from beamstrahlung. From MC studies, the other major contribution to the event-by-event recoil mass resolution arises, as expected, from the track momentum resolution. This is found to contribute $\sim 350\,\mathrm{MeV}$ to the recoil mass resolution. For the detector models considered in this study, the differences in momentum resolution are $\lesssim 5\,\%$, for the relevant momentum range. Even these small differences are diluted by the contribution from the beam energy spread and, as verified in this study, significant differences in the m_{H} mass resolution are not expected.

2.6.2 Tau pairs

The reconstruction of tau pair events at $\sqrt{s} = 500\,\mathrm{GeV}$ provides a powerful test of a number of aspects of the detector performance, *e.g.* π^0 reconstruction and the tracking efficiency for nearby tracks in three-prong tau decays. The performances of the GLD, GLDPrime, GLD4LDC and LDCPrime models are compared for the measurement of the τ polarisation, P_τ which is primarily sensitive to the ability to resolve photons from π^0 decay from the charged hadron in $\tau \to \rho\nu$ decays. Figure 2.6-10 shows the reconstructed π^0 and $\rho^\pm$ invariant mass distributions used in the tau decay selections. The numbers of events in the π^0 mass peak reflect the efficiency for reconstructing both photons from $\pi^0 \to \gamma\gamma$ decays. The LDCPrime detector model gives the highest $\pi^0 \to \gamma\gamma$ reconstruction efficiency, demonstrating the advantages of smaller ECAL pixel size ($5 \times 5\,\mathrm{mm}^2$). For the GLD models, all with an ECAL pixel size of $10 \times 10\,\mathrm{mm}^2$, the π^0 reconstruction efficiency increases with detector radius due to the increased spatial separation of the two photons.

Table 2.6-5 summarises the impact of the different detector models on the P_τ measurement from $\tau \to \pi\nu$ decays. The $\tau \to \pi\nu$ selection requires that a tau jet consists of a single track and at most 1 GeV of energy not assigned to the track. Cuts to remove $\tau \to e\nu\overline{\nu}$ and $\tau \to \mu\nu\overline{\nu}$ decays are also applied. The P_τ is determined from the cosine of the $\pi^\pm$ decay angle in the τ rest-frame (which is determined by the charged pion energy). The differences in the different detector models are most evident in the purities of the $\tau \to \pi\nu$ selection. The advantages of smaller ECAL pixels (LDCPrime compared to GLDPrime) are clear and it can be seen that higher purities are obtained for larger detector radii. However, similar sensitivities to P_τ are obtained from the $\tau \to \pi\nu$ channel. One should not draw too strong a conclusion from this as the measurement of P_τ from $\tau \to \rho\nu$ and $\tau \to a_1\nu$ decays could show a stronger dependence on the detector model.

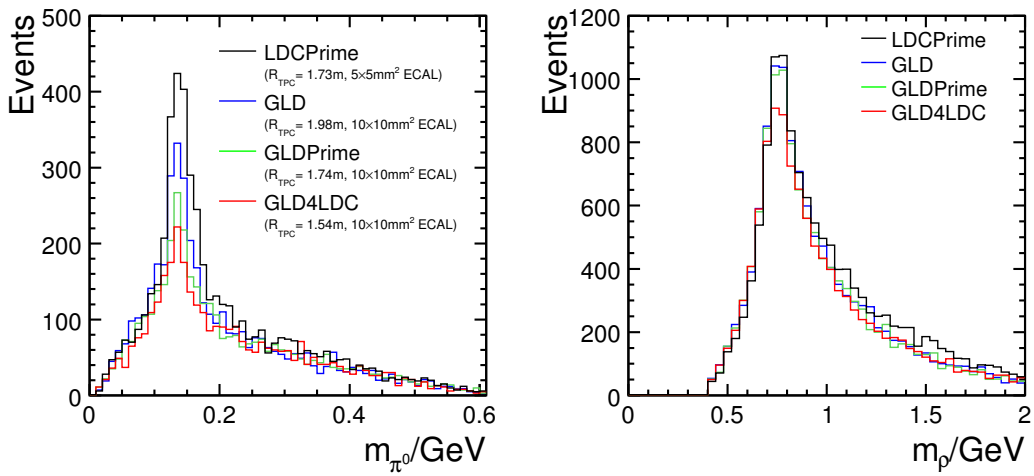

FIGURE 2.6-10. a) The reconstructed π^0 invariant mass distribution in the selected $\tau^+\tau^-$ events at $\sqrt{s} = 500\,\text{GeV}$. Only events where more than one photon is reconstructed are shown. b) The corresponding reconstructed $\rho^\pm \to \pi^\pm\pi^0$ mass distribution for decays where ≥ 1 photon cluster is reconstructed. For both plots the distributions include all tau decay modes.

Detector	ECAL/mm^2	R_{TPC}/m	Eff	Purity	σ_{P_τ}
GLD	10×10	1.98	84.5 %	85.7 %	0.0454 ± 0.0005
GLDPrime	10×10	1.74	85.2 %	83.6 %	0.0452 ± 0.0005
GLD4LDC	10×10	1.54	84.9 %	80.8 %	0.0460 ± 0.0006
LDCPrime	5×5	1.73	84.1 %	88.5 %	0.0430 ± 0.0005

TABLE 2.6-5
Summary of $\tau^\pm \to \pi^\pm\nu$ selection efficiencies and purities for events generated with the GLD, GLDPrime, GLD4LDC, and LDCPrime detector models. The efficiencies are calculated with with respect to the $\tau^+\tau^-$ selection and the purities only include the background from the different tau decay modes. The statistical uncertainties on the efficiencies and purities are all $\pm 0.5\,\%$. The uncertainty on the tau polarisation measurement assumes an electron-positron polarisation of $(-80\,\%, +30\,\%)$ and corresponds to 80 fb^{-1} of data.

2.6.3 Chargino and neutralino production

Chargino and neutralino pair production at $\sqrt{s}$ =500 GeV is studied in the context of SUSY point-5 benchmark scenario. The main signal is jets plus missing energy from $\chi_1^+\chi_1^- \to \text{W}^+\text{W}^-\chi_1^0\chi_1^0$ and $\chi_2^0\chi_2^0 \to \text{ZZ}\chi_1^0\chi_1^0$. The process $\chi_2^0\chi_2^0 \to \text{ZZ}\chi_1^0\chi_1^0$ is the main background to study $\chi_1^+\chi_1^- \to \text{W}^+\text{W}^-\chi_1^0\chi_1^0$ and *vice versa*. The identification of the separate chargino and neutralino final states relies on the ability to distinguish W^+W^- from ZZ and thus is sensitive to the jet energy resolution of the detector. Figure 2.6-11a shows the reconstructed invariant masses of hadronically decaying $W^\pm$ and Z bosons from decays of $\chi_1^\pm$ and χ_2^0, respectively. Neutralino and chargino event samples were separated based on the consistency of the reconstructed di-jet masses with the Z and W boson hypotheses. The selection efficiencies for $\chi_1^\pm$ and χ_2^0 events for the GLD-based detector models are summarised in Table 2.6-6. The different detector models give statistically compatible selection efficiencies. This is consistent with the fact that the differences in the jet energy resolutions for the three detector models

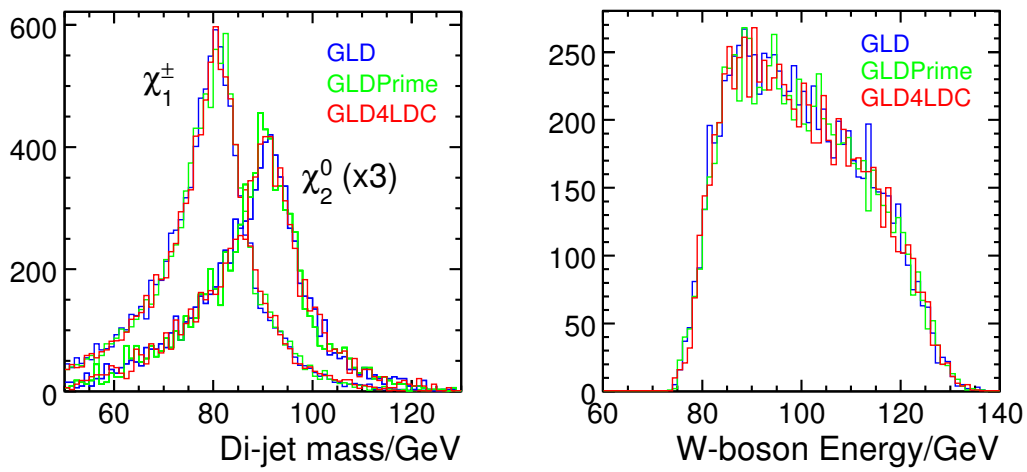

FIGURE 2.6-11. (a) The reconstructed masses of W and Z bosons from the decays of $\chi_1^\pm$ and χ_2^0. (b) The energy distribution of the reconstructed W bosons from $\chi_1^\pm$ decays.

	Chargino selection		Neutralino selection	
	Efficiency ($\chi_1^\pm$)	Efficiency (χ_2^0)	Efficiency ($\chi_1^\pm$)	Efficiency (χ_2^0)
GLD	$47.9 \pm 0.3\,\%$	$1.0 \pm 0.1\,\%$	$11.2 \pm 0.5\,\%$	$33.8 \pm 0.6\,\%$
GLDPrime	$48.4 \pm 0.3\,\%$	$1.0 \pm 0.1\,\%$	$11.4 \pm 0.5\,\%$	$33.3 \pm 0.6\,\%$
GLD4LDC	$48.8 \pm 0.3\,\%$	$1.1 \pm 0.1\,\%$	$11.4 \pm 0.5\,\%$	$34.1 \pm 0.6\,\%$

TABLE 2.6-6
The efficiency for $\chi_1^\pm$ and χ_2^0 selection.

considered are at the level of $3 - 4\,\%$ for the jet energy range $50 - 100\,\mathrm{GeV}$ (Table 2.2-2).

Because $\chi_1^\pm \to W^\pm\chi_1^0$ and $\chi_2^0 \to Z\chi_1^0$ are two body decays, the masses of $\chi_1^\pm$, χ_2^0, and lightest SUSY particle (LSP), χ_1^0, can be derived by using the energy distributions of the W and Z bosons. The energy distributions of the reconstructed W bosons are shown in Figure 2.6-11b. The different detector models result in very similar distributions and, consequently, have the same sensitivity to the $\chi_1^\pm$, χ_2^0 and LSP masses.

2.7 CONCLUSIONS

The studies described above informed the choice of parameters for the baseline ILD concept. The conclusions of these studies are:

- **B-field (vertex reconstruction):** The radius of the beam background envelope scales as $B^{-0.5}$. This determines that the minimum acceptable inner radius of the vertex detector goes from $\sim 14\,\mathrm{mm} \to 16\,\mathrm{mm}$ for $B = 4\,\mathrm{T} \to 3\,\mathrm{T}$. The effect on impact parameter resolution is $\lesssim 10\,\%$ and the resulting differences in flavour tagging efficiency are small ($\sim 2\,\%$).
- **B-field versus Radius (particle flow):** The confusion term in particle flow reconstruction scales as R^{-1}. This can be partially compensated by the magnetic field,

although the dependence is weak, $B^{-0.3}$. For the entire range of detector parameters spanning the GLD and LDC concepts, the ILC jet energy resolution requirements can be met. The differences in particle flow performance between the LDC and GLD parameters are small, $\lesssim 6\,\%$, with the larger radius/lower field option being preferred.

- **B-field versus Radius (momentum resolution):** In terms of momentum resolution, the differences between the models considered are small $\lesssim 10\,\%$. For high p_{T} tracks, larger radius/lower field detector is preferred. For low p_{T} tracks the opposite is true. All detector models considered here meet the ILC momentum resolution goals.
- **TPC aspect ratio (particle flow):** the aspect ratio of the TPC ($R : z = 1 : 1.3$) used in the studies is close to optimum for particle flow; there is no significant advantage in a longer TPC and a shorter TPC would significantly degrade the performance in the forward region.
- **ECAL Segmentation (particle flow):** The ECAL pixel size should be no greater than $10 \times 10\,\mathrm{mm}^2$ in order to meet the ILC jet energy resolution goals for the jets relevant at $\sqrt{s} = 500\,\mathrm{GeV}$. Within the context of the current reconstruction, $5 \times 5\,\mathrm{mm}^2$ gives significant advantages over $10 \times 10\,\mathrm{mm}^2$, particularly for higher energy jets.
- **ECAL Segmentation (physics):** For the reconstruction of tau decays, a $5 \times 5\,\mathrm{mm}^2$ ECAL pixel size is favoured over $10 \times 10\,\mathrm{mm}^2$.
- **Physics Performance:** The models considered give comparable physics performance. This is not surprising; the differences in the underlying detector performance measures are small because the models trade-off R against B in such a way that *each* represents a reasonable detector choice.
- **HCAL Segmentation/Depth (particle flow):** For sufficient containment of jets at $\sqrt{s} = 500\,\mathrm{GeV}$, the HCAL should be between $5 - 6\lambda_I$. The baseline for the ILD was chosen to be $6\lambda_I$ to ensure good jet containment for the highest energy jets and to allow for possible differences between the simulation of hadronic showers and reality. For the current reconstruction, there appears to be no significant advantage in going below $3 \times 3\,\mathrm{cm}^2$.
- **Vertex Detector:** two detector layouts were considered: five single layers and six layers arranged in three doublets. Both conceptual designs meet the ILC goals for impact parameter resolution, with the doublet structure giving an impact parameter resolution which is better, particularly for high momentum tracks.
- **SiW versus Scintillator-W ECAL:** results from studies of the strip reconstruction and the resulting jet energy resolution of the Scintillator/Tungsten option, whilst promising, have yet to reach the level of sophistication where the performance of the strip based ECAL option can be fully evaluated. For this reason, the SiW ECAL is used in the simulation of the ILD for the physics studies in the next section.
- **AHCAL versus DHCAL:** results from studies of the digital HCAL option are not yet at the level where its performance has been demonstrated. For this reason the AHCAL option with $3 \times 3\,\mathrm{cm}^2$ tiles is used in the simulation of ILD.
- **Cost:** From the studies presented in this section it is clear any of the detector models listed in Table 2.1-1 are viable detectors for the ILC. For the same subdetector technologies, the differences in the costs for the detector parameters considered are estimated to be $\sim 10 - 20\,\%$; a large $B = 3\,\mathrm{T}$ detector is disfavoured on grounds of cost. However, given the large fluctuations in raw material costs (as seen in the last year) and the difficulty extrapolating detector sensor costs to the future, it is not yet possible to choose between the models on this basis.

2.8 CHOICE OF ILD PARAMETERS

On the basis of the considerations above, the ILD detector parameters (listed Table 2.1-1) are chosen to be close to those of the LDCPrime/GLDPrime models. The main arguments for the choices are as follows:

- **Choice of B-field:** The operational magnetic field is chosen to be 3.5 T, although it is assumed that the solenoid would be designed for 4.0 T to allow a safety margin in the mechanical design. This can be achieved without extrapolating significantly beyond the current CMS design. The arguments for a higher field are relatively weak: the benefits are marginal, and it would increase the cost of the detector. Whilst a lower B-field is not excluded, it is felt that until the likely ILC backgrounds and their impact on the ILD concept are better understood, it would be unwise to go to 3 T.
- **Choice of Radius:** The ECAL inner radius is chosen to be 1.85 m. The ILD concept is designed for particle flow calorimetry and the jet energy performance is the main motivation for this choice. For B=3.5 T the gain in going to an ECAL radius of 2.0 m is modest and may not justify the increase in cost. For a B=3.5 T, the ILC jet energy goals suggest that the radius should be greater than $1.5 - 1.6$ m. However, the studies presented above rely on the simulation of hadronic showers. By selecting a detector radius of 1.85 m, it is likely that the ILD concept will meet the ILC jet energy goals, even if the current performance estimates are on the optimistic side.
- **Choice of Sub-detector Technologies:** At this stage we are not in a position to choose the ECAL, HCAL and vertex detector technologies. All options are considered on an equal basis. Nevertheless, for the physics studies that follow it is necessary to define a baseline for the simulation. The six layer (three doublets) vertex detector layout is used on the basis that it gives the best impact parameter resolution. For the calorimetry, the SiW ECAL and the AHCAL are used in the simulation as they have been well studied and we are confident that they give the desired jet energy resolution. The strip-based ECAL and DHCAL will be actively supported in simulation and software with the intention of evaluating their ultimate performance.

The optimisation of the ILD parameters was performed in a rigorous manner using information from a number of detailed studies. On this basis, we are confident that the ILD concept is well optimised for physics at the ILC operating in the energy range 200 GeV$-$1 TeV.

CHAPTER 3

Physics Performance

The performance of ILD is established using a detailed GEANT4 model and full reconstruction of the simulated events. Both detector performance measures and physics analyses are studied. Whilst the simulation and reconstruction are not perfect, they are at least as sophisticated as those used in the majority of studies for previous large collider detector TDRs.

3.1 SOFTWARE FOR ILD PERFORMANCE STUDIES

To demonstrate the physics capabilities of ILD, more than 30 million Monte Carlo (MC) events have been fully simulated and reconstructed for the benchmark reactions [24] and other physics channels of interest at the ILC. Signal samples typically correspond to an integrated luminosity of 500 fb^{-1} or more. These are combined with sufficiently large sets of SM events for background estimation. The "simulation reference ILD detector model", ILD_00, is implemented in Mokka. The silicon based tracking detectors are modelled with the appropriate material thicknesses and support structures without specifying the exact readout technology. Instead, in the digitisation stage, simulated hits are smeared by the effective point resolutions listed in Table 3.1-1. These represent the most realistic estimates from the relevant subdetector R&D groups. The SiW option with 5×5 mm^2 transverse cell size and the Steel-Scintillator option with $3 \times 3\,\mathrm{cm}^2$ tiles are used for the ECAL and HCAL respectively. As discussed in Section 2.2.6, these are the most mature of the technology options in terms of simulation and reconstruction; this does not imply any pre-decision on the ultimate technology choice. The main parameters of the ILD_00 model are listed in Table 2.1-1 and a drawing of this model is shown in Figure 3.1. Further details of the geometrical parameters can be found in [25].

	$\sigma_{r-\phi}/\mu\mathrm{m}$	$\sigma_z/\mu\mathrm{m}$		$\sigma_{r-\phi}/\mu\mathrm{m}$	$\sigma_z/\mu\mathrm{m}$
VTX	2.8	2.8	FTD	5.8	5.8
SIT/SET	7.0	50.0	ETD	7.0	7.0
TPC	$\sigma_{r\phi}^2 = 50^2 + 900^2 \sin^2\phi + \left((25^2/22) \times (4/B)^2 \sin\theta\right)(z/\mathrm{cm})\,\mu\mathrm{m}^2$ $\sigma_z^2 = 400^2 + 80^2 \times (z/\mathrm{cm})\,\mu\mathrm{m}^2$				

TABLE 3.1-1
Effective point resolutions used in the digitisation of the MC samples.

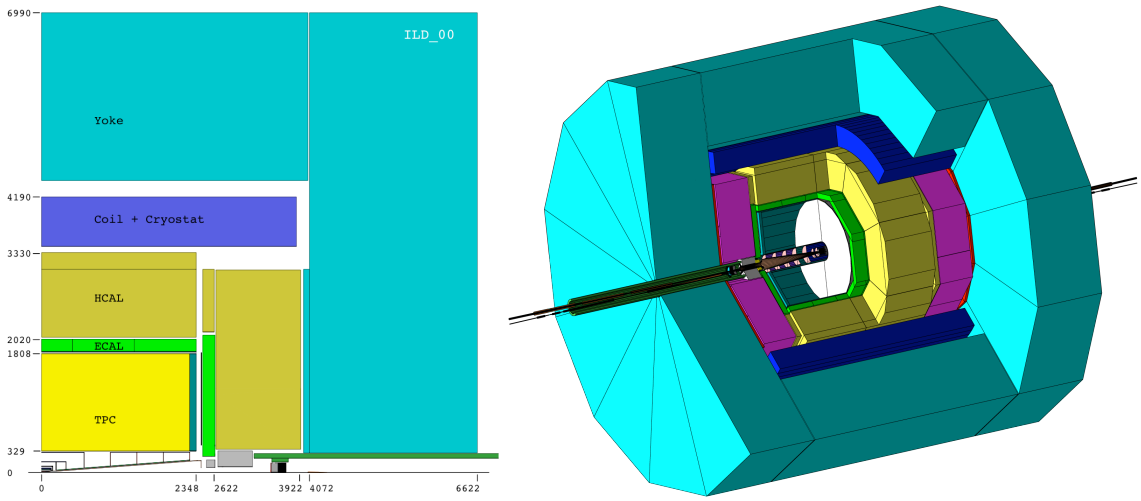

FIGURE 3.1-1. The ILD_00 detector model as implemented in Mokka. From the inside to the outside, the detector components are the: VTX, SIT, TPC, SET, ECAL, HCAL and Yoke. In the forward region the FTD, ETD, LCAL, LHCAL and BCAL are shown.

Most of the subdetectors in the ILD_00 model have been implemented including a significant amount of engineering detail such as mechanical support structures, electronics and cabling as well as dead material and cracks. This provides a reasonable estimate of the material budget and thus the effect of multiple scattering in the tracking detectors; it is also crucial for a realistic demonstration of particle flow performance. In the simulation, the vertex detector has a staggered layout of six 50 μm thick silicon ladders and corresponding support structures. The additional silicon tracking detectors, FTD/ETD (forward Si tracking) and SIT/SET (inner and outer Si tracking), are modelled as disks and cylinders respectively. The material thicknesses for these detectors give the effective radiation lengths listed in Table 4.2-3. The TPC model includes the material in the inner and outer field cage, this corresponds to a total of 4.5 % X_0 including the drift gas mixture. The hits from charged particles were simulated according to an end-plate layout with 224 rows of pads, 1 mm wide and 6 mm high. The ECAL simulation includes the alveolar structure and also the dead regions around the silicon pixels and between the modules. The HCAL simulation includes steel and aluminium support structures which result in dead regions. The energy response of the scintillator tiles was corrected according to Birks' law. The simulation of the forward region includes realistic support structures and the shielding masks. All subdetectors are enclosed by a dodecagonal iron yoke, instrumented in the simulation with ten layers of RPCs. The superconducting coil and cryostat are simulated as a 750 mm thick aluminium cylinder, corresponding to 1.9 λ_I.

All events are reconstructed using the Kalman-Filter based track reconstruction in MarlinReco, the PandoraPFA particle flow algorithm and the LCFIVertex flavour tagging. The flavour tagging artificial neural networks (ANNs) have been trained using fully simulated and reconstructed ILD_00 MC events. The boost resulting from the 14 mrad crossing angle is taken into account in the analyses that use BCAL hit distributions as an electron veto.

3.2 ILD DETECTOR PERFORMANCE

3.2.1 ILD Tracking Performance

The tracking system envisaged for ILD consists of three subsystems each capable of standalone tracking VTX, FTD and the TPC. These are augmented by three auxiliary tracking systems the SIT, SET and ETD, which provide additional high resolution measurement points. The momentum resolution goal [26] is

$$\sigma_{1/p_T} \approx 2 \times 10^{-5}\,\mathrm{GeV}^{-1},$$

and that for impact parameter resolution is

$$\sigma_{r\phi} = 5\,\mu\mathrm{m} \oplus \frac{10}{\mathrm{p(GeV)}\sin^{3/2}\theta}\,\mu\mathrm{m}.$$

3.2.1.1 Coverage and Material Budget

Figure 3.2-2a shows, as a function of polar angle, θ, the average number of reconstructed hits associated with simulated 100 GeV muons. The TPC provides full coverage down to $\theta = 37°$. Beyond this the number of measurement points decreases. The last measurement point provided by the TPC corresponds to $\theta \approx 10°$. The central inner tracking system, consisting of the six layer VTX and the two layer SIT, provides eight precise measurements down to $\theta = 26°$. The innermost and middle double layer of the VTX extend the coverage down to $\theta \sim 16°$. The FTD provides up to a maximum of five measurement points for tracks at small polar angles. The SET and ETD provide a single high precision measurement point with large lever arm outside of the TPC volume down to a $\theta \sim 10°$. The different tracking system contributions to the detector material budget, including support structures, is shown in Figure 3.2-2b.

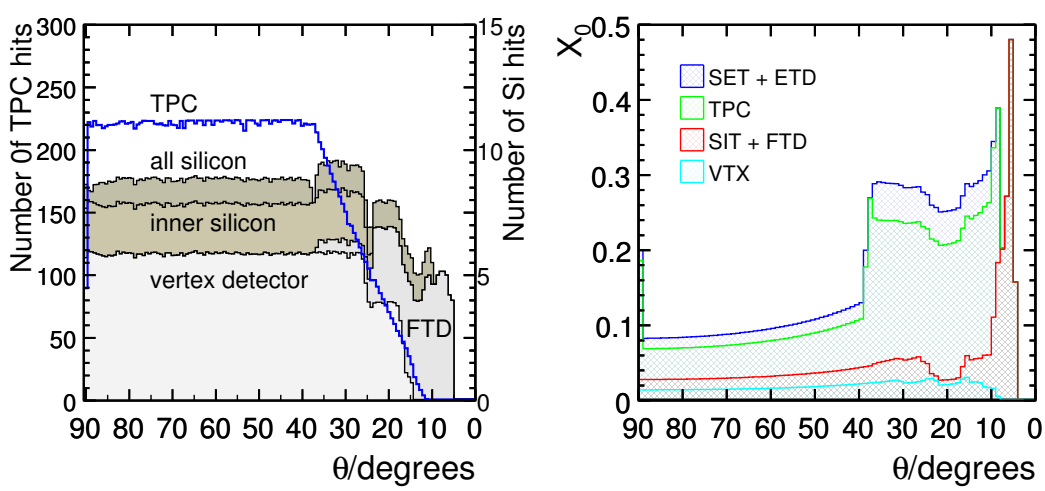

FIGURE 3.2-2. a) Average number of hits for simulated charged particle tracks as a function of polar angle. b) Average total radiation length of the material in the tracking detectors as a function of polar angle.

3.2.1.2 Momentum Resolution for the Overall Tracking System

The momentum resolution achieved with the ILD simulation and full reconstruction is shown in Figure 3.2-3a. The study was performed using muons generated at fixed polar angles of $\theta = 7°, 20°, 30°$ and $85°$, and the momentum was varied over the range $1 - 200\,\mathrm{GeV}$. For two polar angles, this is compared to the expected parametric form of, $\sigma_{1/p_T} = a \oplus b/(p_T \sin\theta)$, with $a = 2 \times 10^{-5}\,\mathrm{GeV}^{-1}$ and $b = 1 \times 10^{-3}$. As can be seen, at a polar angle of 85°, the required momentum resolution is attainable over the full momentum range from 1 GeV upwards, this remains true over the full length of the barrel region of the detector, where the TPC in conjunction with the SET is able to provide the longest possible radial lever arm for the track fit. For high momentum tracks, the asymptotic value of the momentum resolution is $\sigma_{1/p_T} = 2 \times 10^{-5}\,\mathrm{GeV}^{-1}$. At $\theta = 30°$, the SET no longer contributes, the effective lever-arm of the tracking system is reduced by 25 %. Nevertheless, the momentum resolution is still within the required level of performance. In the very forward region, the momentum resolution is inevitably worse due to the relatively small angle between the B-field and the track momentum.

3.2.1.3 Impact Parameter Resolution

Figure 3.2-3b shows $r\phi$ impact parameter resolution as a function of the track momentum. The required performance is achieved down to a track momentum of 1 GeV, whilst it is exceeded for high momentum tracks where the asymptotic resolution is $2\,\mu$m. The rz impact parameter resolution (not shown) is better than $\sim 10\,\mu$m down to momenta of 3 GeV and reaches an asymptotic value of $< 5\,\mu$m for the whole barrel region. Because of the relatively large distance of the innermost FTD disk to the interaction point, the impact parameter resolution degrades for very shallow tracks, $\theta < 15°$. It should be noted that these studies do not account for the possible mis-alignment of the tracking systems.

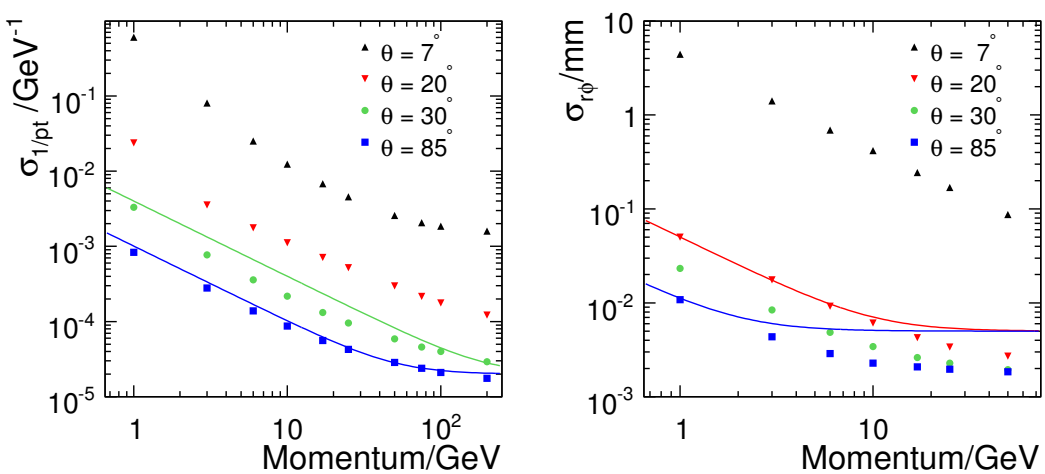

FIGURE 3.2-3. a) Transverse momentum resolution for muons plotted versus polar angle for four different simulated muon momenta. The lines show $\sigma_{1/p_T} = 2 \times 10^{-5} \oplus 1 \times 10^{-3}/(p_T \sin\theta)$ for $\theta = 30°$ (green) and $\theta = 85°$ (blue). b) Impact parameter resolution for muons versus polar angle for four different simulated muon momenta.

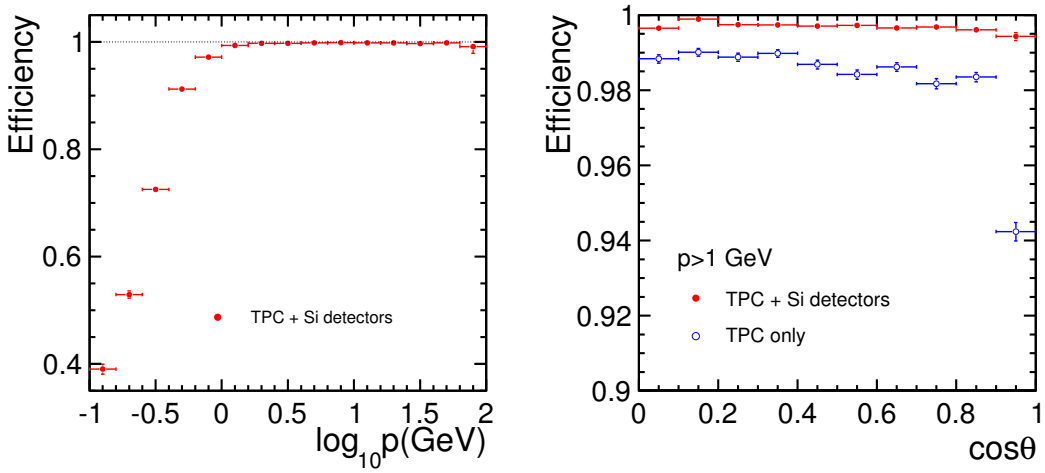

FIGURE 3.2-4. Tracking Efficiency as a function for $t\bar{t} \rightarrow$ 6 jets at 500GeV plotted against a) momentum and b) $\cos\theta$. Efficiencies are plotted with respect to MC tracks which leave at least 4 hits in the tracking detectors including decays and V^0s.

3.2.1.4 Tracking Efficiency

With over 200 contiguous readout layers, pattern recognition and track reconstruction in a TPC is relatively straightforward, even in an environment with a large number of background hits. In addition, the standalone tracking capability of the VTX enables the reconstruction of low transverse momentum tracks which do not reach the TPC. Hermetic tracking down to low angles is important at the ILC [27] and the FTD coverage enables tracks to be reconstructed to polar angles below $\theta = 7°$.

Figure 3.2-4 shows, as a function of momentum and polar angle, the track reconstruction efficiency in simulated (high multiplicity) $t\bar{t} \rightarrow$ 6 jet events at $\sqrt{s}$ =500 GeV. For the combined tracking system, the track reconstruction efficiency is approximately 99.5 % for tracks with momenta greater than 1 GeV across almost the entire polar angle range. The effects of background from the machine and from multi-peripheral $\gamma\gamma \rightarrow$ hadrons events are not yet taken into account; dedicated studies form part of the ongoing simulation R&D effort. Nevertheless, a study of the TPC reconstruction efficiency as a function of the noise occupancy is described in Section 4.3.3. This demonstrates that there is no loss of efficiency for 1 % noise occupancy.

3.2.2 Background Studies

The studies presented above do not include the effects of background from the machine and from multi-peripheral $\gamma\gamma \rightarrow$ hadrons events. The impact of machine background has been studied in the context of the ILD concept. These studies are based on the expected simulated detector hits from approximately 2000 bunch crossings (BXs). The hits are super-imposed on simulated physics events taking into account the 369 ns bunch structure of the ILC and conservative estimates of the readout rates of the tracking detector components.

3.2.2.1 Background in the TPC

For a conservative value for the TPC gas drift velocity, $4\,\mathrm{cm}\,\mu\mathrm{s}^{-1}$, the maximum TPC drift length of 2.25 m corresponds to 150 BXs. Nominal background in the TPC is thus simulated as 150 BXs appropriately shifted in z. Prior to the reconstruction, nearby hits are merged taking into account the expected $r\phi$ and z extent of the charge cloud. For the TPC readout assumed for ILD, 150 BXs of beam-related background correspond to a voxel occupancy of approximately 0.05 % (the TPC voxel size is taken to be 1 mm in the ϕ direction, 6 mm in r and 5 mm in z).

Figure 3.2-5 shows the TPC hits for a single $\mathrm{t\bar{t}}$ event at $\sqrt{s} = 500\,\mathrm{GeV}$ overlayed with 150 BXs of pair-background hits. On average there are 265,000 background hits in the TPC, compared to the average number of signal hits of 23100 (8630 from charged particles with p_T >1 GeV). Even with this level of background, the tracks from the $\mathrm{t\bar{t}}$ event are clearly visible in the $r\phi$ view. A significant fraction of the background hits in the TPC arise from low energy electrons/positrons from photon conversions. These low energy particles form small radius helices parallel to the z axis, clearly visible as lines in the rz view. These "micro-curlers" deposit charge on a small number of TPC pads over a large number of BXs. Specific pattern recognition software has been written to identify and remove these hits prior to track reconstruction. (Whilst not explicitly studied, similar cuts are expected to remove a significant fraction of hits from beam halo muons.) Figure 3.2-6 shows the TPC hits after removing hits from micro-curlers. Whilst not perfect, the cuts remove approximately 99 % of the background hits and only 3 % of hits from the primary interation and the majority of these are from low p_T tracks. Less than 1 % of hits from tracks with p_T >1 GeV originating from the $\mathrm{t\bar{t}}$ event are removed.

This level of background hits proves no problem for the track-finding pattern recognition software, as can be seen from Figure 3.2-7. Even when the background level is increased by a factor of three over the nominal background no degradation of TPC track finding efficiency is observed for the 100 events simulated. This study demonstrates the robustness of TPC tracking in the ILC background environment.

These conclusions are supported by an earlier study based on a detector concept with

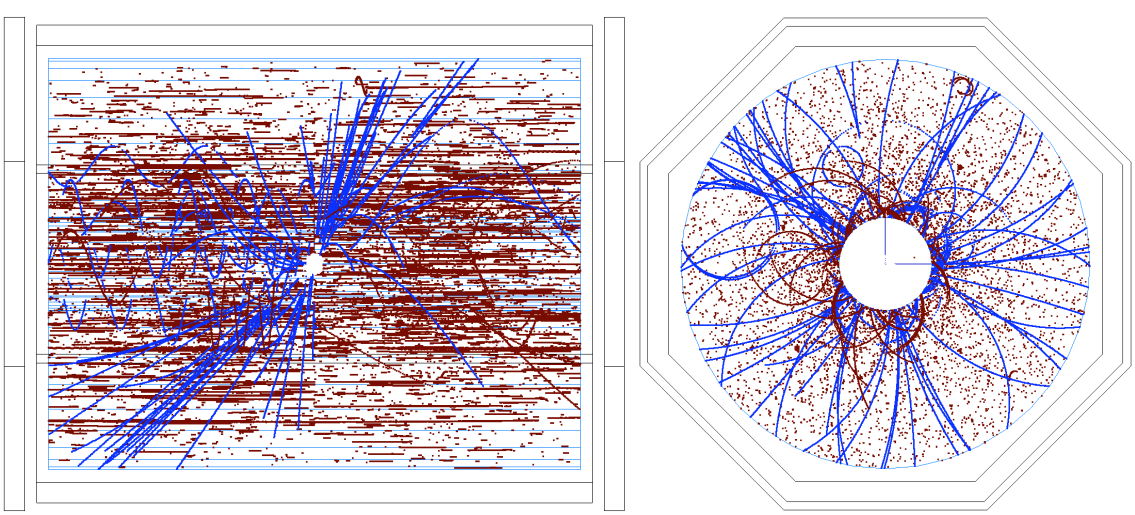

FIGURE 3.2-5. The rz and $r\phi$ views of the TPC hits from a 500 GeV $\mathrm{t\bar{t}}$ event (blue) with 150 BXs of beam background (red) overlayed.

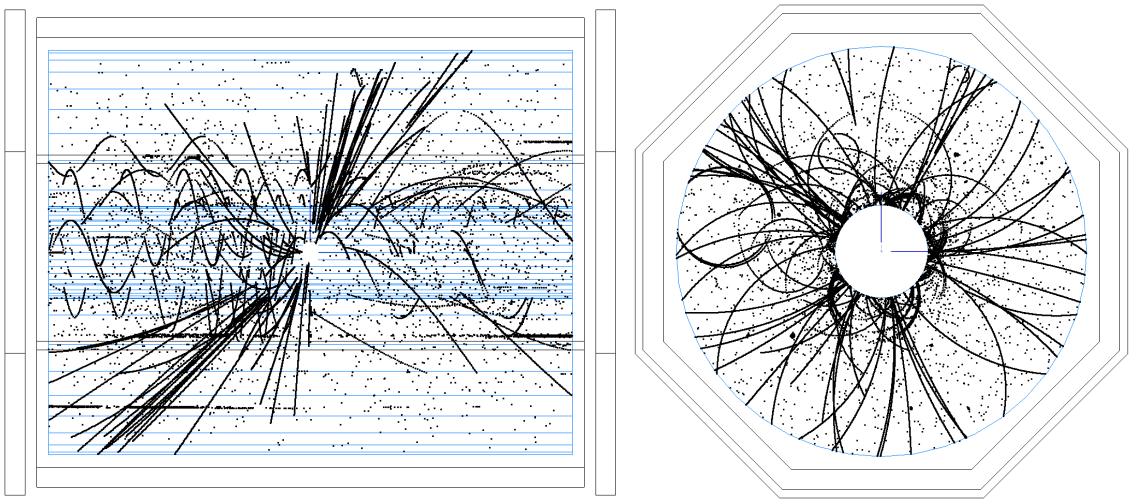

FIGURE 3.2-6. The same event as the previous figure, with the micro-curler removal algorithm applied. This is the input to the TPC track finding algorithm.

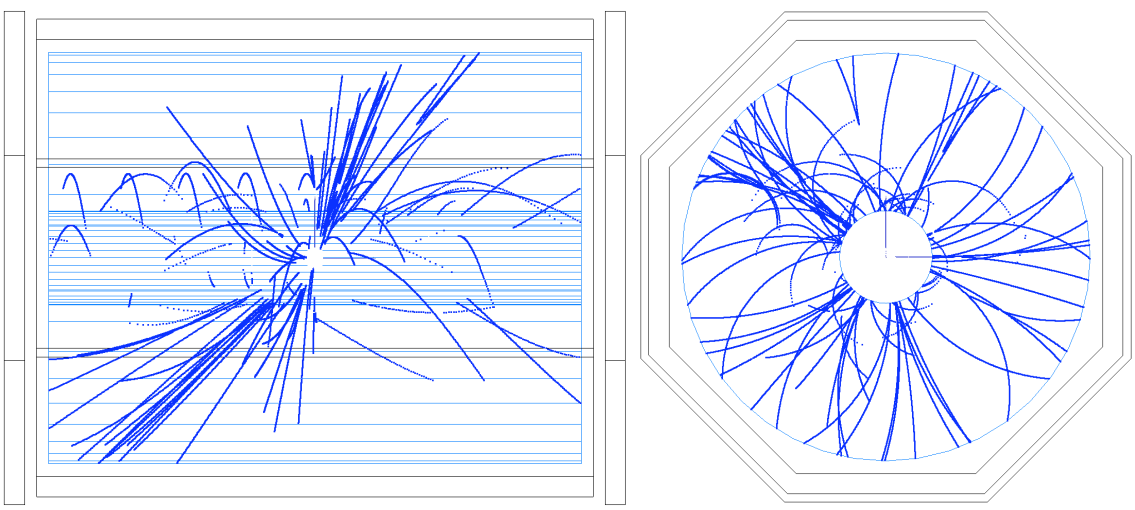

FIGURE 3.2-7. The same event as the previous plot, now showing the reconstructed TPC tracks.

$B = 3.0\,\mathrm{T}$, a TPC radius of $1.9\,\mathrm{m}$ and TPC readout cells of $3\times10\,\mathrm{mm}^2$. This earlier study used a uniform distribution of background hits in the TPC volume, but included a very detailed simulation of the digitised detector response and full pattern recognition is performed in both time and space. The TPC reconstruction efficiency as a function of the noise occupancy remains essentially unaffected for $1\,\%$ occupancy (uniformly distributed through the TPC). It should be noted that this level of occupancy is twice the nominal occupancy at the TPC inner radius and about fifty times the typical total occupancy in the TPC. This earlier study is presented in more detail in Section 4.3.2.

3.2.2.2 Background in the Vertex Detector

The impact of background in the vertex detector (VTX) depends on the assumptions made for the Silicon read-out time. If one were to assume single BX time-stamping capability in the vertex detector, the anticipated background level is negligible. However, it is anticipated

that the readout of the Silicon pixel ladders will integrate over many BXs. For the studies presented here, it is assumed that vertex detector readout integrates over 83 and 333 BXs for the inner two and outer four layers respectively. For the silicon strip-based SIT detector, single BX time-stamping is assumed. Hence the background hits which are superimposed on the physics event correspond to 1 BX in the SIT, 150 BXs in the TPC and 83/333 BXs in the VTX. It should be noted that the background studies have not yet been extended to the FTD.

With the above assumptions, the background in the vertex detector corresponds to approximately 2×10^5 hits per event, with the corresponding layer occupancies listed in Table 3.2-2. The hit occupancies account for the finite cluster size reflecting the fact that a single charged particle crossing a layer of the VTX will deposit hits in multiple pixels. The distribution of cluster sizes, taken to be the product of the z and $r\phi$ extent of the energy deposition in the Silicon, are determined from the full simulation of the beam related background. The mean background cluster size is found to be 10 pixels, where a pixel is taken to be $25 \times 25\,\mu$m.

Layer	radius/mm	BXs	Pixel Occupancy
0	16.0	83	3.33 %
1	17.9	83	1.90 %
2	37.0	333	0.40 %
3	38.9	333	0.33 %
4	58.0	333	0.08 %
5	59.9	333	0.06 %

TABLE 3.2-2
Vertex detector occupancies for the readout times assumed in the background studies. The occupancies account for the finite cluster size.

Pattern recognition in the environment of 10^5 background hits is non-trivial and required modifications to the existing Silicon track finding code. Specifically, tracks in the Silicon detectors are now seeded using only layers $2-5$ of the vertex detector and the two layers of the SIT. Seeded tracks are then projected inwards to pick up hits in the inner two silicon layers (layers 0 and 1). Tracks with transverse momentum of $p_T < 200\,\text{MeV}$ are rejected. There are a number of questions which can be asked: i) Can the number of "ghost" tracks, *i.e.* those formed from random combinations of hits be reduced to an acceptable level; ii) how many genuine tracks from the pair background remain; iii) how do any additional cuts used to reduce the beam background affect the signal; and iv) what is the loss of efficiency due to hits from the primary interaction being merged with the clusters of pixels from background hits. These four questions are addressed below.

Figure 3.2-8a) shows the p_T distribution of reconstructed tracks in the Silicon detectors with the background overlayed. Due to the conservative assumptions for the VTX readout times, an average of 34 low-p_T silicon tracks are reconstructed per physics event, reflecting the integration over 83/333 BXs. The number of background tracks would be dramatically reduced by the requirement the reconstructed track is in the same BX as the underlying physics interaction. Tracks are thus required to have at least one SIT hit (which provides unambiguous BX identification) or to be associated with at least 10 TPC hits (where the

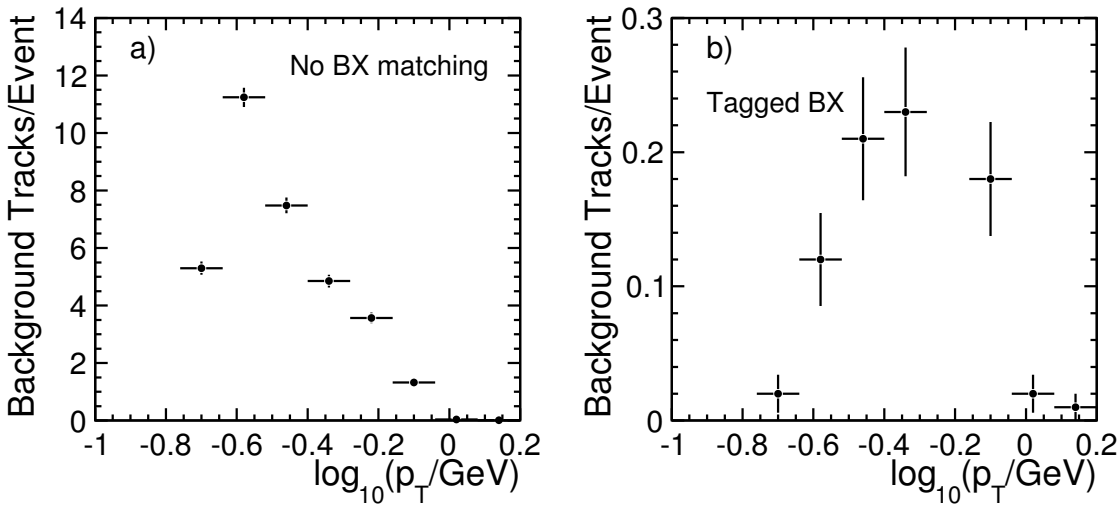

FIGURE 3.2-8. The p_T distribution of reconstructed background tracks in the Silicon detectors (VTX+SIT) a) before requiring the track to be in time with the physics interaction beam crossing (BX) and b) after requiring at least 1 SIT hit or a match to at least 10 TPC hits. A track is considered to be from background if more than 20 % of the associated hits come from the overlayed background events.

matching in z can be used to identify the BX). Figure 3.2-8 shows the resulting p_T distribution of the remaining background tracks. On average 1.2 background tracks per event remain with a mean p_T of 500 MeV. The majority of the remaining background tracks are either from relatively high p_T electrons/positrons or from combinations of signal and background hits. Firstly, there may be a loss of efficiency due to the additional requirements of associated SIT or TPC hits. For tracks from the primary physics interaction (*i.e.* the $t\bar{t}$ event), the SIT/TPC requirements remove approximately 1 % of tracks with $p_T < 1$ GeV, whilst for $p_T > 1$ GeV there is no observed loss of efficiency.

The presence of a large number background hits not only results in a small number of background tracks, it may also lead to a degradation of the pattern recognition performance. In addition, if a charged particle from the interaction passes close to a cluster of pixels from the pair background, a single larger cluster will be formed. It is assumed such an extended cluster will not be included in the track-finding algorithm, and hence hits close to background clusters effectively will be lost. In addition to overlaying 83/333 BXs of background, the pixel occupancies in Table 3.2-2 are used to remove the appropriate number of hits from the primary interaction. The effect of the overlayed background and the resulting hit inefficiencies is studied for simulated $t\bar{t} \rightarrow 6$ jets events at $\sqrt{s} = 500$ GeV. Figure 3.2-9a) shows the overall track reconstruction efficiency with and without background. The main effect of the background is to reduce the efficiency for tracks with $p_T < 300$ MeV. For tracks $p_T > 1$ GeV, the presence of background reduces the track finding efficiency by less than 0.1 %. In the presence of background the efficiency for tracks with $p_T > 1$ GeV is 98.8 %. Care has to be taken in interpreting this number; the efficiencies depend on how the denominator is defined. For example, the inefficiency for high p_T tracks arises almost entirely from tracks which decay or interact within the volume of the VTX/SIT. Figure 3.2-9b) shows the track finding efficiency for tracks which (in simulation) deposit energy in the TPC gas volume. For this sample, the efficiency is greater than 99.9 % for tracks with $p_T > 1$ GeV, with or without background. It is concluded that the ILD tracking efficiency is not significantly degraded by

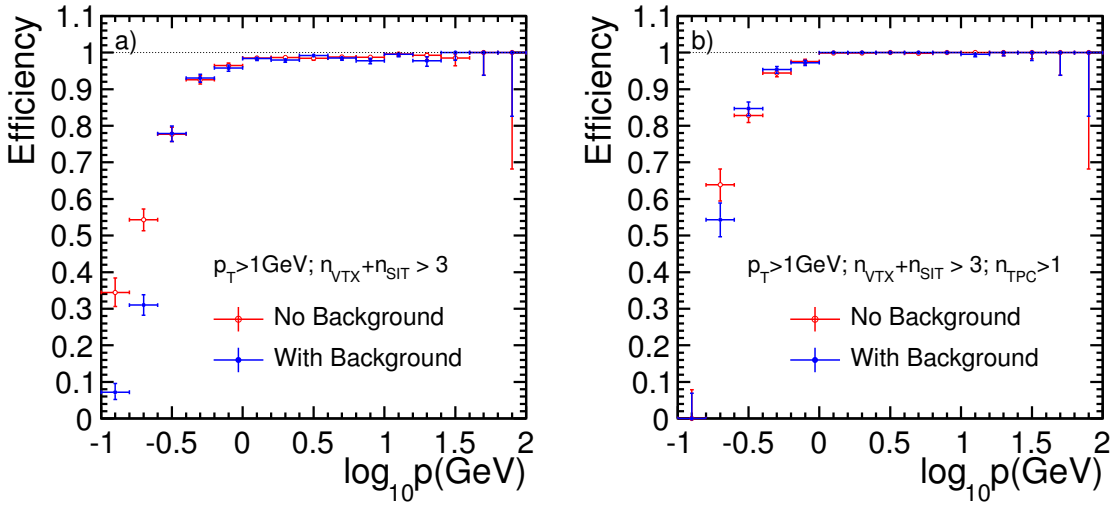

FIGURE 3.2-9. Tracking efficiency with overlayed background in the vertex detector vs transverse momentum for $t\bar{t} \rightarrow 6$ jets at 500GeV ($|\cos\theta| < 0.8$) a) for all charged particles and b) for charged particles which deposit at least one hit in the TPC. The tracking efficiency is shown for tracks with $p_T > 1$ GeV with a total of at least 4 hits in the VTX and SIT. Tracks are considered to be well reconstructed if there is at least one associated SIT hit or more than 10 TPC hits and if at least 70 % of the hits on the track are from the original Monte Carlo Particle.

the nominal level of background expected at the ILC.

3.2.2.3 Impact of background on physics analyses

To fully simulate the effect of background on a particular physics channel would require overlaying 1 BX in the SIT, 150 BXs in the TPC and 83/333 BXs in the VTX on each simulated physics event and would require vast CPU resources. From the studies above it is expected that the track finding inefficiencies for the high momentum muons in the $ZH \rightarrow \mu^+\mu^- X$ channel will be negligibly small. In addition, the presence of the relatively few low p_T background tracks will not affect the recoil mass distribution. The possibility that the loss of hits in the vertex detector due to background occupancy might distort the recoil mass distribution has been investigated (see Figure 3.2-10). The observed differences are negligibly small.

3.2.3 ILD Flavour Tagging Performance

Identification of b-quark and c-quark jets plays an important role within the ILC physics programme. The vertex detector design and the impact parameter resolution are of particular importance for flavour tagging. The LCFIVertex flavour tagging (see Section 2.5) uses ANNs to discriminate b-quark jets from c and light-quark jets (b-tag), c-quark jets from b and light-quark jets (c-tag), and c-quark jets from b-quark jets (bc-tag).

The flavour tagging performance [22] of ILD is studied for the two vertex detector geometries considered, three double-sided ladders (VTX-DL) and five single-sided (VTX-SL) ladders. No significant differences in the input variables for the ANNs are seen for two geometries, and therefore the ANNs trained for the VTX-DL option were used for both VTX configurations. The samples used in the training consisted of 150000 $Z \rightarrow q\bar{q}$, at the Z pole

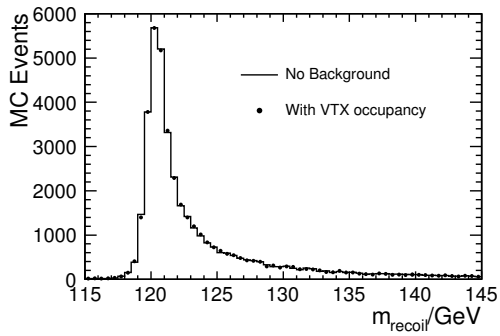

FIGURE 3.2-10. The Higgs recoil mass distribution in the $\mu^+\mu^- X$ channel from 50000 generated MC events after selection for the case of no background and with inefficiencies in the vertex detector due to the occupancy level expected from the pair background.

energy, equally distributed among the three decay modes $q = b, c$ and light quarks. The test samples used to evaluate the flavour tagging performance were generated independently and consist of 10000 events of $Z \to \mathrm{q\bar{q}}$ generated at both $\sqrt{s} = 91\,\mathrm{GeV}$ and $\sqrt{s} = 500\,\mathrm{GeV}$, with the SM flavour mix of hadronic final states. The ILD flavour tagging performances at 91 GeV for the two vertex detector options are shown in Figure 3.2-11a). The performance differences between the two VTX geometries are small ($\lesssim 1\%$). Uncertainites due to the statistical fluctuations of the test sample and in those introduced in the ANN training are estimated to be $\lesssim 2\%$. The performance for $Z \to \mathrm{q\bar{q}}$ at $\sqrt{s} = 500\,\mathrm{GeV}$ is shown in Figure 3.2-11b). It should be noted that for the 500 GeV results the ANNs were not retrained, *i.e.* those obtained for $\sqrt{s} = 91\,\mathrm{GeV}$ were used. Consequently, improvements in the performance are expected.

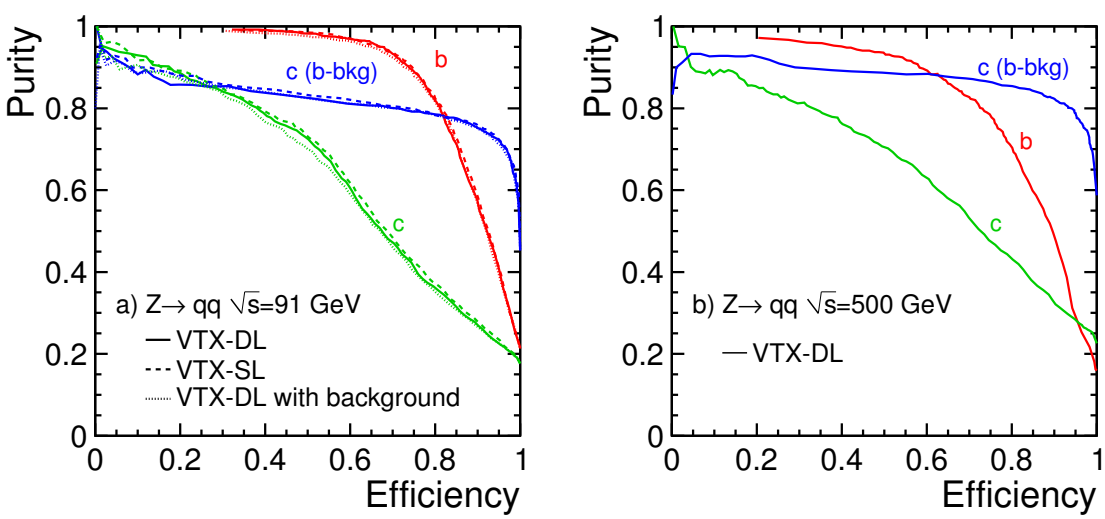

FIGURE 3.2-11. a) Flavour tagging performance of the ILD detector for 91 GeV $Z \to \mathrm{q\bar{q}}$ events for both the three double-sided ladders (VTX-DL) layout and with five single-sided ladder layout (VTX-SL). Also shown for the VTX-DL is the impact of background on the flavour tagging performance. b) Flavour tagging performance of the ILD detector for 500 GeV $Z \to \mathrm{q\bar{q}}$ events for the VTX-DL layout. In all cases the acceptance corresponds to $|\cos\theta_{\mathrm{jet}}| < 0.95$.

3.2.3.1 Impact of Background

Do to the large computational requirements in overlaying background hits from many BXs a parametric approach is taken to assess the impact of background on the flavour tagging performance. In Section 3.2.2.2 is was demonstrated that hits from pair background integrated over 83 (333) BXs for layers 0 and 1 ($2-5$) of the VTX-DL doublet layout of six ladders does not result in a significant number of background tracks and that the overall tracking efficiency is not significantly reduced. The main impact on flavour tagging is likely to be from the resulting hit inefficiencies particularly in the inner layers. To simulate the effect of background the pixel occupancies of Table 3.2-2 are used to randomly remove Silicon hits from the events before track finding and flavour tagging. This results in a slight degradation in tracking performance in the Silicon detectors; the number of TPC tracks associated with a complete track in the vertex detector (6 hits) decreases by 2 %. The resulting flavour tagging performance is shown in Figure 3.2-11a). Although there is a suggestion of a small degradation in the performance of the c-tag in the low efficiencies/high purity region, the presence of pair background does not significantly degrade the flavour tagging performance.

3.2.4 ILD Particle Flow Performance

Many important physics channels at the ILC will consist of final states with at least six fermions, setting a "typical" energy scale for ILC jets as approximately 85 GeV and 170 GeV at $\sqrt{s} = 500\,\mathrm{GeV}$ and $\sqrt{s}$ =1 TeV respectively. The current performance of the PandoraPFA algorithm applied to ILD Monte Carlo simulated data is summarised in Table 3.2-3. The observed jet energy resolution (rms_{90}) is not described by the expression $\sigma_E/E = \alpha/\sqrt{E/\mathrm{GeV}}$. This is not surprising, as the particle density increases it becomes harder to correctly associate the calorimetric energy deposits to the particles and the confusion term increases. The single jet energy resolution is also listed. The jet energy resolution (rms_{90}) is better than 3.8 % for the jet energy range of approximately $40-400\,\mathrm{GeV}$. The resolutions quoted in terms of rms_{90} should be multiplied by a factor of approximately 1.1 to obtain an equivalent Gaussian analysing power[12].

Jet Energy	raw rms	rms_{90}	$\mathrm{rms}_{90}/\sqrt{E_{jj}/\mathrm{GeV}}$	σ_{E_j}/E_j
45 GeV	3.3 GeV	2.4 GeV	25.0 %	(3.71 ± 0.05) %
100 GeV	5.8 GeV	4.1 GeV	29.5 %	(2.95 ± 0.04) %
180 GeV	11.2 GeV	7.5 GeV	40.1 %	(2.99 ± 0.04) %
250 GeV	16.9 GeV	11.1 GeV	50.1 %	(3.17 ± 0.05) %

TABLE 3.2-3
Jet energy resolution for Z →uds events with $|\cos\theta_{\mathrm{q\bar{q}}}| < 0.7$, expressed as, rms_{90} for the di-jet energy distribution, the effective constant α in $\mathrm{rms}_{90}/E = \alpha(E_{jj})/\sqrt{E_{jj}/\mathrm{GeV}}$, and the fractional jet energy resolution for a single jets, σ_{E_j}/E_j. The jet energy resolution is calculated from rms_{90}.

Figure 3.2-12 shows the jet energy resolution for Z →uds events plotted against the cosine of the polar angle of the generated $\mathrm{q\bar{q}}$ pair, $\cos\theta_{\mathrm{q\bar{q}}}$, for four different values of $\sqrt{s}$. Due to the calorimetric coverage in the forward region, the jet energy resolution remains good down to $\theta = 13°$ ($\cos\theta = 0.975$).

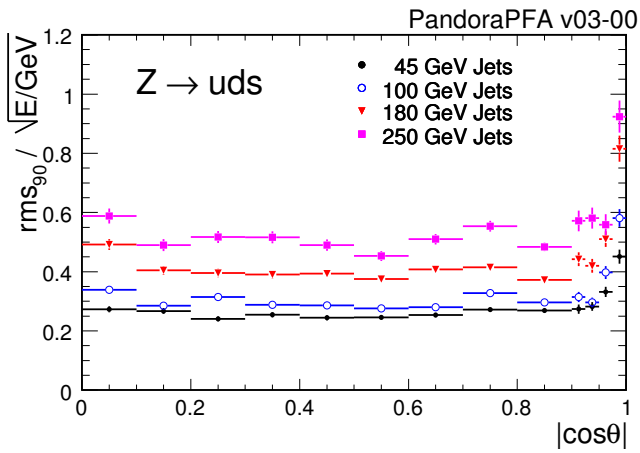

FIGURE 3.2-12. The jet energy resolution, defined as the α in $\sigma_E/E = \alpha\sqrt{E/\mathrm{GeV}}$, plotted versus $\cos\theta_{\mathrm{q\bar{q}}}$ for four different jet energies.

3.3 PHYSICS PERFORMANCE

The ILD detector performance has been evaluated for a number of physics processes. The analyses, described below, all use the full simulation of ILD and full event reconstruction. Jet finding is performed using the Durham algorithm[28] with the hadronic system being forced into the appropriate number of jets for the event topology. The benchmark physics analyses[24] are studied at $\sqrt{s} = 250\,\mathrm{GeV}$ and $\sqrt{s} = 500\,\mathrm{GeV}$. Unless otherwise stated, the results for $\sqrt{s} = 250\,\mathrm{GeV}$ ($\sqrt{s} = 500\,\mathrm{GeV}$) correspond to an integrated luminosity of $250\,\mathrm{fb}^{-1}$ ($500\,\mathrm{fb}^{-1}$) and a beam polarisation of $P(\mathrm{e}^+,\mathrm{e}^-) = (+30\,\%, -80\,\%)$.

3.3.1 Higgs Boson mass

The precise determination of the properties of the Higgs boson is one of the main goals of the ILC. Of particular importance are its mass, m_{H}, the total production cross section, $\sigma(\mathrm{e}^+\mathrm{e}^- \to \mathrm{HZ})$, and the Higgs branching ratios. Fits to current electroweak data[29] and direct limits from searches at LEP and at the Tevatron favour a relatively low value for m_{H}. Studies of these measurements with ILD are described below. A data sample of $250\,\mathrm{fb}^{-1}$ at $\sqrt{s} = 250\,\mathrm{GeV}$ is assumed and m_{H} is taken to be $120\,\mathrm{GeV}$. For these values, the dominant Higgs production process is Higgs-strahlung, $e^+e^- \to \mathrm{ZH}$.

The Higgs boson mass can be determined precisely from the distribution of the recoil mass, m_{recoil}, in $\mathrm{ZH} \to \mathrm{e}^+\mathrm{e}^-X$ and $\mathrm{ZH} \to \mu^+\mu^-X$ events, where X represents the Higgs decay products. The recoil mass is calculated from the reconstructed four-momentum of the system recoiling against the Z. The $\mu^+\mu^-X$-channel yields the most precise measurement as the $\mathrm{e}^+\mathrm{e}^-X$-channel suffers from larger experimental uncertainties due to bremsstrahlung from the electrons and the larger background from Bhabha scattering events. The study[30, 31] is performed for two electron/positron beam polarisations: $P(e^+, e^-) = (-30\,\%, +80\,\%)$ and $P(e^+, e^-) = (+30\,\%, -80\,\%)$. In the simulation, Gaussian beam energy spreads of $0.28\,\%$ and $0.18\,\%$ are assumed for the incoming electron and positron beams respectively.

The first stage in the event selection is the identification of leptonically decaying Z bosons. Candidate lepton tracks are required to be well-measured, removing tracks with large uncertainties on the reconstructed momentum. Lepton identification is performed using the

associated calorimetric information resulting in an event efficiency of 95.4 % for identifying both in $\mu^+\mu^- X$ events and 98.8 % for both electrons in $e^+e^- X$ events. Candidate Z decays are identified from oppositely charged pairs of identified leptons within a mass window around m_Z. Background from $Z \to \ell^+\ell^-$ is rejected using cuts on the transverse momentum of the di-lepton system and the acollinearity of the two lepton tracks. Additional cuts reject $Z \to \ell^+\ell^-$ events with initial and final state radiation. The backgrounds from $e^+e^- \to ZZ$ and $e^+e^- \to W^+W^-$ are reduced using a multi-variate likelihood analysis based on the acoplanarity, polar angle, transverse momentum and the invariant mass of the di-lepton system.

The reconstructed m_{recoil} distributions are shown in Figure 3.3-13. The combination of signal and background is fitted using a function which assumes a Gaussian-like signal and that the background can be approximated by a polynomial function. The results of the fit for m_H and $\sigma(e^+e^- \to ZH)$ are listed in Table 3.3-4. Also shown are the results obtained when assuming the SM decay modes and branching fractions. In this case, labelled "Model Dependent", the background is further reduced by requiring charged particle tracks in addition to those generated by the Z boson decay products.

3.3.1.1 Influence of Bremsstrahlung

From figure 3.3-13 it is clear that Bremsstrahlung from final state electrons and positrons significantly degrades the recoil mass resolution in the $e^+e^- X$ channel. One possible strategy to mitigate this effect is to identify the final state photons and include these in the recoil mass calculation. A dedicated algorithm to identify Bremsstrahlung photons is used [32] and the four momenta of the $e^+e^- X + n\gamma$ system is used in the event selection and recoil mass calculation. Figure 3.3-14a) compares the recoil mass distribution with and without including identified Bremsstrahlung photons. Figure 3.3-14b) shows the recoil mass distribution for the model independent impact analysis including Bremsstrahlung photons. To extract the mass and cross section a modified fitting function is used. The results of the fits ($e^+e^- X n\gamma$) for m_H and $\sigma(e^+e^- \to ZH)$ are listed in Table 3.3-4. Including Bremsstrahlung photons improves

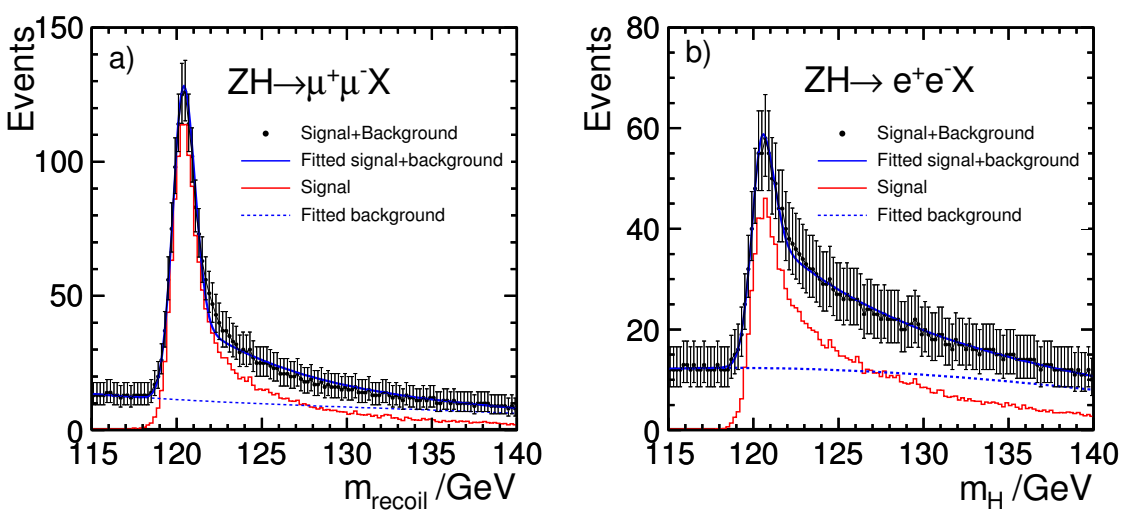

FIGURE 3.3-13. Results of the model independent analysis of the Higgs-strahlung process $e^+e^- \to HZ$ in which a) $Z \to \mu^+\mu^-$ and b) $Z \to e^+e^-$. The results are shown for a beam polarisation of $P(e^+, e^-) = (+30\,\%, -80\,\%)$.

Analysis	Polarisation (e^-, e^+)	Channel	$\sigma_{m_{\mathrm{H}}}$	Cross section	
Model Independent	$(+80\,\%,\ -30\,\%)$	$\mu^+\mu^- X$	40 MeV	± 0.28 fb	$(3.6\,\%)$
		$\mathrm{e}^+\mathrm{e}^- X$	88 MeV	± 0.43 fb	$(5.1\,\%)$
		$\mathrm{e}^+\mathrm{e}^-(n\gamma)X$	81 MeV	± 0.36 fb	$(4.3\,\%)$
	$(-80\,\%,\ +30\,\%)$	$\mu^+\mu^- X$	36 MeV	± 0.39 fb	$(3.3\,\%)$
		$\mathrm{e}^+\mathrm{e}^- X$	72 MeV	± 0.61 fb	$(4.8\,\%)$
		$\mathrm{e}^+\mathrm{e}^-(n\gamma)X$	74 MeV	± 0.47 fb	$(4.0\,\%)$
Model Dependent	$(+80\,\%,\ -30\,\%)$	$\mu^+\mu^- X$	36 MeV	± 0.26 fb	$(3.3\,\%)$
		$\mathrm{e}^+\mathrm{e}^- X$	77 MeV	± 0.38 fb	$(4.5\,\%)$
		$\mathrm{e}^+\mathrm{e}^-(n\gamma)X$	73 MeV	± 0.31 fb	$(3.8\,\%)$
	$(-80\,\%,\ +30\,\%)$	$\mu^+\mu^- X$	31 MeV	± 0.32 fb	$(2.7\,\%)$
		$\mathrm{e}^+\mathrm{e}^- X$	64 MeV	± 0.47 fb	$(3.7\,\%)$
		$\mathrm{e}^+\mathrm{e}^-(n\gamma)X$	59 MeV	± 0.37 fb	$(3.1\,\%)$

TABLE 3.3-4
Expected statistical uncertainties on m_{H} from the recoil mass distribution in Higgs-strahlung events where the Z decays into either $\mathrm{e}^+\mathrm{e}^-$ or $\mu^+\mu^-$. Results are listed for both the model independent and model dependent analyses. Also listed are the experimental uncertainties on the Higgs-strahlung cross section. The results are given for two different beam polarisations. In the case of the $\mathrm{e}^+\mathrm{e}^- X$-channel results are given without $(\mathrm{e}^+\mathrm{e}^- X)$ and with $(\mathrm{e}^+\mathrm{e}^-(n\gamma)X)$ the inclusion of identified Bremsstrahlung photons.

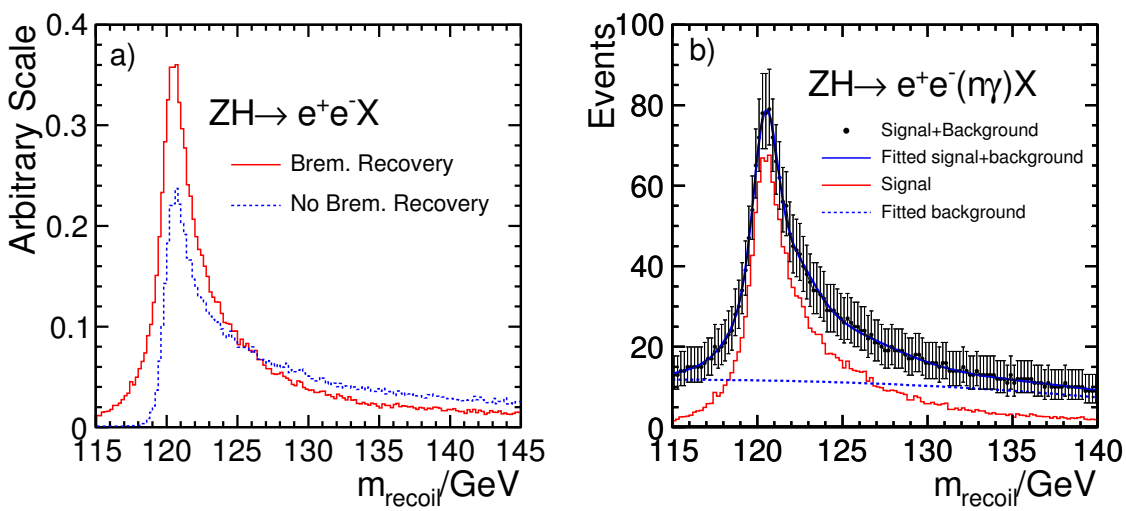

FIGURE 3.3-14. The effect of including identified Bremsstrahlung photons in the $\mathrm{e}^+\mathrm{e}^- X$ channel: a) comparison of the recoil mass distribution with and without inclusion of Bremsstrahlung photons and b) the fitted recoil mass distribution for the model independent analysis with Bremsstrahlung recovery. The plots are shown for a beam polarisation of $P(e^+, e^-) = (+30\,\%, -80\,\%)$.

the mass resolution by 10 % and the cross section resolution by 20 %. The improvement to the mass resolution is limited by the degradation in the sharpness of the leading edge of the recoil mass distribution. It should be noted that a more complete treatment would involve a refit of the track taking into account the candidate Bremsstrahlung photons; at this stage no strong conclusions should be drawn.

3.3.1.2 Influence of Beam Energy Uncertainties

The width of the peak of the recoil mass distribution is a convolution of the detector response and the luminosity spectrum of the centre-of-mass energy from the intrinsic beam energy spread and beamstrahlung. For the $\mu^+\mu^-X$ channel, the contribution from the detector response is primarily due to the momentum resolution, whereas for the e^+e^-X channel bremsstrahlung dominates. Figure 3.3-15 shows the recoil mass spectrum for the $\mu^+\mu^-X$ channel obtained from the generated four momenta of the muon pair compared to that obtained from the reconstructed momenta. The detector response leads to the broadening of the recoil mass peak; an increase from 560 MeV to 650 MeV. The contribution from momentum resolution is therefore estimated to be 330 MeV. For the beam energy spectrum used in the simulation, the effect of detector resolution is not negligible, however, the dominant contribution to the observed width of the $\mu^+\mu^-X$ recoil mass distribution arises from the incoming beams rather than the response of ILD.

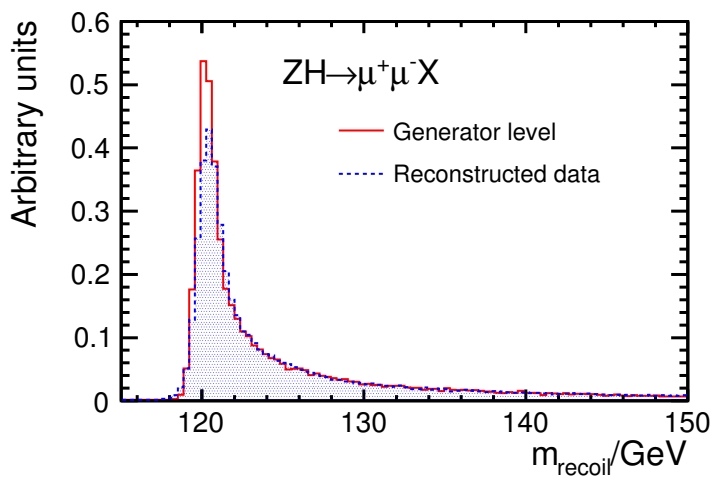

FIGURE 3.3-15. The Higgs recoil mass distribution in the $\mu^+\mu^-X$ channel obtained from the generator level and reconstructed muon pair momenta.

3.3.1.3 Conclusions

From Figure 3.3-13 and Table 3.3-4 the following conclusions can be drawn: i) using the recoil mass distributions in the e^+e^-X and $\mu^+\mu^-X$ final states and 250 fb^{-1} of data with $P(e^+, e^-) = (+30\,\%, -80\,\%)$ beam polarisation, m_{H} can be determined with a statistical uncertainty of 32 MeV independent of its decay modes and the Higgs-strahlung cross section can be measured with a precision of 2.5 %; ii) the precision on m_{H} obtained in the e^+e^-X channel is approximately a factor two worse than that obtained from the $\mu^+\mu^-X$ channel; iii) with the current algorithm, the inclusion of Beamstrahlung photons in the recoil mass distribution in the e^+e^-X channel improves the Higgs mass resolution by approximately 10 %. iv) the ILD track resolution does not significantly degrade the m_{H} resolution obtained from the $\mu^+\mu^-X$ recoil mass distribution.

3.3.2 Higgs Boson Branching Fractions

The determination of the Higgs boson branching fractions is central to the ILC physics programme. In the context of the SM, this allows a test of the hypothesis that the strength of the Higgs coupling depends linearly on the particle masses. The statistical uncertainties on the branching ratios are estimated, for an integrated luminosity of $250\,\mathrm{fb}^{-1}$ at $\sqrt{s} = 250\,\mathrm{GeV}$, based on the analysis of the Higgs-strahlung process $\mathrm{e^+e^-} \to \mathrm{ZH}$ for the three possible Z decay topologies: $\mathrm{Z} \to \mathrm{q\bar{q}}$, $\mathrm{Z} \to \nu\bar{\nu}$, and $\mathrm{Z} \to \ell^+\ell^-$. Heavy flavour tagging is essential to the analysis; cuts on the c-tag and b-tag for the two jets from the candidate Higgs decay are employed. In addition, the c-tag information from two jets is combined into a single variable, c-likeness. For each topology, the uncertainty on the exclusive cross sections are determined, *e.g.* $\sigma(\mathrm{e^+e^-} \to \mathrm{ZH} \to \mathrm{q\bar{q}c\bar{c}})$. This is combined with the 2.5 % uncertainty on the total cross section, $\sigma(\mathrm{e^+e^-} \to \mathrm{ZH})$, obtained from the model Independent analysis described in the previous section, to give the uncertainty on the branching ratios.

3.3.2.1 $ZH \to \ell^+\ell^-\mathrm{q\bar{q}}$

Although statistically limited compared to the other Z decay channels, $\mathrm{Z} \to \mathrm{e^+e^-}$ and $\mathrm{Z} \to \mu^+\mu^-$ provide a clean signal which can be identified with high efficiency, independent of whether the Higgs decays to $\mathrm{b\bar{b}}$, $\mathrm{c\bar{c}}$ or gg [33]. The dominant background is ZZ production. The event selection requires a pair of oppositely-charged electrons or muons with an invariant mass consistent with m_Z. The recoil mass is required to be consistent with m_H as is the invariant mass of the recoiling hadronic system. Events in which the Z candidate is close to the beam axis are rejected to suppress background from ZZ. The final selection is performed by cutting on the value of a likelihood function formed from variables related to the thrust, di-jet and di-lepton masses and angular distributions. The hadronic system is reconstructed as two jets. To extract the Higgs branching ratios it is not sufficient to simply apply cuts to select, for example, $\mathrm{H} \to \mathrm{c\bar{c}}$ events since one of the main background is from $\mathrm{H} \to \mathrm{b\bar{b}}$ for which the branching ratio also needs to be determined. Instead, the fractions of $\mathrm{H} \to \mathrm{b\bar{b}}$, $\mathrm{H} \to \mathrm{c\bar{c}}$, $\mathrm{H} \to gg$ and background present are determined from the distribution of b-likeness and c-likeness which is fitted using templates made from exclusive samples of each type as shown in Figure 3.3-16. The measurement accuracy obtained is $(2.7 \oplus 2.5)\,\%$ for $BR(\mathrm{H} \to \mathrm{b\bar{b}})$, $(28 \oplus 2.5)\,\%$ for $BR(H \to \mathrm{c\bar{c}})$ and $(29 \oplus 2.5)\,\%$ for $BR(\mathrm{H} \to gg)$.

3.3.2.2 $\mathrm{ZH} \to \nu\bar{\nu}\mathrm{H}$

The signal topology comprises two jets plus missing energy. Events are selected based on missing mass, net transverse momentum, and net longitudinal momentum. Background containing high momentum leptons is rejected using lepton identification cuts and by requiring that the maximum track momentum in the event is less than 30 GeV. The dominant remaining backgrounds are $\nu\bar{\nu}\mathrm{q\bar{q}}$ and $\tau\nu_\tau\mathrm{q\bar{q}}$ from ZZ and $\mathrm{W^+W^-}$ respectively. These backgrounds are suppressed using y_{12} and y_{23}, the y-cut values in the Durham jet-finding algorithm for the transitions between one or two and two or three reconstructed jets. The selection efficiencies for $\mathrm{ZH} \to \nu\bar{\nu}\mathrm{c\bar{c}}$ and $\mathrm{ZH} \to \nu\bar{\nu}\mathrm{b\bar{b}}$ are both approximately 44 %. The branching ratios $BR(\mathrm{H} \to \mathrm{b\bar{b}})$ and $BR(\mathrm{H} \to \mathrm{c\bar{c}})$ are determined using the b-, c-, and bc- flavour tags. The reconstructed di-jet mass distribution after applying a cut on the c-tag is shown in Figure 3.3-17b. To extract the Higgs branching ratios the template fit of Section 3.3.2.1 is extended to three dimensions by including the bc-tag information. It is assumed that the non-Higgs background is well understood. By fitting the signal contributions to this distribution, the

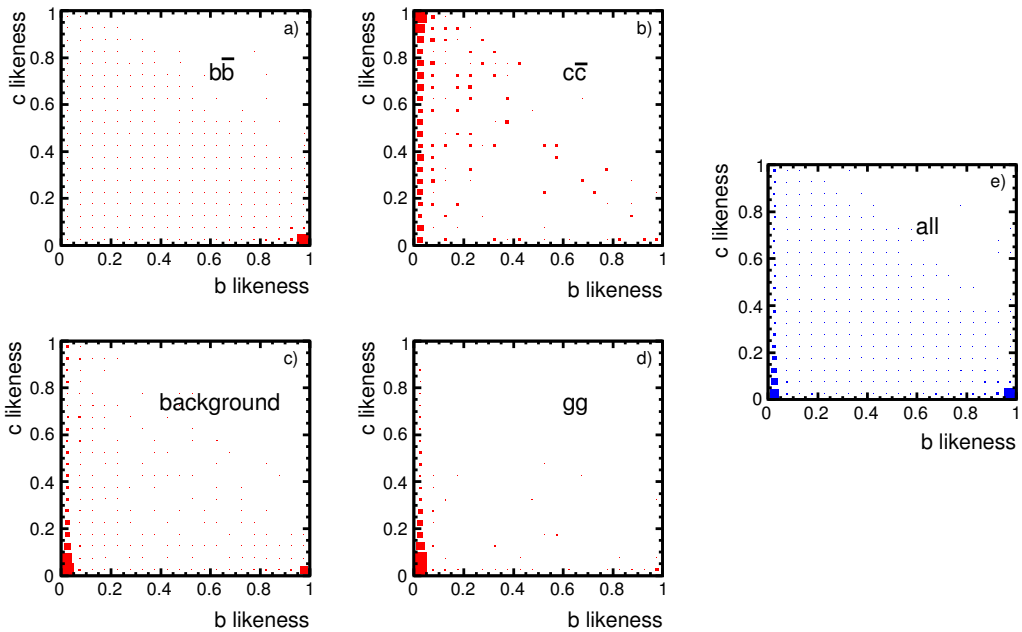

FIGURE 3.3-16. Distributions of b- and c-likeness for exclusive samples of $H \to b\bar{b}$, $H \to c\bar{c}$, $H \to gg$, background and an independent combined "data" sample.

$\mathrm{H} \to \mathrm{c\bar{c}}$ and $\mathrm{H} \to \mathrm{b\bar{b}}$ cross sections can be determined. The measurement accuracies for $BR(\mathrm{H} \to \mathrm{c\bar{c}})$ and $BR(\mathrm{H} \to \mathrm{b\bar{b}})$ are $(13.8 \oplus 2.5)$ and $(1.1 \oplus 2.5)\,\%$ repectively.

3.3.2.3 ZH → $\mathrm{q\bar{q}c\bar{c}}$

The decay topology for $\mathrm{ZH} \to \mathrm{q\bar{q}c\bar{c}}$ consists of four jets, two compatible with m_Z and two compatible with m_H. The main backgrounds are $\mathrm{e^+e^-} \to \mathrm{W^+W^-/ZZ} \to \mathrm{q\bar{q}q\bar{q}}$ and four-jet events from the fragmentation of $\mathrm{e^+e^-} \to \mathrm{Z}/\gamma^\star \to \mathrm{q\bar{q}}$. For the $\mathrm{Z}/\gamma^\star \to \mathrm{q\bar{q}}$ background, four-jet events arise mainly from the $q\bar{q}gg$ final state in which the gluon jets are generally less energetic and are produced at relatively small angles to the quark jets. Consequently, cuts on event shape variables, such as the smallest jet-jet angle, are used to reject the $\mathrm{Z}/\gamma^\star$ background. Background from $\mathrm{q\bar{q}q\bar{q}}$ production are suppressed using kinematic fits. A second fit, which imposes energy-momentum conservation and constrains one di-jet mass to equal m_Z, is used to reconstruct the Higgs mass, m_H^{fit}. The $\mathrm{ZH} \to \mathrm{q\bar{q}c\bar{c}}$ sample is selected by requiring $115 < m_\mathrm{H}^{fit} < 125\,\mathrm{GeV}$ and using cuts on the c-likeness and the $c-$tags of the two jets from the Higgs decay, shown in Figure 3.3-17. For an integrated luminosity of $250\,\mathrm{fb}^{-1}$, the expected numbers of signal and background events after all cuts are 37.2 and 121.2 respectively. This leads to a $(30 \oplus 2.5)\,\%$ uncertainty on $BR(\mathrm{H} \to \mathrm{c\bar{c}})$ [1] .

3.3.2.4 Combined Result

The results for the Higgs branching ratios are summarised in Table 3.3-5. The statistical uncertainties are from the exclusive measurements and the 2.5 % uncertainty on the total cross section. After taking into account the different integrated luminosity and different

[1] Ongoing studies show that the expected statistical uncertainty from a more optimal analysis is more than a factor two smaller than the value quoted here.

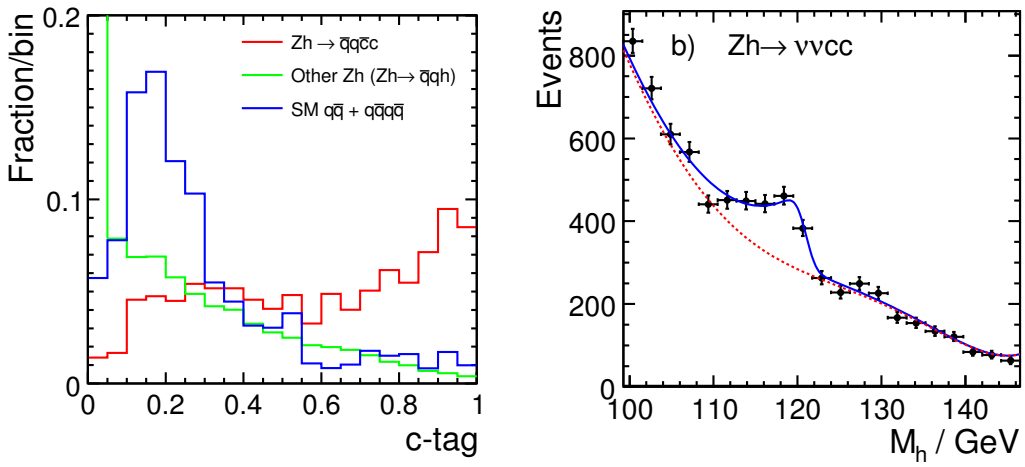

FIGURE 3.3-17. a) The c-tag of the two jets in candidate $\mathrm{ZH} \to \mathrm{q\bar{q}c\bar{c}}$ events after all other cuts apart from the c-tag and c-likeness cut. b) Distribution of the reconstructed di-jet mass for the $\mathrm{ZH} \to \nu\bar{\nu}c\bar{c}$ sample prepared by bc-tagging.

centre-of-mass energy, the combined results shown in Table 3.3-5 are broadly in agreement with those obtained with a fast simulation analysis performed in the context of the TESLA TDR [34].

Channel	$Br(\mathrm{H} \to \mathrm{b\bar{b}})$	$Br(\mathrm{H} \to \mathrm{c\bar{c}})$	$Br(\mathrm{H} \to gg)$
$\mathrm{ZH} \to \ell^+\ell^-\mathrm{q\bar{q}}$	$(2.7 \oplus 2.5)\,\%$	$(28 \oplus 2.5)\,\%$	$(29 \oplus 2.5)\,\%$
$\mathrm{ZH} \to \nu\bar{\nu}H$	$(1.1 \oplus 2.5)\,\%$	$(13.8 \oplus 2.5)\,\%$	–
$\mathrm{ZH} \to \mathrm{q\bar{q}c\bar{c}}$	–	$(30 \oplus 2.5)\,\%$	–
Combined	$2.7\,\%$	$12\,\%$	$29\,\%$

TABLE 3.3-5
Expected precision for the Higgs boson branching fraction measurements ($\sqrt{s} = 250\,\mathrm{GeV}$) for the individual Z decay channels and for the combined result. The expected $2.5\,\%$ uncertainty on the total Higgs production cross section is added in quadrature. The results are based on full simulation/reconstruction and assume an integrated luminosity of $250\,\mathrm{fb}^{-1}$. Entries marked – indicate that results are not yet available.

3.3.3 Tau-pairs

The reconstruction of $\tau^+\tau^-$ events at $\sqrt{s} = 500$ GeV provides a challenging test of the detector performance in terms of separating nearby tracks and photons. The expected statistical sensitivities for the $\tau^+\tau^-$ cross section, the $\tau^+\tau^-$ forward-backward asymmetry, A_{FB}, and the mean tau polarisation, P_τ, are determined for and integrated luminosity of $500\,\mathrm{fb}^{-1}$ with beam polarisation, $P(e^+, e^-) = (+30\,\%, -80\,\%)$.

Simulated events with less than seven tracks are clustered into candidate tau jets each of which contains at least one charged particle. Tau-pair events are selected by requiring exactly two candidate tau jets with opposite charge. The opening angle between the two tau candidates is required to be $> 178°$ to reject events with significant ISR (including radiative

return to the Z). After cuts on visible energy, the polar angles of the tau jets, and lepton identification, the purity of the $\tau^+\tau^-$ event sample is 92.4 %. For 500 fb^{-1} the statistical error of the cross section measurement, $|\cos\theta| < 0.95$, corresponds to 0.29%. The uncertainty on A_{FB}, determined from the numbers of τ^- in the forward and backward hemispheres, is ± 0.0025.

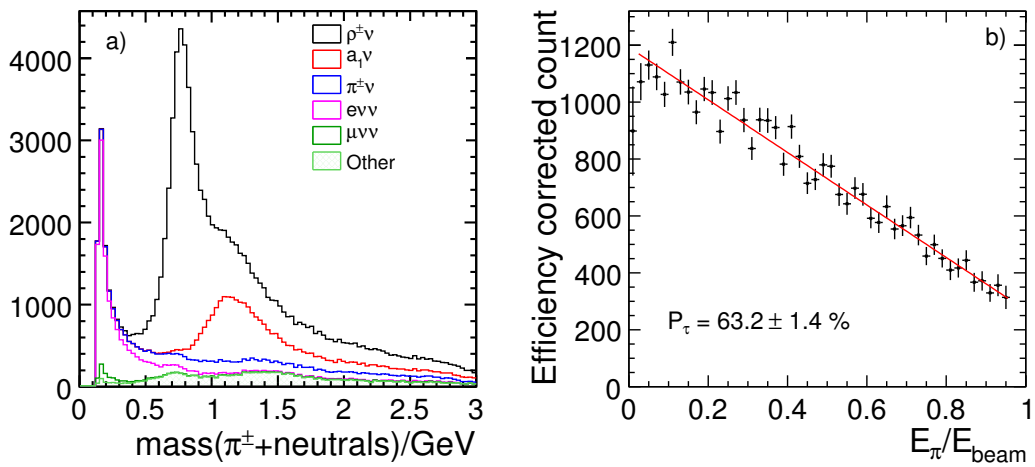

FIGURE 3.3-18. a) The invariant mass distribution for selected 1-prong tau-candidates and b) The efficiency corrected reconstructed pion energy distribution for selected $\tau \to \pi\nu$ candidates.

The $\tau \to \pi\nu$ and $\tau \to \rho\nu$ decays have the highest sensitivity to P_τ. The separation of the 1-prong decay modes relies on lepton identification and the ability to separate the neutral energy deposits from π^0 decays from the hadronic shower. The invariant mass distribution for 1-prong events is shown in Figure 3.3-18a. A neutral network approach based on nine input variables is used to identify the tau decays modes for each tau cone. The variables include: the total energy of the identified photons, the invariant mass of the track and all identified photons (Figure 3.3-18a); and electron and muon particle identification variables based on calorimetric information and track momentum. Table 3.3-6 shows the efficiency and purity achieved for the six main tau decay modes. The high granularity and the large detector radius of ILD results in excellent separation.

For the beam polarisations of $P(e^+, e^-) = (+30\,\%, -80\,\%)$ and $P(e^+, e^-) = (-30\,\%, +80\,\%)$ the mean tau polarisations are -0.625 and $+0.528$ respectively. For the measurement of P_τ, only the $e^\pm\nu\nu$, $\mu^\pm\nu\nu$, $\pi^\pm\nu$, and $\rho^\pm\nu$ decay modes are used. The optimal variable approach [35] is used to obtain the best sensitivity to the tau polarisation. In the case of the $\pi^\pm\nu$ decay mode, the optimal observable is the simply reconstructed $\pi^\pm$ energy divided by the beam energy, shown in Figure 3.3-18b. For the selected event sample and decay mode identification the resulting statistical uncertainties on the measured mean tau polarisations are ± 0.007 and ± 0.008 for $P(e^+, e^-) = (+30\,\%, -80\,\%)$ and $P(e^+, e^-) = (-30\,\%, +80\,\%)$ respectively.

3.3.4 Chargino and Neutralino Production

In the SUSY "point 5" scenario with non-universal soft SUSY-breaking contributions to the Higgs masses, $\tilde{\chi}_1^\pm$ and $\tilde{\chi}_2^0$ are not only nearly mass degenerate but decay predominantly into $W^\pm\tilde{\chi}_1^0$ and $Z\tilde{\chi}_1^0$, respectively. This benchmark point has the following parameters: $M_0 =$

Mode	Efficiency	Purity
$e\nu\nu$	98.9 %	98.9 %
$\mu\nu\nu$	98.8 %	99.3 %
$\pi\nu$	96.0 %	89.5 %
$\rho\nu$	91.6 %	88.6 %
$a_1\nu$ (1-prong)	67.5 %	73.4 %
$a_1\nu$ (3-prong)	91.1 %	88.9 %

TABLE 3.3-6
Purity and efficiency of the main tau decay mode selections. The selection efficiency is calculated with respect to the sample of $\tau^+\tau^-$ after the requirement that the two tau candidates are almost back-to-back. The purity only includes the contamination from other $\tau^+\tau^-$ decays.

206 GeV, $M_{1/2} = 293$ GeV, $\tan\beta = 10$, $A_0 = 0$, and $\mu = 375$ GeV and the gaugino masses are: $m(\tilde{\chi}_1^0) = 115.7$ GeV, $m(\tilde{\chi}_1^\pm) = 216.5$ GeV, $m(\tilde{\chi}_2^0 = 216.7$ GeV, and $m(\tilde{\chi}_3^0) = 380$ GeV.

Both $e^+e^- \to \tilde{\chi}_1^+\tilde{\chi}_1^- \to qq\tilde{\chi}_1^0 qq\tilde{\chi}_1^0$ and $e^+e^- \to \tilde{\chi}_2^0\tilde{\chi}_2^0 \to qq\tilde{\chi}_1^0 qq\tilde{\chi}_1^0$ result in four jets and missing energy, where the di-jet masses are characteristic of the decays of W^+W^- or ZZ. Separating W and Z decays in the fully-hadronic decay mode relies on good jet energy resolution. It thus provides a benchmark for particle flow based jet reconstruction. The analysis is complicated by the fact that the $\tilde{\chi}_2^0\tilde{\chi}_2^0$ cross section is only 10 % of that for $\tilde{\chi}_1^+\tilde{\chi}_1^-$.

The event selection starts by forcing events into four jets. A cut based preselection retains events consistent with a four-jet plus missing energy topology. All three possible di-jet associations to two bosons are considered. A kinematic fit which constrains the two boson masses to be equal is applied; in terms of mass resolution this is essentially equivalent to taking the average mass of the two di-jet systems. Two analysis strategies are used to assess the expected uncertainty on the measured cross sections: **i)** The first method aims to reduce the SM background as far as possible. Cuts on the number of particle flow objects in each jet, the direction of the missing momentum, and the missing mass are applied. The kinematic fit is required to converge for at least one jet pairing. The jet pairing yielding the highest χ^2 probability is used. Figure 3.3-19a shows the resulting di-jet mass distribution. The Chargino signal has a small shoulder from the Neutralino contribution. The cross sections are obtained from a fit to the mass spectrum using a function with three components: a Breit-Wigner (m_W, Γ_W) convolved with a Gaussian for the W-peak; a Breit-Wigner (m_Z, Γ_Z) convolved with the same Gaussian for the Z peak; and a second order polynomial. The width of the Gaussian is fixed to 3.4 GeV reflecting the mass resolution. The two free parameters of the fit are the normalisations of the W and Z peaks. Figure 3.3-19b shows the result of the fit. The statistical errors on the cross sections are 0.95 % for the Chargino signal and 2.9 % for the Neutralino signal. **ii)** The second approach, which does not use kinematic fitting, is to fit the two-dimensional distribution of the two di-jet masses in each event with MC templates, leaving only the normalisations of the two signal contributions free. The fit is performed after the preselection cuts. All three possible jet pairings are included. This method yields smaller statistical errors of 0.64 % for the Chargino and 2.1 % for the Neutralino production rates.

To determine the $\tilde{\chi}_1^\pm$ and $\tilde{\chi}_2^0$ masses, $\tilde{\chi}_1^+\tilde{\chi}_1^-$ and $\tilde{\chi}_2^0\tilde{\chi}_2^0$ samples are defined on the basis of the di-jet mass distributions (without the kinematic fit). The resulting energy spectra of the W and Z candidates from the kinematic fit are shown in Figure 3.3-19c/d. The masses

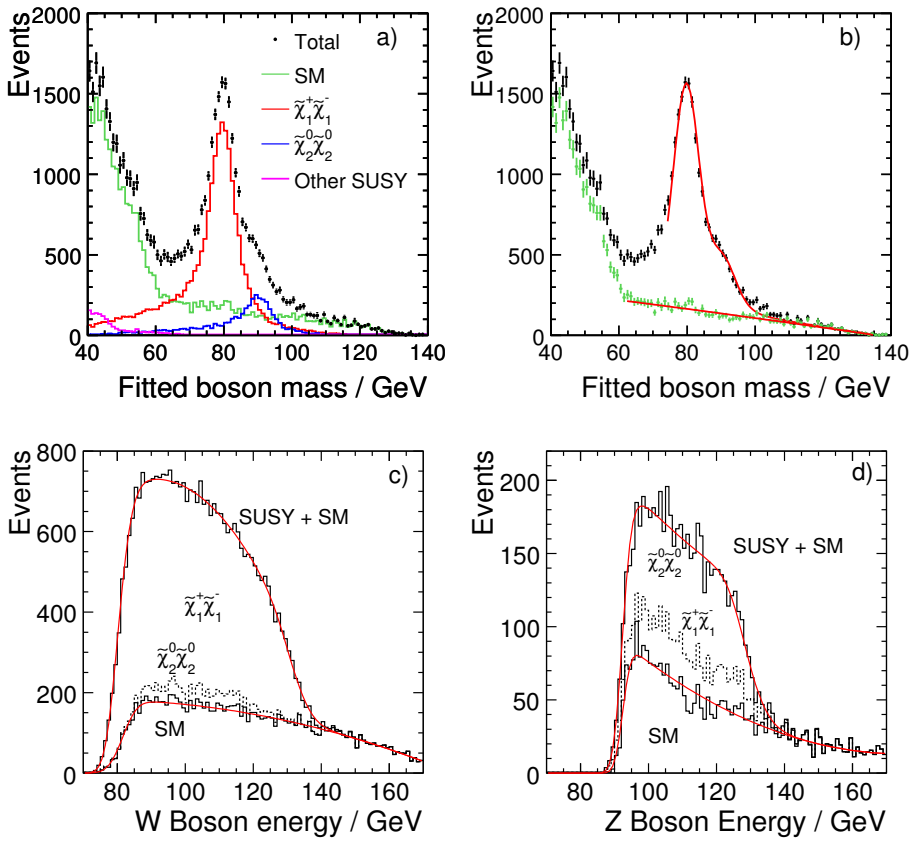

FIGURE 3.3-19. a) Di-jet mass from the 5C kinematic fit after all selection cuts. b) Fit of the background and Chargino and Neutralino contributions. The fit parameters are the normalisations of the W and Z peaks. c) Energy spectra of W and Z boson candidates after the Chargino and d) Neutralino event selections, shown including fits to signal and background contributions.

of the gauginos are determined from the kinematic edges of the distributions located using an empirically determined fitting function for the signal and a parameterisation of the SM background. From the fit results the upper and lower kinematic edges of the $\tilde{\chi}_1^\pm$ sample are determined to ± 0.2 GeV and ± 0.7 GeV respectively. The corresponding numbers for the $\tilde{\chi}_2^0$ sample are: ± 0.4 GeV and ± 0.8 GeV. For the SUSY point 5 parameters, the $\tilde{\chi}_1^\pm$ lower edge is close to m_{W} and, thus, does not significantly constrain the gaugino masses. The other three kinematic edges can be used to determine the gaugino masses with a statistical precision of 2.9 GeV, 1.7 GeV and 1.0 GeV for the $\tilde{\chi}_1^\pm$, $\tilde{\chi}_2^0$, and $\tilde{\chi}_1^0$ respectively. The errors on the masses are larger than the errors on the positions of the edges themselves. This reflects the large correlations between the extracted gaugino masses; the differences in masses are better determined than the sum. If the LSP mass were known from other measurements, *e.g.* from the slepton sector, the errors on the $\tilde{\chi}_1^\pm$ and $\tilde{\chi}_2^0$ masses would be significantly reduced. Furthermore, the resolutions can be improved by about a factor of two using a kinematic fit which constrains the boson masses for chargino (neutralino) candidates not only to be equal to each other, but also to be equal to the nominal W (Z) mass. In this case, statistical precisions of 2.4 GeV, 0.9 GeV, and 0.8 GeV are obtained for the $\tilde{\chi}_1^\pm$, $\tilde{\chi}_2^0$, and $\tilde{\chi}_1^0$ respectively.

3.3.5 Top production

Top physics will be an important part of the scientific programme at the ILC. In particular, the top mass, m_{t}, and top width, Γ_{t}, can be determined with high precision. The measurement of m_{t} and Γ_{t} from the direct reconstruction of $e^+e^- \to \mathrm{t\bar{t}}$ events is studied with the full ILD detector simulation and reconstruction. Two main decay topologies are considered: fully-hadronic, $\mathrm{t\bar{t}} \to (b\mathrm{q\bar{q}})(\bar{b}\mathrm{q\bar{q}})$, and semi-leptonic, $\mathrm{t\bar{t}} \to (b\mathrm{q\bar{q}})(\bar{b}\ell\nu)$. Results are obtained for an integrated luminosity of $100\mathrm{fb}^{-1}$ at $\sqrt{s} = 500\,\mathrm{GeV}$, assuming unpolarised beams.

Events with an isolated lepton are considered to be candidates for the semi-leptonic analysis, otherwise they are assumed to be candidates for the fully-hadronic analysis branch. In the fully hadronic branch, the event is reconstructed as six jets which are combined to form Ws and top quarks. The two b-jets originating directly from the top quark decays are identified using the flavour-tagging information. The four remaining jets are considered as the decay products of the two Ws. The combination of the four jets into two di-jets which gives the smallest value of $|m_{ij} - m_{\mathrm{W}}| + |m_{kl} - m_{\mathrm{W}}|$ is chosen to form the two Ws (where m_{ij} and m_{kl} are the di-jet masses for a given jet pairing). Out of two possible combinations to pair the Ws with the b-jets, the one which yields the smallest mass difference is chosen. The first step in the semi-leptonic branch is to remove the identified lepton and to force the remainder of the event into four jets. The two b-jets are identified using flavour-tagging information. The two remaining jets are assigned to the hadronically decaying W. The identified lepton and the neutrino are assigned to the leptonically decaying W, with the three-momentum of the neutrino defined as the missing momentum. The pairing of the Ws with the b-jets which yields the smallest reconstructed top mass difference is chosen. For each analysis branch, background events are rejected using a multi-variate likelihood technique [36]. Finally, a kinematic fit [37] is applied in order to improve the final m_{t} resolution. Events with a poor fit χ^2 are rejected. The reconstructed mass distributions are shown in Figure 3.3-20.

For an integrated luminosity of $500\,\mathrm{fb}^{-1}$, $\sigma(\mathrm{e^+e^-} \to \mathrm{t\bar{t}})$ can be determined with a statistical uncertainty of $0.4\,\%$ using the fully-hadronic decays only. The invariant mass spectra are fitted with the convolution of a Breit-Wigner function and an asymmetric double Gaussian,

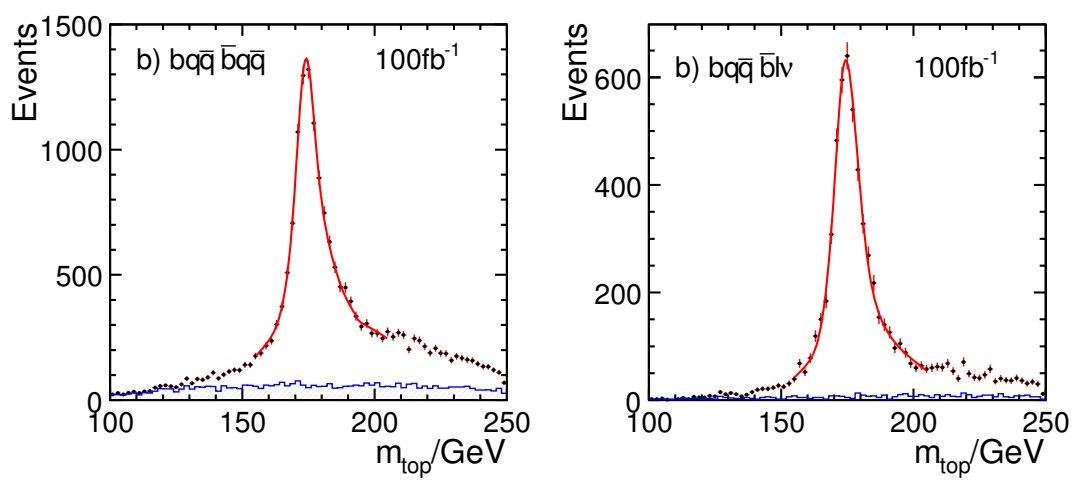

FIGURE 3.3-20. Distribution of the reconstructed top quark mass for a) the fully-hadronic $\mathrm{t\bar{t}} \to (bq\bar{q})(\bar{b}q\bar{q})$ signal sample and b) the semi-leptonic $\mathrm{t\bar{t}} \to (bq\bar{q})(\bar{b}\ell\nu)$ signal sample. The contribution from the non-$\mathrm{t\bar{t}}$ background is indicated by the hashed distribution. The fits to the distributions are also shown.

the latter representing the detector resolution. The combinatoric background and the background from other process is described by a 2nd order polynomial. The fully-hadronic (semi-leptonic) analysis branch results in statistical uncertainties of 90 MeV (120 MeV) and 60 MeV (100 MeV) for m_{t} and Γ_{t} respectively. Scaling the combined results to an integrated luminosity of $500\,\mathrm{fb}^{-1}$ leads to uncertainties of 30 MeV on m_{t} and 22 MeV on Γ_{t}. The relatively small gain in statistical precision from a beam polarisation of $P(e^+, e^-) = (+30\,\%, -80\,\%)$ has not been accounted for.

3.3.5.1 Top Quark Forward-Backward Asymmetry

The top quark forward-backward asymmetry, $A^t_{\mathrm{F}B}$, provides a potentially interesting test of the SM. For the semi-leptonic the analysis is relatively straightforward as the charge of the lepton tags the charge of the W-boson and, thus, enables the t and $\bar{t}$ to be identified. In the fully-hadronic channel the t and $\bar{t}$ can be identified by tagging the $b/\bar{b}$ from the charge of the secondary vertex from charged B-hadron decays. This measurement provides a test of the vertex reconstruction capability of ILD. This study is performed for $500\,\mathrm{fb}^{-1}$ with $P(e^+, e^-) = (+30\,\%, -80\,\%)$. Secondary vertices identified by the LCFIVertex algorithm for the two identified b-jets are used. For each of the two identified b-jets, the jet charge is reconstructed. Events with like sign combinations are rejected as are events with two neutral secondary vertices. In addition, the acollinearity between the two top quark jets is required to be $< 8^\circ$ to reject events with $\sqrt{s'}$ significantly less than 500 GeV. Of the 20 % of fully hadronic $\mathrm{t\bar{t}}$ events which pass these cuts, 79 % have the correctly identified top quark charge. Figure 3.3-21 shows the distribution of the cosine of the reconstructed polar angle of the tagged top-quark, showing a clear forward-backward asymmetry. The relative numbers of events in the forward and backward hemispheres, accounting for the charge identification/misidentification probabilities, are used to determine

$$A^t_{\mathrm{F}B} = 0.334 \pm 0.0079.$$

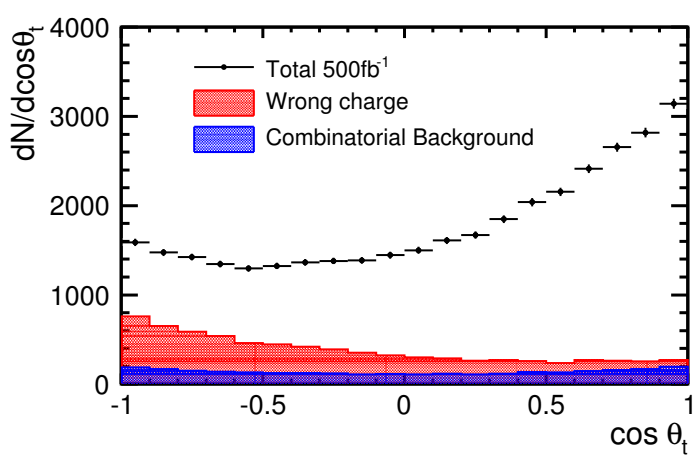

FIGURE 3.3-21. Distribution of the reconstructed polar angle of the identified top quark in fully-hadronic $\mathrm{t\bar{t}}$ events. The contributions from events with the wrong charge (red) and the case where the b-quark is misidentified are shown (blue).

3.3.6 Strong EWSB

If strong electroweak symmetry breaking (EWSB) is realised in nature, the study of the WW-scattering processes is particularly important. At the ILC, the $W^+W^- \to W^+W^-$ and $W^+W^- \to ZZ$ vertices can be probed via the processes $e^+e^- \to \nu_e\bar{\nu}_e q\bar{q}q\bar{q}$ where the final state di-jet masses are from the decays of two W-bosons or two Z-bosons. Separating the two processes through the reconstruction of the di-jet masses provides a test of the jet energy resolution of the ILD detector.

Strong EWSB can be described by an effective Lagrangian approach in which there are two anomalous quartic gauge couplings, α_4 and α_5 [38] which are identically zero in the SM. The WW scattering events are generated at $\sqrt{s} = 1\,\text{TeV}$ with WHiZard [39] assuming $\alpha_4 = \alpha_5 = 0$. Results are obtained for an integrated luminosity of $1\,\text{ab}^{-1}$ with $P(e^+, e^-) = (+0.3, -0.8)$. Event selection cuts, similar to those of [38, 40, 41, 42], reduce the backgrounds from processes other than the quartic coupling diagrams to $\sim 20\,\%$ of the signal. Of the three possible jet-pairings, the one which minimises $|m_{ij} - m_{W/Z}| \times |m_{kl} - m_{W/Z}|$ is chosen. Figure 3.3-22 shows, for $\nu_e\bar{\nu}_e$WW and $\nu_e\bar{\nu}_e$ZZ events, a) the reconstructed di-jet mass distribution, and b) the distribution of average reconstructed mass, $(m_{ij} + m_{kl})/2.0$. Clear separation between the W and Z peaks is obtained.

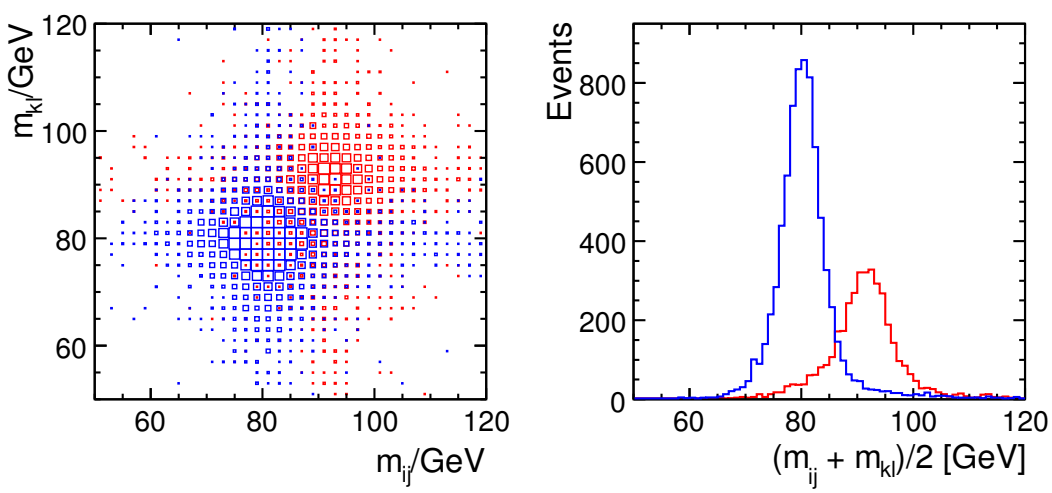

FIGURE 3.3-22. a) The reconstructed di-jet mass distributions for the best jet-pairing in selected $\nu_e\bar{\nu}_e$WW (blue) and $\nu_e\bar{\nu}_e$ZZ (red) events at $\sqrt{s} = 1\,TeV$. b) Distributions of the average reconstructed di-jet mass, $(m_{ij} + m^B_{kl})/2.0$, for the best jet-pairing for $\nu_e\bar{\nu}_e$WW (blue) and $\nu_e\bar{\nu}_e$ZZ (red) events.

The parameters α_4 and α_5 are obtained from a binned maximum likelihood fit to the two-dimensional distribution (10×10 bins) of the boson polar angle in the reference frame of boson pair and the jet polar angle in the reference frame of each boson, giving $-1.38 < \alpha_4 < +1.10$ and $-0.92 < \alpha_5 < +0.77$. These sensitivities are slightly tighter than those from a previous fast simulation study with the TESLA detector concept [41, 42].

3.3.7 Lepton production in SPS1a'

SUSY may provide a rich spectrum of kinematically accessible particles at the ILC operating at $\sqrt{s} = 500\,\text{GeV}$, for example the production of gauginos and sleptons with masses below 250 GeV. The signals for new physics consist of a complex mixture of dominant and

sub-dominant processes, often with identical visible final states [43]. Here we consider final states consisting of missing energy and either two muons or two taus in mSUGRA SUSY with the SPS1a' parameter set: $M_0 = 70\,\mathrm{GeV}$, $M_{1/2} = 250\,\mathrm{GeV}$, $A_0 = -300\,\mathrm{GeV}$, $\mathrm{sign}(\mu) = +1$, and $\tan\beta = 10$. For these parameters the relevant gaugino and slepton masses are: $m(\tilde{\chi}_1^0) = 97.7\,\mathrm{GeV}$, $m(\tilde{\chi}_2^0) = 183.9\,\mathrm{GeV}$, $\mathrm{m}(\tilde{\mu}_R) = 125.3\,\mathrm{GeV}$, $\mathrm{m}(\tilde{\mu}_L) = 189.9\,\mathrm{GeV}$ and $\mathrm{m}(\tilde{\tau}_1) = 107.9\,\mathrm{GeV}$.

3.3.7.1 Muons and Missing Energy

The ILC sensitivity to pair production of the lightest scalar muon, $\tilde{\mu}_R^+\tilde{\mu}_R^-$, leading to a final state of two muons and missing energy has been extensively studied[44]. The study presented here concentrates on sub-dominant di-muon plus missing energy processes which have to compete with the large SUSY background and in particular, the challenging scenario where the di-muon decay modes are suppressed. For these sub-dominant processes, the $\tilde{\chi}_1^0$, $\tilde{\chi}_2^0$, and $\tilde{\mu}_L$ masses can be measured from $\tilde{\chi}_2^0\tilde{\chi}_1^0 \to \mu\mu\tilde{\chi}_1^0\tilde{\chi}_1^0$ ($\sigma = 4.1\,\mathrm{fb}$) and $\tilde{\mu}_L\tilde{\mu}_L \to \mu\mu\tilde{\chi}_1^0\tilde{\chi}_1^0$ ($\sigma = 54\,\mathrm{fb}$). In both cases the signal is characterised by two energetic muons and missing energy. Muons are identified with 95 % efficiency using track, HCAL and muon chamber information. Background is rejected using: missing energy, di-muon invariant mass, recoil mass, transverse momentum, and the direction and speed of the di-muon system. Cuts on these variables are used to define $\tilde{\mu}_L\tilde{\mu}_L \to \mu\mu\tilde{\chi}_1^0\tilde{\chi}_1^0$ and $\tilde{\chi}_2^0\tilde{\chi}_1^0 \to \mu\mu\tilde{\chi}_1^0\tilde{\chi}_1^0$ event samples.

The masses of the $\tilde{\chi}_1^0$ and $\tilde{\mu}_L$ are measured from the kinematic edges of the momentum distribution of the muons in the $\tilde{\mu}_L\tilde{\mu}_L \to \mu\mu\tilde{\chi}_1^0\tilde{\chi}_1^0$ [45] event selection, shown in Figure 3.3-23a. The kinematic edges of the signal, at 32 GeV and 151 GeV, are fitted with a step function giving measurements of the $\tilde{\chi}_1^0$ and $\tilde{\mu}_L$ masses with statistical uncertainties of 1.40 % and 0.27 % repectively. The signal cross section is determined with an uncertainty of 2.5 % from the number of selected events. The sharpness of the kinematic edges, and consequently the mass measurements, are limited by beamstrahlung rather than the track momentum resolution and it is estimated that the uncertainty in the $\tilde{\chi}_1^0$ mass would be a factor two worse for the lowP option for the ILC with the same integrated luminosity. The $\tilde{\chi}_2^0$ mass is determined from the kinematic edge of the di-muon mass distribution in the decay chain $\tilde{\chi}_2^0\tilde{\chi}_1^0 \to \mu\mu\tilde{\chi}_1^0\tilde{\chi}_1^0$ [45]. The distribution of $m_{\mu\mu}$ after selection is shown in Figure 3.3-23b. The kinematic edge of the signal is visible below the Z peak. A fit to the region $40\,\mathrm{GeV} < \mathrm{m}_{\mu\mu} < 85\,\mathrm{GeV}$ is used to determine the mass of the $\tilde{\chi}_2^0$. In this region the statistical significance of the excess corresponds to 9 standard deviations and the $\tilde{\chi}_2^0$ mass resolution obtained is 1.41 %. It should be noted that a higher positron polarisation yields significantly improved precision, particularly for $\tilde{\chi}_2^0\tilde{\chi}_1^0$ production where a positron polarisation of 60 % rather than 30 % results in 50 % more signal events for a relatively small increase in background.

3.3.7.2 Stau Production and Decay

For the SUSY SPS1a' parameters, $e^+e^- \to \tilde{\tau}\tilde{\tau} \to \tilde{\chi}_1^0\tau\tilde{\chi}_1^0\tau$, results in a signal of missing energy and the relatively low energy visible decay products of the tau leptons ($E_\tau \lesssim 43\,\mathrm{GeV}$). Measurements of $\tilde{\tau}\tilde{\tau}$ production requires precision tracking of relatively low momentum particles, good particle identification, a highly hermetic detector, and low machine background.

The stau pair event selection requires two low multiplicity tau-jets and at least 400 GeV of missing energy. The tau jets are required to have $|\cos\theta| < 0.9$ and to have an acoplanarity of greater than 85°. Background is further reduced by cutting on the transverse momentum with respect to the transverse event thrust axis. Given that the tau-jets are relatively low

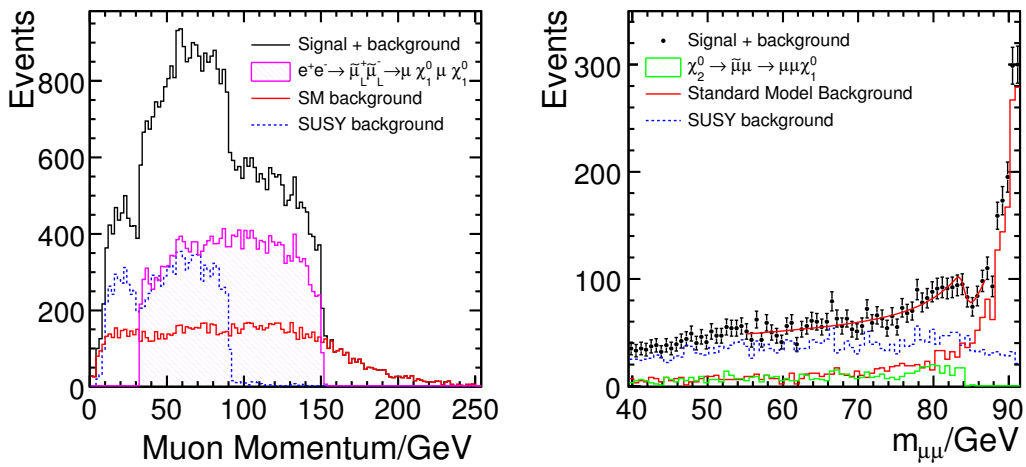

FIGURE 3.3-23. (a) Distribution of the momentum of the μ^+ in the laboratory frame after the selection of the $\tilde{\mu}_L\tilde{\mu}_L$ pair candidates. The total observed signal and the backgrounds (SUSY and SM) are reported. The mass of the $\tilde{\chi}_1^0$ is measured from the kinematic edges of the distribution of the momentum of the di-muons. There are two entries for each event. (b) Fitted $m_{\mu\mu}$ spectrum. The kinematic edge corresponding to the $\tilde{\chi}_2^0 \to \tilde{\mu}_R\mu$ can be extracted from the fit on top of the left tail of the Z peak. Both plots are shown for a beam polarisation of -80 %, 60 % and correspond to an integrated luminosity of 500 fb^{-1}.

momentum, background from multi-peripheral two photon processes, $e^+e^- \to e^+e^-X$, is particularly important due to the very high cross section. This background is reduced using the beam calorimeter (BCAL) to veto the forward going electrons/positrons. Due to the holes in the BCAL acceptance around the incoming and outgoing beam pipes, the regions $\phi \leq 110°$ or $\phi \geq 250°$ are not used (for details see [46]).

The $\tilde{\tau}$ mass can be extracted from the end-point of the tau-jet energy spectrum and knowledge of the $\tilde{\chi}_1^0$ mass, *e.g.* from the study of smuon production. For the stau mass determination, the stau pair selection is augmented by additional cuts on tau-jet masses and the polar angle of the missing momentum vector. Figure 3.3-24a shows the distribution of the tau jet energy after these cuts. The selection efficiency is 12 % and the sample purity is 80 %. The end-point tau energy is determined from a fit to the spectrum of Figure 3.3-24a in the region $30 < E < 41.5$ GeV. The signal, which in this region is dominated by $\tau \to \pi\nu$ decays, is described by a linear function. The resulting statistical uncertainty on the end-point is 0.1 GeV. When accounting for the uncertainty on the $\tilde{\chi}_1^0$ mass, σ_{LSP}, this leads to a measurement precision on $M_{\tilde{\tau}_1}$ of $0.1\,\mathrm{GeV} \oplus 1.3\sigma_{\mathrm{LSP}}$. Systematic uncertainties are not included.

The measurement of tau polarisation, P_τ, in $\tilde{\tau}_1$ decays gives direct access to the mixing of mass and interaction eigenstates in the stau sector, and thus provides sensitivity to a number of SUSY parameters. For SPS1a' $P_\tau = 97\,\%$. P_τ can be measured most cleanly in $\tau \to \pi\nu$ decays where the slope of the $\pi^\pm$ energy spectrum depends on P_τ. The potential signal is large, for 500 fb^{-1}, ~17500 $\pi\nu$ decays are expected. In addition to the stau pair selection, calorimeter and $\mathrm{d}E/\mathrm{d}x$ information are used to identify $\tau \to \pi\nu$ decays. The selection efficiency is 13.8 % and the remaining background fraction is 21 %. The underlying pion spectrum is reconstructed by subtracting the background in a parametrised form and applying an energy dependent efficiency correction. The shape of the spectrum is influenced by the luminosity spectrum of the machine, and this effect is folded into the fit function.

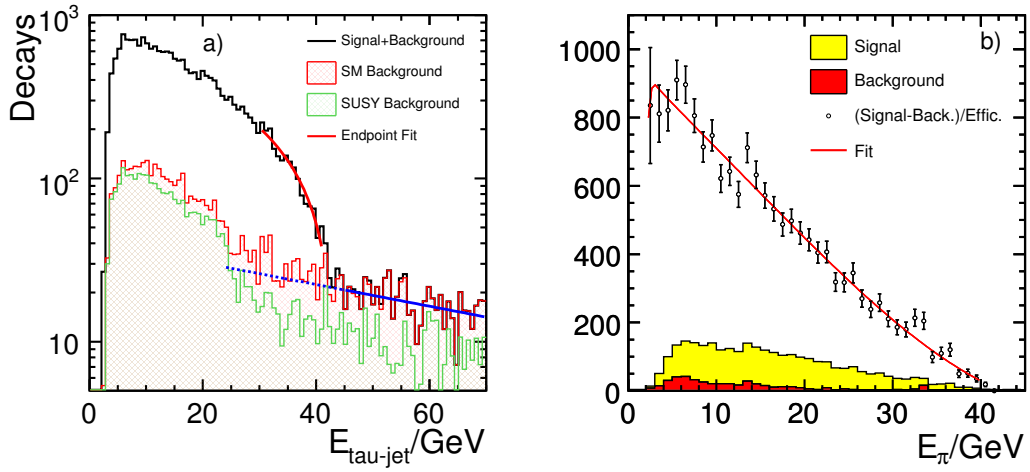

FIGURE 3.3-24. a) Tau-jet energy spectrum, showing the fit to determine the endpoint (two entries per event). b) Energy spectrum of selected tau decays and the fit to determine P_τ.

Figure 3.3-24 shows the reconstructed data together with the fit. This study shows that a measurement of P_τ with an accuracy of 0.15 is realistic.

3.3.8 Photon Final States

Physics beyond the standard model can manifest itself in final states consisting of two (or more) photons and missing momentum. The high granularity and good photon reconstruction capability of the ILD detector is well suited to these measurements.

3.3.8.1 Model-independent WIMP search

Weakly Interacting Massive Particles (WIMPs) are possible candidates for dark matter. If they can pair annihilate into e^+e^-, then the reverse process can be detected at the ILC. In this case the two neutral (undetected) WIMPs are accompanied by photon radiation from the incoming e^+e^-. In these $e^+e^- \to \chi\chi\gamma$ events, the photon recoil mass distribution has a characteristic onset. The location of the onset and shape of the recoil mass distribution depends on the WIMP mass and spin. Experimentally, the WIMP signal has to be resolved from the large irreducible ISR background from $e^+e^- \to \nu\bar{\nu} + n\gamma$. Good photon energy and angular resolution are required in order to detect a clear edge in the photon energy spectrum above this large background. Assuming that the total cross-section for WIMP pair annihilation into SM fermion pairs, $\tilde{\chi}\tilde{\chi} \to f\bar{f}$, is known from cosmological observations, the ILC sensitivity can be expressed in terms of the WIMP pair branching fraction into e^+e^-, κ_e. The ILD detector has been used to study this process [47]. In general, κ_e values of 0.1 are accessible for WIMP masses between 150 GeV and 200 GeV.

3.3.8.2 Long-lived Neutralinos in GMSB

In the Gauge-Mediated SUSY Breaking (GMSB) scenario, $\tilde{\chi}_1^0$ decays into a Gravitino $\tilde{G}$ (the LSP) and a photon. Depending on the SUSY parameters, the lifetime of the $\tilde{\chi}_1^0$ may be such that it decays inside the detector tracking volume. In this case the signal for GMSB neutralino

production is a pair of photons with production point displaced from the origin. The signal is thus two non-pointing photons. The excellent angular resolution for reconstructed photons in the ECAL allows the $\tilde{\chi}_1^0$ lifetime to be determined from photon impact parameter distribution. This process has been studied in detail [48] with the full ILD simulation. For neutralino lifetimes in the range $0.2 - 2.0\,\mathrm{ns}$ a signal to background ratio of approximately unity is achieved. This allows the neutralino mass to be determined with a precision of $\pm 2\,\mathrm{GeV}$ and the lifetime can be measured to 1 %. Decay lengths of 100 cm can be well measured, while a decay length of 10 cm can not be reconstructed with the ECAL only.

3.4 OTHER STUDIES

The previous section described a number of physics studies related to specific aspects of the detector performance, based on full simulation and reconstruction. In addition, a number of other studies have been performed which demonstrate the general purpose nature of the ILD concept. Three of these are described briefly below.

3.4.1 Measurement of Beam Polarisation from WW production

One of the unique features of the ILC is the possibility of both electron and positron beam polarisation [49]. The baseline design foresees a longitudinal electron polarisation of 80 % and a positron polarisation of 30 % with an option of 60 %. This provides a tool for improving the sensitivity to new physics [50]. For many of these applications, the final goal of an ultimate relative precision of 0.2 % of the measurement of the beam polarisations is desirable to bring the systematics from the uncertainty of the beam polarisation to a negligible level.

While polarimeters [51] will be used to measure the polarisation on a bunch-by-bunch basis, the absolute calibration of the average luminosity-weighted polarisation at the interaction point can be achieved using $\mathrm{W^+W^-}$ production. Two methods are considered: i) the modified Blondel scheme [52, 53] which uses the measured $\mathrm{W^+W^-}$ production cross-sections for different beam polarisations; and ii) the angular fit method which uses the distribution of the production angle $\cos\theta_W$ of the W^- with respect to the e^- beam axis [54].

A comparison of these two methods is performed using the full simulation of events in ILD. Semi-leptonic decays of W-pair events ($\mathrm{q\bar{q}}\ell\nu$) are selected with an efficiency of 68.7 % and 93 % purity. The charge of the lepton tags the charges of two W bosons so that the $\mathrm{W^-}$ angular distribution can be determined. In the modified Blondel scheme, the total luminosity necessary to reach the desired relative precision of 0.2 % is around $500\,\mathrm{fb}^{-1}$. Using the angular fit method the same level of precision can be achieved with an integrated luminosity of $250\,\mathrm{fb}^{-1}$. The lower luminosity demand reduces the time spent on the $++$ and $--$ helicity combinations, which are less interesting from the physics point of view. To reach the desired precision for the measurement of the beam polarisation, $\mathcal{L} = 250\,\mathrm{fb}^{-1}$ is required for the case of 60 % positron polarisation, while $\mathcal{L} = 1200\,\mathrm{fb}^{-1}$ is required if only the baseline 30 % positron polarization is available.

3.4.2 Heavy Gauge Boson Production in Littlest Higgs Model

The Littlest Higgs model with T-parity (LHT) has been proposed as a solution to the little hierarchy problem. Since heavy gauge bosons acquire mass terms through the breaking of the global symmetry, precise measurements of their masses allow a determination of the

vacuum expectation value of the breaking (f). Furthermore, since the heavy photon, A_{H}, is a candidate for dark matter, the determination of its properties is important for both particle physics and cosmology. However, at the LHC it is difficult to determine the properties of heavy gauge bosons because they have no colour charge.

The potential of an ILD-like detector concept, studied using the fast simulation of the GLD concept, is described in detail in [55]. Here the processes $e^+e^- \to A_{\mathrm{H}}Z_{\mathrm{H}} \to A_{\mathrm{H}}A_{\mathrm{H}}H$ at $\sqrt{s} = 500\,\mathrm{GeV}$ and $e^+e^- \to W_{\mathrm{H}}^+W_{\mathrm{H}}^- \to A_{\mathrm{H}}W^+A_{\mathrm{H}}W^-$ at $\sqrt{s} = 1\,\mathrm{TeV}$, where A_{H}, Z_{H}, and $W_{\mathrm{H}}^{\pm}$ are the heavy gauge bosons, are studied. The experimental signatures considered for each process are b-jets with missing energy and four-jets with missing energy. The masses and the vacuum expectation value, f, were set to $(M_{A_{\mathrm{H}}}, M_{Z_{\mathrm{H}}}, M_{W_{\mathrm{H}}}^{\pm}) = (81.9\ \mathrm{GeV}, 369\ \mathrm{GeV}, 368\ \mathrm{GeV})$, $m_{\mathrm{H}} = 134\,\mathrm{GeV}$ and $f = 580$ GeV. It is found that the masses of A_{H} and Z_{H} can be measured with an accuracy of 16.2 % and 4.3 % respectively at $\sqrt{s} = 500$ GeV, and those of A_{H} and W_{H} can be determined with an accuracy of 0.2 % and 0.8 % respectively at $\sqrt{s} = 1\,\mathrm{TeV}$ [55]. In addition f can be with measured to 4.3 % at $\sqrt{s} = 500\,\mathrm{GeV}$ and 0.1 % at $\sqrt{s} = 1\,\mathrm{TeV}$. Finally it is shown that the abundance of dark matter relics can be determined to the 10% and 1% levels at $\sqrt{s} = 500\,\mathrm{GeV}$ and $\sqrt{s} = 1\,\mathrm{TeV}$, respectively. These accuracies are comparable to those of the current and future cosmological observations of the cosmic microwave background.

3.4.3 ZHH Production

The Higgs boson tri-linear coupling can be studied at the ILC through the processes $\mathrm{e^+e^-} \to \nu_e\overline{\nu}_e\mathrm{HH}$ and $\mathrm{e^+e^-} \to \mathrm{ZHH}$. For $m_{\mathrm{H}} = 120\,\mathrm{GeV}$, the cross section for the latter process is 0.18 fb at $\sqrt{s} = 500\,\mathrm{GeV}$. The $\mathrm{q\overline{q}b\overline{b}b\overline{b}}$ decay mode (34 % of the ZHH decays) has been studied using the ILD simulation and reconstruction [56]. A multi-variate selection including the invariant masses of jet combinations and flavour tagging information is used. For an integrated luminosity of $500\,\mathrm{fb}^{-1}$, a precision of 90 % on $\sigma(\mathrm{e^+e^-} \to \mathrm{ZHH})$ is achieved. It should be noted that the sensitivity does not yet approach that of earlier fast simulation studies [44]. Whilst significant improvements are expected, this study demonstrates the difficulty of this analysis; excellent particle flow and flavour tagging performance are likely to prove essential for this important measurement.

3.5 CONCLUSIONS

3.5.1 Detector Performance

It has been demonstrated in Section 3.2 that ILD meets the requirements for an ILC detector:

- **Track reconstruction:** The ILD tracking system provides highly efficiency track reconstruction ($\sim 99.5\,\%$), even in a dense multi-jet environment.
- **Momentum resolution:** When hits in the TPC are combined with those in Si tracking detectors, the asymptotic value of the momentum resolution is $\sigma_{1/p_T} \approx 2 \times 10^{-5}\,\mathrm{GeV}^{-1}$, as required.
- **Impact parameter resolution:** For either option for the VTX layout, the required impact parameter resolution is achieved, with asymptotic values of $\sigma_{r\phi} = 2\,\mu\mathrm{m}$ and $\sigma_{rz} = 5\,\mu\mathrm{m}$.
- **Particle flow performance:** A jet energy resolution of $< 3.8\,\%$ is achieved for jets in the energy range $40 - 400\,\mathrm{GeV}$. For the range of energies typical of much of the ILC

physics, $80 - 200\,\mathrm{GeV}$ the jet energy resolutions is $\approx 3\,\%$. The performance does not depend strongly on the polar angle of the jet, except in the very forward region.

3.5.2 Physics Performance

The physics benchmark studies presented above are summarised in Table 3.5-7. However, care is needed in interpreting the results shown. They do not represent the ultimate ILD performance as significant improvements in the analyses are possible. However, the range of different measurements studied and precision achieved demonstrate the general purpose nature of ILD.

Analysis	$\sqrt{s}$	Observable	Precision	Comments
Higgs recoil mass	250 GeV	$\sigma(\mathrm{e^+e^-} \to \mathrm{ZH})$	$\pm 0.30\,\mathrm{fb}$ (2.5 %)	Model Independent
		m_H	32 MeV	Model Independent
		m_H	27 MeV	Model Dependent
Higgs Decay	250 GeV	$Br(\mathrm{H} \to \mathrm{b\bar{b}})$	2.7 %	includes 2.5 %
		$Br(\mathrm{H} \to \mathrm{c\bar{c}})$	12 %	from
		$Br(\mathrm{H} \to gg)$	29 %	$\sigma(\mathrm{e^+e^-} \to \mathrm{ZH})$
$\tau^+\tau^-$	500 GeV	$\sigma(\mathrm{e^+e^-} \to \tau^+\tau^-)$	0.29 %	$\theta_{\tau^+\tau^-} > 178°$
		A_{FB}	± 0.0025	$\theta_{\tau^+\tau^-} > 178°$
		P_τ	± 0.007	exclucing $\tau \to a_1\nu$
Gaugino Production	500 GeV	$\sigma(\mathrm{e^+e^-} \to \tilde{\chi}_1^+\tilde{\chi}_1^-)$	0.6 %	
		$\sigma(\mathrm{e^+e^-} \to \tilde{\chi}_2^0\tilde{\chi}_2^0)$	2.1 %	
		$m(\tilde{\chi}_1^\pm)$	2.4 GeV	from kin. edges
		$m(\tilde{\chi}_2^0)$	0.9 GeV	from kin. edges
		$m(\tilde{\chi}_1^0)$	0.8 GeV	from kin. edges
$\mathrm{e^+e^-} \to \mathrm{t\bar{t}}$	500 GeV	$\sigma(\mathrm{e^+e^-} \to \mathrm{t\bar{t}})$	0.4 %	$(\mathrm{bq\bar{q}})$ $(\mathrm{\bar{b}q\bar{q}})$ only
		m_t	40 MeV	fully-hadronic only
		m_t	30 MeV	+ semi-leptonic
		Γ_t	27 MeV	fully-hadronic only
		Γ_t	22 MeV	+ semi-leptonic
		$A^t_{\mathrm{F}B}$	± 0.0079	fully-hadronic only
Smuons in SPS1a'	500 GeV	$\sigma(\mathrm{e^+e^-} \to \tilde{\mu}_L^+\tilde{\mu}_L^-)$	2.5 %	
		$m(\tilde{\mu}_L)$	0.5 GeV	
Staus in SPS1a'	500 GeV	$m(\tilde{\tau}_1)$	$0.1\,\mathrm{GeV} \oplus 1.3\sigma_\mathrm{LSP}$	
WW Scattering	1 TeV	α_4	$-1.4 < \alpha_4 < 1.1$	
		α_5	$-0.9 < \alpha_5 < +0.8$	

TABLE 3.5-7
A summary of the main observables presented in Section 3.3.

CHAPTER 4

The ILD Sub-Detector Systems

The ILD detector is strongly influenced by two basic assumptions about experimentation at a linear collider: particle flow as a way to reconstruct the overall event properties, and high resolution vertexing. Particle flow calorimetry requires a reliable and redundant tracking system which enables charge particle momenta to be reconstructed with high precision, and in particular, with very high efficiency. ILD is built around a calorimeter system with very good granularity both in the transverse and in the longitudinal direction, and a combination of Silicon and gaseous tracking systems. Vertexing, the other great challenge, is addressed by a high precision pixelated detector very close to the interaction point.

In this section the different sub-detectors are described in more detail, proposed technological solutions are outlined, and necessary development work is highlighted, particularly where it is essential to advance the concept to a point where this detector could be built.

Development of technologies for a detector at a linear collider is an active field, with many ideas being pursued, and great advances in technology are being made. ILD therefore does not at this moment exclude any promising technology from its consideration. Wherever possible, ILD supports that more than one avenue is followed to eventually identify the best solution possible. Therefore, at this stage, all promising technologies are considered as possible candidates for the ILD detector. Consequently for a number of subdetectors more than one option are described.

4.1 VERTEX DETECTOR

The Vertex Detector (VTX) is the key to achieving very high performance flavour tagging by reconstructing displaced vertices. It also plays an important role in the track reconstruction, especially for low momentum particles which don't reach the main tracker or barely penetrate its sensitive volume because of the strong magnetic field of the experiment, or due to their shallow production angle.

The flavour tagging performance needed for physics implies that the first measured point on a track should be as close as possible to the IP. This creates a major technical challenge because of the rapidly increasing beam-related background when approaching the IP. The sensor technology best adapted to the high background environment is not yet defined. It is however clear that existing technologies are not able to satisfy all of the requirements defined by the physics goals (granularity, material budget) and those imposed by the running conditions near the IP (*e.g.* occupancy and radiation dose). Several alternative, innovative, pixel

technologies are being considered and actively developed to satisfy the VTX requirements.

The VTX flavour tagging performance relies on a low material budget for the detector sensors and the support structures. The VTX is also necessary in some physics studies to measure the vertex charge (the net charge of all tracks from the decay chain) which implies distinguishing between the tracks from the primary vertex and the decay chain. This is particularly challenging for low momentum tracks in the jet. Finally, secondary particle production and trajectory kinks due to secondary interactions with the detector material need to be mitigated because of their impact on the particle flow reconstruction. Minimising the VTX material budget therefore motivates an ambitious R&D programme.

4.1.1 Physics Driven Requirements and Running Constraints

To identify the flavor (b or charm) of heavy-flavor jets, to measure the associated vertex charge, and to recognize tau-lepton decays, the VTX design needs to be optimised in terms of single point resolution and distance between the first measured point of tracks and the IP. The high granularity necessary to achieve the single point resolution needs to be complemented with a particularly low material budget allowing high precision pointing with low momentum tracks. A high granularity is also required to separate neighboring tracks in a jet, a constraint which applies predominantly to the detector elements closest to the IP.

Following the usual convention, the performances of the VTX in terms of impact parameter resolution are summarised in a compact way by its well known gaussian expression:

$$\sigma_{ip} = a \oplus b/p \cdot \sin^{3/2}\theta \tag{i}$$

The parameters a and b are required to be below 5 μm and 10 μm·GeV/c, respectively. Monte-Carlo studies show that these specifications are met with the following inputs:

- a single point accuracy of $\lesssim 3\ \mu m$,
- a vertex detector geometry providing a first measured point of tracks at $\sim$ 15 mm from the IP.
- a material budget between the IP and the first measured point restricted to a few per mill of radiation length.

The values of a and b significantly exceed those achieved so far, as illustrated by the comparison made in table 4.1-1, which provides values of a and b obtained with vertex detectors operated at LEP, SLC and LHC as well as planned at RHIC.

To achieve this new tagging performance standard, a beam pipe radius of 14 mm is envisaged, which is still compatible with the need to contain the core of the beam-related pair background within the vacuum pipe. The pipe is assumed to be made of machined beryllium, 250 μm thick, potentially covered with a 25 μm thin foil of titanium against background from synchrotron radiation. Beam-related background, which ultimately sets the performance limits for the VTX, is expected to be dominated by beamstrahlung e^+e^- pairs. Most of these have low transverse momentum and remain trapped inside the vacuum pipe by the 3.5 T solenoid field. Extensive Monte-Carlo simulations, based on the GuineaPig [57] and CAIN generators [58], were performed to estimate the rate of $e^\pm$ reaching the vertex detector. The predicted rates amount to 5.3/4.4 $\pm$ 0.5 hits/cm^2 per bunch crossing (BX) at 15/16 mm radii, including $e^\pm$ backscattered from elements located near the outgoing beam lines [59]. Since most of these $e^\pm$ have a transverse momentum close to the cut-off value of $\lesssim$ 10 MeV/c,

Accelerator	a (μm)	b (μm$\cdot GeV/c$)
LEP	25	70
SLC	8	33
LHC	12	70
RHIC-II	13	19
ILD	< 5	< 10

TABLE 4.1-1
Values of the parameters a and b entering the expression of σ_{ip} foreseen for the ILD, compared to those achieved with past, present or upcoming experiments at existing colliders.

they tend to penetrate the sensitive volume of the VTX sensors at rather shallow angle, and tend to tend to generate pixel clusters which are elongated in the beam direction. This feature may be used offline to reject a substantial fraction of the beamstrahlung clusters. It also impacts the radiation dose. The annual dose was calculated to be in the order of 500 Gy ionising dose per year, with a corresponding fluence of $\lesssim 10^{11}$ n_{eq}/cm^2 at 15 mm radius. To account for the limited accuracy of the simulated beamstrahlung $e^{\pm}$ rate, the latter was multiplied by a safety factor of 3 to derive the sensor specifications. Other backgrounds, such as photon and neutron gas, are expected to add marginal contributions. Overall, the annual radiation levels the sensors have to comply with are in excess of 1 kGy and of 10^{11} n_{eq}/cm^2.

Another environmental concern entering the specifications of the VTX is related to the electrical interference associated with leakage of the beam-related RF from ports used for beam position monitors and other equipment in the interaction region. Their potential effect is motivating specific (delayed) signal processing read-out architectures of the sensors, taking advantage of the ILC beam time structure.

4.1.2 Global Design Aspects

The VTX design is still evolving, but its prominent aspects are well defined. It is made of 5 or 6 cylindrical layers, all equipped with $\lesssim 50$ μm thin pixel sensors providing a single point resolution of 2.8 μm all over the sensitive VTX area (see sub-section 4.1.3.1). The innermost layer has a radius of 15-16 mm, a value for which the beam-related background rate is expected to still be acceptable. As a consequence, the innermost layer intercepts all particles produced with a polar angle (θ) such that $|\cos\theta| \lesssim 0.97$.

Two alternative geometries are being considered, one (called VTX-SL) featuring 5 equidistant single layers (i.e. equipped with one layer of sensors only), and an alternative option (called VTX-DL) featuring 3 double layers (i.e. each layer being equipped with two, $\lesssim 2$ mm apart, arrays of sensors). They are not associated with a specific sensor technology. The double layer option allows spatial correlations between hits generated by the same particle in the two sensor layers equipping a ladder, even if the occupancy is high. It is therefore more robust against (low momentum) beamstrahlung background. It is also expected to provide additional pointing accuracy. Moreover, it should facilitate the internal alignment, allowing the use of a large fraction of tracks traversing the overlapping bands of neighbouring ladders. Finally, it is expected to improve the modeling with tracks reconstructed at shallow angle in the very forward region. This geometry may however be less efficient in reconstructing long lived B mesons decaying outside of the beam pipe. It is also technically more challenging

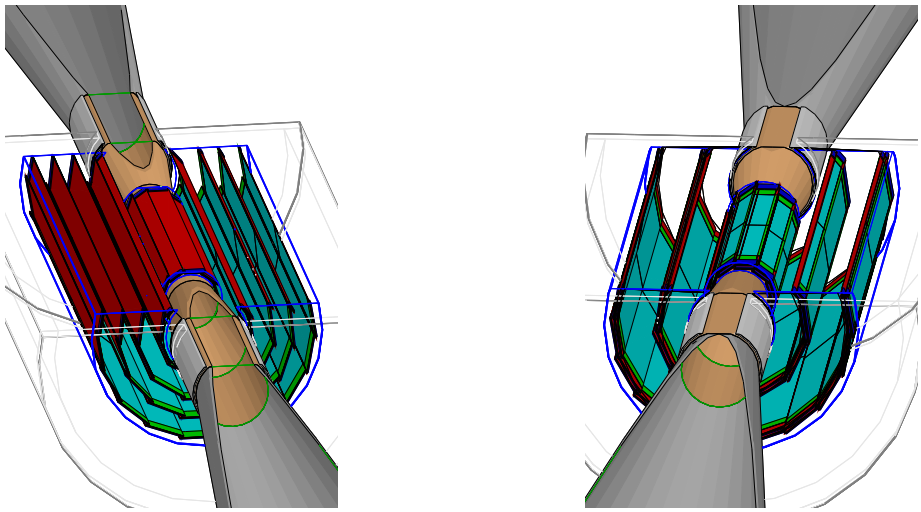

FIGURE 4.1-1. Vertex detector geometries of the two design options. Left: 5 single ladders (VTX-SL). Right: 3 double ladders (VTX-DL).

because of the additional difficulty to realise double ladders as compared to single ones. It may however be robust against mechanical distortions resulting from power pulsing the sensors inside the solenoid field. The two VTX geometries are displayed on figure 4.1-1. Some of their main geometrical parameters are listed in table 4.1-2.

	radius [mm]		ladder length [mm]		read-out time [μs]	
geometry	VTX-SL	VTX-DL	VTX-SL	VTX-DL	VTX-SL	VTX-DL
layer 1	15.0	16.0/18.0	125.0	125.0	25–50	25–50
layer 2	26.0	37.0/39.0	250.0	250.0	50–100	100-200
layer 3	37.0	58.0/60.0	250.0	250.0	100-200	100-200
layer 4	48.0		250.0		100-200	
layer 5	60.0		250.0		100-200	

TABLE 4.1-2
Radius and ladder length for each layer of the two vertex detector geometries. For the double layer option (VTX-DL), the radii are provided for each of both pixel arrays equipping a ladder.The read-out times are provided for each layer in the specific case of a continuous sensor read-out (see subsection 4.1.3).

The complete VTX-SL ladder thickness is equivalent to 0.11 % X_0, while the double ladders of VTX-DL represent 0.16 % X_0. These values assume 50 μm thin silicon pixel sensors. The length of the innermost ladder (125 mm) is limited due to the radial expansion of the pair background envelope as it diverges from the IP. It would shrink significantly when considering the so-called "low-P" option of the machine parameter. In this case, the innermost ladders should be shortened to $<$ 100 mm and/or the inner radius should be increased in ordre to accommodate the increased beam-beam disruption. The loss in physics performance consecutive to the geometrical acceptance shrinkage and to the potential impact parameter resolution degradation is still being evaluated.

Both device options are enclosed in a $\sim$ 500 μm thick (0.14 % X_0), 65 mm radius, cylindrical beryllium support. The latter is surrounded by a light foam cryostat (0.05 % X_0), complemented with a 0.5 mm aluminum foil (0.55 % X_0) which acts as a Faraday cage. The whole system, including support, cryostat and cage adds up to 0.74 % X_0. While the ladders of the three (resp. two) external layers of VTX-SL (resp. VTX-DL) are mounted on the beryllium support, the ladders composing the inner layers are supported by straight sections of the vacuum pipe.

The detector alignment is expected to proceed through two main steps. The ladders will first be aligned inside their layer. An overlap of $\lesssim$ 500 μm between the sensitive areas of neighbouring ladders is foreseen for this purpose. Tracks with momentum in excess of a couple of GeV/c traversing these overlapping bands will be used. Next the layers will be aligned with respect to the rest of the detector using straight tracks such as those of $\mu^+\mu^-$ final states.

The pros and cons of each design option are still being assessed. Moreover, the concept itself, which assumes extended cylinders, rather than shorter ones complemented with disks at small polar angle, is based on the present understanding of the minimal material budget which would separate the barrel from the disks. Depending on the evolution of technologies and materials, the choice between both alternatives may be reconsidered.

4.1.3 Pixel Technology and System Integration Studies

4.1.3.1 R&D on Pixels and Read-out Architectures

Intensive R&D has been under way for several years, addressing the numerous challenging issues underlying the vertex detector specifications. Because of the scale of the challenge and of its complexity, several alternative sensor technologies are being developed in parallel, aiming for the best suited ones. The goal of the development is to optimise the charge sensing system and the charge to electrical signal conversion, as well as the read-out, steering and control micro-circuits. The technologies presently concentrating most of the R&D effort within the ILD group are CMOS sensors [60, 61, 62, 63], DEPFETs [64, 65], FPCCDs [66, 67], and ISIS [64]. Since recently, CMOS sensors exploiting vertical integration technology [68] are also developed. Alternative technological approaches mentioned in [64] may also be considered, though not currently developed inside the ILD group. The R&D achieved so far has already demonstrated that the goals of a single point resolution of ($\lesssim$ 3 μm), double hit separation of ($\lesssim$ 40 μm) and sensor thickness of ($\lesssim$ 50 μm) are achievable.

The most demanding requirement for all technologies is to comply with the occupancy generated by the beam related background in the innermost layers. Two alternative approaches are being investigated, one where the sensors are read out continuously, and one where the signal is stored during the whole train duration and read out during the beamless period separating two consecutive trains.

In the continuous read-out approach, most of the R&D effort is invested in achieving the low noise high read-out frequency required for the inner layers, while keeping the power consumption at an affordable level. Typical read-out time target values are summarised in table 4.1-2 for each layer. Present R&D achievements indicate that the upper bounds of each time interval can already be considered as within reach.

Power dissipation estimates, based on fabricated sensors and accounting for power cycling, were performed. It was assumed that the beam time structure can be used to suppress the power during a large fraction of the inter-train time by about two orders of magnitude,

estimating to about $1-2$ milliseconds before and after the train the transient time needed to switch on and off all sensors in a well controlled way. In this case, Lorentz forces applied to the ladders are expected to remain acceptable. With a rather conservative duty cycle of 2% (while the machine duty cycle is 0.5%), the average power dissipation would amount to a few tens of watts only (e.g. 30 W for CMOS sensors [60]). Such values are compatible with modest cooling, based on air flow, which does not require introducing additional material in the VTX fiducial volume.

Power consumption may even be mitigated more with the delayed read-out approach because of the very low read-out clock frequency it allows for, a feature which also translates into reduced Lorentz forces on the ladders. Moreover, if the signal charge is converted into an electrical signal only after the end of the train (e.g. like in FPCCD or ISIS devices), immunity against EMI can be reinforced.

Most pixel technologies and read-out architectures still need at least a couple of years until all main VTX specifications have been addressed. The recently considered vertical integration approach, which may have the highest potential, is likely to need more time to reach maturity. It may be a technological solution for a second generation VTX, to be used a couple of years after the start of the ILC programme. It is in particular a promising solution for the machine operation near 1 TeV, where the beam-related background may call for sensors substantially faster than those needed at 500 GeV.

4.1.3.2 System Integration Studies

The R&D on the sensors and their read-out circuits is complemented with studies addressing their main system integration issues. One of the main aims of these studies is to tackle the design goal of $\lesssim 0.1$ % X_0 thickness per layer over their active area. Attempts are made to find materials which combine low density and high rigidity against potential vibrations generated by the air cooling system and by power cycling (temperature gradient, Lorentz forces). The latter also requires good thermal expansion compatibility between the support and the sensors. Low density materials were tested [64], such as silicon carbide foam, which have a thermal expansion coefficient close to silicon, and feature a density of a few per-cent only. They may actually also be used for the structural material of the entire VTX assembly.

Trials to use silicon as a support material are also made [65]. They consist in using the silicon substrate of the sensors, excavating the silicon bulk wherever it is not essential for the ladder stability. The latter is provided by "window frames" left after the bulk excavation. This approach is currently followed for the upgrade of the SuperBELLE vertex detector [69].

Finally, a third approach consists in extrapolating from the current state-of-the-art. It relies on the ladders equipping the upcoming PIXEL vertex detector of the STAR experiment at RHIC [70]. With a total material budget of ~ 0.3 % X_0, its concept may be extended to the ILD with an ultimate budget of $\lesssim 0.2$ % X_0.

4.1.4 Outlook

Definite choices concerning the sensor technology, the read-out architecture and the ladder design still have to wait until full-scale fully-serviced ladders, as well as still more realistic simulation studies are available. For instance, a detailed understanding of the handling of the beam-related background will impact the maximal background rate acceptable, with direct consequences on the read-out architecture and the sensor technology. The validation

of the VTX concept will follow, including the outcome of current studies of servicing issues, presumably around 2012.

4.2 SILICON TRACKING

The tracking system of the ILD has been optimised to deliver outstanding resolution together with excellent efficiency and redundancy. The choice of ILD is a combination of gaseous tracking, giving a large number of hits, and the redundancy this gives, with a sophisticated system of silicon based tracking disks and barrels. Together the system achieves excellent resolution, and covers the solid angle down to the very forward region.

An important consideration is the ability of the system to be calibrated to the desired precision. Here the combination of gaseous and silicon based tracking offers some unique advantages due to the very different nature of possible systematic distortions, and due to the possibility to cross-calibrate the different systems. For example, the Silicon tracker will help in monitoring possible field distortions in the TPC, as well as contributing to alignment and time stamping (bunch tagging). Silicon tracking is relatively easy to calibrate and as such it is expected to provide robustness, redundancy, and ease in the calibration of the overall tracking system.

The silicon tracking system of the ILD has been developed by the SiLC collaboration. Detailed descriptions of the wide ranging R&D activities conducted within the SiLC collaboration can be found in the latest documents and presentations issued by the SiLC Collaboration, and references therein [71, 72, 73, 74, 75, 76].

4.2.1 Baseline Design of the Silicon Trackers

Combined with the Silicon vertex detector and the central gaseous tracker TPC, a Silicon Tracking system is proposed for the ILD. It is based on modern Silicon detector technology, deep sub micron CMOS technology for the front-end (FE) electronics with a new on-detector electronics connection and new material technology for the support architecture. Special challenges for the ILD are a significant reduction in material compared to the most recent examples of large scale silicon detectors (*e.g.* LHC detectors), operating at very low power, and reaching excellent point resolution and calibration. The Silicon tracker is made of two sets of detectors:

- The first set is located in the central barrel and is made of the SIT (Silicon Internal Tracker), and the SET (Silicon External Tracker). Both devices have false double-sided Silicon strip detectors, together providing three precision space points.
- The second set is located in the forward region and is constituted of the FTD (Forward Tracking Detector) in the very forward region, and the ETD (end cap Tracking Detector), providing a space point between the TPC endplate and the calorimeter in the endcap region.

The complete silicon tracking system is implemented in the MOKKA simulation of the ILD, including estimates of support structures.

4.2.1.1 The Silicon Tracker in the Barrel: SET and SIT

The SIT is positioned in the radial gap between the vertex detector and the TPC. The role of the SIT is to improve the linking efficiency between the vertex detector and the TPC; it

improves the momentum resolution and the reconstruction of low p_T charged particles and improves the reconstruction of long lived stable particles.

The SET is located in the barrel part between the TPC and the central barrel electromagnetic calorimeter (ECAL). The SET gives an entry point to the ECAL after the TPC end wall (3% X_0). It acts as the third Silicon layer in the central barrel and also improves the overall momentum resolution. The SIT and SET, in addition to improving momentum resolution (Fig. 4.2-3), provide time-stamping information for separation between the bunches and thus allowing the bunch-tagging of each event. These two central Silicon components may serve in monitoring the distortion of the TPC and for the alignment of the overall tracking.

4.2.1.2 The Endcap and Forward Silicon Tracking: ETD and FTD

The FTD is positioned in the innermost part of the tracking region, and covers the very forward region down to about 0.15 radians. In total seven disks are foreseen in this region.

The ETD is positioned between the TPC end cap and the end cap calorimeter system. The role of the ETD is to serve as entry point for the calorimeter and to improve the momentum resolution for the charged tracks with a reduced path in the TPC. Moreover it helps reducing the effect of the material of the TPC End Plates (currently estimated to be 15% X_0). It thus might improves the matching efficiency between the TPC tracks and the shower clusters in the EM calorimeter. It also contributes to extending the lever arm and angular coverage of the overall tracking system at large angle. Both the ETD and the FTD ensure the full tracking hermeticity.

4.2.2 Performances of the Silicon tracking system

The main detector performances of the Silicon tracking ILD system are summarized in terms of its contribution to i) full angular coverage, ii) momentum and impact parameter resolution, iii) calibration of distortions, iv) alignment, v) time stamping (bunch tagging), and vi) redundancy and robustness of the overall tracking system. Full simulation studies are being performed in order to best understand the performances of the Silicon tracking system in terms of momentum and spatial reconstruction and pattern reconstruction. These detailed simulations are completing the already available performance studies based on fast simulation (LiC Detector Toy Monte Carlo "LDT" and SGV) [71].

4.2.2.1 Angular Coverage

Combining the Silicon components with the vertex detector and the TPC ensures efficient tracking over the full angular coverage down to very small angles close to the beam. It helps in crucial regions such as: i) the transition from the central barrel to the End Cap region, ii) the end cap regions and iii) the very forward regions (Fig. 4.2-2).

4.2.2.2 Momentum and Impact Parameters Performances

To demonstrate the contribution of the various Si tracking components to the improvement of the overall tracking performances in terms of momentum and impact parameter resolution, a number of studies have been performed based on both fast simulation and the MOKKA-Marlin and GEANT 4 simulation. Some of the most relevant results (evaluation using fast Monte Carlo, muon tracking) are shown in Figure 4.2-3.

SIT characteristics (current baseline = false double-sided Si microstrips)					
Geometry			Characteristics		Material
R[mm]	Z[mm]	cosθ	Resolution R-ϕ[μm]	Time [ns]	RL[%]
165	371	0.910	R: σ=7.0,	307.7 (153.8)	0.65
309	645	0.902	z: σ=50.0	σ=80.0	0.65
SET characteristics (current baseline = false double-sided Si microstrips)					
Geometry			Characteristics		Material
R[mm]	Z[mm]	cosθ	Resolution R-ϕ[μm]	Time [ns]	RL[%]
1833	2350	0.789	R: σ=7.0,	307.7 (153.8)	0.65
1835	2350	0.789	z: σ=50.0	σ=80.0	0.65
FTD characteristics (current baseline = pixels for first 3 disks, microstrips for the other 4))					
Geometry			Characteristics		Material
R[mm]	Z[mm]	cosθ	Resolution R-ϕ[μm]		RL[%]
39-164	220	0.985-0.802			0.25
49.6-164	371.3	0.991-0.914			0.25
70.1-308	644.9	0.994-0.902			0.25
100.3-309	1046.1	0.994-0.959	σ=7.0		0.65
130.4-309	1447.3	0.995-0.998			0.65
160.5-309	1848.5	0.996-0.986			0.65
190.5-309	2250	0.996-0.990			0.65
ETD characteristics (current baseline = single-sided Si micro-strips, same as SET ones)					
Geometry			Characteristics		Material
R[mm]	Z[mm]	cosθ	Resolution R-ϕ[μm]		RL[%]
419.3-1822.7	2426	0.985-0.799	x:σ=7.0		0.65
419.3-1822.7	2428	0.985-0.799	y:σ=7.0		0.65
419.3-1822.7	2430	0.985-0.799	z:σ=7.0		0.65

TABLE 4.2-3
The projected values of basic SIT, SET, FTD, and ETD characteristics.

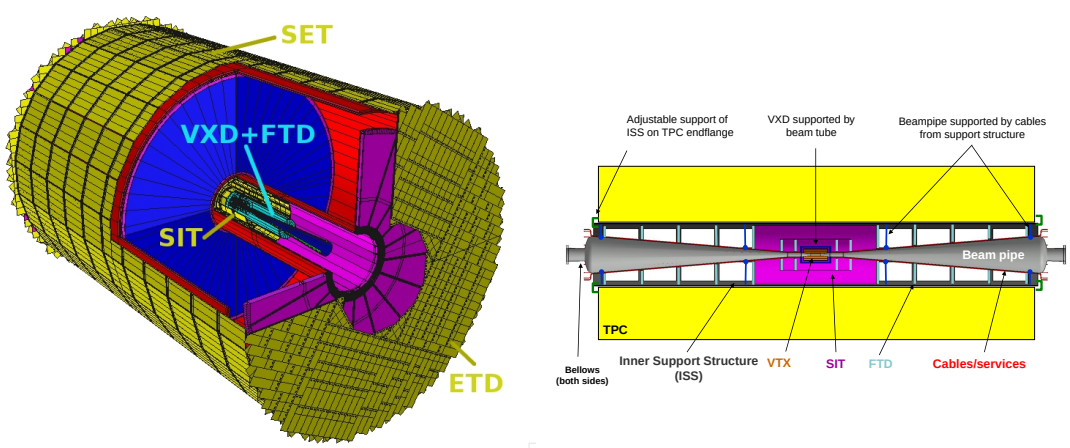

FIGURE 4.2-2. Silicon tracking components as described in the Table 4.2-3 (GEANT 4-based simulation). The plot on the right shows a side-view of the inner silicon tracking system, including the support structure.

For tracks in the barrel region the present combined Silicon and TPC tracking system delivers an outstanding momentum resolution of $\sigma(\Delta p_T/p_T^2) < 2 \cdot 10^{-5}$ GeV as shown in Fig. 4.2-3(left). The plots compare four different arrangements: the ILD setup as described above (blue), a setup without the inner tracker SIT (red), a setup without the external tracker

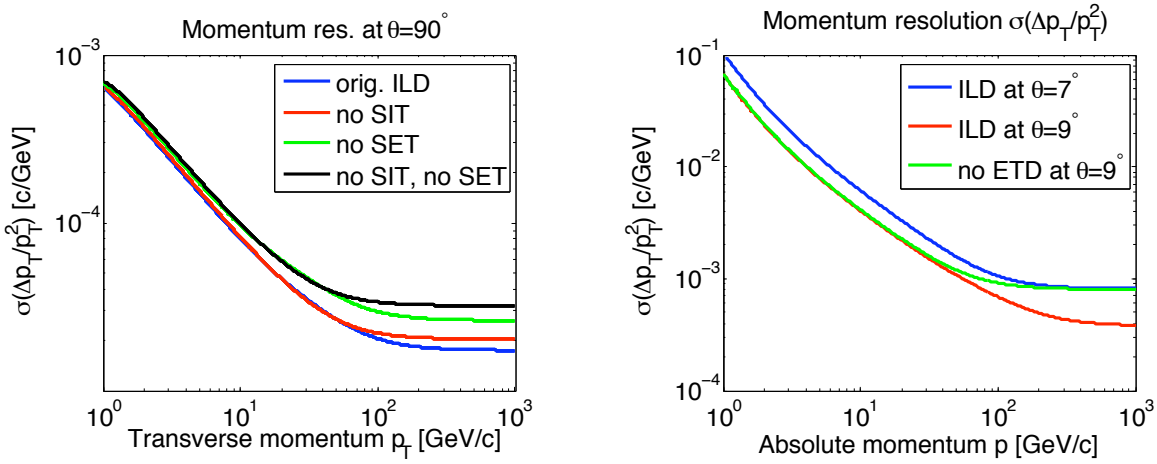

FIGURE 4.2-3. Left plot: barrel region, transverse momentum reduced resolution as function of p_T. Right plot: forward region, transverse momentum reduced resolution as function of absolute momentum p. The different scenarios are described in the text.

	VTX ($3 \times 3\mu m^2$)	VTX ($5 \times 5\mu m^2$)	VTX ($3 \times 3\mu m^2$) + SIT ($5 \times 10\mu m^2$)	VTX ($3 \times 3\mu m^2$) + SET ($5 \times 50\mu m^2$)
σ(R-ϕ)@ R = 150cm	1.3 cm	2.2 cm	0.6 mm	78 μm
σ(z)@ R = 50cm	35 μm	60 μm	16 μm	28 μm
σ(z)@ R = 100cm	77 μm	126 μm	39 μm	30 μm
σ(z)@ R = 118cm	118 μm	192 μm	50 μm	39 μm

TABLE 4.2-4
The precision of the extrapolated R-ϕ and z-coordinates for a 100 GeV track at $\theta = 90°$, at three radii in the TPC volume.

SET (green), and a setup without SIT and SET (black).

Figure 4.2-3(right) shows the momentum resolution for very forward going tracks, for three different angular ranges. While the addition of the silicon tracking system improves the momentum resolution, the impact parameter resolution remains virtually unchanged.

Table 4.2-4 offers an alternative illustration to the improvement generated by both SIT and SET on spatial resolution.

4.2.2.3 Distortion Monitoring and Handling

The Silicon trackers are mechanically stable devices which will help improve the absolute alignment of the overall tracking system, and of the ILD as a whole. This alignment is sensitive in particular to temperature fluctuations, which will need to be understood to the 2 μm level. These alignment systematics will be very different from the TPC ones. The TPC is sensitive to ambient temperature and to atmospheric pressure variations, to non-homogeneities in E and B fields, etc. In particular the E drift field in the TPC may depend on space charge transient effects due to variations in the machine backgrounds. The SIT and SET give an independent and effective means to monitor accurately such effects on real data. Experience at LEP has shown that this capability gives an invaluable redundancy during data analysis, and a unique mean to disentangle and understand anomalous behaviours. It is a necessary complement to the unique pattern recognition capabilities of the TPC.

4.2.2.4 Electronic Time Stamping

Based on the performances of the front end (FE) chip currently developed, currently a bunch crossing tagging with a precision of 160 ns can be obtained corresponding to a shaping time around 0.5-0.7 μs and 8 sampling cells. This precision depends on the sampling frequency. A more refined estimate based on the Cleland and Stern algorithm [77], and function of the signal to noise, the number of samples, and the shaping time, indicates that the currently developed framework could allow identifying the bunch crossing with a resolution of order of 20 to 40 ns.

4.2.3 Calibration Procedures

The Front End Electronics as currently available in the current 130nm CMOS technology includes a full readout electronic chain with a high level digital control of the functionality of the overall chip. In particular a fully programmable test pulse system is included. It will allow calibrating and monitoring of this signal processing device and play a crucial role in the silicon DAQ.

Environmental conditions around the detector due to local temperature gradients, humidity changes, etc. will induce some instability of the support structures comparable in size to the precision of the detectors. Consequently, independent alignment systems monitoring these changes will be needed. For the case of silicon trackers one can profit from the weak (but non-zero) absorption of infrared light in Silicon and use laser beams as pseudo-tracks that traverse consecutive sensors.

For the SIT and FTD subdetectors, which have several Silicon layers, the alignment procedure is based on the use of their own tracking detectors as photo-sensors; the transmittance of Silicon to infrared beams compared to the existing AMS and CMS tracker systems can be improved by a further 20-30%, leading to a transmittance value between 70 to 80%. Resolutions on the order of 2 microns can be obtained with this procedure [78].

The SET and ETD are single layer detectors; the SET can be aligned with respect to fiducial marks on the outer cage of the TPC at the level of 100 microns by standard procedures. The monitoring of the SIT position could be done one order of magnitude better [79]. Similar procedures can be done for the ETD. Finally, tracks will be used for internal alignment at the precision level of few microns, by using adequate χ^2 minimisation algorithms already employed in the LHC and other experiments.

4.2.4 Silicon Tracker Material Budget

A crucial concern of the design of the silicon tracking system has been to minimise the material budget. New silicon sensors and modern material technology based on carbon fibre composite materials (CFC) provide optimal solutions for the silicon tracking components. New front end electronics based on DSM CMOS feature less power dissipation (see already achieved performance of the newly developed FE chip) and allow a direct connection onto the detector, thus removing the need for cooling. All these facts allow a reduction of the sensitive thickness of the sensors to at least 250 μm, or 0.25% X_0. Engineering studies have shown that a support structure for the envisioned silicon detectors equivalent to a 1 mm thick CFC layer are possible, corresponding to a contribution of 0.4%X_0 per layer. Together with services etc a thickness of 0.65% X_0 per layer seems in reach (see table 4.2-3). The final goal

is 0.5% RL per layer in the innermost part of the detector, which will need further R&D. A further reduction might be possible if new sensor and support technologies become available.

4.2.5 Baseline construction and Integration of Silicon components

The baseline design to construct the ILD Silicon system is an unified design for all the components apart from the very small FTD disks. The SIT, SET and ETD components will be made of Silicon strip sensors with a unique sensor type. The current baseline are sensors of square shape from a 6″ wafer, 200μm thick, 50μm readout pitch (true pitch of 25μm). The modules will be made of one up to a few sensors depending on the location of the module in the detector. The readout chip will be directly connected onto the sensor. The chip will be made in deep sub-micron technology (current prototypes are in 130nm technology), most probably in 90 nm. It is a mixed analogue-digital FE and readout chip with a full processing of the analogue signal, long shaping time (1μs), sparsification, digitisation and a high level of digital processing allowing full programmability of the chip. A full prototype is presently developed [80]. The power dissipation of at most 1m W per channel is achieved and power cycling is included. The goal is to avoid a dedicated liquid cooling system, but instead to rely on a forced gas cooling as is also considered for the VTX and the TPC systems. Details of this however are not yet worked out.

The integration of the silicon tracking components depends critically on the neigbbouring detectors. The SET will be made of 24×2 identical super-modules, each covering 2.35×0.5 m^2 supported by a light structure made from composite material. The support structure will be supported from the TPC end-flange, and might also rest at intermediate z-positions on the TPC field cage. The two SIT layers will be made in the same way as the SET, namely 18 and 12 super-modules for the external and the innermost layers, respectively. Together with the outer four FTD disks the SIT layers will be supported by a CFC support structure, fixed to the TPC end-flange at their inner radius. The ETD, thanks to its XUV geometry is built in the same way as the barrel components and will be fixed to the electromagnetic end cap calorimeter.

The support architecture of SIT, SET and ETD will be designed in the same way focusing on robust, very light and easy to mount structures. The design for the FTD disks is currently based on pixels (same type as the vertex detector) for the first three disks and false double sided strips for the other four disks. These four disks will be made of trapezoidal sensors and altogether 16 petals as in the present ATLAS forward detector.

4.2.6 R&D needs and prospects for Silicon tracking

The Silicon technology for large-area tracking systems will continue to evolve over the next years because of the stringent needs of the Large Collider experiments (LHC upgrades, ILC and CLIC). The SiLC R&D collaboration takes an active part in these worldwide efforts dedicated to novel and high technology. The group will continue to develop novel sensors. Options include, as a first step, the edgeless planar micro-strip sensors followed by the 3D planar micro-strips sensors. The goal is to have thinner, lower voltage biased strip sensors and larger wafer size (8″). In addition, the application of pixel technology to at least dedicated regions of the Silicon tracking, including 3D based pixel technology is part of this R&D objective. The ongoing development of Front End and readout electronics based on ASICs in very deep sub micron CMOS technology, with a high degree of processing of digital information on the detector, low noise, low power consumption, robustness (redundancy

and fault tolerance), will be further pursued. New interconnection technologies of the ASIC directly onto the sensors by bump bonding and then by 3D vertical interconnect as well as new cabling techniques will be addressed. Challenging aspects on mechanics in order to build light, robust, and large area mechanical structures, with stringent mechanical constraints on alignment, stability (ex: push pull) and quality control will impact the final design and construction of these devices. A reduced material budget resulting in improved tracking performance, robustness, reliability, easy to build (and not expensive) are the main goals of this ambitious R&D program [71].

4.3 THE TIME PROJECTION CHAMBER

4.3.1 Motivation

The subdetectors for the linear collider detector must be designed coherently to cover all possible physics channels because their roles in reconstructing these channels are highly interconnected. Two important aspects for tracking are, (a) precision-physics measurements require that the momentum of charged tracks be measured an order of magnitude more precisely than in previous experiments, and (b) high resolution measurements of the jet-energy using the particle-flow technique require efficient reconstruction of individual particles within dense jets. Aspects (a) and (b) for the ILD detector are demonstrated in Section 3.2.1 and 3.2.4. of this document.

A TPC as the main tracker in a linear collider experiment offers several advantages. Tracks can be measured with a large number of three-dimensional $r\phi$,z space points. The point resolution, σ_{point}, and double-hit resolution, which are moderate when compared to silicon detectors, are compensated by continuous tracking. The TPC presents a minimum amount of material X_0 as required for the best calorimeter performance. A low material budget also minimizes the effect due to the $\sim 10^3$ beamstrahlung photons per bunch-crossing which traverse the barrel region. Topological time-stamping in conjunction with inner silicon detectors is precise to $\sim$2 ns so that tracks from interactions at different bunch-crossings or from cosmics can readily be distinguished. To obtain good momentum resolution and to suppress backgrounds, the detector will be situated in a strong magnetic field of several Tesla, for which the TPC is well suited since the electrons drift parallel to $\vec{\mathrm{B}}$. The strong B-field improves σ_{point} and the two-hit resolution by compressing the transverse diffusion of the drifting electrons to $\mathcal{O}$(1 mm) [81].

Continuous tracking facilitates reconstruction of non-pointing tracks, e.g. from V^0s or certain Susy (GMSB) channels, which are significant for the particle-flow measurement and in the reconstruction of physics signatures in many standard-model-and-beyond scenarios. The TPC gives good particle identification via the specific energy loss dE/dx which is valuable for the majority of physics analyses and for electron identification. The TPC will be designed to be robust while easy to maintain so that an endcap readout module can readily be accessed if repair is needed.

A Time Projection Chamber (TPC) is chosen for the central tracker because of its demonstrated performance in past collider experiments [82]. The main design issues at the linear collider are covered in Section 4.3.2. In Section 4.3.3, the R&D by the LCTPC groups[83, 84] to determine the best state-of-the-art technology for the TPC is described.

4.3.2 Design

There are important, and interconnected, design issues related to the performance, endcap, electronics, fieldcage, robustness in backgrounds, corrections and alignment. Since methods of investigating these issues have been established from past operational experience, the LCTPC groups have been actively investigating all aspects since 2001.

4.3.2.1 Performance

Main goals for the TPC performance at the linear collider are given in Table 4.3-5. Understanding the properties and achieving the best possible point resolution have been the object of R&D studies of Micro-Pattern Gas Detectors (MPGD), MicroMegas[85] and GEM[86] (Section 4.3.3), and results from this work are reflected in Table 4.3-5. More details about the issues are explained in the following paragraphs.

TABLE 4.3-5
Goals for performance and design parameters for an LCTPC with standard electronics.

Size	$\phi = 3.6$m, L = 4.3m outside dimensions
Momentum resolution (3.5T)	$\delta(1/p_t) \sim 9 \times 10^{-5}$/GeV/c TPC only ($\times$ 0.4 if IP incl.)
Momentum resolution (3.5T)	$\delta(1/p_t) \sim 2 \times 10^{-5}$/GeV/c (SET+TPC+SIT+VTX)
Solid angle coverage	Up to $\cos\theta \simeq 0.98$ (10 pad rows)
TPC material budget	$\sim 0.04\mathrm{X}_0$ to outer fieldcage in r
	$\sim 0.15\mathrm{X}_0$ for readout endcaps in z
Number of pads/timebuckets	$\sim 1{\times}10^6/1000$ per endcap
Pad size/no.padrows	$\sim$ 1mm$\times$4–6mm/$\sim$200 (standard readout)
σ_{point} in $r\phi$	$< 100\mu$m (average over $\mathrm{L}_{sensitive}$, modulo track ϕ angle)
σ_{point} in rz	$\sim$ 0.5 mm (modulo track θ angle)
2-hit resolution in $r\phi$	$\sim$ 2 mm (modulo track angles)
2-hit resolution in rz	$\sim$ 6 mm (modulo track angles)
dE/dx resolution	$\sim$ 5 %
Performance	$>$ 97% efficiency for TPC only ($\mathrm{p_t} > 1$GeV/c), and
	$>$ 99% all tracking ($\mathrm{p_t} > 1$GeV/c) [87]
Background robustness	Full efficiency with 1% occupancy,
	simulated for example in Fig. 4.3-4(right)
Background safety factor	Chamber will be prepared for 10 $\times$ worse backgrounds
	at the linear collider start-up

4.3.2.2 Endcap

The two TPC endcaps will have an area of 10 m^2 each. The readout pads, their size, geometry and connection to the electronics and the cooling of the electronics, are all highly

correlated design tasks. The material of the endcap and its effect on ECAL for the particle-flow measurement in the forward direction must be minimized, and the goal is to keep it below 15%X_0. Designing for the finest possible granularity will minimize the occupancy arising from the TPC drifttime integrating over about 100 bunch-crossings[88]. The sensitive volume will consist of several$\times 10^9$ 3D-electronic standard-readout voxels (two orders of magnitude more than at LEP) or 10^{12} voxels in case of pixel readout. Development of the layout of the endcaps, i.e. conceptual design, stiffness, division into sectors and dead space, has started, and first ideas are shown below (Section 4.3.3).

4.3.2.3 Electronics

For the readout electronics, one of the important questions is the density of pads that can be accommodated while maintaining a stiff, thin, coolable endcap. The options being studied are (A) standard readout of several million pads or (B) pixel readout of a thousand times more pads using CMOS techniques. Table 4.3-5 assumes standard readout electronics; a similar table for pixel electronics will be made when the R&D is further advanced [83] [84]. A basic ingredient for the front-end electronics will be the use of power-pulsing which is possible due to the bunch-train time structure and is assumed to give a power reduction of order 100; what can be achieved in practice is an important R&D issue (Section 4.3.3).
(A) Standard readout:
Small pads, $\sim$ 1mm$\times$5mm, have been found to provide good resolution from the R&D work and to guarantee the low occupancy in Table 4.3-5. Studies have started to establish the realistic density of pads that can be achieved on the endcap. A preliminary look at the FADC approach (à la Alice[89][90]) using 130 nm technology indicates that even smaller sizes might be feasible. An alternative to the FADC-type is the TDC approach (see [84][90]) in which time of arrival and charge per pulse by time-to-charge conversion are measured. In preparation for the possibility that the material budget requires larger pads, the resistive-anode charge-dispersion readout technique[91] is being studied as an option to maintain the good point resolution. Since this technique could compromise the two-track resolution, more R&D is required.
(B) CMOS pixel readout:
A new concept for the combined gas amplification and readout is under development [84][92]. In this concept the "standard" MPGD is produced in wafer post-processing technology on top of a CMOS pixel readout chip, thus forming a thin integrated device of an amplifying grid and a very high granularity endcap with all necessary readout electronics incorporated. For a readout chip with $\sim$ 50μm pixel size, this would result in $\sim 2 \cdot 10^9$ pads ($\sim 4 \cdot 10^4$ chips) per endcap. This concept offers the possibility of pad sizes small enough to observe the individual primary electrons formed in the gas and to count the number of ionisation clusters per unit track length, instead of measuring the integrated charge collected. The R&D program (Section 4.3.3) will determine on what time scale this technology will become feasible for a large TPC[83].

4.3.2.4 Fieldcage

The design of the inner and outer fieldcages involves the geometry of the potential rings, the resistor chains, the central HV-membrane, the gas container and a laser system. These must be laid out to sustain at least 100kV at the HV-membrane with a minimum of material. The goals for the inner and outer fieldcage thicknesses are about 1%X_0 and 3%X_0, respectively,

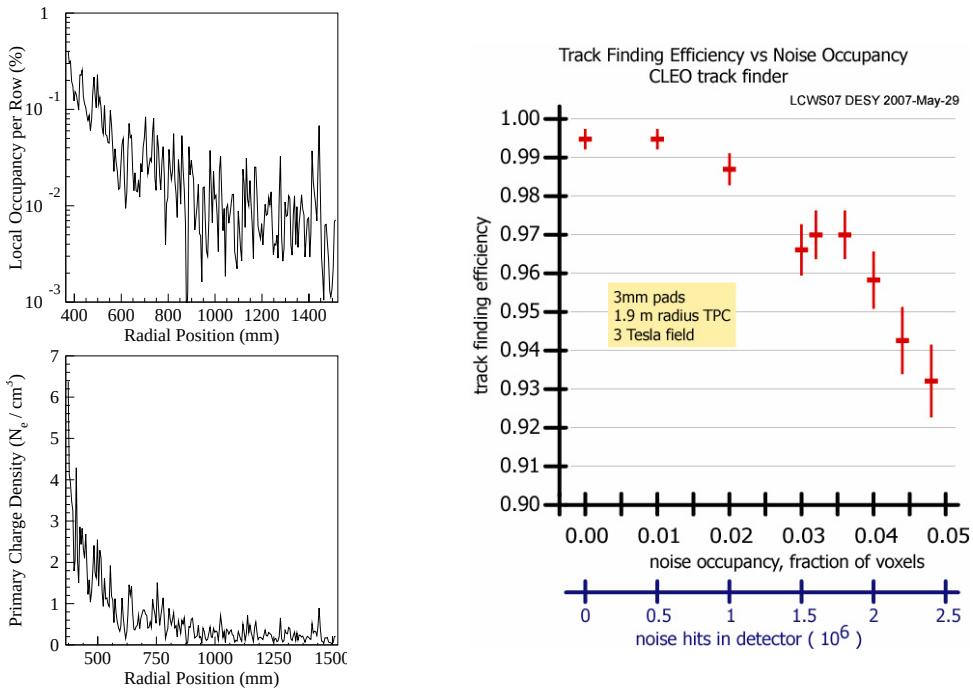

FIGURE 4.3-4. Occupancy for xyz $= 1 \times 5 \times 5\text{mm}^3$ voxels (left, top) and space charge(left, bottom) due to the major beam-beam effects (beamstrahlung photons, electron-positron pairs and neutrons) as simulated in [88]. Study of the tracking efficiency in the presence of backgrounds (right); this study [94] assumed a conservative voxel size of $3 \times 10 \times 40\text{mm}^3$.

while the chamber gas adds another $1\%X_0$. For alignment purposes the laser system is foreseen and may be integrated into the fieldcage [89][93]. The non-uniformities due to the fieldcage design and fabrication can be minimized using the experience gained in past TPCs.

4.3.2.5 Backgrounds and robustness

The issues are the space-charge, covered in the next item below, and the track-finding efficiency in the presence of backgrounds which will be discussed here. There are backgrounds from the collider, from cosmics or other sources and from physics events. The main source is the collider, which gives rise to gammas, neutrons and charged particles due to $\gamma\gamma$ interactions and beam-halo muons being deposited in the TPC at each bunch-crossing [83]. Simulations of the main sources [88] arising from beam-beam effects–gammas, pairs and neutrons–under nominal conditions indicate an average occupancy of the TPC of less than 0.1%, Fig. 4.3-4 (left). The TPC track finding remains robust at these occupancies; the continuous 3D-granularity tracking is inherently simple and suffers no loss in efficiency even with a uniform 1% noise occupancy as demonstrated by the study in Figure 4.3-4(right). Note that the latter study was performed for a slightly different TPC design than the one adopted by ILD. The study was based on a TPC with a radius of 1.9m, readout cells of $3 \times 10\text{mm}^2$ immersed in a 3T magnetic field. A uniform distribution of hits was assumed, and a very detailed simulation of the signal development and digitisation was performed. The 1% uniform noise occupancy mentioned above is about twice the beam-related occupancy in Figure 4.3-4(left) at the TPC inner radius and about fifty times the total occupancy in the TPC.

Since the backgrounds at the beginning of operation could be much larger until the linear collider machine is well understood, the LCTPC is preparing for an occupancy of 10%.

4.3.2.6 Corrections for non-uniform fields

Both fields, (A) magnetic and (B) electric, can have non-uniformities which must be corrected. The (C) chamber gas will play a crucial role in minimizing corrections.

(A) Magnetic field

Non-uniformity of the magnetic field of the solenoid will be by design within the tolerance of $\int_{\ell_{\rm drift}} \frac{B_r}{B_z} dz < 2-10$mm as used for previous TPCs. This homogeneity is achieved by corrector windings at the ends of the solenoid. At the ILC, larger gradients will arise from the fields of the DID (Detector Integrated Dipole) or anti-DID, which are options for handling the beams inside the detector at an IR with ±7 mrad crossing-angle. This issue was studied intensively and summarized in [95], where it is concluded that the TPC performance will not be degraded if the B-field is mapped to around 10^{-4} relative accuracy and the procedures outlined below (under **Alignment**) are followed. These procedures will lead to an overall systematic error due to the field components of ~ 30 μm over the whole chamber which has been shown to be sufficient [95] and was already achieved by the Aleph TPC. Based on past experience, the field-mapping gear and methods will be able to accomplish the goal of 10^{-4} for the relative accuracy. The B-field should also be monitored during running since the currents in the DID or corrector windings may differ from the configurations mapped.

(B) Electric field

Three sources of space charge are (*i*) primary ion build-up in the drift volume, (*ii*) ion build-up at the readout plane and (*iii*) ion backdrift, where ions created at the readout plane could drift back into the TPC volume.

(*i*) Primary ion build-up in the drift volume. An irreducible positive-ion density due to the primary ionisation collected during about 1s (the time it takes for an ion to drift the full length of the TPC) will be present in the drift volume. The positive-ion density will be higher near the cathode, where the local volume integrates over backgrounds from up-to-five bunch trains, and using Fig. 4.3-4(middle)[1], the charge will reach ∼1 fC/cm^3 at the inner fieldcage and ∼0.02 fC/cm^3 at the outer fieldcage. The effect of the charge density will be established by the R&D program, but the experience of the STAR TPC [93] indicates that 100 fC/cm^3 is tolerable[83] and is two orders of magnitude larger than expected for the LCTPC.

(*ii*) Ion build-up at the readout plane. At the surface of the gas-amplification plane during an ILC bunch train of about 3000 bunch crossings spanning 1 ms, there will be few-mm sheet layer of positive ions built up due to the gas amplification of the incoming charge followed by ion backflow. An important property of MPGDs is that they suppress naturally the backflow of ions produced in the amplification stage; studies show that this backflow can be reduced to about 0.25% [83]. Using the results from Fig. 4.3-4 (middle), this layer of readout-plane ions will attain a density of $\mathcal{O}(80)$ fC/cm^3 at the inner radius and $\mathcal{O}(2)$ fC/cm^3 at the outer radius of the TPC. Its effect will be simulated, but it should affect coordinate measurement only by a small amount since the incoming drift electrons experience this environment during only the last few mm of drift. The TPC must plan to run with the lowest possible gas gain, meaning of order $\sim 2 \times 10^3$ or less, in order to minimize this effect.

[1]The numbers in the text derived from this figure have been multiplied by a safety factor of two to account for other sources of backgrounds.

(*iii*) Ion backdrift and gating. The ion buildup described in (*ii*) will drift as an "ion sheet" back through the TPC volume unless eliminated by a gating plane. In the drift volume, an ion sheet would be followed by sufficient drift distance to result in track distortions. Thus an intra-train gate is foreseen to guarantee a stable and robust chamber operation. The ILC bunch train structure requires an open-gate operation, without intra-train gating between bunch crossings, to optimally utilize the delivered luminosity. The gate will remain open throughout one full train and be closed between bunch trains. As the ion drift velocity is much less than that of the electrons, the gate timing allows collection of all of the ions. The added amount of material for a gating plane will be small (e.g., $< 0.5\%X_0$ was the average thickness for the Aleph TPC gate).

(C) Chamber gas
The choice of the gas for the LCTPC is crucial for efficient and stable operation at the linear collider[81]. The σ_{point} resolution achievable in $r\phi$ is dominated by the transverse diffusion, which should be as small as possible; this implies that $\omega\tau$ for the gas should be large so that the transverse diffusion is compressed by the B-field. Large $\omega\tau$ means that the drifting electrons follow the B-field, for which there is a program to measure well[95], and has the added advantage of making the chamber less sensitive to space-charge effects and other sources of electric field non-uniformities. Simultaneously a sufficient number of ionisation electrons should be created for the position and dE/dx measurements. The drift velocity at a drift field of at most a few times 100 V/cm should be around 5–10 cm/μs to limit the central cathode voltage and the event overlap. The choice of operating voltage must also take into account the stability of the drift velocity due to fluctuations in temperature and pressure.

4.3.2.7 Alignment

Achieving a momentum resolution an order of magnitude better than any of the collider detectors to date will be a challenge. The systematics of alignment of tracking subdetectors must be well thought through from the beginning to guarantee the integrity of tracking over a radius of two meters. Redundant tools for solving this issue are Z-peak running, the laser system, the B-field map as described in [95] and monitored by a matrix of Hall-plates/NMR-probes outside the TPC, and Si-layers inside the inner fieldcage and outside the outer fieldcage. In general based on experience at LEP[96], about 10 pb^{-1} of data at the Z peak are requested during commissioning for the alignment of the different subdetectors, and typically 1 pb^{-1} during the year may be needed depending on the backgound and operation of the linear collider machine (e.g., after push-pull or beam loss).

The strategy learned at LEP for aligning the tracking subdetectors is also applicable for the ILD. Needed to start with are: a common alignment software package for all subdetectors, the fabrication tolerances for each subdetector $\simeq$ 10–20μm internal and $\simeq$ 0.1–0.2mm external (with respect to the other subdetectors) and the B-field mapped to the requirements outlined in [95]. Then the steps are: first pass through a subset of data (hadronic tracks or μ pairs from Z-peak or from $\sqrt{s}$ running), each tracking detector is aligned internally; second pass, the tracking subdetectors are lined up with respect to one another using a subset of data; finally the preceeding two steps are iterated until the correct momentum for $Z \to \mu\mu$ events

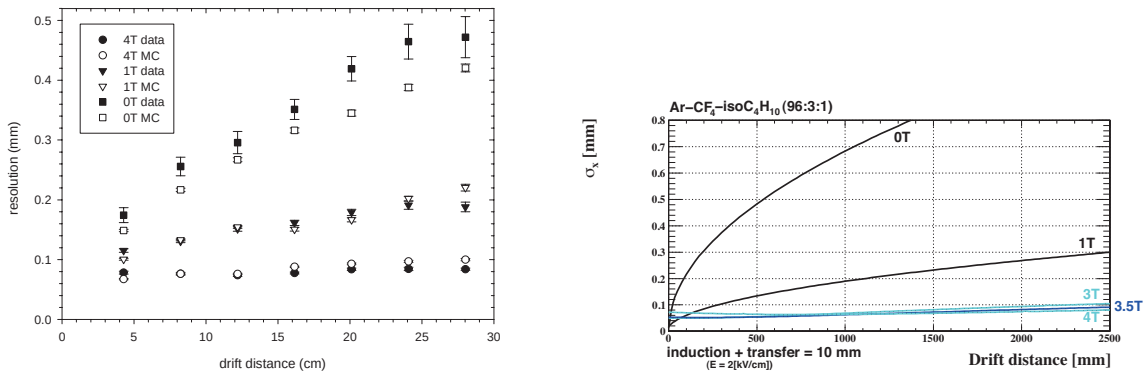

FIGURE 4.3-5. (left): Example of resolution results from a small prototype [97] measurements with TDR gas, $ArCH_4CO_2$ (95-3-2); other candidate gases are e.g. P5 and $ArCF_4$Isobutane. (Right): Theoretical resolution for $ArCF_4$Isobutane (96-3-1) gas (right), based on an algorithm [84] verified during SP studies.

is achieved.

4.3.3 R&D Effort for the LCTPC

All of the issues affecting the TPC performance are being addressed by the R&D program; a recent status report with extensive references to past and on-going work is contained in [84]. As described in the LCTPC-Collaboration MoA, the R&D is proceeding in three phases: (1) Small Prototypes (SP), (2) Large Prototypes (LP), and (3) Design.

Up to now during Phase(1), about 6 years of MPGD experience has been gathered, gas properties have been well measured, the best achievable point resolution is understood, the resistive-anode charge-dispersion technique has been demonstrated, CMOS pixel RO technology has been demonstrated, the proof of principle of TDC-based electronics has been shown and commissioning has started for the LP.

The Phase(2) LP and SP work is expected to take another two–three years. Regular bi-weekly WP phone meetings started in May 2006 where details for the LP design were worked out and next R&D steps developed. The LP commissioning is well advanced as evidenced by Fig. 4.3-5(left), while the fruits of the SP work resulting in the expected resolution are shown in Fig. 4.3-5(center) and Fig. 4.3-5(right).

The following list gives an overview of the currently envisioned timeline for completing the studies and the construction of the ILD TPC.

• 2009-12: Continue R&D on technologies at LP, SP, pursue simulations, verify performance goals (details are available in [84]).

• 2009-11: Plan and do R&D on advanced endcap; power-pulsing, electronics and mechanics are critical issues.

• 2011-12: Test advanced-endcap prototype at high energy and power-pulsing in high B-field.

• 2012-18: Design and build the LCTPC.

Construction of endplates that satisfy the material requirements of the ILD, as well as the structural requirements of the TPC, will require extensive R&D.

This work has started with first ideas having been developed in a series of “advanced-endcap” meetings during the past year. Examples are presented in Fig. 4.3-6, and the groups agree that there will be an evolution of endcaps towards a true prototype for the LCTPC.

During the R&D period 2009-2011, engineering studies of detailed computer models of advanced endplate designs will be performed. The models will be evaluated relative to the requirements of material limits and distribution, space limits, rigidity in response to applied

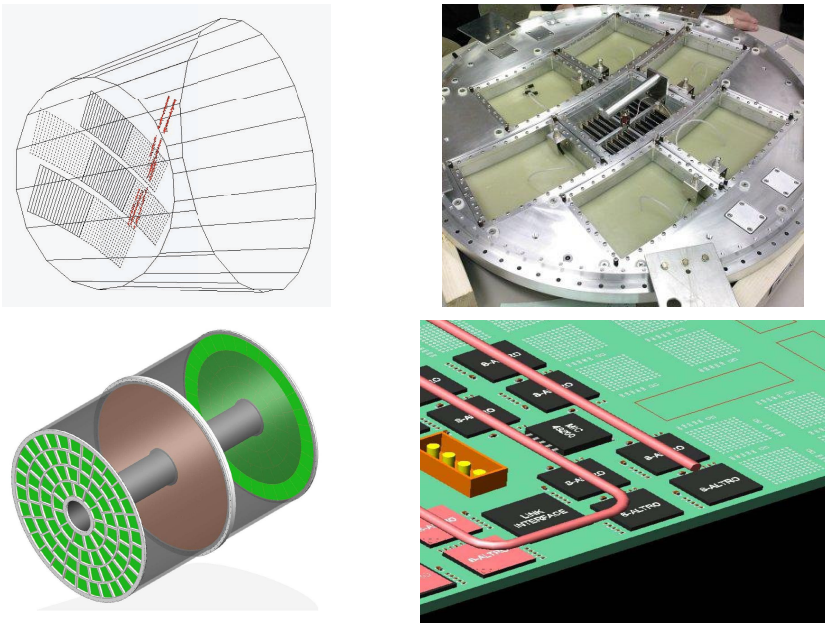

FIGURE 4.3-6. (Top left): Event display from the LP beam tests. (Top right) View of the Endcap subdivision as used for the Large Prototype. (Bottom left)Conceptual design of enplate for LCTPC. (Bottom right) Possible layout of PCB, electronics and cooling for the LCTPC.

forces, manufacturing complexity and manufacturing precision. Possible endcap designs fall into two general groups. The first group is the evolution of a traditional machined endplate, as used in the first endcap of the LP, Fig. 4.3-6 (left), but with significant use of lighter materials; in addition, unnecessary material must be removed from the machined structure. The second group is the simulation of true space-frame designs which can be constructed utilizing various techniques, e.g., fully machined, bonded composites and assembly of individual components.

During the period 2011-2012, further study of designs that were successful as computer models will follow. Several prototypes of the advanced endplate will be manufactured; both scale-models (20-50% full size) and sections of the full size endplate will be used to evaluate the manufacturing integrity and uncover sources of loss of precision or rigidity in the design. Finite element analysis will be used to predict the strength of the full size endplate; this analysis will be calibrated by comparison with measurements on the prototypes.

At the beginning of the period 2012-18, the selection must be made from the different technological options – GEM, MicroMegas, resistive anode, pixel, electronics, endcap structure – to establish a working model for the design of the LCTPC. This design will be used for the ILD proposal in 2012 and include pad segmentation, electronics, mechanics, cooling and integration, so that performance, timeline and cost can be estimated reliably.

For the technology selection, a scenario could be that questions must be answered as to which options give the best performance based on R&D results from LP, SP, electronics and endcap studies. Main performance criteria could be endcap thickness and σ_{point}, double-hit and momentum resolution for single tracks and for tracks in a jet environment. Choice of criteria to use will be decided over the next two years.

Finally, as to the $\sqrt{s}$ coverage, simulations in Chapter 2 of this LOI have shown that, with the performance goals in Table 4.3-5, the LCTPC will give good performance up to and well beyond 1 TeV.

4.4 THE CALORIMETER SYSTEM

4.4.1 Introduction to calorimeters

Tagging of electroweak gauge bosons at the ILC, based on di-jet mass reconstruction, makes the reconstruction of multijet events a major goal for detectors at the ILC. The particle flow approach (see e.g. [98]), which consists of individual particle reconstruction dictates many fundamental aspects of the calorimeter design, most notably the requirement for very fine transverse and longitudinal segmentation of the calorimeters, as studied in Section 2.2. It has to be noted that a highly granular calorimeter, optimised for PFA, leads also to a way to have a very efficient software compensation, as it is shown in 4.4.4.2. The choice of technology for the ECAL and HCAL are driven by the requirements of pattern recognition more than the intrinsic single particle energy resolution, although the latter is still an important consideration.

Several technologies for electromagnetic and hadronic calorimeters are being pursued, with a number of prototypes in test beams. Next generation prototypes are being constructed with dimensions and integration issues very close to those of final ILD detector modules. The research and development work is carried out in the context of the CALICE collaboration [99].

4.4.2 General Layout

The calorimeter system is divided in depth into an electromagnetic section, optimised for the measurement of photons and electrons, and a hadronic section dealing with the bulk of hadronic showers. The two parts are installed within the coil to minimise the inactive material in front of the calorimeters. To follow the symmetry imposed by the beams and the coil, the calorimeter is divided into a cylindrical barrel and two end-caps.

The electromagnetic calorimeter consists of tungsten absorber plates interleaved with layers of Silicon (pads or pixels), or Scintillator detectors with very fine segmentation of the readout. The hadronic calorimeter is planned as a sampling calorimeter with steel absorber plates and fine grained readout. Two options are currently proposed. The first uses scintillator cells with fine granularity and multi-bit (analogue) readout. The second is based on gaseous detectors and uses even finer granularity. Due to the large number of cells, in the second case one- or two-bit (semi-digital) readout is sufficient.

4.4.3 The Electromagnetic Calorimeter

For the electromagnetic calorimeter the requirements on granularity, compactness and particle separation lead to the choice of a sampling calorimeter with tungsten (radiation length $X_0 = 3.5\,\mathrm{mm}$, Molière Radius $R_M = 9\,\mathrm{mm}$ and interaction length $\lambda_I = 99\,\mathrm{mm}$) as absorber material. This allows for a compact design with a depth of roughly $24\,X_0$ within 20 cm and, compared to e.g. lead, a better separation of EM showers generated by near-by particles.

To achieve an adequate energy resolution, the ECAL is longitudinally segmented into around 30 layers, possibly with varying tungsten thicknesses. The active layers (either silicon diodes or scintillator) are segmented into cells with a lateral size of $5 - 10\,\mathrm{mm}$ to reach the required pattern recognition performance.

4.4.3.1 Geometry and Mechanical Design

One of the requirements for the calorimeter is to ensure the best possible hermeticity. Three regions are of particular concern for this question: the boundaries between mechanical modules, the overlap between barrel and end-cap, and the small angle region with the connection to the luminosity monitor. To minimise the number and effect of cracks in the barrel, a design with large modules is preferred, with inter-module boundaries not pointing back to the IP. The cylindrical symmetry of the coil has been approximated by an eight-fold symmetry and the modules are designed in a such a way (c.f. fig. 4.4-7 that the cracks are at very large angle with respect to the radial direction. This octagonal shape optimises the barrel module sizes and their mechanical properties without diverging too far from a circle. One eighth of the barrel calorimeter is called a stave. Each stave is fastened to the HCAL front face with a precise system of rails. Some space is left between the ECAL and the HCAL to accommodate different services such as cooling, electrical power and signal distribution. Along the beam axis, a stave is subdivided into five modules. The ECAL end-caps are attached to the front face of the hadronic end cap calorimeters using a similar rail system.

A detailed mechanical design of the modules has been prepared, and is tested under real conditions in several test beam experiments. More details can be found in [100].

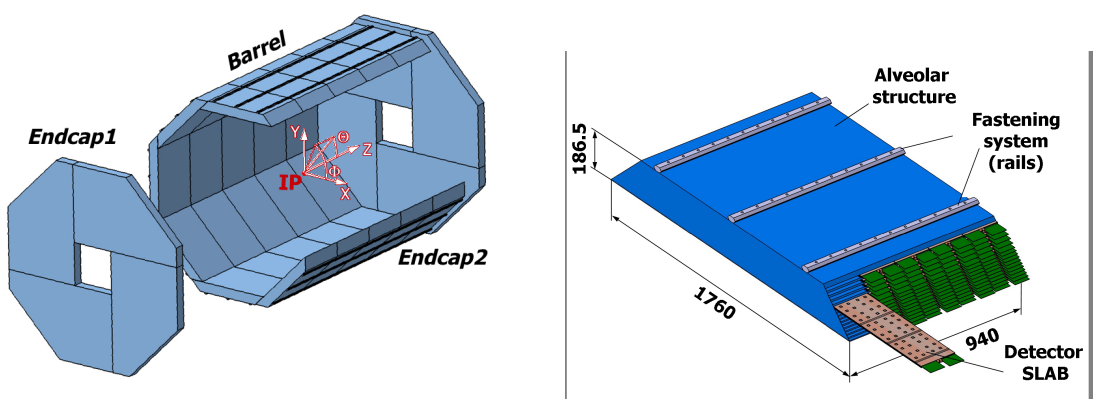

FIGURE 4.4-7. Global layout of the ECAL (left) and layout of one module (right).

4.4.3.2 Optimisation

For the final detector, a global optimisation study of the longitudinal profile has to be performed, by varying the thickness of the Silicon and Tungsten layers as a function of the depth, in order to minimise cost, lateral spread and energy resolution.

The dependence of the ECAL energy resolution as a function of the longitudinal sampling scheme has been studied in simulation [101]. For a given number of sampling layers, the energy resolution improves if the first part of the calorimeter is more finely segmented than the latter part. The effect of the silicon cell size on ECAL performance has been studied in simulation, focusing on the photon reconstruction capability in di-jet events and hadronic τ decays. Three different cell-sizes ($5 \times 5\,\mathrm{mm}^2$, $10 \times 10\,\mathrm{mm}^2$ and $20 \times 20\,\mathrm{mm}^2$) have been investigated. In both cases a specialised photon reconstruction algorithm (GARLIC [102]) has been applied. The algorithm was separately tuned for each cell-size.

Figure 4.4-8 shows the mean ratio of calorimetric energy reconstructed as photons to the true photon energy, in simulated di-jet events at $E_{\mathrm{CM}} = 400\,\mathrm{GeV}$ for a variety of cell sizes. A

	$5 \times 5\,\mathrm{mm}^2$			$10 \times 10\,\mathrm{mm}^2$			$20 \times 20\,\mathrm{mm}^2$		
	π_{sim}	ρ_{sim}	$a1_{\mathrm{sim}}$	π_{sim}	ρ_{sim}	$a1_{\mathrm{sim}}$	π_{sim}	ρ_{sim}	$a1_{\mathrm{sim}}$
π_{rec}	98.8	2.8	1.9	98.7	5.9	1.6	98.6	27.1	7.0
ρ_{rec}	1.2	96.5	9.2	1.3	93.4	15.0	1.4	72.3	54.4
$a1_{\mathrm{rec}}$	0	0.7	88.9	0	0.7	83.4	0	0.6	38.6

TABLE 4.4-6
Reconstruction efficiencies and purities of hadronic τ decays in $ZH \rightarrow \mu\mu\tau\tau$ events with various ECAL cell-sizes

cell-size of $5 \times 5\,\mathrm{mm}^2$ is clearly to reconstruct the correct fraction of photon energy inside jets. The interpretation of these result, which is based on a dedicated photon finding algorithm, requires care. It can not be applied directly to full particle flow reconstruction, which in general shows a weaker dependence.

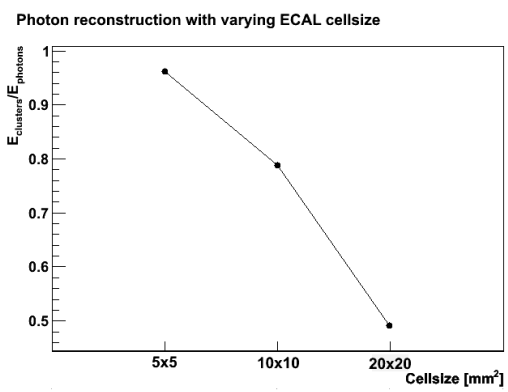

FIGURE 4.4-8. Fraction of energy identified as photon induced to true photon energy (Monte Carlo truth) in di-jet events at $E_{\mathrm{CM}} = 400\,\mathrm{GeV}$.

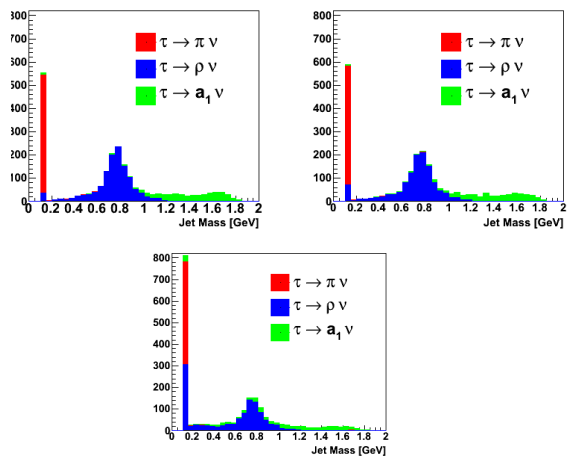

FIGURE 4.4-9.]
Reconstructed invariant mass of hadronic τ decay products in ZH $\rightarrow \mu\mu\tau\tau$ events for different ECAL cell sizes (starting at top left: $5 \times 5\mathrm{mm}^2$, $10 \times 10\mathrm{mm}^2$, and $20 \times 20\mathrm{mm}^2$.

Studies of τ reconstruction have been performed in ZH (H $\rightarrow \tau\tau$) events at $E_{\mathrm{CM}} = 230\,\mathrm{GeV}$ with $m_{\mathrm{H}} = 120\,\mathrm{GeV}$. The three decay modes $\tau \rightarrow \nu\pi$, $\tau \rightarrow \nu\rho$ and $\tau \rightarrow \nu a_1$ have been considered. The reconstructed invariant mass of the visible τ decay products is shown in Fig. 4.4-9 for the three different cell sizes. A simple selection based on particle flow (reconstructed photons) and jet mass (cut at 200 MeV) allows one to reach good efficiency and purity, without the need for the more sophisticated analysis. The efficiencies and purities of the reconstruction of the various decay channels are given in Table 4.4-6. Again a cell size of $5 \times 5\,\mathrm{mm}^2$ is favoured although the performance loss with respect to $10 \times 10\,\mathrm{mm}^2$ cells is smaller than in high-energy jets.

To study the effect of material in front of the ECAL on the particle flow performance, 4 GeV single charged pion events have been simulated. The π^0's produced in interactions

in the tracker region may give rise to additional reconstructed photons in the ECAL. The GARLIC photon identification algorithm [102] has been applied to the single pion events. For the approximately six percent of pions which interact in the tracking volume, Fig. 4.4-10 shows the position of the pion interaction point inside the detector for events in which photon clusters are (red points, 55%) or are not (black points, 45%) found. The TPC end-plates and gas give the largest contribution to the total number of pion interactions in front of the ECAL. When only those interactions which give rise to identified photon clusters are considered, the detector components at the centre of the detector, that is, the vertex detector, SIT, beam tube and FTD support, also give significant contributions. Even though ILD has been designed with with minimum material in the tracker in mind, there is still about one pion per event which interacts in the tracker volume. This underlines the need for continued R&D and continued care toward further material reduction in the tracker.

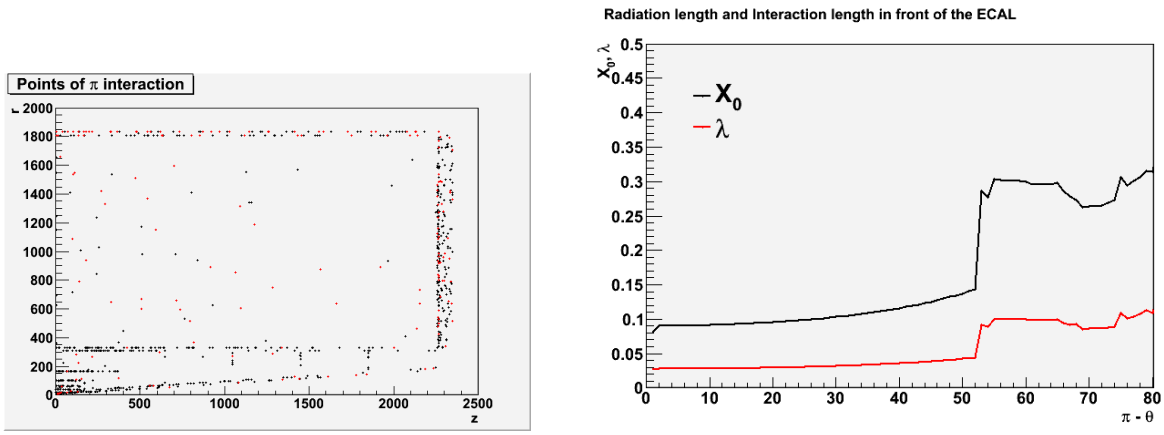

FIGURE 4.4-10. Left: Interactions points of single photons in the tracker region of ILD. The black points correspond to interactions that lead to the creation of clusters in the calorimeter found with the GARLIC photon reconstruction while the red points correspond to interactions that did not create any clusters. Right: Number of radiation and interaction length in front of the ECAL as a function of the polar angle.

4.4.3.3 Silicon - Tungsten Electromagnetic Calorimeter

The general requirement about compactness (small Molière radius) has led to a sandwich calorimeter with a tungsten radiator and silicon for the sensitive medium. To reach an adequate energy resolution the first 12 radiation lengths are filled with 20 layers of $0.6\,X_0$ thick tungsten absorbers (2.1 mm), followed by another 11 radiation lengths made from 9 layers of tungsten $1.2\,X_0$ thick. The calorimeter starts with an active layer. For the chosen geometry the Molière radius is 19 mm. The choice of silicon technology for the readout layer permits a very high transverse granularity, now fixed at $5 \times 5\,\mathrm{mm}^2$.

The final calorimeter will contain around 10^8 readout cells in total. To keep the final system as compact as possible, and reduce dead areas, the very front end electronics will be embedded into the detector layers.

The challenging construction of the SiW ECAL is currently tested by a large scale R&D program pursued by the CALICE Collaboration. Results from test beam measurements demonstrating the feasibility to realise the detector have been published in [100, 103]. The energy resolution has been determined to be $(16.6 \pm 0.1)/\sqrt{E(\mathrm{GeV})} \oplus (1.1 \pm 0.1)\,\%$ with a MIP signal over noise ratio $S/N \approx 7.5$.

	% of total interactions	% with clusters	% of total events with clusters
VTX	11.9	64.5	13.9
SIT	11.8	68.7	14.6
Beam pipe	10.4	62.9	11.8
FTD	8.9	66.1	10.6
TPC inner field cage	5.4	63.8	6.2
TPC gas	17.1	23.0	7.1
TPC outer field cage	6.5	50.6	5.9
TPC endplate	22.3	61.4	24.8
SET	3.1	58.0	3.3
ETD	2.8	35.1	1.8

TABLE 4.4-7
Interaction of pions in the different parts of the tracker region.

At present, the CALICE collaboration is preparing the construction of a prototype module with a size and shape close to the modules envisaged for the final calorimeter.

The detector slabs are built around an H-shaped supporting structure incorporating a layer of tungsten absorber. An active layer is placed on each side of this structure. This active layer is a chain of identical Active Sensor Units (ASUs), which consist of a printed circuit board (PCB) integrating the Silicon sensors, Front-End electronics and electrical infrastructure. Each ASU can run as a standalone unit, allowing testing of each piece before, during and after slab assembly, resulting in a high detector yield, and thus a reduced cost.

Since the electronics are deeply embedded in the detector volume, and no space is available for active cooling, their power consumption must be kept to a minimum to prevent overheating. By power-pulsing the electronics according to the duty-cycle of the ILC machine, the consumption can be kept below $25\,\mu\mathrm{W}$ per channel.

The sensors are based on high resistivity silicon ($5\,\mathrm{k}\Omega/\mathrm{cm}$) with individual pin-diodes of $5 \times 5\mathrm{mm}^2$ size. This size is also feasible for the readout electronics. A test batch of sensors based on 6" wafers has been used by Hamamatsu to produce $9 \times 9\,\mathrm{cm}^2$ matrices. The bonding of the sensors onto the PCB is performed using a well controlled gluing technique.

The silicon sensors are built and integrated using well known, widely used and well controlled technologies. The matrix of PIN diodes is burned onto 330 μm thick raw silicon wafers using standard manufacturing processes from the microelectronics industry such as acceptor/donator ion implantation, oxide growth or metal deposit. The bonding of the sensors onto the PCB is performed using a well controlled gluing technique: standard glue (EPOTEK 410) applied by a robotic gluing machine. Prototypes of sensors have been ordered to various companies and academic centres with two different sizes of PIN diodes. No problems due to the gluing technique have been observed over a time span of several years.

The total surface of sensors for the whole ECAL is about $2500\,\mathrm{m}^2$. The sensors and their integration are kept as simple as possible to avoid any dependence on a proprietary technique owned by a single manufacturer; allowing for a variety of suppliers and manufacturers to share the production will decrease the inherent financial risks and enable a competitive downscaling of the costs.

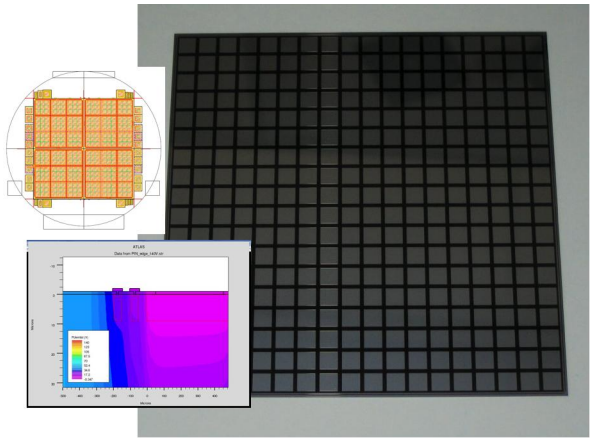

FIGURE 4.4-11. $5 \times 5\,\mathrm{mm}^2$ pad Hamamatsu sensor (right). Layout of prototype sensors with optimised edges (upper left). In depth simulation of the potential near a guard ring (lower left).

4.4.3.3.1 Calibration The charge produced by a MIP in the silicon depends only on the silicon thickness, and is therefore expected to be stable with time. A single calibration before detector assembly will therefore be sufficient. The ASUs will be calibrated in a muon beam before the assembly of detector slabs and their integration into detector modules.

The VFE electronics will be calibrated by means of the VFE chips' charge injection calibration system.

Since the tracks of muons and non-interacting charged pions in the ECAL can easily be identified due to the ECAL's high granularity, they can be used to monitor the calibration during the lifetime of the detector.

4.4.3.4 Scintillator - Tungsten Electromagnetic Calorimeter

The scintillator-tungsten sandwich ECAL (ScECAL) is proposed to realise a fine-segmented calorimetry in a stable, robust and cost effective way. The fine grained readout is realised by planes of 1 cm wide and 4.5 cm long strips, arranged in orthogonally in adjacent layers. Thanks to the strip structure, the number of necessary readout channels is significantly reduced ($\sim 10^7$ channels) relative to the Si-W option. Scintillator strips can be cheaply produced by the extrusion method. Compact photo-sensors (MPPC) and highly integrated readout electronics make dead area in the ScECAL almost negligible. Keeping the required granularity and these merits, the ScECAL has good energy resolution and linearity.

The ScECAL consists of 24 super-layers. A schematic view of a few super-layers of the ScECAL is shown in Figure 4.4-12. They will be mounted in an alveolar structure similar to the case of the SiW ECAL. A super-layer is made of a tungsten plate (3 mm thick), scintillator strips (2 mm thick), and a readout/service layer (2 mm thick). Scintillator strips in adjacent super-layers are arranged to be orthogonal aiming for better effective granularity. The thickness of a super-layer is 7 mm. The total ScECAL thickness is 172 mm, or $20.6\,\mathrm{X}_0$ in radiation length.

4.4.3.4.1 The active layers The dimension of an individual scintillator strip (see Fig. 4.4-12) is $1 \times 4.5 \times 0.2\,\mathrm{cm}^3$. Although a strip width of 5 mm, to realise an effective granularity of $5 \times 5\,\mathrm{mm}^2$, is thought to be feasible, further R&D is necessary. Each strip is covered by a mirror reflector film to improve collection efficiency and uniformity of the scintillation light. Photons from each scintillator strip are read out via an 1 mm diameter wavelength shift-

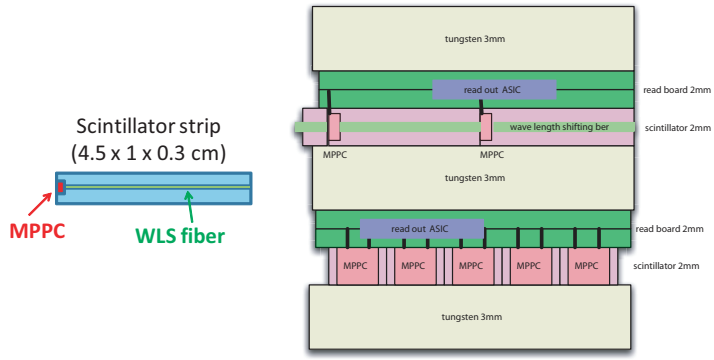

FIGURE 4.4-12. Dimension of the scintillator-strip (left, view from top) and side view of the ScECAL layer structure (right).

ing fibre (WLSF) embedded in a straight groove by a very compact photon sensor, MPPC, attached at the end of the strip.

The MPPC is a version of a novel semiconductor photo-sensors consisting of a matrix of micro APD pixels operated in Geiger mode. Photo-detection performance and amplification power is comparable with conventional photomultiplier tubes. The dynamic range of an MPPC is limited by the number of APD pixels. A MPPC with 1600 APD pixels in an area of $1\,\mathrm{mm}^2$ is already commercially available. However MPPC with ~ 3000 pixels should be developed to precisely measure up to $\sim 100\,\mathrm{GeV}$ electromagnetic clusters.

Signals from about 80 MPPC are fed into a readout chip through micro-strip lines. They are arranged on one identical flexible readout board (FPC) (c.f. Fig. 4.4-13). After shaping, digitisation and zero-suppression of the analog signals on the chip, signals are taken out serially from the detector and brought to a digitisation board by a thin FPC cable ($\sim 200\,\mu\mathrm{m}$) through detector gap.

4.4.3.4.2 Calibration systems A light distribution system has been designed to monitor possible gain drifts of MPPCs by monitoring photo-electron peaks. The system consists of a pulse generator, a chip LED, and a notched fibre. A schematic structure of the system is shown in Figure 4.4-14. The pulse generator circuit and the chip LED are arranged on a thin ($\sim 200\,\mu\mathrm{m}$) FPC board. The chip LED is directly connected to the notched fibre to distribute lights to ~ 80 strips through its notches.

Each scintillator strip can be calibrated with data by monitoring the MIP peak using multi-hadron events at the ILC. Monte Carlo simulation shows that more than 100 MIP hits per strip will be obtained if running at the Z^0. With this method the strips can be calibrated to better than $5\,\%$ with $1\,\mathrm{fb}^{-1}$ of $\mathrm{Z}^0 \to jj$ events).

4.4.3.4.3 Status and Future R&D plans The feasibility of the ScECAL has been proven by a test of a small prototype using $1-32\,\mathrm{GeV}$ electron beams. At the test clean MIP signal and electron energy spectra are observed with negligible contamination from electrical noise. The energy resolution is measured to be $\sigma_E/E = 14/\sqrt{E} \oplus 2\,\%$ which is consistent with expectation from simulation.

In order to fully establish the feasibility of the ScECAL, further extensive R&D efforts are necessary to clarify the remaining technical issues as follows:

- Photon sensors: properties of the MPPC have to be further studied and improved. The

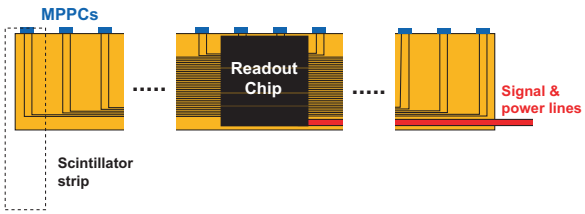

FIGURE 4.4-13. Layout of the MPPC, micro-strip line and readout chip on the FPC board.

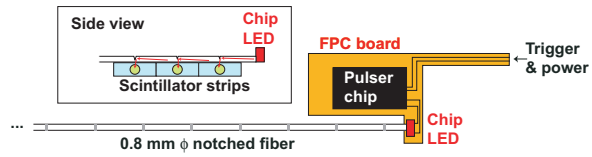

FIGURE 4.4-14. Schematics of the MPPC gain monitoring system with LED and notched fibre. Light pulses from the LED are scattered and distributed into each strip.

increase of the dynamic range is especially important.

- Development of readout electronics: A highly integrated readout chip is needed due to the limited space in the detector.
- Strip clustering: The strip structure is chosen in order to improve the effective granularity of the calorimeter. A clustering algorithm has been developed which can cope with the strip structure as well as the usual square-tile structure. The algorithm is being further improved, and performance of the strip structure must be demonstrated.

4.4.3.5 Digital (MAPS) Silicon-Tungsten Electromagnetic Calorimeter

The silicon-tungsten digital ECAL (DECAL) is an alternative to the analogue silicon design described in Section 4.4.3.3. The basic principle is to replace the high resistivity pad diodes with CMOS based binary readout pixels sufficiently small in size that, even in the core of high energy electromagnetic showers where the density is typically equivalent to $\sim 100\,\mathrm{MIPs/mm^2}$, the probability of a pixel being hit by more than a single particle will be low. This allows the shower energy to be measured by the number of binary pixels above threshold. To ensure that linearity of response is preserved even at higher energies, pixels are required to be $O(50 \times 50\,\mu\mathrm{m}^2)$, leading to $O(10^{12})$ pixels in the complete ECAL. A very high level of integration of the readout in the pixel is therefore mandatory.

The active layers are based on CMOS Monolithic Active Pixel Sensors (MAPS) which allow data reduction and processing logic to be contained within each pixel. The target noise level is 10^{-6}. A new process ("INMAPS" [104], developed by the CALICE UK groups) ensures efficient charge collection by using deep p-wells and charge collection by diffusion in the sensor. Signals (time stamp and pixel address) are stored on the sensor during a bunch train and read out in the interval between bunch trains. By using industry standard CMOS processes available from a large number of foundries, costs are potentially lower per unit area than analogue silicon diodes, with reduced risk to production schedules.

The performance of the DECAL has been studied using Mokka in the context of LDC [105, 106, 107], including effects of dead area, digitisation and clustering. A preliminary study of the energy resolution of the DECAL to single photons, implemented by adapting only the ECAL sensitive region in the ILD00 silicon-tungsten model in Mokka, gives $\sigma_E/E = 19.7\,\%/\sqrt{E}$. A first prototype sensor (TPAC1.0) was designed in 0.18 µm process, having 28224 ($50\times50\,\mu\mathrm{m}^2$) pixels [104]. This $9 \times 9\,\mathrm{mm}^2$ sensor was fabricated and characterised, e.g. [108, 109, 110] during 2007–8. A second revision of the sensor is expected for 2009. A proof-of-principle R&D project is in progress to develop and test a 16 layer DECAL prototype large enough to contain electromagnetic showers [111] by 2012.

The DECAL option is designed to work with the same mechanical structure as the Si-W ECAL, thus profiting from the large R&D done in this area. A topic for future R&D is the reduction and control of the power consumption, which at the moment is expected to be larger though uniformly distributed across the sensor unlike the analogue SiW sensor.

4.4.4 The Hadronic Calorimeter

In a particle flow calorimeter the HCAL plays a crucial role in separating and measuring the energy deposits of charged and neutral hadrons. Since the energy deposited by neutral hadrons fluctuates widely, its precise measurement is a key component of a well performing particle flow calorimeter. Consequently, the imaging capabilities of the HCAL are of prime importance and demand high transverse and longitudinal segmentation and a design with a minimum of uninstrumented ("dead") regions. However, a very good hadronic energy resolution is also mandatory, both to assist the topological assignment of clusters and tracks, and to optimise the precision of the hadronic energy part characterised as neutral. The high granularity allows the application of weighting techniques to compensate for differences between hadronic and electromagnetic response and for "invisible" energy depositions ("software compensation") and improves the hadronic energy resolution further.

4.4.4.1 Geometry and Mechanical Design

The HCAL is conceived as a sampling calorimeter with steel as absorber and scintillator tiles (analogue HCAL) or gaseous devices (digital HCAL) as active medium. As the HCAL must be located within the coil, the absorber has to be non-magnetic. Stainless Steel has been chosen both for mechanical and calorimetric reasons. Due to its rigidity, a self-supporting structure without auxiliary supports (and thus dead regions) can be realised. Moreover, in contrast to heavier materials, iron with its moderate ratio of hadronic interaction length ($\lambda_{\mathrm{I}} = 17\,\mathrm{cm}$) to electromagnetic radiation length ($\mathrm{X}_0 = 1.8\,\mathrm{cm}$) allows a fine longitudinal sampling in terms of X_0 with a reasonable number of layers in a given total hadronic absorption length, thus keeping the detector volume and readout channel count small. This fine sampling is beneficial both for the measurement of the sizable electromagnetic energy part in hadronic showers as for the topological resolution of shower substructure, needed for particle separation and weighting.

4.4.4.1.1 Overall architecture The overall structure follows the "short barrel" concept, with two large endcaps with about the same outer radius as the barrel. The total hadronic absorption length corresponds to a minimum of $5.5\,\lambda_{\mathrm{I}}$ in addition to the ECAL. The endcaps are subdivided into four quadrants, their absorber plates are oriented perpendicular to the beam line. The mechanical engineering of the absorber structure has so far concentrated on the barrel. It is assumed that the solutions can be transferred to the endcaps later-on. Compared with existing hadron calorimeters, the ILD HCAL has a rather fine longitudinal sampling, with a correspondingly high pressure on the thickness of the active layer gaps, but also on mechanical tolerances. This, together with the requirement of minimum dead zones represents a challenge to the large scale engineering which is presently being addressed with prototypes within the EUDET/CALICE framework.

For the barrel, two design approaches are being followed: one with long barrel modules, subdivided only once in z, and with electronics and service connections at the end faces, and a second, with 5 rings and interfaces situated at the outer barrel perimeter. The main

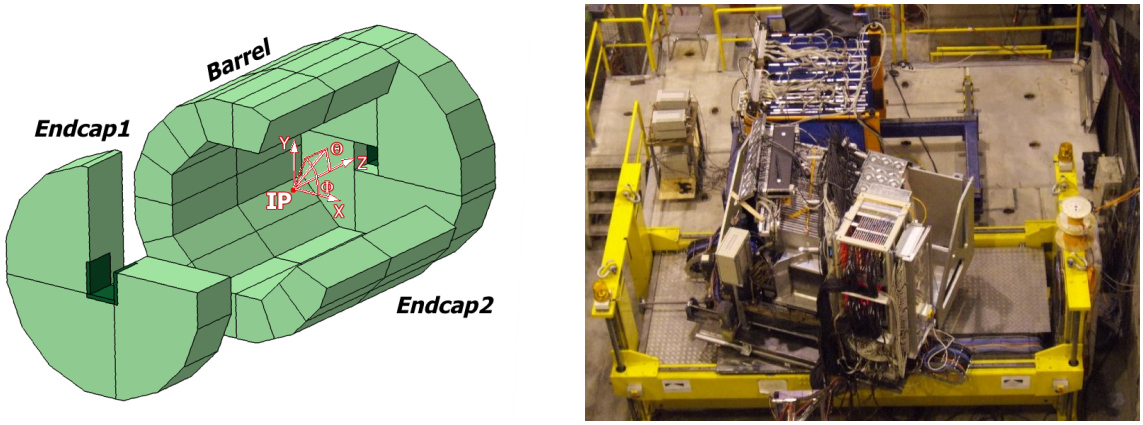

FIGURE 4.4-15. Layout 1 of the HCAL (left), and view of the integrated ECAL and HCAL beam test setup (right).

advantages of the first are the accessibility of the electronics and a maximum filling of the detector volume limited by the coil radius, whereas the second provides better rigidity in the transverse plane, eliminates pointing cracks and allows for a tighter barrel end-cap transition. In principle, each concept can be instrumented with both scintillator and gaseous devices. In practice, the detailed engineering is presently being worked out for scintillator in the first, and for gaseous readout in the second approach.

4.4.4.1.2 Design 1 In the first version of the HCAL design, the barrel is subdivided into two sections in z and eight octants in φ, each octant has two halves which constitute the basic modules, 32 in total. Each module has a weight of almost 20 tons, which is manageable with standard installation techniques. The modules are constructed independently of the active layers, which can be inserted before or after installation of the modules. There are 48 absorber plates, 16 mm thick each, held together by 3 mm thick side panels in the rz planes; no additional spacers are foreseen. The active layers will contribute 4 mm of steel to each absorption layer, and require 5.5 mm for instrumentation (3 mm thick scintillator plus readout and calibration devices). A drawing of the structure is shown in figure 4.4-15(left). The HCAL structure has been extensively simulated using finite element methods, including the integration of the heavy ECAL structure. Maximum deformations are found to be less than 3 mm, if the barrel structure is supported by two rails in the cryostat.

Presently the boundaries between modules are pointing in φ and in z. Variants with non-pointing boundaries have been validated in finite element calculations as well, but are disfavoured to ease the mechanical construction. The pointing geometry does not degrade the performance as long as the cracks are filled with absorber material, and if the active instrumentation extends up to the boundary within tolerances, which is the case in the present scintillator layer design.

4.4.4.1.3 Design 2 This design intends to reduce cracks both in φ and θ and to reduce the distance between the barrel and the endcaps. The barrel part is made of 5 independent and self supporting wheels along the beam axis which eliminates the θ=90 degree crack. The segmentation of each wheel in 8 identical modules is directly linked with the segmentation of the ECAL barrel. A module is made of 48 stainless steel absorber plates (welded with 2 transverse 10 mm stainless steel plates) with independent readout cassettes inserted between

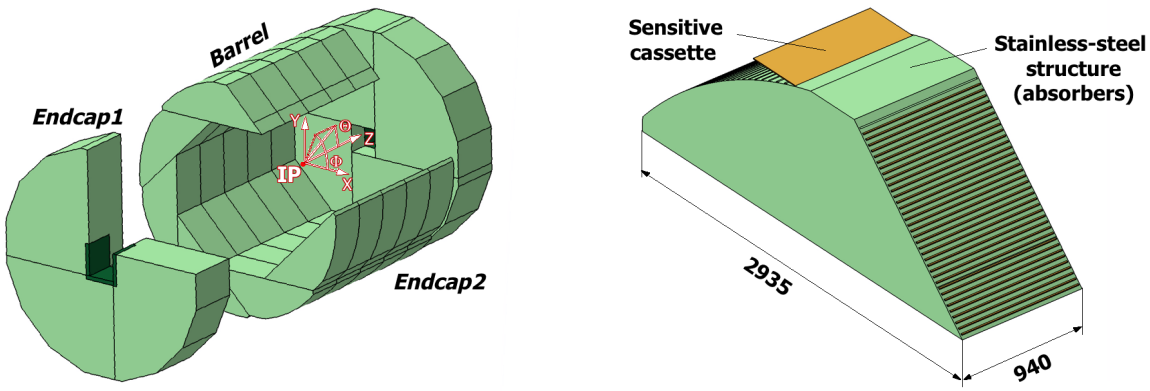

FIGURE 4.4-16. Design 2 layout of the HCAL (left) and layout of one module (right).

the plates. They define the rigid structure on to which the corresponding ECAL modules are mounted. A drawing of the structure is shown in figure 4.4-16(right). The absorber plates consist of a total of 20 mm stainless steel: 16 mm absorber from the welded structure and 4 mm from the mechanical support of the detector layer.

Each wheel is independently supported by two rails on the inner wall of the cryostat of the magnet coil. The cables as well the cooling pipes will be routed outside the HCAL in the space left between the outer side of the barrel HCAL and the inner side of the cryostat. The HCAL endcaps the same geometrical structure proposed in design 1. The distance between the barrel and the endcaps, which have the same structure as in design 1, is thus reduced, as only space to ensure inner detector cabling is required.

4.4.4.2 Analogue Hadronic Calorimeter

With the advent of novel, multi-pixel Geiger mode silicon photo-diodes, so-called SiPMs, high granularities as required for a particle flow detector can be realised with the well-established and robust scintillator technology at reasonable cost. The scintillator tiles provide both energy and position measurement and thus allow to trade amplitude versus spatial resolution. The transverse segmentation suggested by simulations is about $3\times3\,\mathrm{cm}^2$ and leads to a number of read-out channels an order of magnitude smaller than in the digital case with $1 \times 1\,\mathrm{cm}^2$ cells.

4.4.4.2.1 The Active Layers The arrangement of the active layers with internal and external electronics components is sketched in Figure 4.4-17. The layer consists, from bottom to top, of a 2 mm thick steel support plate covered with reflector foil, the scintillator tiles (3 mm), the printed circuit board with electronics components (2 mm), covered with reflector foil from underneath, and a polymide foil for insulation. The PCB carries the SPIROC readout ASICs (described in section 4.4.5.1)and auxiliary components as well as an LED based optical calibration system, whilst interfaces for data acquisition, clock and control, for power distribution and for calibration system steering are accessible at the end face. Since the ASICs are operated in power-pulsed mode, no cooling is needed inside the detector volume. The PCB is subdivided into units (HCAL base units, HBUs) of smaller size, manageable for automated mounting and soldering techniques. The standard unit is 12 by 12 tiles, $36 \times 36\,\mathrm{cm}^2$, so six units are aligned along z to fill a half barrel. In order to accommodate

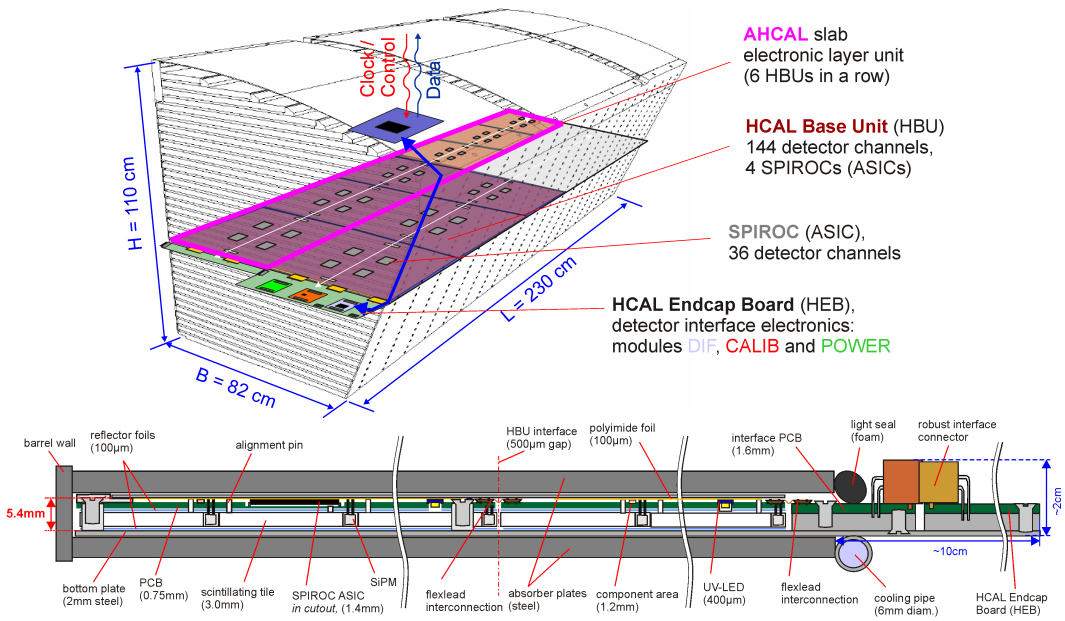

FIGURE 4.4-17. Arrangement of AHCAL layers with electronic components (top), cross section of an active layer (bottom).

the variation in layer width with increasing radius, 4 different HBUs, 8 to 12 tiles wide, are needed. At the layer edges, tiles with smaller size, e.g. $2 \times 3\,\mathrm{cm}^2$, are placed such that the uninstrumented region near the sector boundary is never larger than 5 mm and 2.5 mm on average.

The electronics at the end face will require cooling, mainly due to the use of FPGAs in the DIF (Detector InterFace board described in 4.4.5.2). The boards will extend 5 to 10 cm in z, but occupy only a fraction of the full width in φ, thus leaving space for ECAL and main tracker services as well as for the TPC support along radial directions. The required extra separation between barrel and endcap is therefore much smaller.

4.4.4.2.2 Scintillators and Photo-Sensors, R&D The successful operation of the 8000 channel CALICE HCAL test beam prototype over several years has proven that the new sensor and scintillator technology is robust and reliable. Less than one per-mil of the SiPMs showed signs of aging in form of increasing noise levels. In the meantime, progress was made by various manufacturers, e.g. in Russia or Japan, to provide sensors with lower dark count rate and / or smaller inter-pixel cross-talk which allow to decrease the noise occupancy above threshold of 10^{-3} in the present prototype by an order of magnitude and thus fulfill the requirements from both physics (for neutron hit identification) and DAQ band width. The demands on dynamic range are less critical than for the ECAL.

For the coupling of sensors to scintillator and PCB different approaches are being followed, based on either wavelength-shifting WLS fibre mediated or direct read-out with blue-sensitive photo-diodes. The WLS option was successfully operated in the HCAL (and ECAL) testbeam prototypes. The production, test and integration of sensors has been industrialised further, e.g. the grove for the fibre can be included in the injection moulding process (or the hole in the extrusion process). The positioning of the tiles must match the precision of the PCBs, for example with alignment pins. Alternatively, so-called mega-tiles (plastic modules comprising several cells, separated by groves) are also being discussed.

In the direct coupling case, the sensor is mounted in SMD style with its sensitive surface in the PCB plane, and collects the scintillation light directly from the tile. The tile has to be shaped in a dedicated way to compensate for the otherwise prohibitive light collection non-uniformities. Verification of both concepts in beam tests are important; besides uniformity also the stability of the light collection must be ensured.

Machine-related backgrounds are not a concern for the AHCAL. Simulations have shown that only in the innermost regions of the end-caps, the neutron fluence reaches levels which may degrade the visibility of single photo-electron signals for SiPM monitoring, but not the MIP detection capability. One may have to revert to alternative monitoring strategies here, or use more robust sensors which are under development.

4.4.4.2.3 Calibration The calibration procedure has to relate the electronic readout signal to the energy deposition in the cell. For the pre-amplifiers and discriminators, charge injection is used as in the ECAL or DHCAL case. The gain of the photo-diodes is monitored by means of an optical calibration system, and adjusted via the bias voltage, by observing the spacing between single photo-electron peaks in LED-induced pulse-height spectra. Using test bench measurements this cares also for sensor efficiency variations, correlated with the gain.

We follow two approaches for the technical realisation of the LED system, one based on a central driver located at the end faces of the modules and optical light distribution via fibres, and one with electrical signal distribution and surface-mounted LEDs for each tile. To check for long-term effects, track segments in hadronic showers can be used for a large fraction of the calorimeter volume. This has been shown with test beam data and simulated for ILD multi-jet events. Also systems based on radio-active sources might need to be considered.

4.4.4.2.4 Optimisation and Performance The main cost- and performance driving parameters of the AHCAL are the depth and the longitudinal and transverse segmentation. These parameters have been varied, and their current settings have been found, using detailed simulations and particle flow reconstruction as described in the overall detector optimisation section 2.2. The simulations include a modeling of inactive regions at module boundaries which is more conservative than the present engineering design.

The performance of a scintillator-tile HCAL with SiPM read-out and the proposed segmentation has been demonstrated with test beam data taken with the CALICE physics prototype. The detector showed very good imaging capabilities which reveal the substructure in hadronic showers, see Fig. 4.4-18.

Using test bench data and in-situ measurements, temperature induced variations and SiPM saturation effects could be corrected, and a linearity of better than 2 % for electron induced showers up to 50 GeV was achieved. The calorimeter is non-compensating, but the e/π ratio is not large and the observed linearity is also good for hadronic showers, see Fig. 4.4-19. A hadronic energy resolution of $61\,\%/\sqrt{E}$ is obtained on the electromagnetic scale, which can be reduced to $49\,\%/\sqrt{E}$, preserving linearity, with a simple weighting algorithm, which takes only the energy per tile, but not yet any shower substructure into account.

Based on experimental results from the CALICE prototype a reasonable agreement of the shower profiles with GEANT 4 based simulations has been found, as shown in figure 4.4-20. We found that it is essential to model details of the detector response, such as saturation effects in the scintillator according to Birks' law and the shaping time of the readout electronics, in order to reach this good agreement. These primarily affect the response to neutrons

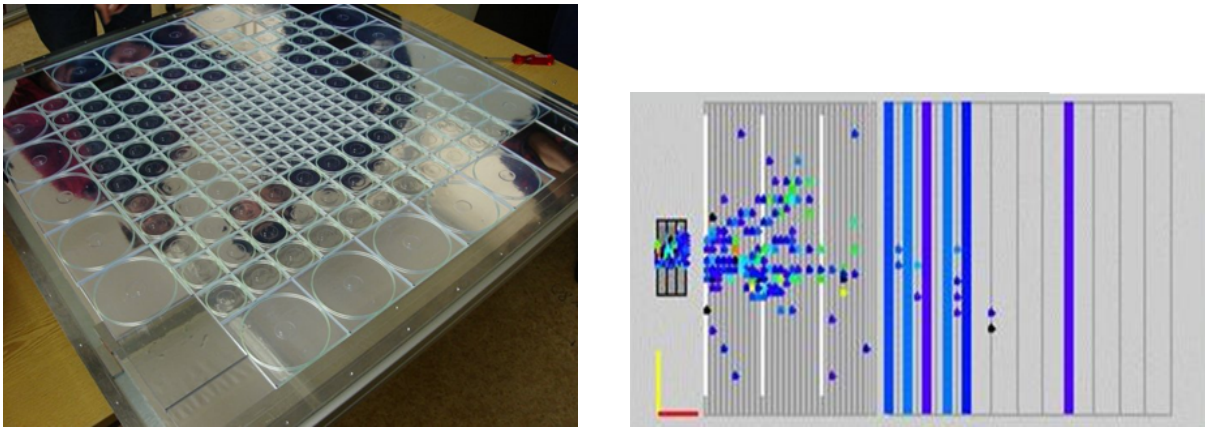

FIGURE 4.4-18. AHCAL physics prototype layer (left), event display (right).

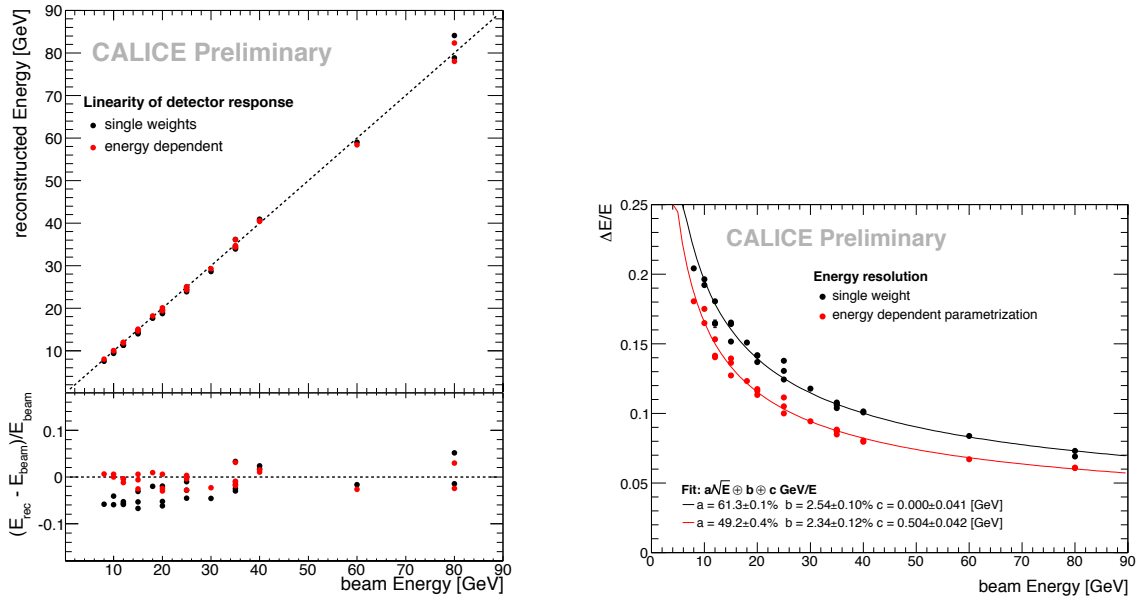

FIGURE 4.4-19. Linearity (left) and resolution (right), on electromagnetic scale and after weighting.

which would otherwise be overestimated.

4.4.4.3 Semi-Digital Hadronic Gas Calorimeter

The capacity to apply successfully the particle flow algorithms can be enhanced by increasing the granularity of the different ILD sub-detectors. In the hadronic calorimeter this will doubtlessly help reduce the confusion between charged and neutral hadronic particles by providing a better separation of the associated showers. However, the cost related to such an increase in detector segmentation should be minimised. To satisfy both, a gas hadronic calorimeter with a semi-digital readout is proposed. The study of such an HCAL has been going on for few years in order to validate this option.

The choice of gaseous detectors as the sensitive medium in the HCAL offers the possibility to have very fine segmentation while providing high detection efficiency. The glass resistive plate chamber (GRPC) is one of these detectors which can be built in large quantities at

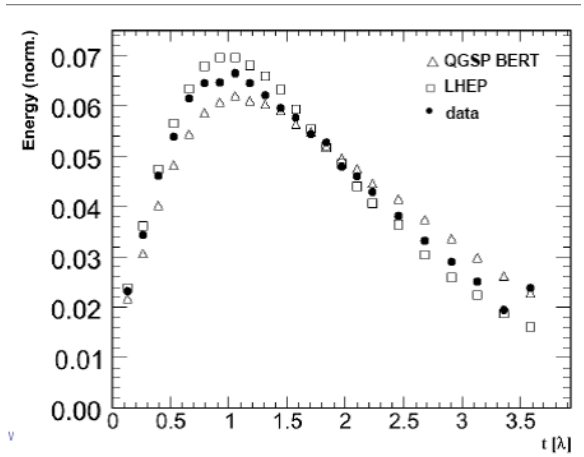

FIGURE 4.4-20. Longitudinal shower profile, test beam data and simulations.

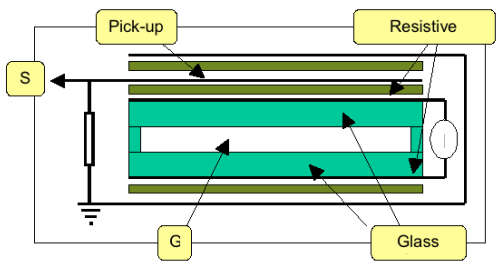

FIGURE 4.4-21. Single gap GRPC scheme

low cost. Large GRPCs as the ones required for the ILD HCAL can be easily produced. This is an important advantage with respect to other detectors since it guarantees very good homogeneity. Several experiments like BELLE have been using such large detectors with success for years. However, the GRPCs to be used in the ILD HCAL need to be more elaborate. As the HCAL is situated inside the magnet coil, the sensitive medium thickness is an important issue. Very thin GRPCs are requested and 3.3 mm thick GRPCs were indeed produced and successfully tested. In figure 4.4-21 a scheme of such a single gap GRPC is shown. Some key properties of these detectors are:

- GRPC operated in avalanche mode and have been shown to show no ageing for the accumulated charge expected over the ILC running period.
- Test beam performed at DESY have shown that a strong magnetic field has negligible effect on GRPC performance.
- GRPC detectors are insensitive to slow neutrons preventing thus an additional confusion.

Increasing the granularity will lead to a large number of channels. To limit the amount of data we propose a semi-digital readout solution. This simplifies the data treatment while minimising the consequences on the energy resolution performance. Indeed, based on several independent simulation studies, a two-bit readout would provide better energy resolution in the low-energy jet range (1–20 GeV) and a comparable one at higher energies when compared to an analogue readout [112].

Similiar to the case of the analogue HCAL the readout electronics will be integrated into the sensitive layer of the system, thus minimising dead areas. Large electronics boards

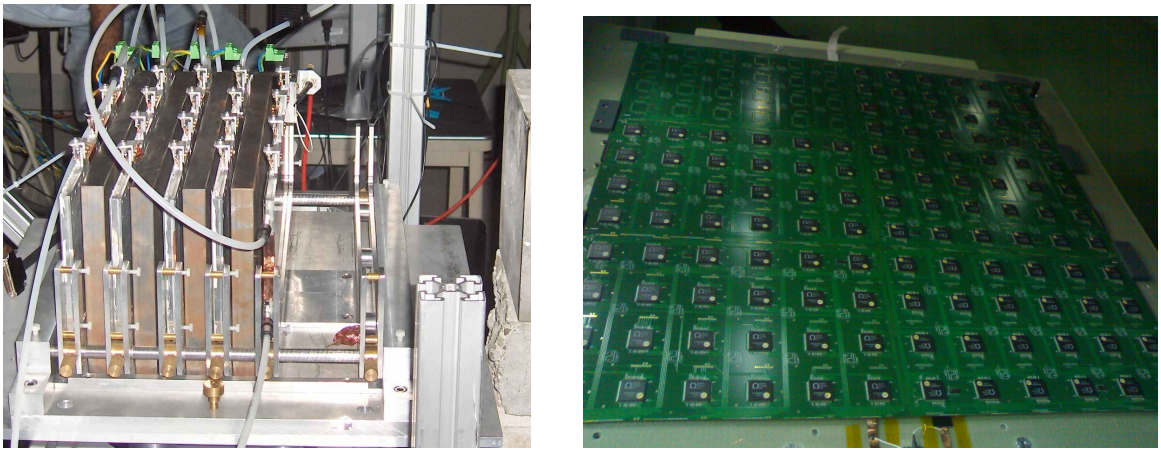

FIGURE 4.4-22. Mini-DHCAL prototype (left); Prototype of a large instrumented GRPC (right).

are assembled together to form extra large boards before they are attached to the GRPCs. The board assembly will be made possible thanks to a mechanical structure made of 4 mm stainless steel plate. In addition, to keep the HCAL as compact as possible, the fully equipped electronic boards are designed to have less than 3 mm thickness in all. A mini hadronic calorimeter using this concept was built and successfully tested in beam conditions at CERN in 2008 (see figure 4.4-22).

4.4.4.3.1 The Active Layers R&D activities on large GRPC detectors are being followed. Different kinds of spacers are tested to reduce detector noise and inefficiency while increasing the detector robustness. New gas distribution schemes as well as gas recycling systems are worked out to lower gas consumption and pollution. Although the present GRPC detection rate of 100 Hz/cm^2 obtained with efficiencies greater than 90 % is enough for the needs of ILC, a new development based on using semi-conductive glass will lead to increase this rate. Multi-gap GRPCs are also investigated. This allows reducing the spread of the MIP charge spectrum leading to a better exploitation of the semi-digital information.

Few large GRPCs with different options were built and are currently tested using a 1 m^2 fully equipped electronics board (see figure 4.4-22(right)). This will allow to build the most appropriate GRPC detector to be used in the ILD DHCAL.

In addition to the GRPCs activities, development on other thin and large gaseous detectors like GEM and MICROMEGAS are also followed.

The GRPCs produces strong electric currents (a few 10 pC in 10-20 ns) in the DHCAL pads. In order to reduce cross-talk effects between the pads below the percent level the very front end electronics is located on the other side of the PCBs, (semi-)buried vias are used.

4.4.4.3.2 Energy Reconstruction & Calibration The semi-digital HCAL cell energy reconstruction can, to first order, be estimated as $E_{\text{cell}} = 1$, 5 and 10 MIP if the charge is above the thresholds typically placed at 0.1, 2 and 8 MIPs (for the envisaged GRPC about 0.26, 5.2 and 20.8 pC). Preliminary results on simulation, without algorithm optimisation, show PFA performances comparable to the AHCAL reconstruction.

An interesting aspect of the gaseous semi-digital HCAL is the simplicity with which the detector calibration is performed, if one is needed at all. The sDHCAL energy calibration requires 3 independent steps:

- *An intercalibration of the ASIC thresholds in charge*: All ASICs will have to be tested and calibrated by injecting a precisely controlled charge, adapted for each of the threshold, at the entrance of their final ASU/PCB pad. The variations can be compensated channel by channel in the ASIC by adjusting the channel gains (over a range of 0–2 coded on 8 bits in the current version of HaRDROC, described in sec 4.4.5.1);
- *A calibration of the multiplicity of the RPC*: The multiplicity response curve of the RPC to muons as a function of high voltage applied, thresholds, position and gas flow and atmospheric pressure can be measured on a cosmic test bench or muon beam and parametrised for each type of RPC.
- *A calibration with physics*: The two first steps bring an absolute calibration at the level of the MIP, which can be cross-checked with cosmic muons or $Z \to \mu\mu$ events; the final energy scale will be a complex interplay in the scope of the PFA analysis between the clustering algorithms, jet and particle energies and types.

The definition of the calibration procedure, and an estimation of the achievable precision, is a part of the DHCAL $1\,\mathrm{m}^3$ programme.

4.4.4.3.3 Status and Future R&D Plans A technological prototype of $1\,\mathrm{m}^3$ HCAL based on the same principle is currently under study. It aims to validate at large scale the semi-digital HCAL concept. Questions related to the mechanical structure mentioned in the previous section as well as the management of the limited space for services will be addressed. The prototype is to be built by 2010. Combined test beams with the different ECAL prototypes developed within the CALICE collaboration will then be organised at FERMILAB and CERN.

4.4.5 Calorimeter Readout System

A considerable effort has been made in the framework of the CALICE collaboration to standardise the read-out of different type of calorimeter with embedded Very Front-End (VFE) electronics while minimising the space needed for the configuration distribution and the data readout.

4.4.5.1 Very Front End (VFE) ASIC description

The front-end ASICs should ensure a data format uniformity in all the calorimeters, thus having identical back-ends to allow a standardised detector interface board (DIF) for all detectors.

Ensuring such a compatibility between all electronics components involves a unique readout system based on token ring that allows a number of ASICs to be read out by one output line, using the same protocol. That protocol will help reducing the number of data lines outputted from the calorimeters where the front-end ASICs are now embedded.

All the VFE will feature three operating mode : Acquisition (1 ms), A/D conversion (1 ms), and data outputting during inter-bunch (199 ms) using an ultra low power protocol. When a FE ASIC is in neither of the above modes, it is turned to an idle mode to save up to 99.5 % of power, bringing the power down to 10 to 25 µW per channel.

Three ASICs differing mostly on their analog front-end have been developed to fit the different detectors.

- SKIROC ("Silicon Kalorimeter Integrated Read-Out Chip"): 64 channels charge preamplifier for charge measurement down to the MIP (3.84 fC) to a maximum around 2500 MIP. Dual gain shaping, analog memory, 12 bit-digitisation, self-trigger capability on single MIP. 25 μW/ per channel to run without any active cooling ensuring therefore an extreme compactness of the calorimeter.
- SPIROC ("Si-Pm Integrated Read-Out Chip"): auto-triggered, dual-gain voltage preamp, 36-channel ASIC which allows to measure for each channel the charge from 1 to 2000 photo-electrons with a 12 bit internal ADC and the time with a 1 ns accurate TDC. One 8-bit 5 V input DAC per channel ensures operation of the SiPM at its optimum bias.
- HARDROC("HArdronic RPC Detector ReadOut Chip"): 24 channels semi-digital readout for RPCs or MicroMegas pads, allowing both good tracking and coarse energy measurement. Each channel made of a variable gain low input impedance current preamp followed by 3 variable gain shapers and 3 low offset discriminators to auto-trig down to 10 fC up to 10 pC. A 128 deep digital memory to store the encoded outputs of the discriminators as well as the bunch crossing identification.

Prototypes of each type have been produced in the years 2007-2008. Boards equipped with 4 HARDROC(v1) ASICs have been designed for the DHCAL. The electronics readout under beam conditions has been validated. Some key points such as the digital daisy chaining for configuration and readout, the stability, the efficiency, and the capability of the chip to be used without any external components have been checked. A small production is foreseen in Fall 2009 to equip a technological prototype (called EUDET prototype) in 2010.

4.4.5.2 Detector Interface

The ASICs are managed by specifically designed DIF (Detector InterFace) cards; one DIF handles a full slab, whose maximum size are of $260 \times 141\,\mathrm{cm}^2$ for the AHCAL structure, and $90 \times 273\,\mathrm{cm}^2$ for the DHCAL structures. The corresponding maximum number of ASIC per slab are respectively 576 and 420. For an estimated occupancy per ASIC of the HCAL of 5 events / train of 2600 BC, the expected data volume to be read in the inter-train is of 336000 bits; readout at a speed of 5 MHz this takes 67 ms. During the readout phase the ASICs will be on standby except when explicitly addressed.

4.4.5.3 DAQ system

The data acquisition (DAQ) system is defined to start with the detector interface boards (DIF) which service the detector slabs from the ends and which are specific to the VFE of the subsystem. The DIF provides a generic interface, independent of the calorimeter type, to the DAQ system. Because of the limited space available for cabling and services, data are concentrated onto a single optical communication channel with the off-detector electronics, by a link-data aggregator (LDA) inside the detector. The resulting data volume is mainly determined by the zero-suppression scheme incorporated in the self-triggering Front-End electronics. But as the calorimeter has over 100 million readout channels, significant demands are put on the scalability and on an attractive price/performance ratio of the readout electronics and the associated data-acquisition systems. Therefore the design should minimise the number of LDAs and maximise the data rates on the link which are expected to be 10 GB Ethernet links.

With the data delivered over optical high-speed links, an optical switch is used to dynamically redirect the data streams coming from the detector towards available data receivers of the off-detector system. The off-detector is currently realised as a PCIexpress card hosted in a commodity PC but can be easily implemented in a μTCA crate for the future detector.

For the event building the machine clock will be fed into the off-detector system to the data concentrators and the detector interfaces. The requirements on the clock are a low jitter and fixed latency between the machine clock and the clock in the detector interfaces. This part of the system needs to be custom built to guarantee delivery times and latencies.

For all of the introduced systems (detector interface, data concentrator, off detector system and the clock) prototypes already exist which have been built within the EUDET [113] project. The prototypes perform the same tasks as in the final detector, however the prototypes are build for a proof of principle and need to be optimised for the final detector design.

4.4.6 Status and future R&D plans

The technology-specific R&D will continue in CALICE. However, in order to study the system performance of the proposed solutions, to validate the accuracy of simulations, and to develop the reconstruction techniques further, large test beam experiments are indispensable. The particle flow approach demands integrated set-ups with ECAL and HCAL together. This programme is pursued for the calorimeters in the framework of the CALICE collaboration, in a cooperative way maximising the use of scarce resources with common mechanical structures, electronics components, DAQ systems and software frameworks.

CALICE has completed a series of full-size proof-of-principle tests with so-called physics prototypes of both ECAL technologies and the scintillator HCAL. The programme is to be completed by tests with a RPC-based DHCAL at Fermilab in 2009-10, and by a test of a MAPS-based DECAL prototype until 2012. Large data sets have been and will be collected and form the basis for test and refinement of hadron shower simulations. The emphasis in the more realistic second generation "technological prototypes" is shifted more toward a demonstration of the feasibility of a compact integrated detector design fulfilling the ambitious demands of compactness and hermeticity. Operational challenges not yet addressed with physics prototypes are the power-pulsed front end electronics and the on-detector zero-suppression in auto-triggered mode, which requires continuous and precise on-line control of thresholds. Therefore also technological prototypes need to undergo full-size beam tests. While the focus is rather on calibration and stability than on shower physics, beam campaigns of several weeks in combined set-ups are foreseen to start in 2010.

4.5 FORWARD DETECTORS

Special calorimeters are foreseen in the very forward region of the ILD near the interaction point - LumiCal for the precise measurement of the luminosity and BeamCal for the fast estimate of the luminosity [114]. The LHCal will extend the coverage of the HCAL endcap to smaller polar angles. Together they will improve the hermeticity of the detector.

A third calorimeter, GamCal, about 100 m downstream of the detector, will assist in beam-tuning. Also for beam-tuning a pair monitor is foreseen, positioned just in front of BeamCal.

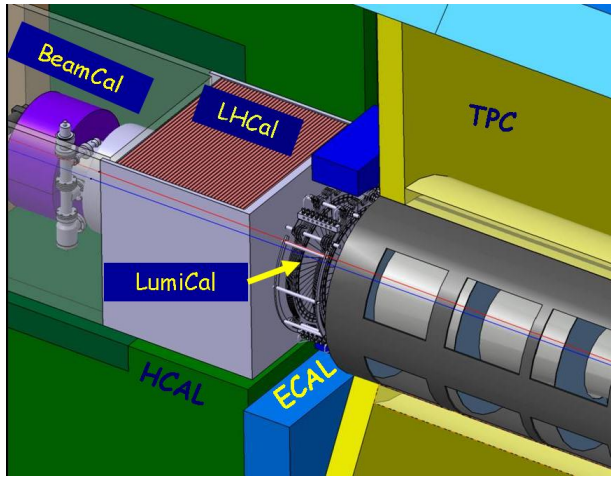

FIGURE 4.5-23. The very forward region of the ILD detector. LumiCal, BeamCal and LHCAL are carried by the support structure of the QD0 magnet.

LumiCal will measure the luminosity using Bhabha scattering, $e^+e^- \to e^+e^-(\gamma)$ as gauge process . To match the physics benchmarks, an accuracy of better than 10^{-3} is needed[2]. Hence, LumiCal is a precision device with challenging requirements on the mechanics and position control.

BeamCal is positioned just outside the beam pipe, in front of the final focussing quadupoles. A large amount of low energy electron-positron pairs originating from beamstrahlung will deposit their energy in BeamCal. These deposits, useful for a bunch-by-bunch luminosity estimate and the determination of beam parameters [116], will lead, however, to a radiation dose of several MGy per year in the sensors at lower polar angles. Hence extremely radiation hard sensors are needed to instrument BeamCal.

A pair monitor, consisting of a layer of pixel sensors positioned just in front of BeamCal, will measure the distribution of beamstrahlung pairs and give additional information for beam parameter determination.

These detectors in the very forward region have to tackle relatively high occupancies, requiring special FE electronics and data transfer equipment. A small Molière radius is of invaluable importance for BeamCal and LumiCal. It ensures an excellent electron veto capability for BeamCal even at small polar angles, being essential to suppress background in new particle searches where the signatures are large missing energy and momentum. In LumiCal, the precise reconstruction of electron and positron showers of Bhabha events is facilitated and background processes will be rejected efficiently.

LHCal will be a hadron calorimeter extending the coverage of the HCAL endcaps to small polar angles. It will allow a fair hadron shower measurement in the polar angle range of LumiCal and enhance the particle identification capabilities.

4.5.1 The Design of the Very Forward Region

A sketch of the very forward region of the ILD detector is shown in Figure 4.5-23. The design of these devices is complicated by the small crossing angle of the two beams. LumiCal and BeamCal are cylindrical electromagnetic calorimeters, centered around the outgoing beam. LumiCal is positioned inside and aligned with the forward electromagnetic calorimeter.

[2]For the GigaZ option an accuracy of 10^{-4} is the goal [115].

BeamCal is placed just in front of the final focus quadrupole. The pair monitor will be positioned just in front of BeamCal.

The structure of the ECAL end cap leaves a square hole at its centre. LumiCal needs to be positioned very precisely with a well defined fiducial zone around the outgoing beam and is therefore restricted to a minimal size to facility mechanical stability and position control. The "ECAL ring" fills the gap between the LumiCal and the ECAL. This device could be realised in the same technology as the ECAL, i.e. a 30 layer tungsten-silicon sandwich providing 24 radiation lengths.

The 30 mm gap between the ring and the end cap is partly filled by the electronics concentrating cards. This gap is covered in the back by the HCAL which ensures hermeticity in that region. The gap between the ring and the LumiCal contains the electronics of the latter and provides space for the tie-rods which suspend the magnet support structure from the coil cryostat. This gap is covered on the back by the LHCAL.A laser position monitoring system is foreseen to monitor the position of LumiCal and BeamCal with respect to the beam-pipe and the distance between them [117]. More details on the integration of the forward region are given in [118].

4.5.2 LumiCal

Monte Carlo studies have shown that a compact silicon-tungsten sandwich calorimeter is a proper technology for LumiCal [119]. In the current design [120], as sketched in Figure 4.5-24, LumiCal covers the polar angular range between 32 and 74 mrad. The 30 layers of tungsten absorbers are interspersed with silicon sensor planes. The FE and ADC ASICS are positioned at the outer radius in the space between the tungsten disks. The small Molière radius and finely radially segmented silicon pad sensors ensure an efficient selection of Bhabha events and a precise shower position measurement. The luminosity, $\mathcal{L}$, is obtained from $\mathcal{L} = \mathcal{N}/\sigma$, where $\mathcal{N}$ is the number of Bhabha events counted in a certain polar angle range and σ is the Bhabha scattering cross section in the same angular range calculated from theory. The most critical quantity to control when counting Bhabha scattering events is the inner acceptance radius of the calorimeter, defined as the lower cut in the polar angle. The precise determination of luminosity requires an excellent knowledge of the lower acceptance of the calorimeter. From Monte Carlo studies of the present design a tolerance of a few μm has been estimated [121]. Since there is bremsstrahlung radiation in Bhabha scattering, cuts on the shower energy will also be applied. The criteria to select good Bhabha events hence define requirements on the energy resolution and, more challenging, on the control of the energy scale of the calorimeter. The latter quantity must be known to about a few per mille [122]. Monte Carlo simulations are also used to optimise the radial and azimuthal segmentation of silicon pad sensors for LumiCal [119] to match the requirements on the shower measurement performance.

A first batch of prototype sensors [123], as shown in Figure 4.5-25, has been delivered from Hamamatsu Corp.. At the first stage these sensors will be characterised and qualified, in a later stage, they will be instrumented with Front-End (FE) electronics for investigations in the test-beam and eventually the construction of a calorimeter prototype.

Front-end and ADC ASICS are designed with a shaping and conversion time less than 300 ns, being potentially able to readout the calorimeter after each bunch crossing. The range of sensor pad capacitance and the expected signal range in electromagnetic showers originating from Bhabha events are taken from Monte-Carlo simulations [124]. Prototypes of the FE ASICS and pipeline ADC ASICS, manufactured in 0.35 μm AMS technology, are

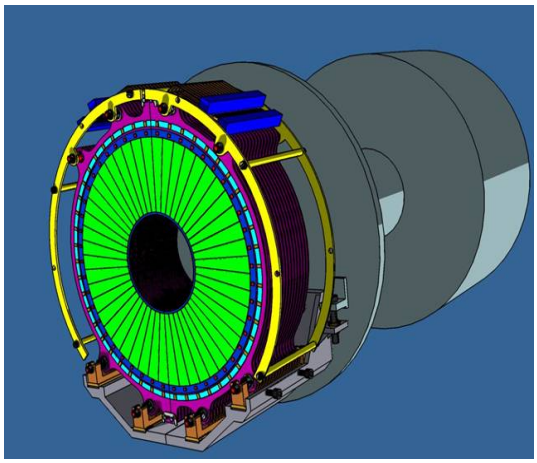

FIGURE 4.5-24. LumiCal designed as a silicon-tungsten sandwich calorimeter. In green the silicon sensor segments are shown and in yellow the mechanical frame which ensures the necessary mechanical stability.

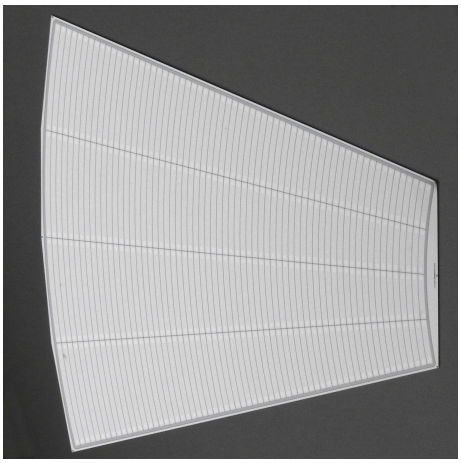

FIGURE 4.5-25. A prototype of a silicon sensor for LumiCal. The sensor in manufactured using 6 inch wafer of n-type silicon, the strip pitch is 1.8 mm.

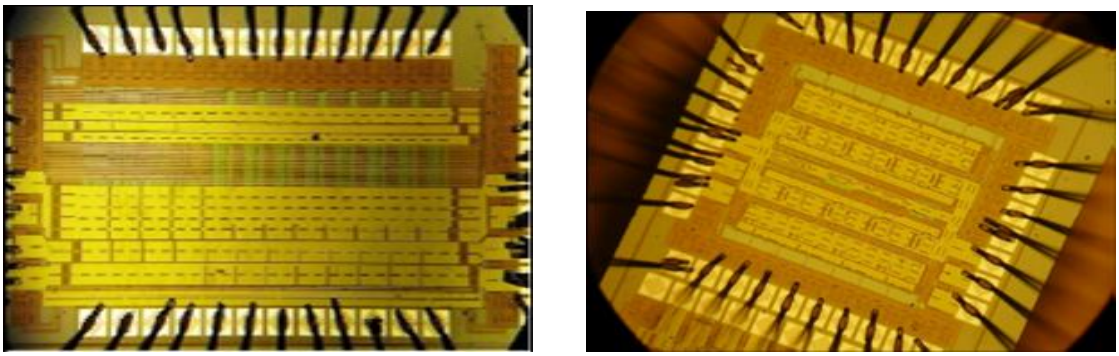

FIGURE 4.5-26. Prototypes of the FE (left) and ADC ASICS (right) prepared for systematic tests in the laboratory.

shown in Figure 4.5-26. The FE ASIC can be operated in low and high amplification mode. The high amplification mode allows to measure the depositions of minimum ionising particles. Hence muons can be used from the beam halo or from annihilations for the calibration and sensor alignment studies. The low amplification mode will be used for the measurement of electromagnetic showers. Tests of these ASICS prototype are ongoing [125]. Results on linearity, noise and cross talk measured are matching the requirements for the performance derived from Monte-Carlo simulations. For 2010 multi-channel prototypes of the ASICS are planned, allowing to instrument prototypes of sensor planes to investigate the performance of the full system in the test-beam.

4.5.3 BeamCal

BeamCal is designed as a solid state sensor-tungsten sandwich calorimeter, as shown in Figure 4.5-27, covering the polar angle range between 5 and 40 mrad. The tungsten absorber disks will be of one radiation length thickness and interspersed with thin sensor layers

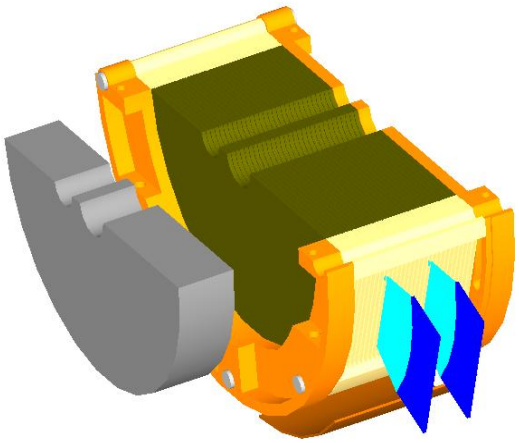

FIGURE 4.5-27. One half of BeamCal designed as a sensor-tungsten sandwich calorimeter. The graphite block is shown in gray, the tungsten absorber and the sensors in green and the FE electronics in blue.

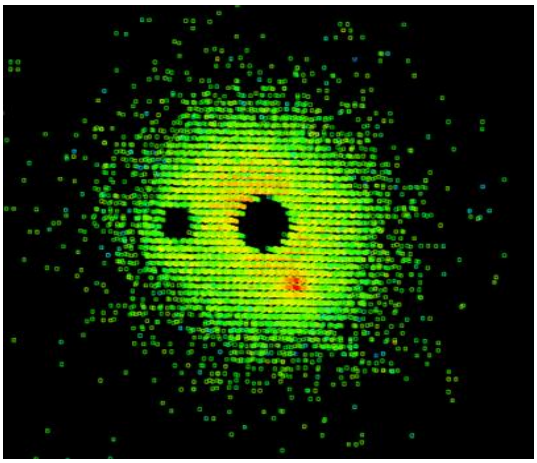

FIGURE 4.5-28. The distribution of depositions of beamstrahlung pairs after one bunch crossing on BeamCal. Superimposed is the deposition of a single high energy electron (red spot in the bottom part). The black holes correspond to the beam-pipes.

equipped with FE electronics positioned at the outer radius. In front of BeamCal a 5 cm thick graphite block is placed to absorb low energy back-scattered particles.

BeamCal will be hit after each bunch crossing by a large number of beamstrahlung pairs, as shown in Figure 4.5-28. The energy, up to several TeV per bunch crossing, and shape of these deposition allow a bunch-by-bunch luminosity estimate and the determination of beam parameters [116]. However, depositions of single high energy electrons must be detected on top of the wider spread beamstrahlung. Superimposed on the pair depositions in Figure 4.5-28 is the local deposition of one high energy electron, seen as the red spot at the bottom. Using an appropriate subtraction of the pair deposits and a shower finding algorithm which takes into account the longitudinal shower profile, the deposition of the high energy electron can be detected with high efficiency and modest energy resolution, sufficient to suppress the background from two-photon processes in a search e.g. for supersymmetric tau-leptons [126] in certain scenarios.

The challenge of BeamCal is the development of radiation hard sensors, surviving up to 10 MGy of dose per year. Polycrystalline CVD diamond sensors of 1 cm^2 size, and larger sectors of GaAs pad sensors as shown in Figure 4.5-29 have been studied. Polycrystalline CVD diamond sensors have been irradiated up to 7 MGy and were found to be still operational [127]. GaAs sensors are found to tolerate nearly 2 MGy [128]. Since large area CVD diamond sensors are still very expensive, they might be used only at the innermost part of BeamCal. At larger radii GaAs sensors seem to be a promising option. These studies will be continued in the future for a better understanding of the damage mechanisms and possible improvements of the sensor materials.

The FE ASIC development for BeamCal, including a fast analog summation for the beam feedback system and an on-chip digital memory for readout in between two bunch trains [129] is ongoing, first prototypes are expected in 2009.

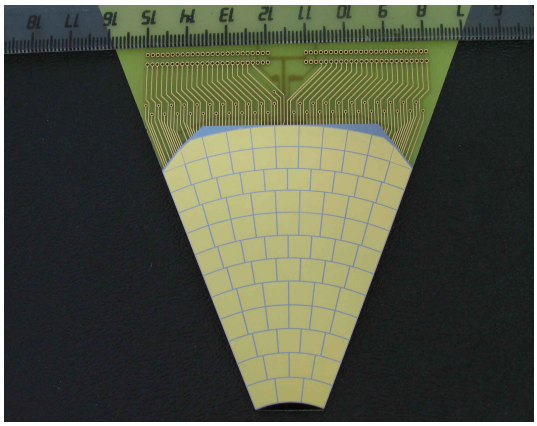

FIGURE 4.5-29. A prototype of a GaAs sensor sector for BeamCal with pads of about 1 cm2 area.

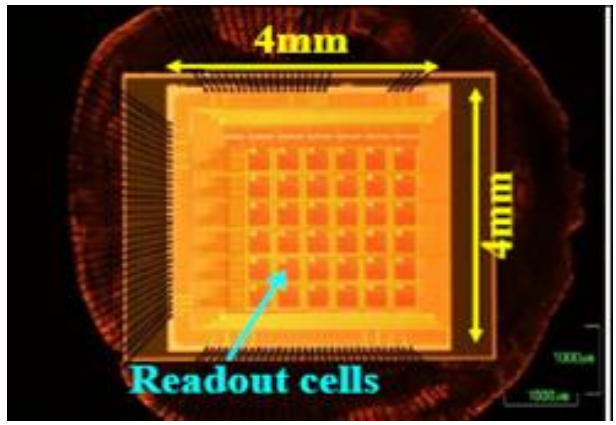

FIGURE 4.5-30. A prototype ASIC for the Pair Monitor Pixel layer. The pixel size is 400x400 μm^2.

4.5.4 The Pair Monitor

The pair monitor consists of one layer of silicon pixel sensors just in front of BeamCal to measure the distribution of the number of beamstrahlung pairs. Monte Carlo simulation have shown that the pair monitor will give essential additional information for beam tuning. For example, averaging over several bunch crossings, the beam sizes at the interaction point can be reconstructed with per cent precision [130]. A special ASIC, shown in Figure 4.5-30, is developed for the pair monitor. Prototypes manufactured in 0.25 μm TSMC technology are under study. At a later stage, the pixel sensor and the ASIC are foreseen to be embedded in the same wafer. The latter development will be done in SoI technology [131].

4.5.5 GamCal

GamCal is supposed to exploit the photons from beamstrahlung for fast beam diagnostics. Near the nominal luminosity the energy of beamstrahlung photons supplements the data from BeamCal and Pair Monitor improving the precision of beam parameter measurements and reducing substantially the correlations between several parameters [116]. At low luminosity the amount of depositions on BeamCal will drop dramatically, however, GamCal will still give robust information for beam tuning.

To measure the beamstrahlung spectrum a small fraction of photons will be converted by a thin diamond foil or a gas-jet target about 100 m downstream of the interaction point. The created electrons or positrons will be measured by an electromagnetic calorimeter. A conceptual design of GamCal exists, more detailed Monte Carlo studies are necessary to fully understand the potential of GamCal for beam tuning and beam parameter determination.

4.5.6 LHCal

The LHCal fits in the square hole of the HCAL and embraces the beam tube which is centred on the outgoing beam. It has a thickness of four interaction lengths comprised by 40 layers of tungsten of 1 cm thickness. The sensitive medium could be silicon sensors similar to the ECAL ones. LHCAL is supported by two vertical plates which are part of the forward structure. It would be made of two halves separated vertically, making it easy to dismantle.

The electonics concentrating cards would be on the top and the bottom.

4.5.7 Priority R&D topics

The current research work covers several fields of high priority to demonstrate that the designed devices match the requirements from physics. These are:

- Development of radiation hard sensors for BeamCal. The feasibility of BeamCal depends essentially on the availability large area radiation hard sensors.
- Development of high quality sensors for LumiCal, integration of the FE electronics in a miniaturised version and tuning of the full system to the required performance.
- Prototyping of a laser position monitoring system for LumiCal. In particular the control of the inner acceptance radius with μm accuracy is a challenge and must be demonstrated.
- Development and prototyping of FE ASICs for BeamCal and the pair monitor. There are challenging requirements on the readout speed, the dynamic range, the buffering depth and the power dissipation. In addition, a system for the data transfer to the back-end electronics has to be developed.

Also of high priority, but not covered for the moment, is the design of GamCal and an estimate of its potential for a fast feedback beam-tuning system.

4.6 COIL AND RETURN YOKE

The basic layout of the ILD detector has always followed the strategy of tracking in a magnetic field. The ILD detector design therefore asks for a 4 T field in a large volume, with a high field homogeneity within the TPC volume and with a reduced fringe field outside the detector.

The parameters of the ILD magnet being very similar to the CMS ones (c.f. [132], [133]), basic designs of both magnets are similar. An anti DiD (Dipole in Detector) is also added in the design, which allows to compensate the effect of the crossing angle for the outgoing beam (and pairs) behind the I.P.

4.6.1 Physics Requirements

The main requests from the physics for the ILD magnet are a solenoidal central field of nominal 3.5 T and maximum 4 T, in a volume of 6.9 m in diameter and a length of 7.35 m with the following requests:

- A high integral field homogeneity:

$$|\int_0^{2.25m} (B_r/B_z)\, dz\,| \leq 10\ mm; B_r = B_x(x/r) + B_y(y/r)$$

  within the TPC volume, which is a cylinder 3.6 m in diameter and 4.5 m long. This high homogeneity requests incorporating compensation windings.

- A fringe field in the radial direction less than 50 G at R = 15 m to not magnetically perturb the second detector when in operation on the beam line.

- A yoke instrumented for the detection of muons and for tail catching (see section 4.7).

4.6.2 Magnet Design

The magnet consists of the superconducting solenoid, including the correction coils, and of the iron yoke, one barrel yoke in three pieces and two end-cap yokes, also in two pieces each. The anti DiD is located outside the solenoid.

Concerning the correction coils, it seemed practically simpler and less space consuming to incorporate them into the main winding, by adding extra currents in appropriate locations of the winding.

The cross section of the ILD detector magnet is shown on Figure 4.6-31. Its main geometrical and electrical parameters are given in Table 4.6-8.

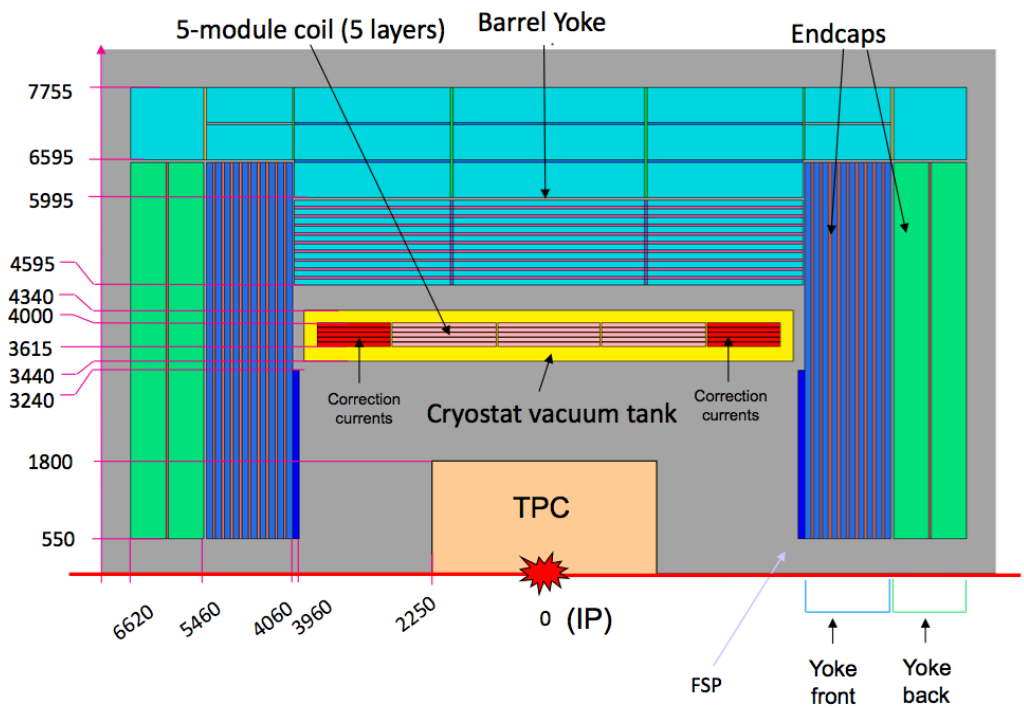

FIGURE 4.6-31. Cross section of the ILD magnet.

The coil is divided into five modules, electrically and mechanically connected: there are three central modules, 1.65 m long each, and two external modules, 1.2 m long each. All modules consist of a four-layer winding.

The nominal main current, 18.2 kA for a central field of 4.0 T, runs through all the turns of the solenoid. An extra correction current of about 15.8 kA is added in the turns of the four layers of the two external modules to get the integral field homogeneity.

The barrel yoke has a dodecagonal shape. It is longitudinally split into three parts. In the radial direction, the inner part of the yoke is made from 10 iron plates of 100 mm thickness, with a space of 40 mm between each to house detectors for tail catching and muon detection. Three thicker iron plates of 560 mm each with 40 mm spaces for muon detectors form the outer part of the barrel yoke. The weight of the barrel yoke is around 7000 t.

The end-cap yokes, also of dodecagonal shape, have a similar split structure, with 10 iron plates of 100 mm thickness in the inner part, with a space of 40 mm between each to house the tail catcher and muon detectors, and two external thick plates, each 560 mm thick, to

Cryostat inner radius (mm)	3440	Maximum central field (T)	4.0
Coil inner radius (mm)	3615	Maximum field on conductor (T)	5.35
Coil outer radius (mm)	4065	Stored energy (GJ)	2.0
Cryostat outer radius (mm)	4340	Stored energy/ cold mass (kJ/kg)	12.2
Barrel yoke inner radius (mm)	4595	Nominal main current (kA)	18.2
Barrel yoke outer radius (mm)	7755	Nominal correction current (kA)	15.8
Coil length (mm)	7350	Ampere-turns main coil (MAt)	1.52
Cryostat length (mm)	7810	Ampere-turns correction coils (MAt)	1.36
Yoke overall length (mm)	$6620 * 2$		

TABLE 4.6-8
Main geometrical and electrical parameters

make up the total iron thickness. A 100 mm thick field shaping plate (FSP) will be added inside each end-cap to improve the field homogeneity. The weight of each end cap yoke is around 3250 t and thus the total weight of the yoke is around 13400 t.

The main design challenge of the yoke endcaps is to contain the magnetic forces themselves. A weight equivalent of ≈18000 t pulls at each endcap. A FEM analysis shows that if the endcaps are constructed in radially fixed segments (c.f. figure 4.6-32) the deformation of the endcaps due to the magnetic force could be less than 3 mm; alternative designs which lead to comparable small deformations are also under study. These deformations are far smaller than e.g. at CMS where the endcaps are deformed by ≈16 mm during the powering of the magnet.

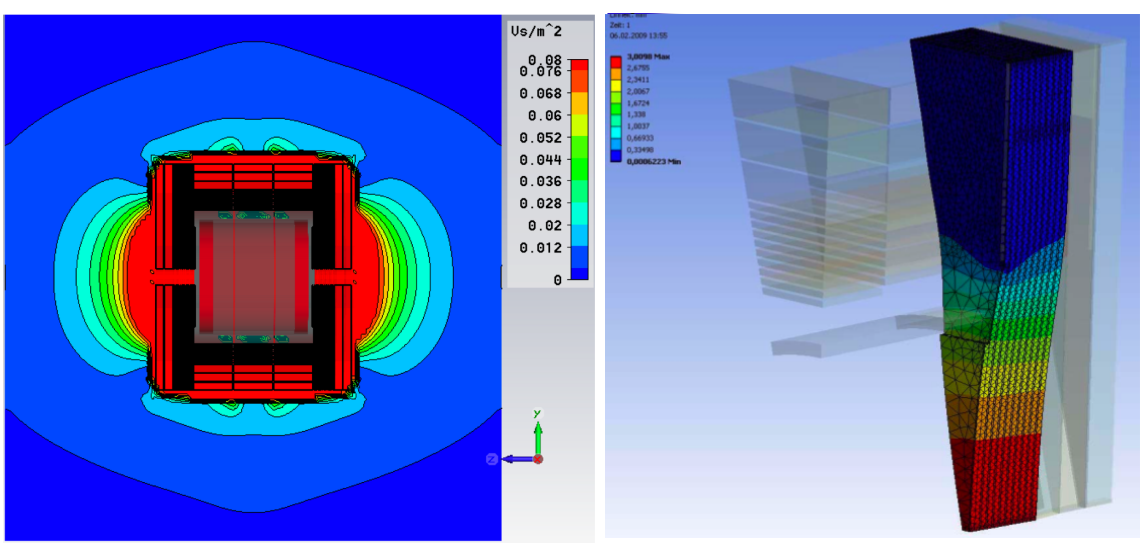

FIGURE 4.6-32. Stray fields outside the yoke (left). Deformation of an endcap segment (right).

4.6.3 Magnetic Field

The calculated integral field homogeneity, with the nominal values of the main and correction currents given in table 4.6-8 meets the requirement (maximum value of 7 mm at 4 T). Note that the effect of the anti DiD is not taken into account in this calculation.

With the yoke structure described, the calculated fringing field is ≈40 Gauss at 15 m in the radial direction and therefore fulfils the requirements (c.f. figure 4.6-32).

4.6.4 Technical Aspects

As several technical aspects are quite similar for the ILD and CMS magnets, the experience gained during the construction of the CMS magnet will be of great help for ILD.

The conductor will consist of a superconducting cable coextruded inside a low electrical resistivity stabiliser and mechanically reinforced by adding high-strength aluminum alloy. Two different conductors will be necessary, using different superconducting cables and different ratio of mechanical reinforcement, but with the same overall dimensions.

The winding will be done using an inner winding technique. The magnetic forces will be contained both by the local reinforcement of the conductor and by an external cylinder. The coil will be indirectly cooled by saturated liquid helium at 4.5 K, circulating in a thermo-siphon mode.

The central barrel yoke ring will support the vacuum tank. Internal sub-detectors will be supported on rails inside the vacuum tank.

4.7 MUON DETECTOR

The identification of leptons is an important part of the physics programme at the ILC. For muons above a few GeV, the instrumented iron return yoke is used as a high efficiency muon identifier. The clean environment of an electron-positron Linear Collider allows for a muon system design that is much simpler compared to the ones that have been developed for the hadron colliders. There is no need to trigger on muon tracks; instead the clean nature of the events at the ILC allows the linking of track candidates from the inner detectors with tracks in the muon system.

In addition to its muon tagging ability the system will be instrumented to allow for a limited calorimetric performance. In this way it can act as a tail catcher, tagging late developing showers and thus improving the energy measurement.

A muon is most easily identified by a track in a muon detector behind significant material. At the ILD, the muon system is reached by muons with a momentum above about 3 GeV. The strong central magnetic field will keep lower energy particles from reaching the muon system. The main challenge then for these type of muons is the joining of a signal in the calorimeter with a track segment outside the coil. Multiple scattering in the calorimeters and the coil will have a large impact on this, and the efficiency of association will increase with momentum. At lower momenta, the signal in the calorimeter will be used to identify muons. In particular inside jets this is difficult, and more in - depth studies are needed within ILD to reach strong conclusions.

4.7.1 Conceptual Design

The muon system in ILD will cover a large area of several thousand square meters. The detectors therefore need to be reliable, easy to build, and economical. Signals from the detectors should be large so that simple readout systems and cable routings can be used to the readout modules. The detectors should have a reasonable temporal and spatial resolution. Searches for long-lived particles and tagging of cosmics and beam halo muons requires that a few nsec time resolution be achievable. Since multiple scattering is significant, spatial resolutions in the range of cm are sufficient. Occupancies are low, so that both strip and pixel devices can be considered. The efficiency and reliability of muon identification somewhat depends on the iron longitudinal segmentation as do calorimetric performances. Mechanical construction and practical considerations indicate that plate thickness cannot be below 10 cm. For the ILD design, the total thickness needed to close the magnetic flux is ≈ 275 cm (see 4.6). It is instrumented with 10 layers of detector with 10 cm thick absorber plates in between, and a few layers at larger distance in the remainder of the yoke.

Both gas detector and extruded scintillator strips can in principle fulfill the requirements. Plastic Streamer Tubes (PST) or Resistive Plate Chambers (RPC) are candidates for the gas detector. However, RPCs tend to be preferred over PSTs due to their reduced cost and greater flexibility in the segmentation achievable. For the RPC option one could use strips $3-4$ cm wide to obtain the desired resolution. Each gap could provide two orthogonal coordinates, with orthogonal strips on the two sides of the gas gap, while energy would be measured for non muon-hits just by hit counting. The electronics would consist of single bit information per strip; the front-end would include a variable threshold discriminator. The channel count would range around 100K.

An alternative solution relies on extruded plastic scintillator strips. Wavelength shifting fibres are embedded into the strips, and are read out at either end of the strips with silicon photomultipliers (SiPMs). The small size, low operating voltages and magnetic field immunity of the SiPMs implies that they can be placed inside the detector, thus obviating the need for routing fragile fibres. Orthogonal placement of strips can provide space-points with the required resolution. A prototype based on this technology, the tail-catcher/muon tracker (TCMT), has been built and exposed to a test beam by the CALICE collaboration at CERN and Fermilab during the 2006-2008 period. The extended operation of the TCMT has clearly demonstrated its excellent reliability and performance (see Fig. 4.7-33). It should be noted that useful synergies may exist between the muon system and the hadron calorimeter since RPCs and scintillator are both potential technology options for the HCAL.

4.7.2 Performance

Performances of the muon identification system described in the previous paragraph have been evaluated both with single particles and high multiplicity final states. In order to assess the linking capabilities of the proposed detector, single particle efficiency has been evaluated as shown in Figure 4.7-34(left top). In the same figure (left bottom) the efficiency is shown for muons identified in $b\bar{b}$ events. The plots in Figure 4.7-34 show that the performance remains excellent also in complex high multiplicity events .

The muon system also does have a limited calorimetric capability. On average the energy leakage into the muon system is small but with large event-to-event fluctuations. For K_L^0 the average energy leakage is 3% for a range of energies, but energy leakage four or five times the average is not uncommon. The use of the muon system to estimate and correct for the leakage

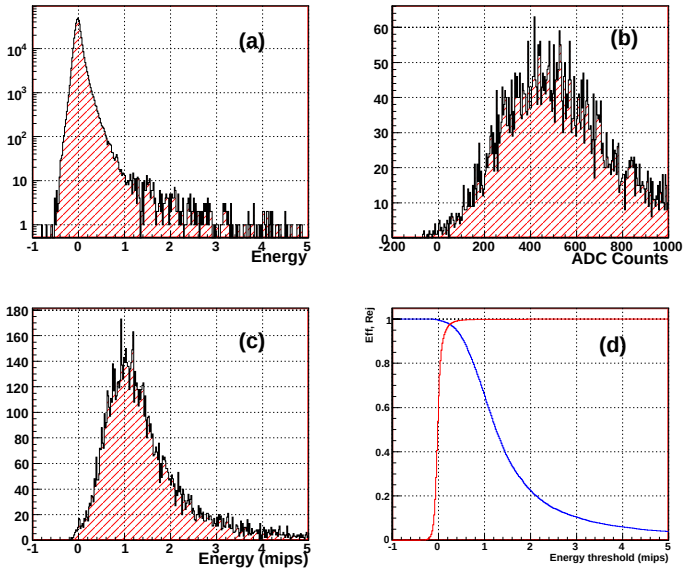

FIGURE 4.7-33. For a typical TCMT strip:(a) pedestal distribution (b) pedestal subtracted MIP signal from muons (c) MIP calibrated signal (d) efficiency (blue) and noise rejection (red) as a function of the energy threshold.

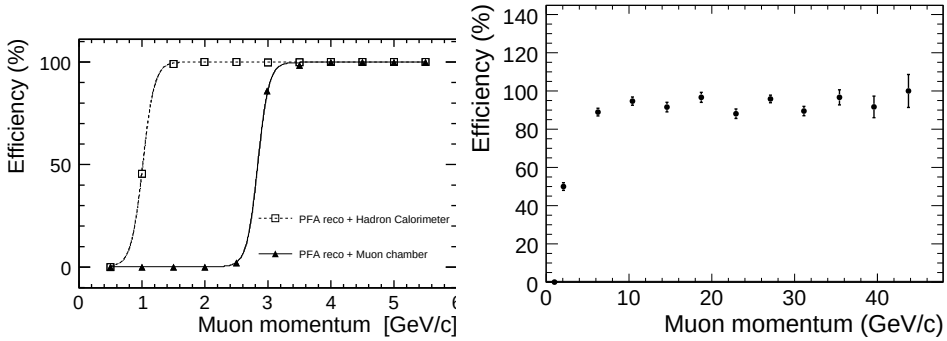

FIGURE 4.7-34. (top): Muon identification efficiency vs. momentum for single muon. The right curve represent muon found only in the muon system, the left curves muons which were found by a combination of HCAL and muon system. (bottom): Muon finding efficiency in $b\bar{b}$ events.

is hampered by the presence of the coil, which introduces close to two interaction lengths of dead material between the last calorimeter layer and the first muon layer. Nevertheless a correlation between the energy of hadrons and the leakage signal recorded in the muon system can be observed and used to improve resolution in simulation and test beam data (see Fig. 4.7-35).

4.7.3 Outlook

The proposed muon system for the ILD concept is well matched to the requirements as laid down in this document. Two alternative technological implementations are discussed, one based on gaseous detectors and the other based on plastic scintillator strips. The system will

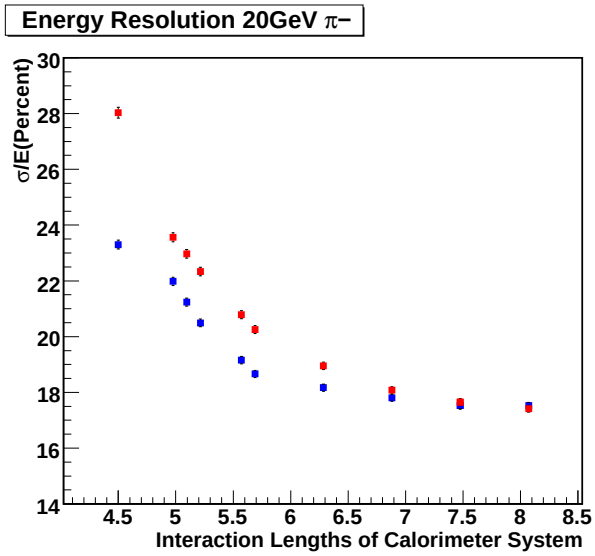

FIGURE 4.7-35. Resolution improvement for 20 GeV pions by including energy beyond the coil using CALICE testbeam data. The red points correspond to the resolution obtained for a given thickness of the calorimeter system while the black points supplement the energy in the calorimeter system with that from beyond the coil. The change in length of the calorimeter system, the material contained in the coil and energy beyond the coil are simulated by rejecting or accepting layers in the TCMT.

serve primarily as a muon identifier, but will also play an important role as a tail catcher to compensate for leakage from the calorimeter system. Continued R&D is required to establish a detailed, realistic design and make an informed technology choice.

4.8 CALIBRATION AND ALIGNMENT

The ILD detector is a sophisticated precision instrument. It consists of a high precision tracking detector, surrounding the interaction point, followed by a granular calorimeter system covering nearly the entire solid angle.

To reach the anticipated performance calibration and alignment of the sub-detectors and of the overall detector system are a central part of the detector design and is important for the complete life cycle of the experiment, from the design over the construction to the operation of the device.

For the rest of this section we define calibration to be all tasks which deal with the internal description of the detectors. Alignment is the relative positioning of internal parts of the subdetectors or of sub-detectors relative to each other.

Calibration and alignment of all sub-systems will be based on a mixture of data from dedicated calibration systems and from particles recorded during physics running.

During construction tolerances must be carefully controlled, during commissioning systematic metrology of the different detector parts is needed. This will provide an initial alignment of the modules internally, and of the different systems relative to each other. The need for a high precision metrology has consequences for the mechanical design of the differ-

ent sub-systems, which from the beginning need tolerances determined to allow the necessary level of mechanical precision. In particular in the tracking system care has to be taken to ensure that the mechanical systems are stable enough to allow an alignment at the level of 10μm or better.

After installation, and throughout the lifetime of the detector, constant measurements will be taken using dedicated hardware to monitor the position of the different detector components, improving the alignment from the initial situation.

The final calibration of the detector will be done using particles. Tracks from the decay of the Z - boson will play an important role here, as they are of well known high momentum. The best source of such tracks are from short and dedicated runs of the collider on the peak of the Z resonance, at 91 GeV. For the discussions in the following sections we assume that around $1pb^{-1}$ of data can be collected within a few hours of running at 91 GeV. This will result in some 30000 Z bosons, of which around 1000 will decay as $Z \rightarrow \mu^+\mu^-$.

The final high precision calibration will be derived from tracks in the data sample taken at high energies. Stiff tracks e.g. from W decays or from $q\bar{q}$ pair events will provide a large sample of tracks. The design of the detector has been optimised in a way to allow a calibration heavily relying on such data.

The detector alignment at the ILC is a particular challenge because of the intended push-pull mechanism to switch between two detectors. This implies that each detector will move out and back in into the interaction region frequently, and that the overall alignment of the system should be re-established rapidly after a push-pull operation. As discussed in 6.4 the switchover times between the two detectors should be of order of a few days with consequently the need to do a rapid re-establishment of calibration constants within a day or so. Both the detector design and the alignment concept need to take these requirements into account.

Another challenge will be the need to power-pulse the detectors inside the magnetic coil to limit the total power consumption. Most detectors will be switched off or switched to reduced power in between trains of the collider. This procedure of power pulsing will potentially apply significant forces to the detector structure, during the ramp up or ramp down of the power, and stress the components with significant swings in temperature. Special care must be exercised during the design of the mechanical system to ensure that the structure does not move during these cycles, and that the alignment does not suffer from train to train.

In this section the calibration and alignment strategies of the overall detector are discussed. Calibration strategies for individual sub-detectors have been discussed in the relevant sections describing the sub-detector technologies.

4.8.1 Tracking System Calibration and Alignment

A main purpose of the tracking system is the efficient finding of charged particles, the reconstruction of their momenta and their impact parameters. The anticipated precision for the momentum and the impact parameter are significantly above anything ever achieved before in a detector of this size and complexity. Using a simple model of the track parameters dependence on alignment tolerances, the following limits for the alignment of each of the tracking sub-systems have been derived:

- coherent displacement of the VTX, 2.8 μm;
- coherent displacement of the SIT, 3.5 μm;
- coherent displacement of the SET, 6 μm; and
- coherent displacement of the TPC, 3.6 μm.

These values must be confirmed by further studies.

An important aspect of the overall alignment of the tracking system is the knowledge of the central magnetic field. Uncertainties on the size and direction of the field within the tracking volume will directly impact the momentum resolution. Using sophisticated magnetic field probes the field will be measured to a precision of $dB/B < 10^{-4}$. This level of precision has been reached in previous experiments using large volume magnetic fields [95].

The above distortion limit defines the precision required for the magnetic field calibration. In a TPC, the drifting electrons follow the magnetic field lines; field components perpendicular to B_z result in deflections of the track as measured at the readout plane. The magnet is designed to have a field uniformity of $\int B_r(constructed)/B_z dz = 2$ mm $-$ 10 mm. These deflections are largely corrected with the application of the magnetic field map. However, residual misunderstanding of the magnetic field will result in track distortions. Thus, the mapping of the magnetic field must be significantly improved beyond the initial probe precision stated above, $dB/B < 10^{-4}$. Based on the limit of the internal fit sagitta above, the magnetic field map must have a precision of $\int B_r(correction)/B_z dz < 20 - 30\mu$m. For the case that magnetic field distortions that are coherent along the drift length of about 2 meters, the integral is equivalent to the requirement that $dB/B < 10^{-5}$. It is envisioned that stiff tracks as observed in either Z decays of in high energy collisions will provide the necessary information.

4.8.1.1 Silicon Tracking Alignment

Calibration and alignment of the detectors are an important consideration already during the design and construction phase of the different silicon based sub-detectors. These aspects are discussed in detail in section 4.2.6. The alignment among different sub-detectors, and relative to the rest of the ILD detector, will be based on a three-fold approach: two laser based alignment systems will be combined with a sophisticated alignment strategy based on tracks.

The extent of the challenge for alignment becomes clear if one considers the number of degrees of freedom which need to be determined. For the ILD silicon tracker this number is of the order of 100.000 (calculated as six times the number of sensors). If the relative sensor positions in the module are known to the required precision (from survey data or from other hardware alignment systems) the number of degrees of freedom is reduced by a large factor (a factor five in SET that dominates the NDOF count, a factor two or three in ETD). The contribution of the outer tracking system is larger than that of the inner tracker by a factor 10.

If we can assume that the different support structures are basically rigid, and do not change dimensions internally, within the precision anticipated, we only need to worry about the overall alignment of the different sub-detectors relative to the rest of the detector. The goal of ILD is that this situation is reached for a re-alignment after a push-pull operation. In this case the number of degrees of freedom is greatly reduced:

- The outer Silicon tracker, SET, is fixed to the TPC. It is supported by a rigid carbon fibre structure. It probably needs to be split in the middle. In this case 12 degrees of freedom are needed to determine the position of the overall SET.
- The ETD is attached to the endcap calorimeter in one piece. In total 8 degrees of freedom need to be considered.
- The SIT and the FTD are connected to a common support structure. The movement of this structure has 6 degrees of freedom.

Component	number of layers	number of modules	# of sensors/ module	# of channels	area m^2
SIT1	layer 1	33	3	66000	0.9
	layer 2	99	1	198000	0.9
SIT2	layer 1	90	3	180000	2.7
	layer 2	270	1	540000	2.7
SET	layer 1	1260	5	2520000	55.2
	layer 2	1260	5	2520000	55.2
ETD_F	X,U,V	984		2000000	30
ETD_B	X,U,V	984		2000000	30
FTD	7	350		5000000	

TABLE 4.8-9
Number of modules, channel count, and sensitive area for the different Silicon based detectors.

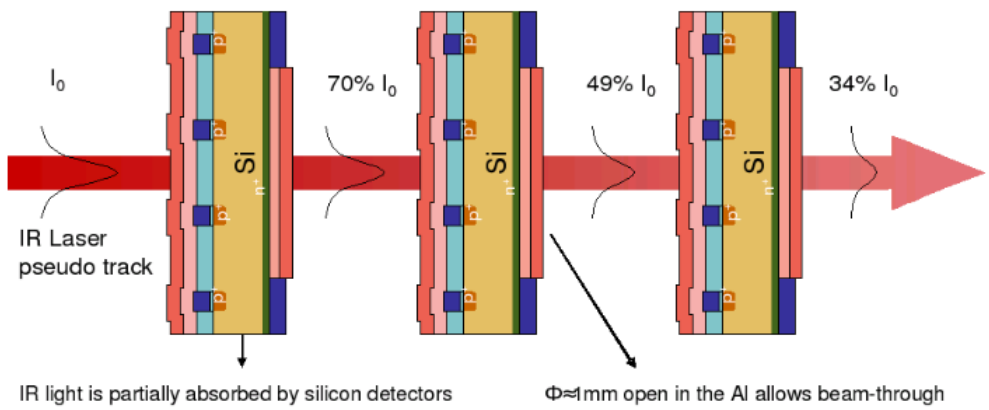

FIGURE 4.8-36. Schematic view of the infra-red laser beam traversing several micro-strip sensors.

In total 26 degrees of freedom are present in this case. This reduces the initial problem to one which can be solved in fairly short amount of time.

Details about the module and channel count in the silicon system are given in Table 4.8-9.

4.8.1.2 A laser based alignment system

A hardware position monitor system based on infra-red laser beams mimicking straight tracks will be installed in the ILD detector. The laser beams traverse several sensors optimized for IR laser transmittance (see Fig. 4.8-36). The signals from the laser are readout using the module sensor and front end electronics. Therefore, there is no added contribution to the error budget associated to the mechanical transfer between monitored fiducial marks and strips. The resolution expected on sensor transversal movements will depend on the number

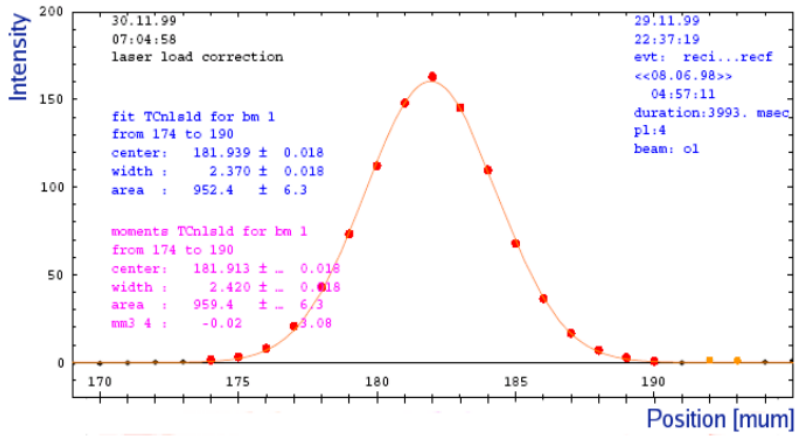

FIGURE 4.8-37. AMS results on the reconstruction of the laser signal on the third sensors in the stack. The data points are the result of averaging 480 readings. The position of the laser pulse can be reconstructed with a resolution of 1 micron.

of strips illuminated by the beam and the sensor pitch. For a pitch value of 50 μm with a gaussian width of the laser beam of $\sigma = 300\mu$m, resolutions below 1μm are achievable. A similar system is in use im the AMS experiment where a silicon tracker with a geometry similar to the FTD (comparable tracking volume, number of layers and cylindrical symmetry) has reached an accuracy of 2μm [134] (see Fig. 4.8-37). The laser alignment system provides the possibility to precisely monitor relativly fast movements. The current design of the ILD forward tracking disks incorporates this system. The system is able to constrain several degrees of freedom of a large fraction of the installed micro-strip sensors in the FTD and the other strip detector, and of the third tracking disk based on pixel technology. The extension to other sub-detectors is being investigated.

Particularly challenging is the connection between the inner and the outer silicon detectors, because of the large distance between them, and the connection between the silicon tracker and other detector elements. Here a pixel based monitoring system (PMD), excited by an IR laser through optical fibres is under consideration. In this system special pixel detectors are attached to the sensors to be aligned. The pixel devices will be installed in several strategic places of the tracking system

The IR laser systems will be complemented by a network of fiber optic sensors (Fiber Bragg System or FBS) that will monitor structural changes like deformations or relative displacements among structures, and environmental parameters as humidity and temperature. These sensors are based on Bragg gratings built into mono-mode optical fibers. In this technology, the carrier fiber is also the readout line. Compared to other traditional sensing techniques they are immune to electromagnetic interference and temperature effects.

4.8.1.3 Alignment of the Time Projection Chamber

The large volume time projection chamber is a central piece of the ILD tracking system. The TPC will provide more than 200 space points along a track. The longest drift distance possible is around 2.3 m. The anticipated spatial resolution in the device is around 60-100 μm.

In addition to the calibration issues discussed in the previous chapters, the TPC is particularly sensitive to the magnetic field in the detector. The survey and calibration of the magnetic field will be a major part of the TPC calibration.

Mechanically the Silicon tracking detectors will all be mounted relative to the TPC. Most probably - though a detailed engineering design has not yet been done - the inner Silicon tracking system will be suspended from the end - plate of the TPC on either side. The external Silicon tracking in the barrel will be supported by the field cage, the external Silicon tracking behind the TPC endplate will be supported by the endplate itself, or possibly by the endcap electromagnetic calorimeter. The TPC as a whole will be suspended from the coil of the ILD detector.

The PMD laser system will possibly be used to reference the TPC relative to the Silicon detectors, and transfer the location of the TPC to the coil. With this system the main degrees of rotation and shift between the TPC and the rest of the Silicon can be determined, and serve as starting point for the overall determination of alignment constants.

4.8.1.3.1 Internal TPC Alignment The internal alignment of the TPC will be based on a well understood and measured field cage of the system. A construction of the field cage at the 0.1 mm level seems possible, and a survey of the finished field cage at the level of 30μm might be not unrealistic.

The B-field, which is as important to the ultimate measurement precision as the mechanical components, will be mapped using probes to a level of $dB/B < 10^{-4}$ as described in [95]. Starting from a well understood magnetic field, unambiguous preliminary tracks can be defined in the TPC. These will be used to iterativly improve the calibration of the TPC, and will eventually serve as starting points for tracks spanning the full tracking system.

In the TPC, the internal components, i.e. the detector readout modules, will be manufactured to tolerances of 20μm, while tolerances for placing the modules on the end-plate will be about 60μm. The internal TPC alignment process must provide the final required precision for both the mechanical alignment and the magnetic field measurement. Achieving these goals will require iteration. As mechanical distortions and magnetic field distortions can lead to similar track distortions, supplementary alignment systems will be used to resolve the ambiguities.

The internal alignment in the TPC will be helped by laser systems installed on the TPC in two ways: using a system of mirrors straight tracks created by a laser are created inside the drift volume, and can be used to determine many calibration constants. In addition diffuse light will be shone on the cathode surface, on which an appropriate coating creates a pattern of charge, which can e.g. be used to calibrate field distortions and the drift velocity.

4.8.1.4 Maintaining the alignment

Probes mounted on the fieldcage of the TPC will be used to monitor the B-field during running. Pressure and temperature will be measured continuously and will be corrected for on the fly. Cosmic-ray tracks and laser systems will be used to check for changes of the internal alignment in the TPC. Tracks from Z running will be used to extend coverage to the whole detector because lasers can only monitor a limited number of reference points, and cosmic rays give reasonable coverage of the vertical direction only.

The PMD laser system will provide a constant stream of alignment data and monitor in real-time the position of the TPC relative to the rest of the detector.

4.8.1.5 Track Based Alignment

While the hardware based systems are invaluable to do a fast re-calibration of the tracking system for the most relevant degrees of freedom, they are not suited for the final high precision alignment. This will need to be based on data from particle tracks. Previous experiments have developed a sophisticated machinery and have shown that the alignment transform can be determined to a precision well below the intrinsic resolution of their detectors, assuming that a large enough sample of high quality alignment tracks can be collected. The most important consideration in selecting the track sample is to tightly constrain all degrees of freedom of the detector geometry, including those that leave the track residual distributions (nearly) unchanged. Typically, the alignment sample is composed of a mixture of collision data and tracks from other sources. High p_T tracks are particularly valuable as they minimize the influence of multiple scattering. A strong constraint on the detector geometry derives from tracks that traverse overlapping detector modules (in the vertex detector and silicon tracking systems). Tracks from cosmic rays and beam halo are useful as they allow to relate different parts of the detector (upper and lower half, both end-caps). Tracks with known momentum are extremely valuable, both as a means to determine some of the weakly constrained alignment parameters and as a monitoring tool to validate the alignment. This role has traditionally been played by tracks from resonances with a well-known mass (the Z-resonance is the most popular as it provides stiff tracks, but J/Ψ and Upsilon have been used as well).

One of the main limitations of the track based system is that it will not be able to follow fast changes in the detector. Given the rather small production rate for $Z->\mu^+\mu^-$ events in the ILC at 500 GeV the typical time constant to align all degrees of freedom of the detector is likely to be of the order of months . However, reduced sets of degrees of freedom, corresponding to higher-level mechanical units like ladders and rings, or even complete cylinders and disks, can be aligned with much less statistics and, hence, at a much greater frequency. In how far tracks from high energy running can be used is a matter of discussion, and will need further in-depth investigation.

4.8.2 Calorimeter Calibration and Alignment

A central part of the ILD detector is a highly granular calorimeter. At the moment a number of different technology options for the different parts are under consideration. In general though they all display a large number of channels, to obtain the excellent spatial resolution needed for particle flow. For any sort of stochastic calibration or alignment uncertainly this is an asset rather than a burden, since the precision with which these effects need to be known scale with $1/\sqrt{N}$, where N is the number of channels. Nevertheless the detailed procedures and the way calibration is implemented differ significantly from technology to technology, and will be discussed separately below.

4.8.2.1 Si-W electromagnetic calorimeter

The information used for defining the alignment and calibration procedures of the ILD electromagnetic calorimeter comes from two sources: a very detailed simulation of the calorimeter and the results from a prototype exposed to beam for now four years. Alignment: The requirements on alignment come from the precision we can reach in measuring the position of a shower. This is of the order of $1\text{mm}/\sqrt{E}$. Therefore an alignment precision of 100μm is

the goal. The main uncertainty comes from the play of the slabs inside the alveoli. With a survey of the module and a careful positioning we can reach 250μm, we need then an alignment with tracks in situ. A small number of electrons, thousands, should be enough to align the calorimeter with respect to the tracking system at the required precision.

4.8.2.1.1 Energy calibration An early study had shown that the energy measurement in our calorimeter is robust against dead channels. Provided they are quite randomly distributed, a fraction up to 5% dead channels does not harm the resolution. The mean response is restored by estimating the dead channels response from their neighbours and the resolution is very marginally touched. The measurement of the channel noise provides the identification of the dead ones.

A good energy calibration is the result of a suite of dedicated actions. First the design of the detector is chosen to provide an intrinsic stability with variables like temperature, humidity, radiation, voltages, etc. Second a monitoring of these variables and of the detector response evolution with them is ensured. Third the cells are, at construction time, inter-calibrated at an adequate level of precision. Finally the absolute calibration is determined in test beams for few modules and globally at running time. The large number of cells is an asset, as teh calibration fluctuations decrease with $\sqrt{N}$ os the number of cells. The estimation of energy uses a combination of two estimators, the deposited energy and the counting of cells. The fully depleted silicon diodes offer a very stable behaviour. The tungsten plates can be checked. A complete cosmic ray testing produces the accuracy needed by measuring the minimum ionising particle peak. This has been done in the prototype with success. It is estimated to be a work of 200 days. The electronics is monitored accurately by injecting charges calibrated by a band gap device. It can be noted that the two estimators of energy are sensitive to very different systematic effects providing a powerful global test. After the inter-calibration, the absolute calibration is done by comparison with the tracker or using electrons and photons kinematically constrained like Bhabha's or return to the Z. This does not require any running at the Z peak

4.8.2.2 Scintillator Tungsten Electromagnetic Calorimeter

The scintillator ECAL consists of 1 cm $\times$ 4.5 cm scintilator strips, readout with Multi Pixel Photon Counters (MPPC). The calibration of these devices, similar to the analogue HCAL, needs to be done for the energy scale and limearity, and should be monitored against changes of environmental conditions such as temperatur etc.. The calibration will be based on a mixture of built-in calibration systems and the use of particle, either from cosmic-ray muons, or from test beams, before installation.

A further calibration of the strips may be done using tracks during operation of the device. To reach an accuray of 5% per channel, about 100 calibration quality tracks are needed. An ideal data sample for this would be an extended run at the Z-pole; to collect enough tracks about $100pb^{-1}$ would be sufficient. This amount of data will only be available at rather infrequent intervals, since it corresponds to a few weeks of running on the Z pole. However once calibrated the system is intrinsically stable if monitored well, and no frequent channel-by-channel recalibration is needed.

The photon sensor MPPC has a powerful built-in calibration capability, which is also used in the AHCAL. By identifying the response to single, two, three etc photons, a precise response and energy dependence can be established from data, for every single MPPC channel. THe single photon signals will be produced by a system of light fibres and blue LEDs, which

illuminate each channel with a well defined intensity. This system will be used to monitor the time dependence of the calibration constants as well.

4.8.2.3 Hadron calorimeter alignment

Depending on the choice of technology the hadronic calorimeter has cell sizes as small as $10 \times 10\text{mm}^2$, thus requiring a mechanical precision at the mm level for the absorber and sensor structures. This precision will be somewhat less stringent for the analogue hadronic calorimeter, which has larger cells. From the construction and survey the location of the cells to this accuracy will be known for the installed detector. The alignment required between different parts of the calorimeter system are also at a level of mm and will be established with data, based on muons from different sources.

4.8.2.3.1 Scintillator analogue hadronic calorimeter energy calibration The scintillator tile HCAL, segmented in 48 layers and 32 barrel, 32 end-cap modules, has 8 million read out channels. While electromagnetic and hadronic energy scales can be established with sample structures of the HCAL alone or in conjunction with the ECAL exposed to beams of muons, electrons and hadrons, the inter-calibration of the detector cells must be established with muon beams for all active layers of the detector. Based on test beam experience, we estimate that this can be accomplished in about two months. The calibration accuracy is maintained using LED monitoring of the photo-sensor gain, in-situ MIP calibration based on track segments in hadron showers and classical slow-control recording of the relevant operation parameters, temperature and bias voltage. These methods have been successfully applied to test beam data.

Simulating ILC events and using algorithms bench-marked with test beam data, we have determined the required luminosity for in-situ MIP calibration of individual cells and of average values for sub-sections of the detector, like module layers. A cell-by-cell in-situ calibration is not possible with realistic running times, but it is also not necessary. Average values for individual module layers can be obtained with a comfortable accuracy of 3% from a data set corresponding to $10pb^{-1}$ at the Z resonance or $20fb^{-1}$ at 500 GeV. For the innermost 20 layers, this accuracy is achieved with $1pb^{-1}$ or $2fb^{-1}$, respectively (see Fig. 4.8-38 for more details).

Using detailed simulations of the ILD detector and reconstruction based on the Pandora PFA, we have modeled different scenarios of statistically independent as well as coherent miscalibration effects, affecting the entire HCAL or parts of it. Purely statistical variations, like those arising from calibration errors or random aging effects, do not affect the resolution at all. However, they may degrade the in-situ MIP calibration capability. From this, a moderate requirement of the inter-calibration stability of 10% is derived. Coherent effects which could for example arise from uncorrected temperature variation induced changes of the response are potentially more harmful, as they directly show up in the constant term, if they affect the entire detector. However, these are easy to detect, and even a 5% variation only mildly propagates into the jet energy resolution. Systematic effects in sub-sections like layers are unnoticeable unless they exceed about 15%, comfortably in range of the in-situ calibration method accuracies.

The concept was experimentally verified by using data from two independent test beam experiments, performed with the same module, at two different locations CERN and Fermilab. The module which had some 9000 channels was calibrated based on data in one location, and

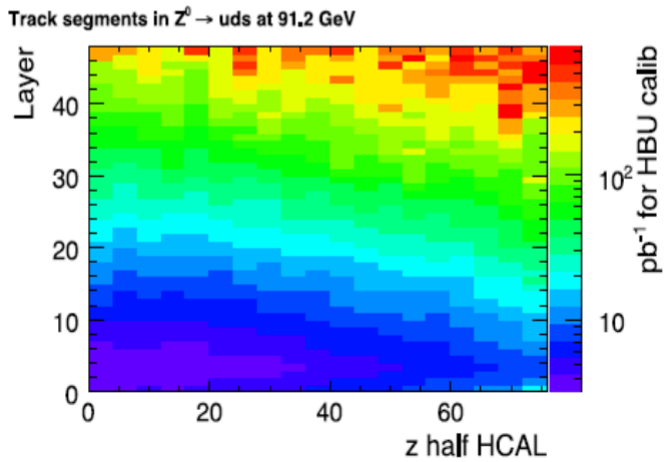

FIGURE 4.8-38. Required luminosity for an in-situ calibration of the AHCAL, as af function of position of the cell to be calibrated. The scale on the right gives the amount of integrated luminosity needed for one HCAL base unit (HBU).

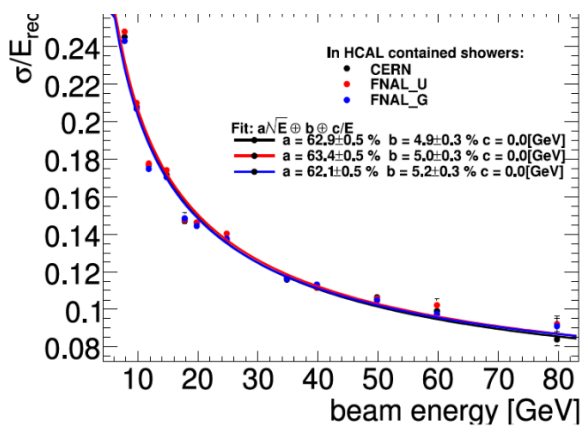

FIGURE 4.8-39. Comparison of measured energy resolution from three independent test beam experiments. The calibration constants were obtained in one experiment, and transported to the other ones. Excellent agreement is achieved, demonstrating the intrinsic stability of the system.

the calibration constants were then applied to the data recorded at the second location. The resulting comparison of the energy resolution of the detector is shown in Fig. 4.8-39.

We convinced ourselves of the validity of these simulation based estimates by treating our test beam experiment like a collider detector, using cell-by-cell inter-calibrations only from data taking at a different site, under different conditions. Applying only in-situ monitoring techniques, we re-established the scale and reproduced the resolution. Imperfections absent in the simulation showed up, but were successfully compensated. All in all, we conclude that the high granularity and channel count is a blessing rather than a curse. On one hand, thanks to the law-of-large-numbers suppression of statistical effects, the requirements on individual cell precision are very relaxed. Coherent effects, on the other hand, can be studied with any desired combination of channels, be it layers, longitudinal sections, electronics units or

according to any other supposed hypothesis of systematic effects. This has been proven to work with data taken at CERN and at FNAL.

4.8.2.3.2 Semi-Digital hadronic calorimeter energy calibration The most important features of the semi-digital HCAL option which have an impact on the calibration strategy are the large number of ≈ 70 million electronic channels, their semi-digital readout which means that efficiency is the meaningful quantity rather than energy, and the stable and homogeneous nature of the sensitive medium made of resistive plate chambers. The electronics calibration includes a gain correction procedure, a noise level measurement and a linearity measurement. The gain correction intends to reduce the dispersion of the electronic channels response to a given charge. A dispersion of a few percent for the threshold levels of the semi-digital electronics readout is currently obtained. The procedure is to inject charges corresponding to the lowest threshold level with different gains. The procedure is completely automated and will be applied to all the electronics boards before installation.

We foresee to apply the same procedure in situ. Based on our experience with a fully equipped $1m^3$ detector (9216 channels) we estimate that 200 minutes are needed to calibrate all the detector channels in parallel. The frequency of the calibration is under study. Preliminary results based on procedures applied one year apart on the same electronics board showed small variation ($< 2\%$).

To perform the detector calibration, a procedure will be used at construction time to qualify every piece, and a global control will be made at running time. The homogeneity of each GRPC detector will be tested by exposing all the HCAL detectors to cosmic rays before installation. To estimate the effort involved we can say that in order to achieve an efficiency measurement resolution better than 1% for each square cm of all the detectors using benches hosting five detectors, 5000 hours will be needed.

After installation, thanks to the detectors homogeneity only global efficiency of each detector needs to be controlled. This will be done using:

- Cosmic rays: Their number will depend on the detector depth. At sea level and taking into account the ILC duty cycle of 5% only a few hours are needed to calibrate the horizontal detectors. More time is needed for the inclined ones.
- Beam halo muons: At the ILC with the best currently proposed shielding scheme, 660 halo beam muons are expected per second to traverse the detector. Only a few seconds of running will be sufficient to calibrate the end-cap detectors based on these muons.
- Tracks produced in hadronic showers: There are few of them in each hadronic shower.
- Muons produced in data: Those produced from direct decay of $Z \rightarrow \mu^+\mu^-$ and those resulting from decays in the tau tau and $b\bar{b}$ channels become an essential source in case the GigaZ scenario is approved. With $10^{33} cm^{-2} s^{-1}$ of instantaneous luminosity less than five hours are needed to calibrate all the detectors.

In addition different procedures will be used to monitor the behaviour of the calorimeter, like following the leakage current, following the ratio of pads above the different thresholds. If necessary, we can consider injecting radioactive gas to check the response homogeneity.

4.8.3 Conclusions

In this section we have discussed the current state of thinking about aligning the different detectors in ILD. We propose to base the alignment on a mixture of harware alignment

systems, and a sophisticated use of tracks taken from data. Even though many details of the alignment systems still have to be finalised, and a lot of technical developments are still needed, we have established a number of key components central to the proposed procedures in test beam experiments. We are therefore confident that the system is adequate and that we realistically can expect to reach the anticipated precision required for physics at the ILC.

We consider the ability of the collider to deliver some luminosity on the peak of the Z resonance to be important and very beneficial for a fast calibration, and in particular a fast re-calibration after a push pull operation.

CHAPTER 5

Data Acquisition and Computing

As outlined in the detector outline documents [2, 3, 135] the data acquisition (DAQ) system of a detector at the ILC has to fulfill the needs of a high luminosity, high precision experiment without compromising on rare or yet unknown physics processes. Although the average collision rate of the order of a few kHz is small compared to the LHC, peak rates within a bunch train will reach several MHz due to the bunched operation. In addition the ILC physics goals require higher precision in many measurements than has ever been achieved in a colliding beam experiment. This improved accuracy can only be achieved by a substantially bigger number of readout channels than in previous detectors. Taking advantage of the bunched operations mode at the ILC, event building without a hardware trigger, followed by a software based event selection was proposed in [34] and has been adopted for the ILD. This will assure the needed flexibility as well as scalability and will be able to cope with the expected complexity of the physics and detector data without compromising on efficiency or performance.

The very large number of readout channels for the ILD will require signal processing and data compression already at the detector electronics level as well as high bandwidth for the event building network to cope with the data flow. The recently commissioned LHC experiments have up to 10^8 front-end readout channels and a maximum event building rate of 100 kHz, moving data with up to 100 GB/s [136]. The proposed ILD DAQ system will be less demanding in terms of data throughput but the number of readout channels is likely to be a factor of 10 or more larger. The computing requirements for the ILC event processing in terms of storage and CPU are also going to be less demanding than those of the LHC experiments. The details of the DAQ and computing system depend to a large extent on the developments in microprocessors and electronics and the final design of the different sub detector electronic components. Therefore the DAQ and computing system presented here will have to be rather conceptual, highlighting some key points to be addressed in the coming years.

5.1 DAQ CONCEPT

In contrast to past and recent colliders, such as HERA, Tevatron or LHC, which have a continuous rate of equidistant bunch crossings the ILC has a pulsed operation mode. The nominal parameter set [137] of the ILC with

- 2625 bunch crossings in a train about 1ms long,

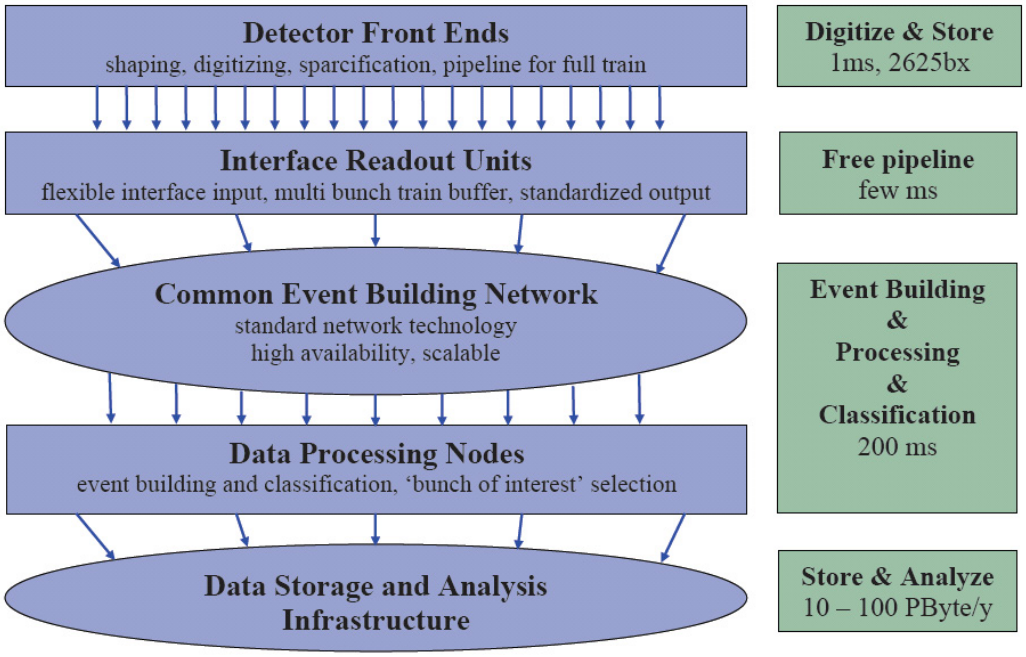

FIGURE 5.1-1. General layout of the DAQ system

- 369 ns between bunch crossings inside a bunch train and
- a bunch train repetition rate of 5 Hz

results in a burst of collisions at a rate of 2.6MHz over 1ms followed by 200ms without any interaction. The overall collision rate of 13kHz is significantly smaller then the expected event building rate for the LHC experiments.

The burst structure of the collisions at the ILC immediately leads to the suggested DAQ system with

- dead time free pipeline of 1 ms,
- no hardware trigger,
- front-end pipeline readout within 200 ms and
- event selection by software.

Rapidly developing fast network infrastructures and high performance computing technologies, as well as the higher integration and lower power consumption of electronic components are essential ingredients for the proposed data acquisition system. Furthermore for such large systems a restriction to standardised components is vital to achieve maintainability at an affordable effort, requiring commodity hardware and industry standards to be used wherever possible.

The general layout of the proposed DAQ system is shown in figure 5.1 The front end electronics on the detector or sensor level has to be detector specific and will digitize and store the data of ≈2600 bunch crossings. But already on or near the detector a standardized interface with additional buffering and processing capability will assure a common protocol for the subsequent event building which is currently estimated to be done by a standard switched network technology like 10G Ethernet. Event building of all data from the bunch train will be done in a single processing unit. Hence all data of the complete train will be available

Subdetector	Channels [10^6]	Occupancy [%]	Data volume [MB]
VTX	800	1.0	50
TPC	2	< 0.1	12
FTD	1	9	2
SIT	1	30	6
SET	5	1	1
ETD	4	10	7
ECAL	100	< 0.1	3
HCAL	8	1	130
MUON	0.1	< 0.1	≤ 1
LCAL	0.2	70	4
BEAMCAL	0.04	100	126
TOTAL	$\approx$920		$\approx$340

TABLE 5.1-1
Data Volume in MB per bunch train for the major ILD detector components

for the event processing without further data transfer which is essential since many detectors will integrate over several bunch crossings. The purpose of this online event processing will be mainly event classification, calibration, alignment and data quality monitoring. Although no event rejection is foreseen a scheme of event finders may be used to identify 'bunches of interest' which could then be used for the physics analysis or for fast analysis streams.

The data volume will be dominated by machine background which in turn is mainly pair production from beam-beam interaction(see section 6.7). For the nominal ILC parameter set it is expected that this background produces per bunch crossing $\approx$ 8000 hits in the HCAL, $\approx$ 150 hits in the ECAL, $\approx$ 400 hits in the TPC and $\approx$ 3 hits/cm^2 in the inner layer of the Vertex detector. Physics events which are less then 0.1 per bunch train will hence contribute less then 1% of the data recorded. Details of the simulated background are described in Section 6.7.

Table 5.1-1 lists the expected data volume per train for the major ILD detector components. Only values for the configuration used in the ILD detector simulation (see table 2.1-1) are shown as an example. For different technologies and options numbers may vary (DHCAL for instance $<$ 20MB). The occupancies are quoted for the detector-spcific time intervals. Some detectors digitise individual bunches, others like the TPC integrate over several bunches or the full bunch train.

The total data volume per trains is estimated to be $\approx$ 340MByte, hence the event building network has to cope with 1.7 GB/s. Assuming a safety factor of 10 on the background estimation and further contributions from electronic noise hits the maximum bandwidth anticipated is less than 20 GB/s. For the ILC Low-P parameter set backgrounds will increase by a factor 5 to 10 for the different subdetectors, with a resulting higher bandwidth demand.

Since machine parameters and beam conditions like beam energy or polarisation will be a vital input for the high precision physics analyses they should be stored alongside with the data. The time structure and data volume are similar, hence a common DAQ and data

storage model is envisaged.

5.2 FRONT END ELECTRONICS

In contrast to the central DAQ system the front end readout electronics for the different subdetector prototypes has to be designed now to allow for a realistic engineering and detector performance tests. Several approaches are underway for the calorimeters, TPC, silicon trackers and vertex detectors. Common to all the designs is a highly integrated front end electronics with signal shaping, amplifying, digitizing, hit detection, data storage and highly multiplexed data transfer to reduce the number of cables. Some designs foresee data processing like noise detection or cluster finding already at this stage to further reduce cables. For a detailed description see for example Section 4.4.5.3 on the calorimeter readout which had been developed for the EUDET project with a unified test beam DAQ system for various ILC Calorimeters.

For a highly granular detector like the ILD with the resulting large channel counts both the material budget as well as the power consumption are areas of concern. Minimizing the number of cables by data processing and multiplexing already on the sensor level is required as well as high density electronics with low power consumption. A common approach to reduce the power consumption is to turn the front end electronics off in the train gaps. First systems have been designed and build with this power pulsing capability.

5.3 DETECTOR CONTROL AND MONITORING

Modern data acquisition, detector control and monitoring systems are closely coupled to ensure good efficiency and data quality. An overall experiment control system will keep DAQ, detector control and monitoring synchronised, and assure proper timing, conditions and error handling. The systems should be designed such that subdetectors can be treated independently for commissioning or calibration runs in parallel to collision data taking.

In addition the ILD will be operated in a truly worldwide collaboration with partners all over the world. Similar to the global accelerator network (GAN) a global detector network (GDN) is proposed to operate the ILD detector remotely from the participating institutes. First experience was gained with the CALICE remote control room at DESY during test beams at CERN and FNAL. In addition the experience from the CMS remote operation centers at CERN, FNAL and DESY will be taken into account. The design of the DAQ and control system should have remote operation features built in from the start.

5.4 DATA PROCESSING

5.4.1 Event Building and Prompt Reconstruction

Event building and prompt reconstruction will be performed on the *Online Filter Farm* – a sufficiently large farm of processing units near the detector, connected to the front end electronics via the Common Event Building Network as shown in figure 5.1. Every data processing unit of the Online Filter Farm will process the data of one complete bunch train at a time. The raw data of a complete bunch train is kept in the raw data file after compression. This is essential as many detectors will integrate over several bunch crossings or even the

full bunch train. The event reconstruction will be an iterative procedure where in a first step a preliminary reconstruction will be done on the data from every subdetector. Bunches of interest are then identified by exploiting correlations in time and space between the data from all subdetectors. After calibration and alignment finally a full event reconstruction is performed on the event data. The reconstructed events are then written to the storage systems in an object oriented data format that is suited for further analysis with appropriate pointers into the raw data file containing the bunch train data. A first version of such an event data model has been developed and is in used for several test beam efforts and for the offline analyses within ILD [10]. An event filter mechanism run at prompt reconstruction will provide the necessary meta data for fast event selection at the physics analysis level.

5.4.2 Offline computing

The further offline data processing will exploit the existing Grid infrastructure for distributed computing using a multi-tier like approach similar to what is done for the LHC-experiments [138, 139]. The offline computing tasks such as the production of more condensed files with derived physics quantities (DST/AOD), Monte Carlo simulations and re-processing of the data will be distributed to the various tiers of the ILC-computing Grid. Setting up a data Grid and suitable data catalogues will allow the physicists to efficiently access the data needed for their analyses.

5.5 SOFTWARE

As is fairly standard with current HEP experiments, ILD will have a modular software framework based on object oriented programming languages such as C++. A component based plugin system together with well defined abstract interfaces will allow the flexible combination and exchange of algorithms with minimal configuration overhead. Using the same software components in the online and offline computing as much as possible will facilitate frequent data re-processing with improved calibrations and algorithms. A common object oriented persistency format that is used from the prompt reconstruction to the final analysis will allow transparent access to lower level data objects at later stages of the data processing chain. The actual raw data format containing the data read out per bunch train will essentially be defined by the front end electronics. Using abstract interfaces for the object oriented event data model will provide the flexibility to change the underlying persistency format in case the need might arise at some point in the lifetime of the experiment. The long term archiving of the data even beyond the experiments lifetime should be taken into account when choosing the persistency format. Data for calibration, slow control and alignment will be stored in a conditions database system that provides a suitable timestamp mechanism and versioning capabilities.

ILD already has two fully functional software frameworks (Sections 2.1.1, 2.1.2) which have been used for the massive Monte Carlo production for detector optimisation. One of the frameworks is also used by a number of ILC testbeam experiments for detector R&D [16] providing important feedback on the usability of the software in real world experimental conditions.

5.6 OUTLOOK AND R&D

Due to the timescales involved and the rapid changing computing and network market a decision on the DAQ hardware will be done as late as possible to profit from the developments in this area.

Nevertheless key elements of the DAQ systems have to be defined to guide the R&D of the subdetectors front end electronics especially when entering the technical prototype stage. This includes standardized interfaces to the central DAQ, online calibration and alignment strategies as well as detector control and monitoring concepts with remote operation build in. To gain experience and prepare for the decision on how to build the central DAQ system new developments and evolving standards, like ATCA [140] for example, should be evaluated in the next years.

In addition efficient event processing and event classification strategies taking realistic background simulations into account have to be developed. The ongoing test beam and simulation efforts will be a first step to learn how to treat the data but a more dedicated effort toward online processing and bunch tagging in a multi bunch environment will be needed to ensure efficient processing.

GRID resources currently available for post-LOI studies are limited. Especially, the inter-regional bandwidth (between Europe and Asia), CPU and storage resources especially in Asia, and the connectivity to OSG-GRID are the area which need more improvement.

A continues effort on improving the software framework according to needs and adapting to new computing hardware, introducing multi-threading capabilities for multi core processors for example, is needed to keep up with the activities both in the subdetector R&D as well as the computing infrastructure

CHAPTER 6

Detector Integration
Machine Detector Interface

6.1 MECHANICAL CONCEPT

The mechanical design of the ILD detector is shown in figures 1.2-1 and 6.1-1. The major components are the five parts of the iron return yoke: three barrel rings and two endcaps. The central barrel ring carries the cryostat with the solenoid coil in which the barrel calorimeters are installed. The TPC and the outer silicon envelope detectors are also suspended from the cryostat using tie rods. The endcap calorimeters are supported by the endcap yoke sections which can be moved independently from the barrel sections to allow an opening of the detector at the beam line. The beam pipe, the vertex detector and the other inner silicon detectors are supported from a structure of carbon fibre reinforced plastic (CFRP), which hangs at the flanges of the TPC field cage. The whole structure can be aligned with respect to the beam axis using actuators and a laser alignment system. The QD0 magnets are mounted independent of the yoke endcaps in a support structure that carries the magnets and the forward calorimeters. This structure is supported from a pillar outside of the detector and is suspended from the solenoid cryostat using tie rods. The QD0 magnets are also monitored

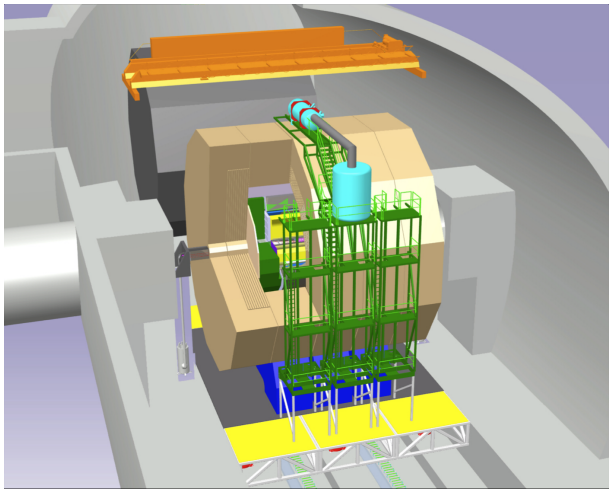

FIGURE 6.1-1. The ILD detector and its services.

by a laser alignment system and can be moved using actuators.

A full 3D CAD model of the ILD detector exists and is the baseline for all engineering and technical studies presented in this LoI. The actual dimensions and masses of the ILD subcomponents can be found in [141]. The engineering model of ILD has been synchronised to the detector model used in the full detector MC studies. A detailed description of the integration of the ILD detector including a conceptual scheme for the cabling is given in [118].

6.2 DETECTOR ASSEMBLY AND OPENING

The ILD detector will be assembled in large parts in a surface building above the underground experimental hall. The pre-assembled sections will then be lowered into the underground cavern using a temporary portal crane. The largest and heaviest (≈3500t) part will be the central barrel ring with the solenoid coil and the barrel calorimeters installed. The underground assembly sequence comprises the following steps:

1. The first pillar for the support of the QD0 magnet is installed. This pillar needs to be movable in the garage position but will not move on the beam line. The service helium cryostat is also carried by the pillar.
2. The QD0 magnet is suspended from the pillar together with its support structure.
3. The endcap yoke with the pre-mounted endcap calorimeters are installed.
4. The first part of the barrel yoke is installed.
5. The central part of the barrel yoke carrying the coil and the barrel calorimeters is installed; the cables are routed through the slits between the central yoke ring and the other rings.
6. The TPC is inserted, the cables follow the same routes as the cables of the barrel calorimeters.
7. The inner part of the detector including the beam pipe and the inner silicon detectors is inserted into the TPC, cables are routed to the outside following the same routes as the cables of the barrel calorimeters.
8. The third part of the barrel is lowered.
9. The second pillar, QD0 (with support) and the second yoke endcap are installed.

The detector can be opened and maintained in the garage position using the above described procedures. The space required is available in a garage zone with side access tunnels (c.f. figure 6.2-2). It is planned to allow the opening of the detector endcaps also at the beam line. As space is limited there due to the machine elements, only limited access can be reached. The QF1 magnets including their ancillaries extend to ≈9 m from the IP. Preliminary studies show that access space of ≈1 m can be gained between the endcap and the barrel yoke. This would allow limited access to the inner detector for short maintenance and connection/deconnection actions at the beam line (c.f. figure 6.2-2). Major interventions would be done in the garage position taking advantage of the push-pull system.

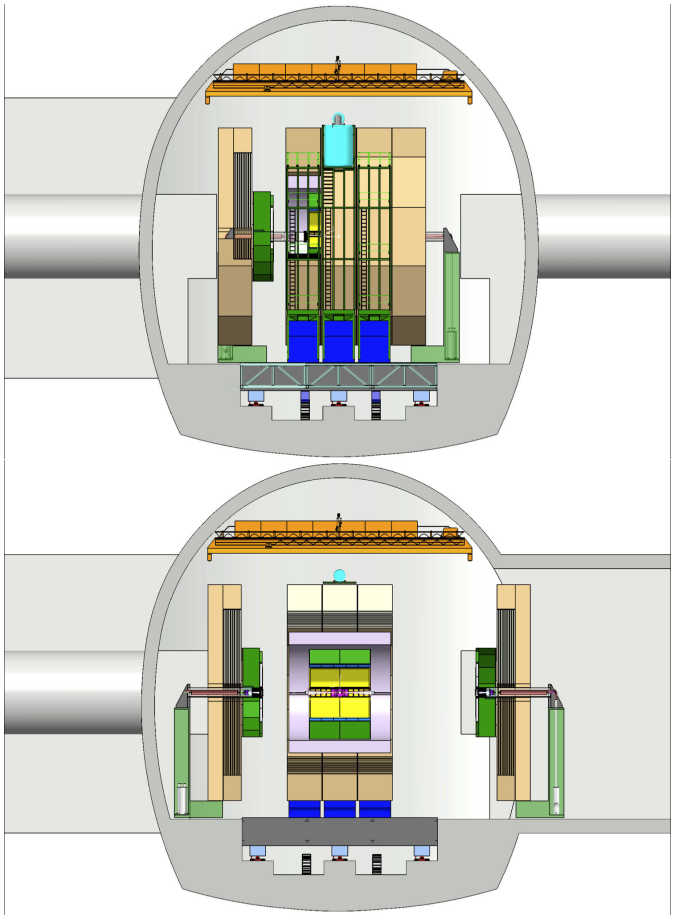

FIGURE 6.2-2. Detector opening on the beamline (top) and in the garage position (bottom).

6.3 CIVIL FACILITIES AND SERVICES

6.3.1 Detector Services

A number of services are needed for the operation of the ILD detector. The concept of push-pull puts stringent requirements on the design, as the services need to be designed for a moving detector. Therefore they must be integrated in the design of the detector and the civil facilities from the beginning.

6.3.1.1 Primary Services

Primary services are usually provided by installations that are located on surface due to their dimensions, possible impact on the detectors (vibrations, etc.) and related risks. Examples are water chillers that provide cooling water, high to medium voltage power transformers (e.g. 18 kV/ 400 V AC tri-phase), UPS facility (Diesel generator), helium storage and compressor plant for the solenoid coil and gas and compressed air plants.

6.3.1.2 Secondary Services

Secondary service plants often need to be close to the detector and should be located in the underground areas. Typical secondary services are temperature stabilised cooling water,

voltage supplies for front-end electronics, AC/DC converters for the super-conducting coil and cryogenics and vacuum services. Data connections for the transmission of the detector readout also need to be included. Due to the push-pull design, these services are permanently connected and run in cable-chains towards the detector. As the flexible pipes and cables in the chains need to be kept within reasonable lengths, it would be very convenient to locate a small service cavern for the secondary services at the end of the main underground cavern with independent ventilation and limited crane access. Electrical noise and vibrations are kept away from the vicinity of the detector, and people working in the main underground cavern would also be protected from physical noise coming from various equipment. The main benefit of the usage of cable chains is the permanent connection of the detector to all its services and readout cables. The chains can be equipped when the detector is still being assembled on the surface, and this would greatly speed up the connection and commissioning time in the underground cavern once the detector parts are lowered. The hall floor can be kept clean and without obstructions by the use of cable chains.

6.3.1.3 On-Board Services

Some secondary services need to be carried on board with the detector if the connection through cable chains are found to be technically difficult or too expensive. As this increases the risks for the detector operation in the push-pull scenario, these on-board services should be kept to a minimum. Examples are the service cryostats for the helium supply for the solenoid and the QD0 magnets.

6.3.1.4 Cryogenics

Figure 6.3-3 shows the block diagram of the cryogenics needed for the operation of the detector solenoid coil and the QD0 magnets. While the primary facilities like the helium storage and compressors are on the surface, the helium liquefier (4K) and the re-heater are in the underground hall. Directly on-board of the detector are the valve box, which distributes the helium to the coil, and the liquid helium tank. Also the 2K sub-cooler and the service cryostat for the QD0 magnet are moving with the detector.

6.3.2 Surface Assembly Hall

The detector will be assembled in a surface hall. The RDR baseline design of the surface hall (100 × 25m, 25 m high, 400 t crane capacity) is well suited for the assembly of the ILD detector. A portal crane with a capacity of 3500 t needs to be installed temporarily at the main shaft to lower the pre-assembled detector elements into the underground cavern.

6.3.3 Underground Experiment Hall

The underground experiment hall needs to accommodate both push-pull detectors. The design of the hall presented in the ILC RDR [137] has not been optimised taking into account realistic assumptions for the services of the detector in the push-pull environment. Figure 6.3-4 shows a design study of the underground hall which has been optimised for ILD taking into account the following criteria:

- minimum impact on civil engineering cost with respect to the RDR baseline (reduced main cavern diameter and length),

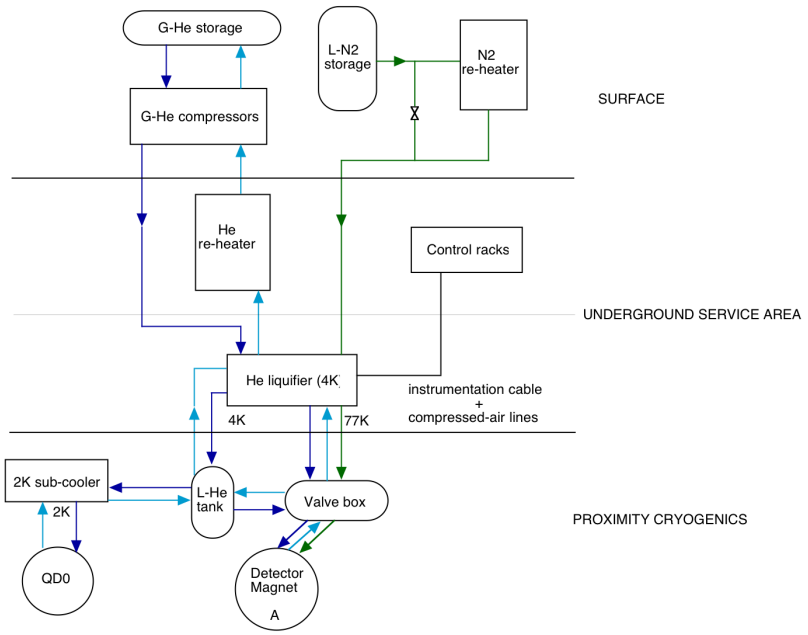

FIGURE 6.3-3. Diagram of the cryogenic services for the detector.

- enhanced safety and reduced time losses by moving the shaft from the cavern ceiling to a side alcove providing also the necessary space for the full opening of the detector,
- small service cavern at the end of the hall for the secondary services (6.3.1.2),
- optimised for push-pull.

A hall width of 25 m is sufficient for the detector assembly and maintenance procedures as the side alcove for the vertical shaft increases the parking positions substantially. The beam height has been assumed to be 12 m from the floor of the hall. This allows for the detector to rest on a 2-m-high platform. It must be noted that if the experimental area is a deep construction in a terrain requesting a cylindrical or semi-cylindrical hall for question of rock stability the space situated below the floor level has to be filled with concrete up to the proper level. The platform and the cave-like structures containing the supporting mechanism and the cable are thus just a special part of this filling. As the heavy parts of the detector will be moved on air pads and on the platform, the crane capacity in the underground hall is modest. Two 40t cranes, which can be connected to form an 80t crane are largely sufficient.

6.4 PUSH-PULL OPERATIONS

The present ILC baseline design foresees one interaction beamline that needs to be shared by two detectors in a push-pull configuration. While one detector is taking data on the beamline, the other one is parked in its garage position in the same underground hall. Following a still-to-be-defined time schedule, the detector on the beam line is moved away to its own garage position to make space for the waiting detector to collect data. This push-pull scenario has never been tested at existing accelerators and poses unprecedented engineering challenges to the detector designs.

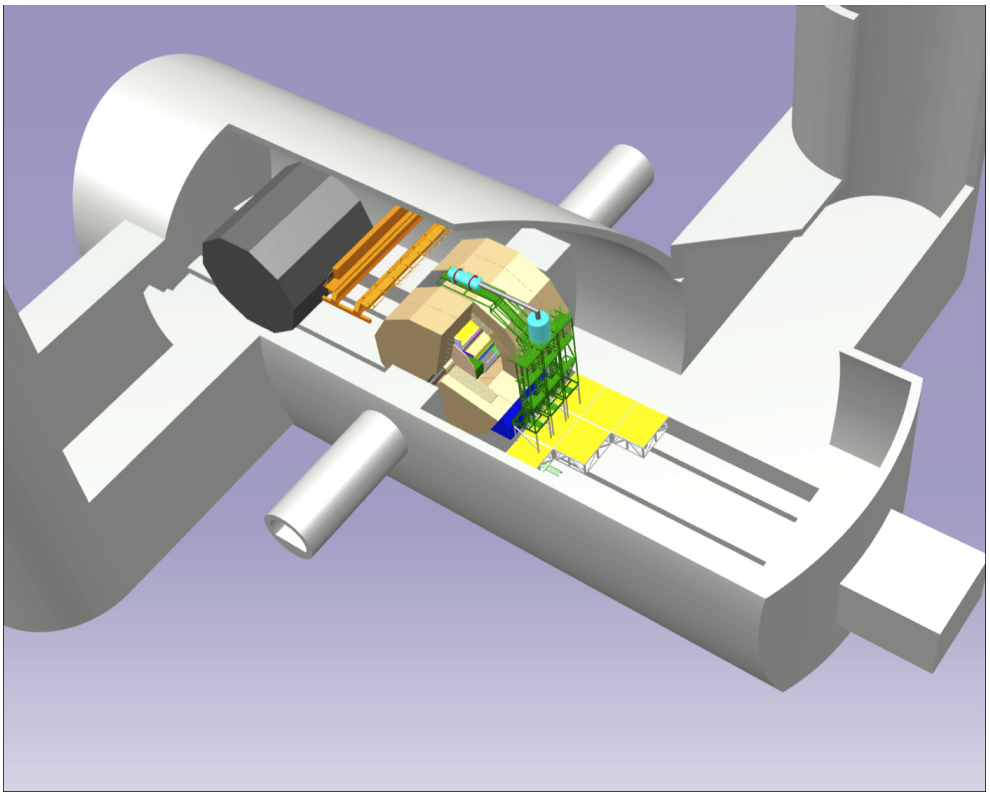

FIGURE 6.3-4. Design study of the underground experiment hall with ILD (left) and the second detector in push-pull configuration.

The LoI concept groups and the ILC Beam Delivery System group have agreed on a set of minimum functional requirements [142] which define the boundary conditions for the push-pull operations. Most of these requirements comprise geometrical boundaries, like the size of the underground hall or the limits of the garage position of the detectors. But also physical limits for ionising radiation and magnetic fields need to be defined to allow a friendly co-existence of two detectors in one hall. In addition direct requirements come from the machine itself. As the QD0 final focus magnets will move with the detectors, requirements on alignment tolerances and vibration limits have been defined.

The timescale for the push-pull operation needs still to be defined, but it is clear that the time for the exchange of both detectors needs to be minimised to maximise the integrated luminosity. The full push-pull procedure comprises for the outgoing detector:

- securing the beams,
- powering down of the detector solenoid,
- removing the radiation shield between detector and hall,
- disconnecting all local supplies (in principle only the main bus-bars),
- disconnecting the beam pipe between the QD0 and the QF1 magnets,
- moving the detector out towards its garage position,
- connecting back the main bus-bars in the garage position.

For the incoming detector the procedure is reversed, but additionally needs to include time for alignment and eventually calibration of the detector system at the beam line. It is

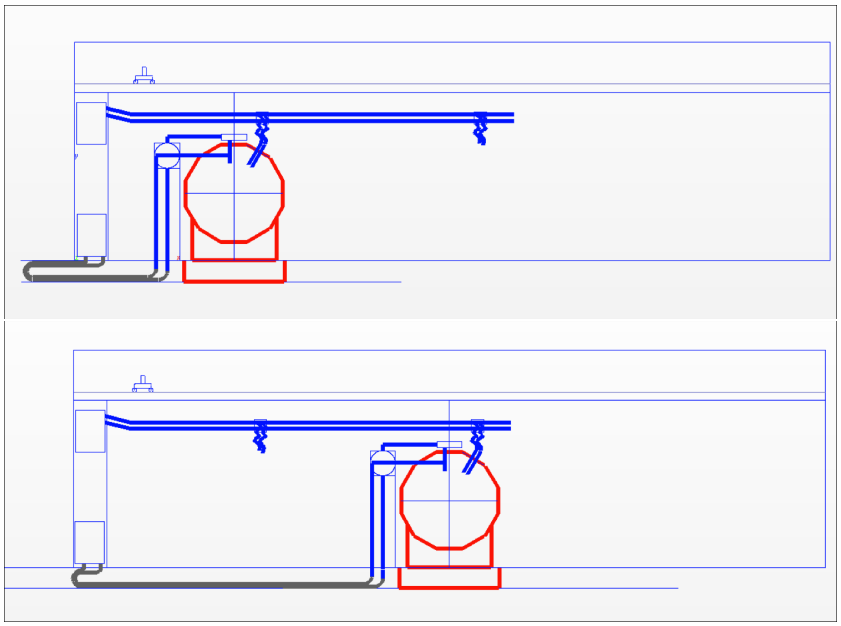

FIGURE 6.4-5. ILD detector in the garage position and on the beam line. The detector will be disconnected from the power bus bars (top, blue) during movement, while the cables and cryogenic service lines run in cable chains (bottom, grey).

envisaged to complete the full push-pull operations on a timescale of about two days after procedures have been optimised based on experience. However, as the full understanding of the challenges requires a detailed engineering design of the hall and the definition of the procedures, a final evaluation of the push-pull operation for ILD is beyond the scope of this LoI and needs to be studied in the following Technical Design Phase. Nevertheless this section describes our conceptual understanding of the ILD operations.

6.4.1 Moving the ILD Detector

The ILD detector will be placed on a concrete platform to avoid possible damages due to non-synchronised movements or from vibrations during push-pull and also to ease internal alignment challenges. The concrete platform will have a size of approximately 15 $\times$ 20m and needs to be $\approx$ 2m thick. Figure 6.3-4 shows the ILD detector on its platform on the beam line. The platform will move on the hall floor using a system of rollers suitable solution for this one-dimensional movement or air pads that may provide more easily a millimetric positioning tolerance.

All supplies for the detector will be provided by using flexible supply lines that move with the platform. This includes the cryogenic lines that supply the detector solenoid and QD0 systems with 4K helium. As the development of flexible cryo lines for 2K helium is challenging, the QD0 magnet will be connected permanently to a service cryostat that moves together with the detector on the platform. As the detector solenoid does not need to be powered during the movement, the detector can be disconnected from the power bus bars and re-connected in the parking position. Figure 6.4-5 shows a schematic drawing of the movement of the detector with the cable chains and the power bus bars. The detector elements can be moved on the platform by using either a roller system, or by using air pads similar to the solution CMS has adopted. As the axial space at the beam line is limited, only the opening

of the detector endcaps is foreseen to allow a limited access to the inner detectors. In the garage position more space is needed to allow major maintenance work, e.g. the removal of the TPC. More details of the opening procedures are described in section 6.2.

6.4.2 Shielding

The ILD detector will be self-shielding with respect to maximum credible accident beam loss scenarios. Detailed simulations show [143] that a proper design of the detector provides shielding which is sufficient to still allow access to the detector hall for professional workers. This is important to fulfil the minimum requirements which are needed to allow access to the other detector in its garage position during beam operations.

A movable concrete shield needs to fill the gap between the detector and the walls of the underground hall. As this shielding needs to fit both detectors, no engineering effort has been pursued so far to find a detailed design. This has been referred to the Technical Design Phase where it will be studied in collaboration with the second detector concept group. Nevertheless, these kind of shieldings have been used in other accelerator experiments (e.g. at HERA) and pose no conceptual design challenge.

6.4.3 Alignment and Calibration

The ILD detector will be moved on a platform that will be repositioned very precisely on the IP. Nevertheless, the alignment of the detector after being brought to the beam position is not trivial. The functional requirements ask for an alignment accuracy of the detector axis $\pm$1mm and 100μrad after push-pull. The requirements for the QD0 magnet are even tighter: $\pm$ 200 μm and 5 μrad. ILD will be equipped with a laser-interferometric alignment system like MONALISA [144]. This system allows for alignment of both QD0 magnets which are carried by the detector to the ILC beam lines on each side of the hall. In addition, the detector itself can be positioned within the required tolerances using this system. The QD0 magnets will be placed on actuators that allow for an independent alignment of the magnets with respect to the detector.

After the alignment of the detector described above and the commissioning of the beam, some calibration data taken at the energy of the Z resonance would allow to check the alignment of the subdetectors. The internal alignment of the subdetectors can then be done most precisely in offline analysis. This technique was used at LEP where experience shows that about 1 pb^{-1} of calibration data on the Z peak will be sufficienct after the push-pull procedure at ILC [96]. If the ILC machine cannot easily switch between Z-peak and $\sqrt{s}$ running, then other techniques than used at LEP will be developed.

6.5 R&D PLANS: DETECTOR INTEGRATION

This Letter of Intent describes a conceptual design of the integration efforts for the ILD detector. Though no show-stoppers have been identified, a challenging engineering programme needs to be set up to transform this conceptual design into a technical design based on engineering studies. Main points of work will be among others:

- Integration of the subdetectors in close collaboration with the subdetector R&D groups.
- Engineering design of the yoke.

- Opening and assembly procedures including a study on the tooling needed for it.
- Development of an engineering solution for push-pull. This includes the very important issue of cryogenic supplies for a moving detector.
- Find an optimised underground hall design in close collaboration with the ILC machine CF&S group and the other detector concept groups. This includes a common shielding strategy.
- Elaborate the alignment strategy and find technical solutions for interferometric systems la MONALISA.

6.6 THE INTERACTION REGION

The interaction region of the ILD detector comprises the beampipe, the surrounding silicon detectors, the forward calorimeters with the masking system and the QD0 magnet with its ancillaries and the support structure. Figure 6.6-6 shows a blow-up of this region.

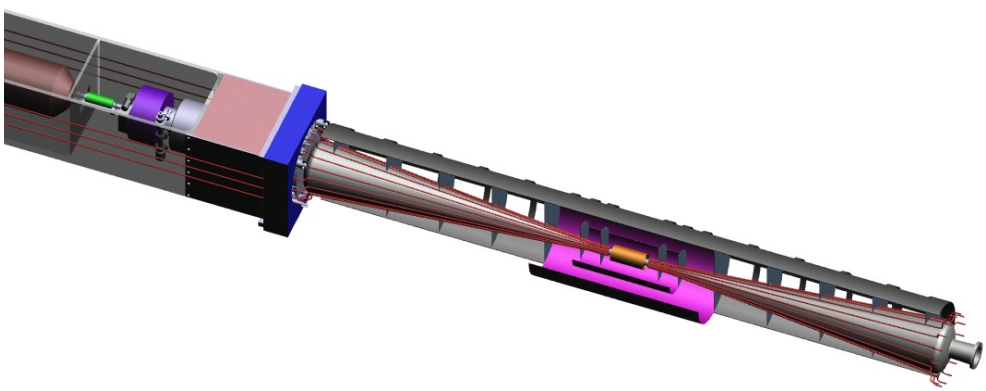

FIGURE 6.6-6. Interaction region of the ILD detector. Shown are the vertex detector (yellow), the SIT (pink), the ECAL plug (blue) with the LumiCal, the LHCAL (light red) and the BeamCal (violet). The routing of the cables is also shown.

6.6.1 The Beampipe

The design of the beam tube has to obey several constraints:

1. It must not interfere with the luminosity.
2. Its central part must be small enough to optimise the measurement of the impact parameter and large enough not to interfere with the background.
3. It must comply with a crossing angle of 7 mrad.
4. It must be as light as possible to reduce photon conversions and hadron interactions, withstanding nevertheless the atmospheric pressure.
5. It must not induce electromagnetic perturbations generating heat.
6. It has to be pumped down to an agreed level.

6.6.1.1 Mechanics

The current mechanical design is shown on figure 6.6-7. The tube is conical, offering very little matter in front of the luminosity monitor LumiCal (LCAL). The tube is made of beryllium with some ring reinforcements at the level of the forward detectors. The part inside the vertex detector is a cylinder, the connection with the large cone is such that background does not interfere. This very thin tube (8 kg total) has to be supported from the inner detector structure. The mechanical behaviour has been studied in detail [145]. The most important constraint is related to the buckling where a safety coefficient of 6 is being considered, see figure 6.6-8. To go beyond this first approach, one would need to work with manufacturers because the technology becomes very important. The example of LHCb tube shows that such a tube results from a strong R&D by the manufacturer on the way to realise cones and to perform the weldings. Figure 6.6-7 shows the dimensions, figure 6.6-8 shows the buckling behaviour.

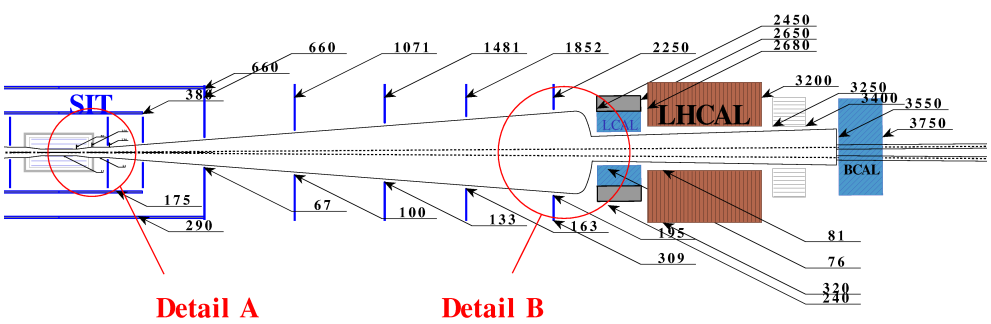

FIGURE 6.6-7. Beam pipe geometry.

6.6.1.2 Vacuum

The vacuum situation in the beam pipe has been studied in detail [146]. It is assumed that the whole beam pipe would be pumped by vacuum pumps which are located in the space between the LHCAL and the BeamCal, about 3.3 m from the IP. Assuming effective pumping speeds of 0.72 (0.12) m^3s^{-1} for H_2 (CO) yields in pressures of approximately 1×10^{-6} (6×10^{-7}) Pa. The limit on the effective pumping speed is given by the conductance of the small pipe at the back side of the conical part. The vacuum profile for H_2 is shown in figure 6.6-8.

6.6.1.3 Wakefield Losses

The wakefields generated by the passing beam in the beam pipe result in parasitic losses which have been studied taking into account the ILC Low-P beam parameters [146]. The parasitic losses are in the range of 20-24 W so that air cooling will be sufficient to remove this additional power. Higher order modes can be excited in the beam pipe, the resulting parasitic losses are small and will be dissipated in the surface region of the beam pipe.

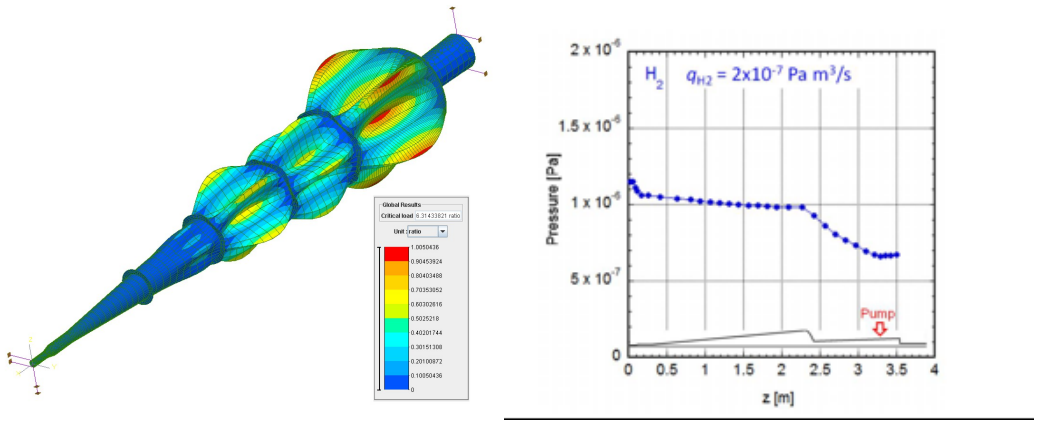

FIGURE 6.6-8. Beampipe buckling (left) and vacuum profile for H_2 (right).

6.6.2 Support of the Final Focus Magnets

While the QF1 magnets of the final doublet will stay fixed in their positions, the QD0 magnets need to move with the detector during push-pull operation. The magnets are installed in a support structure which is supported from pillars residing on the push-pull platform. The support structure has a square cross section and is suspended from the solenoid cryostat using carbon-fibre tie rods (c.f. figure 6.6-9. This assembly allows the opening of the yoke end caps without interference with the alignment of the QD0 magnets. The inner silicon

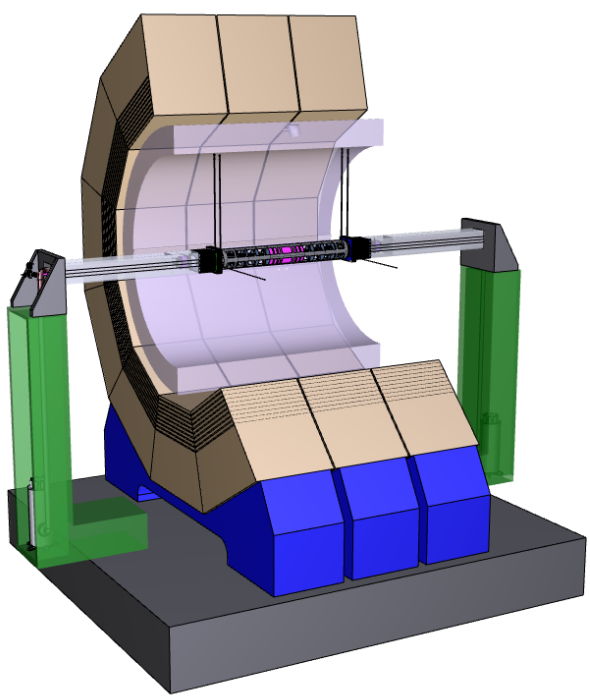

FIGURE 6.6-9. Support of the magnets in the detector. The inner detector part and the beam pipe are suspended from the TPC end flanges, not shown in this figure.

detectors (SIT, vertex detector) and the beam pipe are supported by a CFRP structure

which is suspended from the TPC end flanges. The QD0 magnets reside on actuators in their support structure and are monitored using an interferometric laser alignment system like MONALISA [144]. The service cryostat for the supply of the QD0 magnets on the beam line, in the garage position and during the push-pull operations are located at the bases of the pillars and move with the platform.

The stability of the QD0 support structure has been studied. The vibrations induced by ground motions are at most 2.2 nm at 8.3 Hz which is below the limits of 50 nm defined in the minimum requirements document [142].

6.7 MACHINE-INDUCED BACKGROUNDS

Machine-induced backgrounds have been studied in detail for the ILD detector and its predecessors GLD and LDC [2, 3]. The main relevant background are pairs from beamstrahlung which are produced in the highly charged environment of the beam-beam interaction. The background levels found are well below the critical limit for most sub-detectors. The subdetector most sensitive to beam-related backgrounds is the vertex detector, which features an inner radius value dictated by the maximum affordable beamstrahlung hit rate.

Table 6.7-1 summarises the expected background levels in the ILD subdetectors for several beam parameter sets: the nominal ILC beam parameters for 500 and 1000 GeV cms energy and the Low-P parameter set[1]. The numbers are the result of a study using the same full ILD detector Monte Carlo that has been used for the physics studies described in this LoI (c.f. sections 2 and 3), i.e. with the nominal detector geometries and 3.5 T magnetic field. In these background simulations, the double-layer option of the vertex detector has been chosen. It should be noted that the background numbers for the single-layer option are 15% larger for the inner layer due to the smaller radius. The ILC parameter sets used are the ones described in the ILC Reference Design Report [137]. It should be kept in mind that the numbers given are per bunch crossing (BX). As in the different ILC parameter sets the bunch crossing distance varies, the number of hits per subdetector readout must be scaled accordingly, if the corresponding subdetector integrates over several bunch crossings.

Figure 6.7-10 shows the distribution of the background hit densities on the inner silicon detectors (VTX-DL, SIT, FTD). The correlation of the hit densities with the distance from the interaction point can clearly be seen. The most critical point is the innermost layer of the vertex detector.

6.7.1 Background Uncertainties

As the vertex detector is most critical with respect to beam induced backgrounds, detailed studies have been performed to understand the influence of different detector geometries and simulation parameters like the choice of range cut parameters in Geant4. The number of hits on the vertex detector change up to 30% which gives an order of magnitude of the uncertainties for these simulation results [59]. Another study of the uncertainties of the background simulations has been done in [88] where a general safety factor of 5-10 has been suggested.

[1]The Low-P parameter sets might require modifications to the baseline detector design which are discussed in section 6.7.2. The numbers in the table are valid for the baseline detector design only.

Subdetector	Units	Layer	Nom-500	Low-P-500	Nom-1000
VTX-DL	hits/cm^2/BX	1	3.214±0.601	7.065±0.818	7.124±1.162
		2	1.988±0.464	4.314±0.604	4.516±0.780
		3	0.144±0.080	0.332±0.107	0.340±0.152
		4	0.118±0.074	0.255±0.095	0.248±0.101
		5	0.027±0.026	0.055±0.037	0.046±0.036
		6	0.024±0.022	0.046±0.030	0.049±0.044
SIT	hits/cm^2/BX	1	0.017±0.001	0.031±0.007	0.032±0.012
		2	0.004±0.003	0.016±0.005	0.008±0.002
FTD	hits/cm^2/BX	1	0.013±0.005	0.031±0.007	0.019±0.006
		2	0.008±0.003	0.023±0.007	0.013±0.005
		3	0.002±0.001	0.005±0.002	0.003±0.001
		4	0.002±0.001	0.007±0.002	0.004±0.001
		5	0.001±0.001	0.006±0.002	0.002±0.001
		6	0.001±0.001	0.005±0.002	0.002±0.001
		7	0.001±0.001	0.007±0.002	0.001±0.001
SET	hits/BX	1	5.642±2.480	57.507±10.686	13.022±7.338
		2	5.978±2.360	59.775±8.479	13.711±7.606
TPC	hits/BX	-	408±292	3621±709	803±356
ECAL	hits/BX	-	155±50	1176±105	274±76
HCAL	hits/BX	-	8419±649	24222±744	19905±650

TABLE 6.7-1
Pair induced backgrounds in the subdetectors for nominal (500 GeV and 1 TeV) and Low-P (500 GeV) beam parameters. The numbers for the ECAL and the HCAL are summed over barrel and endcaps. For the vertex detecor, the double-layer option has been chosen for this simulation, the numbers for the single-layer option differ. The errors represent the RMS of the hit distributions of the simulation of ≈ 100 bunch crossings (BX).

6.7.2 Provisions for the Low-P Beam Parameters

The Low-P beam parameter set assumes an ILC machine with less RF-power available. The number of bunches in a train is reduced while the loss in luminosity is compensated by squeezing the bunches to smaller sizes during the collisions. This results in larger losses due to beamstrahlung photons and therefore in a diluted luminosity spectrum. On the other hand the number of pairs produced in beamstrahlung gamma collisions is enhanced significantly.

Table 6.7-1 shows how the increased pair production results in an increase of background hits in the subdetectors. Especially the inner vertex detector layer suffers from the enhanced backgrounds[2]. Matters to remedy the situation are still under study a possible solutions is an increased radius of the inner vertex detector layer. Also the ladder of the inner layers might need to be shortened to keep their read-out electronics out of the hot cone of the beamstrahlung pairs.

[2]It should be remembered, however, that the numbers in the table are given per bunch crossing. As the bunch spacing in the RDR Low-P option is increased to 480.0 ns as compared to the 369.2 ns in the nominal case, the background numbers per readout need to be scaled down by ≈25% for Low-P to make them comparable to the nominal case.

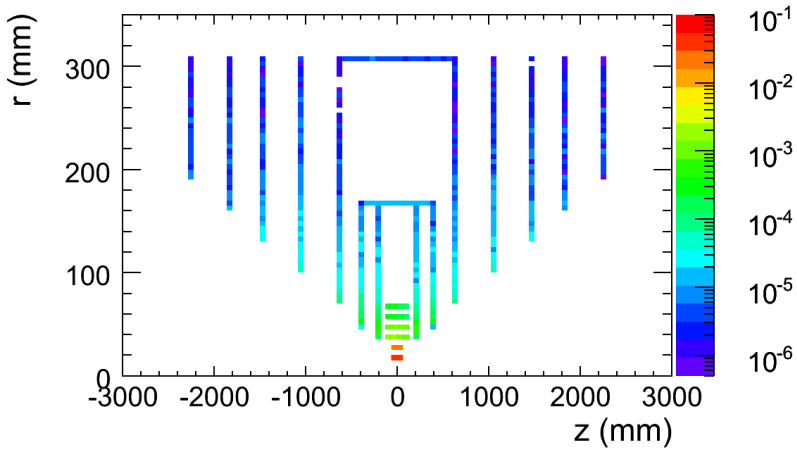

FIGURE 6.7-10. Distribution of the background hit densities on the inner silicon detectors (VTX, SIT, FTD) in units of [hits/mm^2/BX].

6.8 MEASUREMENT OF ENERGY AND POLARISATION

Traditionally the methods of measuring the beam energy and the beam polarisation are also parts of the Machine Detector Interface. As the polarimeters and the energy spectrometers are not a part of the detectors at the ILC but are common facilities in the machine, we will refer here only to the common design efforts [51].

6.9 R&D PLANS: MACHINE DETECTOR INTERFACE

As in the area of detector integration 6.5, also in the integration with the accelerator many topics need to be studied in engineering detail level before the construction of the detector could be envisaged. Important R&D topics are e.g.:

- Engineeering study of the beam pipe including its vacuum behaviour in close collaboration with possible manufacturers.
- Support and monitoring of the QD0 magnets. Adaptions to new BDS schemes which would allow larger L* optics.
- Detailed study of the beam induced backgrounds.

CHAPTER 7

Costing

The cost of the ILD detector as presented in this section has been evaluated based on a common methodology of costing, and a detailed work breakdown structure for each of the sub-detectors. Costing a detector as complex as ILD at this early stage of the project is difficult at best, and certainly not precise. For this document, a rather crude evaluation has therefore been done focusing on the cost driving items. Another important aspect was as well to understand the scaling of the cost of the different sub-systems with the main design parameters, to realize the impact of the sub-system on the overall cost, and to evaluate possible cost savings versus performance.

7.1 METHODOLOGY OF COSTING

The method used here follows the prescriptions from the GDE at the time of the RDR. For each important item a work breakdown structure (WBS) has been developed, and each part has been costed to the best of our knowledge up to a level equivalent to about 1% of the total cost. The bases of the cost have been experience when constructing the LHC detectors and ILD prototypes, and, in some cases, quotes from manufacturers. An attempt has been made to use consistent cost numbers across different sub-detectors. The prices are expressed in ILC units (ILCU) which correspond in 2006 values to 1 US dollars, 117 Yen or 0.83 EUR.

No attempt was made to guess the impact of future escalation. Contingencies are currently not taken into account. No R&D costs are included, except in some cases costs for industrialisation. No maintenance and operation has been estimated. In some instances, prices for the same item vary widely between different countries and regions. In this case the price used is the one proposed by the group in charge of this component. Different options have been costed independently, but the tables and numbers correspond to the detector which has been simulated for physics studies.

It should be noted that the level of detail and even of understanding for the different sub-detectors and options may be different. This may reflect in the cost estimates as well as in the performances. The manpower has been estimated roughly from past experiences for the different items and is added globally. Some options have no estimate yet.

7.2 ILD WORK BREAKDOWN STRUCTURE

The actual WBS for the different sub-systems can be found in [147] . The list of sub-systems under consideration is given in table 7.3.

As a guide we tried to estimate for the different systems the following items:

- the amount of material and a unit price, the manufacturing,
- the sensors,
- the front-end electronics including printed circuit boards,
- the local acquisition, testing and calibration,
- the transportation (not knowing where it is made and where is the experimental site),
- the assembly on site, tooling,
- the spares and miscellaneous.

7.3 ILD CURRENT COST EVALUATION

The following material costs have been used in the estimate:

- Tungsten at 120 ILCU/kg (from a quotation for 40t of pure tungsten plates with tolerances),
- Stainless steel for the Hcal at 18 ILCU/kg (from Atlas), and for the cryostat 15 ILCU/kg for SS304,
- Yoke steel (low carbon) at 4.1 ILCU/kg,
- Silicon strips for tracking at 7 ILCU/cm^2,
- Silicon sensors for ECal at 3 ILCU/cm^2,
- SiPM(MPPC) at 1.2 ILCU per piece from industrial quotation.

The cost estimates for the different sub-systems in ILD are listed in table 7.3. In addition we estimate the cost for other options to be 41 MILCU for the DHCal and 35.7 for the SC-ECal.

The cost driving items are the yoke, and the calorimeters. The price for the yoke is as large as it is as a direct consequence of the push-pull operation. The restriction on the stray-field outside the detector can only be met with a rather thick iron yoke, inflating the price significantly. The cost for the integration is an estimate of the scenario described in section 6, and might vary significantly with different scenarios. It includes the extra cost for the large platform on which the detectors moves, as well as the extra costs of the cryogenics needed to allow a cold move of the detector. In the absence of platform and cable chain, the lower part of the experimental hall would have to be filled with concrete. The cost for this is subtracted. Some integration tooling has been added. The offline computing represents a significant cost. Owing to the continued large advances in computing technology, we have estimated this at 20% of the equivalent cost for the LHC detectors.

A first estimate of the manpower needed has been done for each sub-system (see table 7.3, last column). Detailed estimates are available only for the major components, the rest is estimated to be around 100 MY in total. The average cost per MY has been taken to be 93 kILCU including overheads. This value is typical for the mix of qualifications needed for a sophisticated project like the ILD. The estimate only includes the manpower needed to build

Item	cost	fraction in %	man-years
Magnet yoke	68.4	16.8	
Muon system	8.4	2.1	100
Magnet coil	47.6	11.7	200
Magnet ancillaries	11.0	2.7	
AHCal	48.3	11.9	300
Si-ECal	112.0	27.5	300
Silicon tracking	21.6	5.3	200
Vertex	2.9	0.7	100
TPC	34.3	8.4	100
Forward calorimeter	5.3	1.3	
Beam tube	1.6	0.4	
Integration	1.7	0.4	
Global DAQ	1.2	0.3	
Offline computing	30.0	7.4	
Transport	13.0	3.2	
Total	407.0	100.00	

TABLE 7.3-1
Costs in MILCU and estimate of the manpower in man-years for the technologies retained in the simulation for physics studies. Options for two major sub-systems are included, but not used in the sum.

the detector, and does not include needs to finish the R&D or work out a detailed design of the detector. The manpower is then estimated to be in total 1400 MY, or 130 MILCU.

The overall ILD cost could then be 530 MILCU + 100 / - 50 MILCU.

The study has been carried out assuming that the detector is in a push-pull configuration. Most of the sub-system costs are only marginally affected by this assumption, with the exception of the integration costs, as discussed above. It has been estimated that without these requirements the total cost of the detector might be reduced by some $5 - 10\%$.

7.4 COST SCALING LAWS WITH DETECTOR PARAMETERS

The parameters which have been considered for possible scalings are the following:

- the magnetic field;
- a characteristic transverse size chosen as the inner radius of the ECAL barrel;
- a characteristic longitudinal size chosen as the length of the ECAL barrel or TPC;
- the number of samples for the ECAL (for a given number of radiation lengths);
- the number of samples for the HCAL (for a given layer interaction length or a given total interaction length);
- the calorimeter cell sizes.

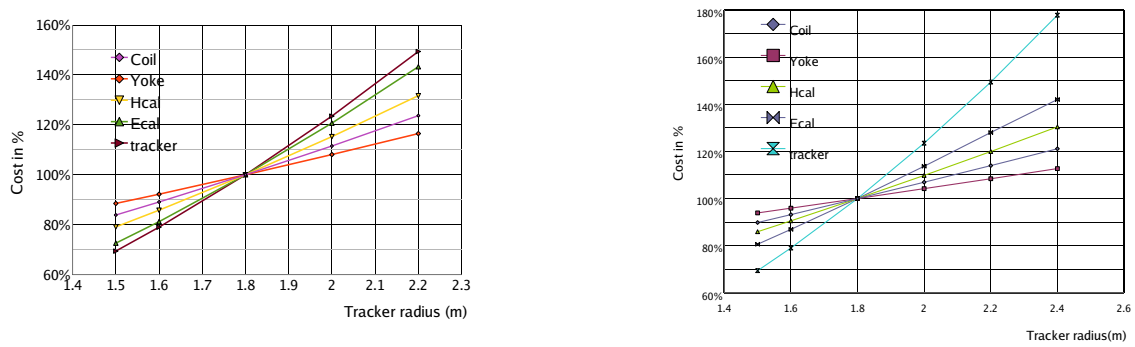

FIGURE 7.4-1. Dependence of the cost of the main items with the size, on the left for a constant angle, on the right changing only the transverse size

The study was done under the assumption that the technologies remain the same. This implies that the range for scaling is rather small, basically at the level of 25%. To go further would in most cases require reassessing the technology choices.

The nominal field is 3.5 T, but the magnet is designed to withstand 4T. Reducing the field below 3.5T might offer cost savings, but also result in a large loss of the physics potential of the detector. ILD therefore does not consider this option of de-scoping. There is a clear impact on the overall cost of the coil from the correction coils. Reducing the requirements on the field quality would result in cost savings. Whether or not this might be acceptable is currently unknown.

The dimensions of the detector parts inside the TPC are dictated by considerations of background and assembly. They are not very relevant for costing. Therefore a characteristic transverse scaling parameter is the radius of the transition from the tracker into the calorimeter, a characteristic longitudinal scaling parameter is the length of the TPC. Moving these parameters impacts calorimetry, coil and yoke. There are two ways we can envisage to scale down the size of the detector, either by keeping the aspect ratio constant, or by reducing only the radius. The estimate of the cost variation with a constant aspect ratio from the reference design is shown in figure 7.4-1 on the left. The figure on the right shows the impact of changing solely the TPC radius. The figure 7.4-2 illustrates the total cost scaling of ILD in the same conditions.

The scaling of the ECal sampling has been done under the assumption that the total number of radiation lengths in the ECAL is kept constant. The area of sensitive medium and the number of readout channels then scale proportional to the number of samplings. On the other hand, as the total amount of radiator does not change, the thickness of the absorber plates changes and the manufacturing of the plates varies in a non negligible way. Reducing the number of samples will reduce the overall thickness of the ECAL even when the total amount of absorber material stays constant. For example, going from 30 to 20 samples will reduce the radial thickness by 20 mm. In the cost scaling we do not consider the impact on the surrounding detectors (see figure 7.4-3).

In the case of the HCAL we investigate two different scenarios for reducing the sampling: either we keep the depth in radiation length constant by increasing the layer thickness, or we keep the layer thickness the same, changing the total number of interaction lengths. The same approach can be taken for the analogue and the digital HCAL option. This impacts the radiator, sensors and all the surrounding subsystems. The global impact on the ILD cost

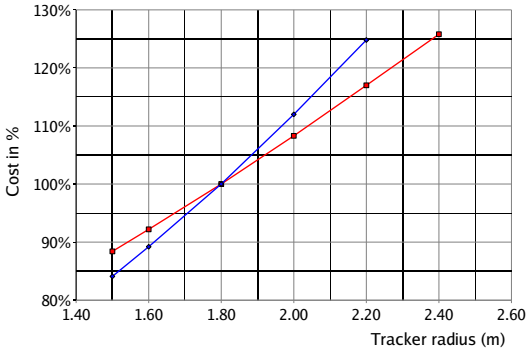

FIGURE 7.4-2. Dependence of the total cost with the size of the detector, in blue when the aspect ratio is kept, in red when the radius only changes.

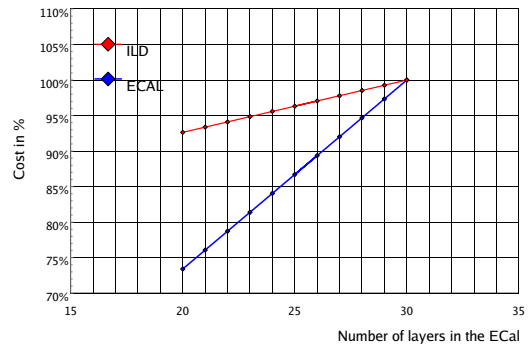

FIGURE 7.4-3. Dependence of the cost with the number of layers in the ECal.

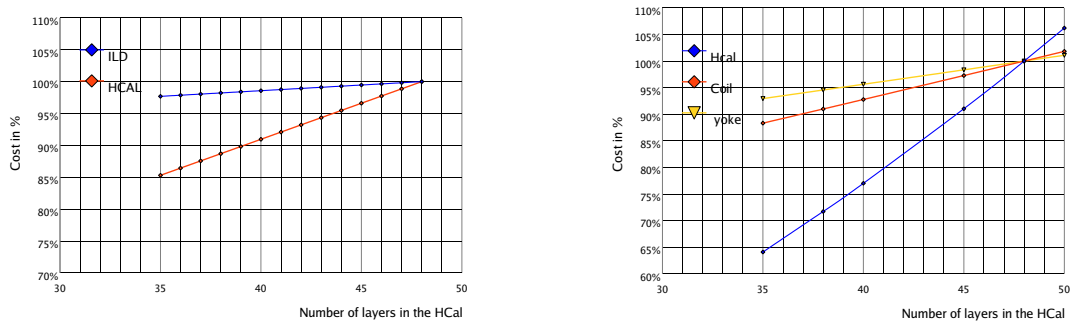

FIGURE 7.4-4. Dependence of the cost with the number of layers in the HCal, on the left if you keep the total number of interaction lengths, on the right if you keep the thickness of the layers.

is about 7% when changing from 48 to 40 layers in the HCAL as can be seen in figure 7.4-4.

The cell sizes of the electromagnetic calorimeter are already quite at a lower limit, as long as the design currently under development is used. To go below, a new design, may be a different approach will be needed. The MAPS ECAL which cost has not been estimated may be one of the possibilities. Increasing the cell sizes within the same technology will have only a minor impact on the cost, as the cost roughly scales with the area of silicon, not the number of readout channels. There is of course some effect due to a different cost of the printed circuit boards and other ancilliary equipment. We estimate that reducing the number of cells by an order of magnitude reduces the cost of the ECAL by less than 10%, or 3% of the total detector cost. The impact on the cost for the scintillator version may be larger but it is unlikely that scaling up the size in this version would be considered.

For the hadronic calorimeter changing the cell sizes will result in a changed number of FE chips, calibration devices etc. We estimate that a reduction of the number of readout channels by an order of magnitude reduces the cost of the digital HCAL by about 20%, of the analogue HCAL by about 10%. This has to be balanced with a large performance loss.

7.5 CONCLUSION

The cost of the ILD detector has been estimated to be about 500 MILCU. It includes the material and labour to build the detector, but does not include cost escalation and contingencies. The dependence of the cost on the main detector parameters has been studied, and effects of order 10% or less per item on the total detector cost have been found. To illustrate the possibilities, a cost reduction of 20% can be reached by reducing the number of HCAL layers from 48 to 40, the number of ECAL layers to 20, the inner radius of the ECAL to 160 cm, and the length accordingly. This reduces clearly the performances of the detector (See section 2). It should be noted that in many instances, a reduced performance of the detector translates into a longer running time of the accelerator until the desired physics measurements can be made.

The quoted cost of the ILD detector is comparable to the total cost of the recently completed large LHC detectors.

Although costs quoted in many instances are based on actual costs of prototypes, together with educated guesses toward mass production etc, there are still large uncertainties. A more reliable cost estimate will only be possible when a more complete and detailed engineering of the ILD detector will have been done.

CHAPTER 8

The ILD group

The ILD concept group was formed in 2007 by the merger of the GLD and the LDC groups. The ILD group has members from all three regions of the world, but is particularly well anchored in Europe and in Asia. More than 650 signatories from about 170 institutions support this Letter of Intent for ILD. Since the ILD group is not yet a collaboration, the membership of the ILD group has not been very clearly defined. The signatories of the Letter of Intent is the first set of names that comes close to the membership of the ILD group. They are, however, in a state of flux. Anybody who has contributed or intends to contribute to the ILD detector concept study is welcome to sign the LoI and can do so without any formal evaluation. On the other hand, the management of the ILD group has been defined clearly and is in operation with well defined membership and distribution of responsibilities.

The combined leadership of the two former groups GLD and LDC elected a joint steering board charged to produce a single letter of intent. The newly formed detector concept was named 'ILD' which stands for 'International Large Detector'. The joint steering board consists of two representatives from each of the three regions - Asia, Europe, and North America. The joint steering board then elected working group leaders, subdetector contacts, and representatives for the research directorate.

There are four working groups - optimisation, MDI/integration, costing, and software - and each has two conveners. The optimisation working group is charged with optimising the detector parameters based on simulations and to evaluate physics performance of the resulting detector. This working group played a key role in unifying the detector parameters of the GLD and LDC detector concepts, and continues to be the main framework for physics analyses. The MDI/integration working group was formed to fill the immediate need to liaise with the accelerator activities on such issues as dimension and shape of the experimental hall, design of push-pull operation, support of the final quads, etc. As the name suggests, the MDI/integration working group handles the issues of overall integration of the detector. There are three technical coordinators which belong to the MDI/integration working group. We believe that system engineers with strong authority are not needed at this stage of the detector development. The costing working group essentially consists of two conveners only, and is charged with estimating the cost of the whole detector and to represent the ILD group in discussions to define common costing rules with other LoI groups in the framework of the ILC research directorate. The responsibility of the software working group is to unify the softwares of the two former concept groups, and manage the development of the resulting software system.

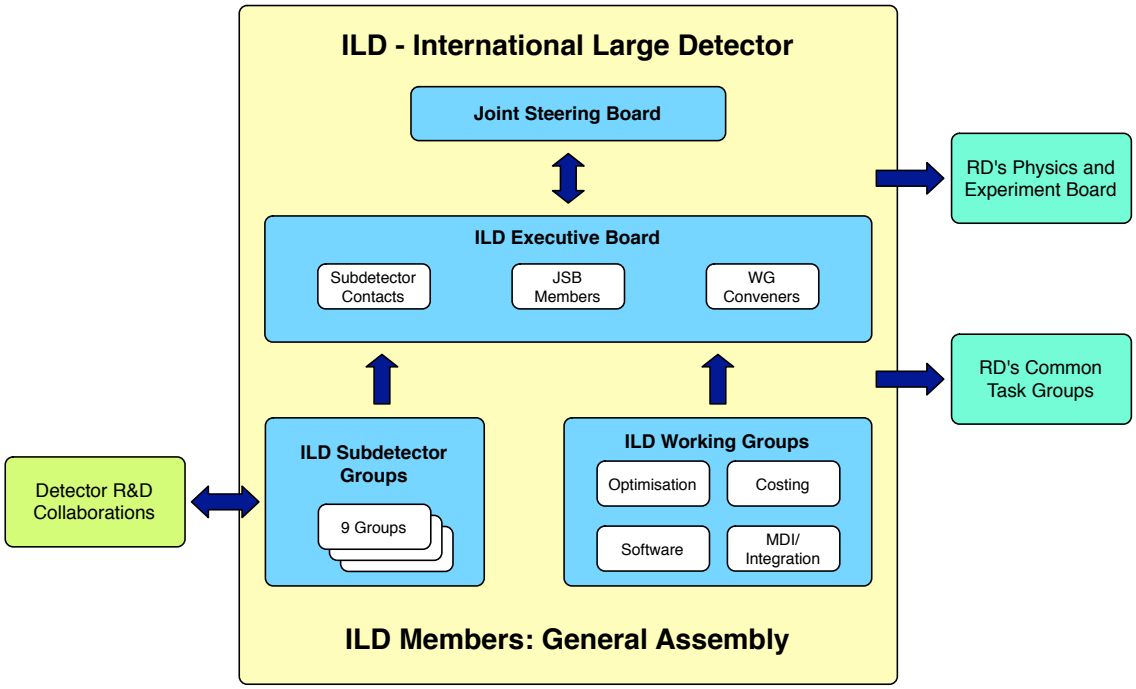

FIGURE 8.0-1. Structure of the ILD group.

The ILC detector R&D groups play a critical role in the ILD detector development. They are sometimes called 'horizontal' collaborations as opposed to LoI groups which are viewed as vertical organisations. Examples are the CALICE collaboration for calorimeters, the SiLC collaboration for silicon trackers, the LCTPC collaboration for TPC, and the FCAL collaboration for the calorimeters and instrumentation in the forward region. These groups are in principle independent of LoI groups and often bound by a "Memorandum of Understanding" to form more formal collaborations. Subdetector contact persons have been selected for vertexing, silicon trackers, TPC, ECAL, HCAL, FCAL, Muon system, DAQ, and solenoid. The number of contact persons is two per subdetector except for FCAL and muon system for which number is one. When relevant detector R&D collaborations exists for a given subdetector, a person appropriate as a liaison for that group was chosen. The subdetector contacts are charged to act as contact points to R&D groups and to make sure that the relevant detector technology is applied to the ILD environment.

In addition, the ILD group nominates members of the common task groups which serve under the ILC research director. There are two representatives of the ILD LoI group, two for MDI, one for engineering tools, three for the R&D common task group, two for the physics group, and two for the software group. They are often the same persons as the corresponding working group conveners or subdetector contacts, and act as a link to the research directorate.

In figure 8.0-1 the organisational structure of the ILD group is shown.

The joint steering board, working group conveners, subdetector contacts, and representatives for the research directorate form an entity called the executive board. The ILD executive board forms the core of the ILD-related activities, and meets roughly biweekly over internet or in person. General ILD meetings lasting a half day to a full day are usually attached to each ILC workshop. Separately we have a few dedicated ILD workshops per year of a few days each. At these meetings and dedicated workshops we have general ILD assembly meetings which take in opinions and comments from the wider community.

CHAPTER 9

R&D Plan

The ILD detector has been developed under the assumptions that particle flow is the most best method for event reconstruction and that an excellent vertex reconstruction is needed for many physics channels. To reach the proposed performance of ILD, significant advances in detector technology are needed, compared to existing detectors. Over the past years R&D collaborations have formed to address the main issues in technological development. ILD is closely cooperating with these R&D collaborations and is discussing and coordinating the needed work with these groups.

Particle flow has consequences in many parts of the detector: it is essential that a calorimeter is built that is capable of imaging the shower, and that it is complemented by a very powerful and efficient tracking system.

ILD has chosen a solution where a highly granular calorimeter is combined with a powerful and highly redundant tracking system, which contains both a large volume gaseous tracker (time projection chamber) and a high precision Si tracker with excellent tracking and vertexing capabilities. The main technological innovation relevant for ILD is the granularity in particular of the calorimeter, and the overall very low material budget projected for the tracking system while reaching excellent spatial resolution for charged particles.

Over the past years significant R&D has taken place to establish the basic feasibility of the main technologies which have been proposed. Major projects have been started to study granular calorimeters, both electromagnets and hadronic, which are organised in the context of the CALICE collaboration. A novel type of time projection chamber is under development, based on micro-pattern gas detectors, organised by the LC-TPC collaboration. New low-mass systems have been developed for all parts of the Si tracking system, in the context of the SiLC, LCFI, the MAPS, the DEPFET collaboration and other groups. Instrumentation in the very forward direction, which is special in that it is the only place in the ILC detector where radiation hardness is required, is studied in the context of the FCAL collaboration. Large area muon chambers, which can also serve as tail catchers, are being developed, also in the context of the CALICE collaboration, and by independent efforts.

The first round of R&D established for most subdetectors the basic feasibility of these systems. Test experiments with highly granular calorimeters were successfully completed at both CERN and Fermilab. The concept of a micro-pattern TPC could be established with small prototypes. First prototypes of extremely low-mass Silicon-based detectors have been developed and tested.

Internationally the linear collider experimental community wants to be able to make a reliable and well understood proposal for experiments at the ILC by 2012. This requires

that a fundamental understanding of the major detector components needs to be achieved by this time, and that a first version of an engineering solution is available. The work needs to advance to a different level than described in this document, and goes beyond the feasibility tests of the last years. It has to address system integration aspects within the sub-detector - integrated mechnical design, realistic integration of readout electronics, power management, cooling etc - but also address questions of integrating different sub-detectors.

Based on this, ILD considers that the experimental investigation of particle flow has the highest priority of R&D. This has a number of different aspects:

- Develop technological solutions for a granular electromagnetic and hadronic calorimeter.
- Develop the alternatives of Si-based and scintillator-based electromagnetic calorimeter to a point that both can be proposed, and that a future ILD collaboration can take a rapid decision after approval.
- Develop the alternatives of analogue and digital hadronic calorimetry to a point where a rapid decision between the options can be taken by a future ILD collaboration after approval. Ensure that both the analogue and the digital hadronic calorimetry are tested at the same level of sophistication in large scale setups.
- Continue to develop the simulation and software tools needed to study particle flow in detail, and continue to refine the particle flow reconstruction tools.
- Develop an experimental program, which can convincingly demonstrate the feasibility of the concept of particle flow.

The very forward detector systems in ILD are small but very different from the rest of the detector. They are the only devices where significant radiation hardness is needed. The flux of electromagnetic radiation seen by these devices is even larger than what is anticipated at the LHC. Dedicated R&D is therefore needed to develop adequate technologies for the precision calorimeters needed at very forward angles.

Particle Flow relies on a very powerful tracking system. ILD is special in all the ILC concept groups that it is proposing a TPC as central tracker. This is central to the overall performance and robustness of the system. The experimental proof that a TPC can be built and operated with the required precision and stability has very high priority for ILD.

ILD includes in its tracker a very powerful Si tracking system. The main challenge here is the development of a technology which is powerful enough and which meets the requirements in terms of material, power consumption and speed. Solutions seem to be in reach for the strip tracking system, many different options are being studied for the pixel-based vertex detector part of the system. ILD considers powerful Si tracking systems to be an essential part of the or detector concept. ILD stresses the need to pursue a broad range of different Silicon detector technologies, in particular for the vertex detector, so that an optimal solution can be chosen as close in time as possible to the construction of the detector. In particular in the rapidly and quickly evolving field of Si detectors which are dominated by commercial developments a final choice of technology should be delayed to the latest possible moment. ILD considers it essential to follow the technological developments, to develop as many alternative solutions as possible to be in a position to pick the optimal one quickly, once needed.

Testing sophisticated hardware components requires adequate testing facilities. The next generation of test beam experiments should address the interplay of different sub-detectors, in addition to novel technologies of the sub-detectors. The experiments should comprise vertexing, tracking and calorimetric components together, in an interchangeable way, in a sufficient magnetic field, at a hadron beam. A beam with an ILC-like particle bunch structure

would be a big bonus. It would test integration aspects, aspects of a common data acquisition, and the data from such an experiment would be very useful in the continuing improvement of the understanding of the different reconstruction techniques needed for ILD. ILD considers the creation of such an integrated test facility of high importance for the eventual success of the programme.

Even though most of the work currently done is on technologies for sub-detectors, the overall detector integration has to be considered as well. The concept of push - pull, which is currently favored to save one beam line, will require dedicated designs for many of the sub-detectors. These points need to be known early on, and may require some significant R&D on their own. Points of concern are sensitivity to vibrations, reproducibility of alignments, and the external monitoring of inter- detector alignments.

The ILD group intends to continue its work toward a full technical design of the detector at the end of the technical design phase 2 (around 2012), in step with the plans of the GDE for the machine. The different R&D plans of the sub-detector components are detailed in the individual sections. For the large components calorimetry and time projection chamber, large second generation prototypes should be running and delivering results by the end of 2012, such that - if the ILD group is transformed into a collaboration, and if the ILC project gets approval - a selection of technologies is possible. The steps needed to advance all options to this point are described in the individual sections. For sub-detectors like the vertex detector, intense R&D into sensor technologies will continue. A decision on the technology can be taken at a later stage, but the integration aspect of the VTX detector will need to advanced enough in 2012, that a realistic design can be proposed. The same is true for the other smaller sub-systems discussed in the context of ILD.

CHAPTER 10

Conclusions

In the summer of 2007, the GLD concept study group, whose membership was largely based in Asia, and the LDC concept study group, which was mostly based in Europe with a strong north american membership, joined forces to produce a single Letter of Intent for a detector at the International Linear Collider, and formed the ILD concept group. Both the GLD and LDC concepts used the particle flow algorithm for jet reconstruction and a TPC for the central tracker. The basic parameters of the two concepts such as the size of the detector and the strength of the solenoid field, however, were quite different and had to be unified in order to write this letter of intent for ILD. Also, other critical details such as the interaction region design had to be unified. This was a non-trivial task, neither politically nor sociologically.

The newly-formed concept study group, the ILD group, created a management team and engaged in intense studies to define the ILD detector concept by scientifically optimising the detector designs. The process has worked remarkably well, and we present here the outcome of this study as well as the large amount of studies that preceded separately by the two older concept groups. The ILD detector concept is now well defined, even though some technology choices are still open. One of the merits of unifying the detector concepts was that it revitalised the studies on physics performance and detector designs. We believe that the level of sophistication of the simulation and physics analyses has reached a high degree of sophistication for a detector group at this stage. This was achieved through collaboration and competition, and is the result of a productive learning process.

The unification had also positive effects on the subdetector R&D efforts. Most R&D on detector technologies relevant to the GLD and LDC groups is being performed within the framework of detector R&D collaborations such as LCTPC, SiLC, CALICE, and FCAL which pursue their own goals of detector technology development. Members of the detector concept groups participate in the R&D collaborations and make sure that the detector technologies are successfully applied to the detector concept designs. By the creation of the ILD concept group, the application efforts became more focused. Currently, the ILD management includes subdetector contacts who are also key members of the detector R&D collaborations. This scheme is working efficiently such that we can finish basic R&D in time for the Technical Design Report which is envisaged around 2012.

Overall, the ILD group structure is efficient while keeping flexibility and openness. Even though we are still short on person power and funding at this time, we believe that we are well positioned to successfully complete a technical design for a detector at the International Linear Collider. The ILD group is firmly committed to the ILD project.

CONCLUSIONS

BIBLIOGRAPHY

[1] **ILC Project**, A. Djouadi *et al.*, eds., *International Linear Collider Reference Design Report Volume 2: Physics at the ILC*. 2007. `arXiv:0709.1893 [hep-ph]`. ILC-REPORT-2007-001.

[2] **GLD Concept Study Group**, K. Abe *et al.*, "GLD detector outline document" `arXiv:physics/0607154`.

[3] **LDC Working Group**, D. Kisielewska *et al.*, "Detector Outline Document for the Large Detector Concept". `http://www.ilcldc.org/documents/dod/`.

[4] **ILC Project**, T. Behnke *et al.*, eds., *International Linear Collider Reference Design Report Volume 4: Detectors*. 2007. `arXiv:0712.2356 [physics.ins-det]`. ILC-REPORT-2007-001.

[5] **GEANT4 Collaboration**, S. Agostinelli *et al.*, "GEANT4: A simulation toolkit" *Nucl. Instrum. Meth.* **A506** (2003) 250–303.

[6] "Linear Collider Physics List Description". `http://www.slac.stanford.edu/comp/physics/geant4/slac_physics_lists/ilc/physlistdoc.html`.

[7] A. Miyamoto, "JLC Study Framework". Prepared for International Workshop on Linear Colliders (LCWS 2002), Jeju Island, Korea, 715-717 Aug 2002.

[8] R. Brun and F. Rademakers, "ROOT: An object oriented data analysis framework" *Nucl. Instrum. Meth.* **A389** (1997) 81–86.

[9] K. Hoshina, "Simulator Status of Jupiter and Satellites". Prepared for APPI Winter Institute, International (APPI2002), APPI, Japan, KEK Proceedings 2002-08, July 2002.

[10] F. Gaede, T. Behnke, N. Graf, and T. Johnson, "LCIO: A persistency framework for linear collider simulation studies" *Proceedings of CHEP 03, La Jolla, California, 24-28 Mar 2003, TUKT001* (2003) , `arXiv:physics/0306114`.

[11] F. Gaede *et al.*, "MarlinReco webpage". `http://ilcsoft.desy.de/portal/software_packages/marlinreco`.

[12] M. A. Thomson, "Particle Flow Calorimetry and the PandoraPFA Algorithm" *Nucl. Instrum. Meth.* **A611** (2009) 25–46.

[13] P. Mora de Freitas and H. Videau, "Detector simulation with MOKKA / GEANT4: Present and future". Prepared for International Workshop on Linear Colliders (LCWS 2002), Jeju Island, Korea, 26-30 Aug 2002.

[14] "GEAR - a geometry description toolkit for ILC reconstruction software". http://ilcsoft.desy.de/portal/software_packages/gear.

[15] F. Gaede, "Marlin and LCCD: Software tools for the ILC" *Nucl. Instrum. Meth.* **A559** (2006) 177–180.

[16] F. Gaede and J. Engels, "Marlin et al - A software Framework for ILC detector R&D". http://www.eudet.org/e26/e27/e584/eudet-report-2007-11.pdf. EUDET-Report-2007-11.

[17] **LCFI**, . D. Bailey *et al.*, "The LCFIVertex package: vertexing, flavour tagging and vertex charge reconstruction with an ILC vertex detector" *Nucl. Instrum. Meth.* **A610** (2009) 573–589, arXiv:0908.3019 [physics.ins-det].

[18] R. Fruhwirth, W. Waltenberger, and P. Vanlaer, "Adaptive vertex fitting" *J. Phys.* **G34** (2007) N343.

[19] M. A. Thomson, "Progress with Particle Flow Calorimetry" arXiv:0709.1360 [physics.ins-det].

[20] D. Jeans, "Particle Flow in a strip calorimeter". http://www.awa.tohoku.ac.jp/TILC08/. Presented at the TILC08 workshop.

[21] M. Battaglia, "The vertex tracker at future e+ e- linear colliders" *Nucl. Instrum. Meth.* **A530** (2004) 33–37, arXiv:physics/0312039.

[22] R. Walsh *et al.*, "Flavour tagging optimisation studies at ILD". http://www.ilcild.org/documents/ild-loi-material/flavour_tagging.pdf/at_download/file.

[23] H. Li *et al.*, "Precision Measurements of SM Higgs Recoil Mass and Cross Section for $\sqrt{s}$ of 230 GeV and 250 GeV at the ILC" arXiv:0901.4893 [physics.hep-ex]. proceedings of LCWS08 and ILC08, Chicago, Illinois, Nov 2008.

[24] **WWS Software Panel**, T. Behnke *et al.*, "Benchmark reactions for the ILC LoI". http://ilcdoc.linearcollider.org/record/14681/files/Benchmark_Reactions_for_the_ILC_LOI.pdf.

[25] "ILD reference detector model". http://www.ilcild.org/documents/ild-loi-material/ILDreferencedetector.pdf/at_download/file.

[26] T. Barklow, "Physics Impact of Detector Performance". http://www-conf.slac.stanford.edu/lcws05/program/talks/18mar2005.ppt. Presented at 2005 International Linear Collider Workshop.

[27] J. Fuster *et al.*, "Forward tracking at the next e^+e^- collider - part I: the physics case" *JINST* **4** (2009) P08002.

[28] S. Bethke, Z. Kunszt, D. E. Soper, and W. J. Stirling, "New jet cluster algorithms: Next-to-leading order QCD and hadronisation corrections" *Nucl. Phys.* **B370** (1992) 310–334.

[29] **The ALEPH, CDF, D0, DELPHI, L3, OPAL, SLD Collaborations, the LEP Electroweak Working Group, the Tevatron Electroweak Working Group, and the SLD electroweak and heavy flavour groups**, "Precision Electroweak Measurements and Constraints on the Standard Model" `arXiv:0811.4682 [hep-ex]`.

[30] H. Li *et al.*, "HZ Recoil Mass and Cross-Section Analysis in ILD". LAL-09-121, LC-PHSM-2009-006.

[31] H. Li, "Ph.D Thesis, LAL/Universite Paris-SUD XI". LAL-09-118.

[32] M. A. Thomson, "ZFinder".

[33] J. Goldstein *et al.*, "Analysis of the higgs hadronic branching ratios in the ZH $\to \ell\ell$qq channel". `http://www.ilcild.org/documents/ild-loi-material/higgs_branching_ratios.pdf/at_download/file`.

[34] T. Behnke, S. Bertolucci, R. D. Heuer, and R. Settles, eds., *TESLA: The superconducting electron positron linear collider with an integrated X-ray laser laboratory. Technical design report. Pt. 4: A detector for TESLA*. DESY, 2001. `http://tesla.desy.de/new_pages/TDR_CD/PartIV/detect.html`. DESY-01-011.

[35] M. Davier, L. Duflot, F. Le Diberder, and A. Rouge, "The Optimal method for the measurement of tau polarization" *Phys. Lett.* **B306** (1993) 411–417.

[36] **OPAL Collaboration**, K. Ackerstaff *et al.*, "Search for the standard model Higgs boson in e+ e- collisions at s**(1/2) = 161-GeV to 172-GeV" *Eur. Phys. J.* **C1** (1998) 425–438, `arXiv:hep-ex/9709003`.

[37] List, B. and List, J., "MarlinKinFit: Kinematic Fitting for the ILC". talk given at ILD optimisation meeting 20/02/2008. `http://ilcagenda.linearcollider.org/getFile.py/access?contribId=0&resId=0&materialId=slides&confId=2538`.

[38] R. Chierici, S. Rosati, and M. Kobel, "Strong electroweak symmetry breaking signals in WW scattering at TESLA". `http://www-flc.desy.de/lcnotes/notes/LC-PHSM-2001-038.ps.gz`. Prepared for 5th International Linear Collider Workshop (LCWS 2000), Fermilab, Batavia, Illinois, 24-28 Oct 2000, LC-PHSM-2001-038.

[39] W. Kilian, T. Ohl, and J. Reuter, "WHIZARD: Simulating Multi-Particle Processes at LHC and ILC" `arXiv:0708.4233 [hep-ph]`.

[40] A. F. Osorio, *WW scattering studies for a future linear collider*. PhD thesis, University of Manchester, 2006.

[41] M. Beyer *et al.*, "Determination of new electroweak parameters at the ILC: Sensitivity to new physics" *Eur. Phys. J.* **C48** (2006) 353–388, `arXiv:hep-ph/0604048`.

[42] P. Krstonosic, K. Monig, M. Beyer, E. Schmidt, and H. Schroder, "Experimental studies of strong electroweak symmetry breaking in gauge boson scattering and three gauge boson production" `arXiv:hep-ph/0508179`.

[43] P. Bechtle, K. Desch, W. Porod, and P. Wienemann, "Determination of MSSM parameters from LHC and ILC observables in a global fit" *Eur. Phys. J.* **C46** (2006) 533–544, arXiv:hep-ph/0511006.

[44] R. Heuer, D. Miller, F. Richard, and P. Zerwas, eds., *TESLA Technical Design Report Part III: Physics at an e^+e^- Linear Collider*. 2001. arXiv:hep-ph/0106315. http://tesla.desy.de/new_pages/TDR_CD/PartIII/physic.html. DESY-01-011.

[45] N. D'Ascenzo, "Study of the neutralino sector and analysis of the muon response of a highly granular hadron calorimeter at the International Linear Collider". http://www-library.desy.de/preparch/desy/thesis/desy-thesis-09-004.pdf. DESY-THESIS-2009-004.

[46] P. Bechtle, M. Berggren, J. List, P. Schade, and O. Stempel, "Prospects for the study of the $\tilde{\tau}$-system in SPS1a' at the ILC" arXiv:0908.0876 [hep-ex].

[47] C. Bartels and J. List, "Model Independent WIMP Search at 500 GeV". http://www.ilcild.org/documents/ild-loi-material/WIMPs.pdf/at_download/file.

[48] N. Wattimena and J. List, "Long-lived χ_1^0 in Gauge Mediated SUSY Breaking" tech. rep., 2009. http://www-flc.desy.de/lcnotes/notes/PREL-LC-DET-2009-001.pdf. LC-DET-2009-002.

[49] **ILC Project**, J. Brau, Y. Okada, and N. Walker, eds., *ILC Reference Design Report Volume 1: Executive Summary*. 2007. arXiv:0712.1950 [physics.acc-ph]. ILC-REPORT-2007-001.

[50] G. A. Moortgat-Pick *et al.*, "The role of polarized positrons and electrons in revealing fundamental interactions at the linear collider" *Phys. Rept.* **460** (2008) 131–243, arXiv:hep-ph/0507011.

[51] S. Boogert *et al.*, "Polarimeters and energy spectrometers for the ILC beam delivery system". http://ilcdoc.linearcollider.org/record/19682/files/loi-PolEnergy.pdf?version=1. ILC-NOTE-2009-049.

[52] A. Blondel, "A scheme to measure the polarisation asymmetry at the Z pole in LEP" *Phys. Lett.* **B202** (1988) 145.

[53] K. Monig, "The use of positron polarization for precision measurements". http://www-flc.desy.de/lcnotes/notes/LC-PHSM-2000-059.ps.gz. LC-PHSM-2000-059.

[54] P. Bechtle, W. Ehrenfeld, and I. Marchesini, "Measurement of the beam polarization at the ILC using the W^+W^- production". http://www.ilcild.org/documents/ild-loi-material/ww_pol.pdf/at_download/file. LC-PHSM-2009-XXX (in preparation).

[55] E. Asakawa *et al.*, "Precision Measurements of Little Higgs Parameters at the International Linear Collider" arXiv:0901.1081 [hep-ph].

[56] M. Giannelli, "Sensitivity to the Higgs Self-coupling Using the ZHH Channel". http://www.ilcild.org/documents/ild-loi-material/Proceedings%20LCWS09.pdf/at_download/file. Prepared for LCWS08.

[57] D. Schulte, "Study of electromagnetic and hadronic background in the interaction region of the TESLA Collider". DESY-TESLA-97-08.

[58] "User's manual of CAIN, Version 2.35". http://lcdev.kek.jp/~yokoya/CAIN/cain235/CainMan235.pdf.

[59] R. D. Masi *et al.*, "Estimate of the background on the vertex detector of ILD from beamstrahlung". http://www.ilcild.org/documents/ild-loi-material/BKGStudies.pdf/at_download/file. LC-Note in preparation.

[60] M. Winter *et al.*, "Development of Swift and Slim CMOS Sensors for a Vertex Detector at the International Linear Collider" 2007. http://iphc.in2p3.fr/Others,116.html. Internal Note.

[61] M. Winter *et al.*, "M.i.p. detection performances of a 100 us read-out CMOS pixel sensor with digitised outputs" arXiv:0902.2717 [physics.ins-det].

[62] G. Rizzo *et al.*, "Development of deep N-well MAPS in a 130 nm CMOS technology and beam test results on a 4k-pixel matrix with digital sparsified readout" in *Nuclear Science Symposium Conference Record. NSS'08*, pp. 3242–3247, IEEE. 2008.

[63] G. Traversi *et al.*, "Performance of a DNW CMOS active pixel sensor designed for the ILC Vertex Detector Development of deep N-well MAPS in a 130 nm CMOS" in *Nuclear Science Symposium Conference Record. NSS'08*, pp. 1361–1368, IEEE. 2008.

[64] C. Damerell *et al.*, "ILC Vertex Detector R&D - Report of Review Committee". http://ilcdoc.linearcollider.org/record/17962/files/Vertex_Detector_Review-final.pdf?version=1. ILC-Report-2008-016.

[65] **DEPFET collaboration**, L. Feld *et al.*, "DEPFET Pixel Vertex Detector for the ILC". http://www.hll.mpg.de/~lca/ilc/DEPFET-VTX-ILC.pdf. Internal Note.

[66] Y. Sugimoto *et al.*, "FPCCD vertex detector R&D for ILC" 2007. http://www-jlc.kek.jp/subg/vtx/pub/FPCCD_Rev.pdf. Internal Note.

[67] Y. Sugimoto *et al.*, "R&D status of FPCCD VTX" arXiv:0902.2067 [physics.ins-det].

[68] FNAL and IPHC-Strasbourg and IRFU-Saclay and Bergamo University, "Consortium for Developing 3D/vertically Integrated Readout Electronics and Sensors". http://3dic.fnal.gov/.

[69] L. Andricek *et al.*, "The DEPFET active pixel sensor for vertexing at ILC and SuperKEKB" in *Proceedings of the TIPP-09 workshop*. Tsukuba (Japan), March 11-17 , 2009. to be published.

[70] M. Szelezniak, "Small-Scale Readout System Prototype for the STAR PIXEL Detector". http://repositories.cdlib.org/lbnl/LBNL-1086E-1. Lawrence Berkeley National Laboratory. Paper LBNL-1086E-1.

[71] **SiLC R&D Collaboration**, A. Savoy-Navarro, ed., *Proposal to the ILCSC R&D Panel on Tracking for the ILC*. submitted January 29, 2007. http://lpnhe-lc.in2p3.fr/DOCS/beijing.pdf.

[72] **SiLC R&D Collaboration**, A. Savoy-Navarro, ed., *Status report to the PRC-DESY*. 2008. http://prc.desy.de/e38/e60/e126/infoboxContent129/PRC65-SiLC_report.pdf.

[73] **SiLC R&D Collaboration**, "Eudet memos". see the references in the Website address of the PRC-DESY status report [72] above.

[74] V. Saveliev and M. Vos, "Presentations at the first ILD meeting". http://ilcagenda.linearcollider.org/conferenceDisplay.py?confId=2389.

[75] A. Ruiz, A. Savoy-Navarro, and M.Vos, "Presentations at TILC08". http://www.awa.tohoku.ac.jp/TILC08/.

[76] V. Saveliev, Z. Drasal, M.Fernandez-Garcia, W. Mitaroff, and A. Savoy-Navarro, "Presentations at ECFA Workshop in Warsaw". http://ilcagenda.linearcollider.org/conferenceDisplay.py?confId=2642.

[77] W. Cleland and E. Stern, "Signal processing considerations for liquid ionization calorimeters in a high rate environment" *Nucl. Instrum. Meth.* **A 338** (1994) 467.

[78] A. R. Jimeno, "Alignment of Silicon tracking systems R&D and First Prototype". http://ilcagenda.linearcollider.org/getFile.py/access?contribId=484&sessionId=21&resId=1&materialId=slides&confId=2628.

[79] A. Charpy *et al.*, "Integration of a Silicon tracking system combined with a TPC for the ILD project". ILC Internal Note under submission.

[80] T. H. Pham, "An 88-channel mixed mode chip in 130nm for Silicon strips readout at the ILC". http://kds.kek.jp/getFile.py/access?contribId=101&sessionId=57&resId=0&materialId=slides&confId=2376.

[81] M. Gruwe, "Gas studies for the TPC of a detector for the future Linear Collider". http://www-flc.desy.de/lcnotes/notes/LC-DET-1999-003-TESLA.ps.gz. LC-DET-1999-003.

[82] M. Ronan, "Time-projection chambers" *PDG Particle Physics Booklet* (2006) 264. http://instrumentationcolloquium.lbl.gov/Time_Projection_Chamber_R&D.pdf.

[83] LCTPC Groups, "TPC R&D for an ILC Detector". http://www-flc.desy.de/lcnotes/notes/LC-DET-2007-005.pdf. LC-DET-2007-005.

[84] **LCTPC Collaboration**, "TPC R&D for a Linear Collider Detector". http://prc.desy.de/sites/site_prc/content/e38/e60/e126/infoboxContent130/PRC65-TPC_report_31March2008.pdf. Status report April 2008 to the DESY PRC65 meeting.

[85] Y. Giomataris, P. Rebourgeard, J. P. Robert, and G. Charpak, "MICROMEGAS: A high-granularity position-sensitive gaseous detector for high particle-flux environments" *Nucl. Instrum. Meth.* **A376** (1996) 29–35.

[86] F. Sauli, "GEM: A new concept for electron amplification in gas detectors" *Nucl. Instrum. Meth.* **A386** (1997) 531–534.

[87] A. Raspiereza, "LDC Tracking Package" (2007) . http://www-zeuthen.desy.de/ILC/lcws07/pdf/Sim_Reco/raspereza_alexei.pdf. Contribution to the Sim/Reco sesstion at LCWS2007, DESY Hamburg 29 May - 4 June 2007.

[88] A. Vogel, *Beam-Induced Backgrounds in Detectors at the ILC*. PhD thesis, Department Physik der Universität Hamburg, 2008. http://www-library.desy.de/preparch/desy/thesis/desy-thesis-08-036.pdf. DESY-THESIS-2008-036.

[89] **ALICE Collaboration**, G. Dellacasa *et al.*, "ALICE technical design report of the time projection chamber". CERN-OPEN-2000-183.

[90] **EUDET Consortium**, "The EUDET facility at DESY". http://www.eudet.org/.

[91] M. S. Dixit, J. Dubeau, J. P. Martin, and K. Sachs, "Position sensing from charge dispersion in micro-pattern gas detectors with a resistive anode" *Nucl. Instrum. Meth.* **A518** (2004) 721–727, arXiv:physics/0307152.

[92] **LCTPC Collaboration**, "A TPC for a future linear collider". http://www-flc.desy.de/lcnotes/notes/LC-DET-2002-008.ps.gz. LC-DET-2002-008.

[93] **STAR Collaboration**, "STAR TPC". http://www.star.bnl.gov/.

[94] D. Peterson, "Presentations at LCWS07 tracking session". http://www.lepp.cornell.edu/~dpp/linear_collider/ILC_Presentations.html.

[95] R. Settles and W. Wiedenmann, "The Linear Collider TPC: Revised Magnetic-field Requirements". http://www-flc.desy.de/lcnotes/notes/LC-DET-2008-002.pdf. LC-DET-2008-002.

[96] R. Settles and M. Thomson, "Suggestion for Amount of Alignment-Data Needed". http://acfahep.kek.jp/subg/ir/bds/ilc-bds.html. See replies linked therein at 4. MDI.

[97] D. Karlen *et al.*, "Tpc performance in magnetic fields with gem and pad readout" *Nucl. Instrum. Meth.* **A555** (2005) 80.

[98] J.-C. Brient and H. Videau, "The calorimetry at the future e+ e- linear collider" arXiv:hep-ex/0202004.

[99] **CALICE Collaboration**. http://polywww.in2p3.fr/flc/calice.html.

[100] **CALICE Collaboration**, J. Repond *et al.*, "Design and Electronics Commissioning of the Physics Prototype of a Si-W Electromagnetic Calorimeter for the International Linear Collider" *JINST* **3** (2008) P08001, arXiv:0805.4833 [physics.ins-det].

[101] H. Videau, "Few considerations on the design of the electromagnetic calorimeter". http://ilcagenda.linearcollider.org/getFile.py/access?contribId=108&sessionId=6&resId=0&materialId=slides&confId=1049. presentation at ECFA meeting, Valencia, Nov. 2006.

[102] M. Reinhard and J.-C. Brient, "GARLIC - GAmma Reconstruciton for the LInear Collider" arXiv:0902.3042 [hep-ex].

[103] **CALICE Collaboration**, J. Repond *et al.*, "Response of the CALICE Si-W Electromagnetic Calorimeter Physics Prototype to Electrons" arXiv:0811.2354 [physics.ins-det]. Submitted to NIMA.

[104] J. A. Ballin *et al.*, "Monolithic Active Pixel Sensors (MAPS) in a quadruple well technology for nearly 100% fill factor and full CMOS pixels" *Sensors* **8** (2008) 5336, arXiv:0807.2920 [Unknown].

[105] J. A. Ballin *et al.*, "A MAPS-based Digital Electromagnetic Calorimeter for the ILC" arXiv:0709.1346 [physics.ins-det].

[106] N. K. Watson *et al.*, "A MAPS-based readout of an electromagnetic calorimeter for the ILC" *J. Phys. Conf. Ser.* **110** (2008) 092035.

[107] **CALICE Collaboration**, C. Adloff *et al.*, "CALICE Report to the Calorimeter R&D Review Panel" arXiv:0707.1245 [physics.ins-det].

[108] M. Stanitzki *et al.*, "A Tera-Pixel Calorimeter for the ILC" in *Nuclear Science Symposium Conference Record. NSS'07*, vol. 1, p. 254, IEEE. 2007.

[109] J. P. Crooks *et al.*, "A Novel CMOS Monolithic Active Pixel Sensor with Analog Signal Processing and 100% Fill Factor" in *Nuclear Science Symposium Conference Record. NSS'07*, vol. 2, p. 931, IEEE. 2007.

[110] J. A. Ballin *et al.*, "TPAC: A 0.18 Micron MAPS for Digital Electromagnetic Calorimetry at the ILC" in *Nuclear Science Symposium Conference Record. NSS '08.*, pp. 2224–2227, IEEE. 2008.

[111] T. S. Group, "Silicon pixel detector r&d". http://ilcagenda.linearcollider.org/categoryDisplay.py?categId=171.

[112] H. Matsunaga, "Software studies of GLD calorimeter" *Pramana* **69** (2007) 1057–1061. http://www.ias.ac.in/pramana/v69/p1057/fulltext.pdf.

[113] V. Bartsch *et al.*, "Status of the DAQ system for the EUDET Calorimetry". http://www.eudet.org/e26/e28/e615/e800/EUDET-Memo-2008-19.pdf. EUDET-Memo-2008-19.

[114] H. Abramowicz *et al.*, "Instrumentation of the very forward region of a linear collider detector" *IEEE Trans. Nucl. Sci.* **51** (2004) 2983–2989.

[115] K. Mönig, "Physics needs for the Forward Region" *V. Workshop: Instrumentation of the Forward Region of a Linear Collider Detector* (2004) . http://www-zeuthen.desy.de/lcdet/Aug_04_WS/talks/moenig_lum04.pdf.

[116] C. Grah and A. Sapronov, "Beam parameter determination using beamstrahlung photons and incoherent pairs" *JINST* **3** (2008) P10004.

[117] W. Daniluk *et al.*, "Laser Alignment System for LumiCal". `http://www.eudet.org/e26/e26/e27/e826/EUDET_report_05.pdf`. EUDET-Report-2008-05.

[118] C. Clerc and M. Joré, "Note on the integration of the ILD detector". `http://www.ilcild.org/documents/ild-loi-material/ILD_integration_note.pdf/at_download/file`.

[119] H. Abramowicz *et al.*, "A Luminosity Detetor for the International Linear Collider". `http://www-flc.desy.de/lcnotes/notes/LC-DET-2007-006.pdf`. LC-DET-2007-006.

[120] W. Wierba *et al.*, "LumiCal mechanical design proposal and integration with ILD". `http://www.eudet.org/e26/e28/e615/e762/EUDET-Memo-2008-13.doc`. EUDET-Memo-2008-13.

[121] A. Stahl, "Luminosity Measurement via Bhabha Scattering: Precision Requirements for the Luminosity Calorimeter". `http://www-flc.desy.de/lcnotes/notes/LC-DET-2005-004.ps.gz`. LC-DET-2005-004.

[122] I. Smiljanic, "Towards a final selection for luminosity measurement" *Proceedings of the Workshop of the Collaboration on Forward Calorimetry at ILC* (Belgrade 2008) . `http://www.vinca.rs/hep/pub/FCAL_Belgrade.pdf`.

[123] W. Wierba *et al.*, "Silicon Sensors for LumiCal Status Report". `http://www.eudet.org/e26/e28/e615/e761/EUDET-Memo-2008-12.doc`. EUDET-Memo-2008-12.

[124] H. Abramowicz *et al.*, "GEANT4 Simulation of the Electronic Readout Constraints for the Luminosity Detector of the ILC". `http://www.eudet.org/e26/e28/e182/e308/eudet-memo-2007-17.pdf`. EUDET-Memo-2007-17.

[125] M. Idzik *et al.*, "Status of LumiCal Readout Electronics". `http://www.eudet.org/e26/e26/e27/e823/eudet_08.pdf`. EUDET-Report-2008-08.

[126] P. Bambade, V. Drugakov, and W. Lohmann, "The impact of BeamCal performance at different ILC beam parameters and crossing angles on stau searches" *Pramana* **69** (2007) 1123–1128, `arXiv:physics/0610145`.

[127] C. Grah *et al.*, "Polycrystalline CVD Diamond Sensors for the Beam Calorimeter of the ILC" *IEEE Trans.Nucl.Sci., accepted for publication* (2009) .

[128] C. Grah *et al.*, "Radiation hard sensor for the BeamCal of the ILC detector" in *Nuclear Science Symposium Conference Record. NSS'07*, vol. 3, pp. 2281–2284, IEEE. 2007.

[129] A. Abusleme *et al.*, "BeamCal front-end electronics: Design and Simulation" *Proceedings of the Workshop of the Collaboration on Forward Calorimetry at ILC* (2008) . http://www.vinca.rs/hep/pub/FCAL_Belgrade.pdf.

[130] Y. Sato, "Study of Pair-Monitor for ILD" *Proceedings of the Workshop of the Collaboration on Forward Calorimetry at ILC* (2008) . http://www.vinca.rs/hep/pub/FCAL_Belgrade.pdf.

[131] Y. Takubo, "Development of Pair Monitor" *Proceedings of the Workshop of the Collaboration on Forward Calorimetry at ILC* (2008) . http://www.vinca.rs/hep/pub/FCAL_Belgrade.pdf.

[132] **CMS Collaboration**, G. Acquistapace *et al.*, "CMS, the magnet project: Technical design report". http://cmsdoc.cern.ch/ftp/TDR/MAGNET/magnet.html. CERN-LHCC-97-10.

[133] A. Hervé, F. Kircher, *et al.*, "Experience Gained from the Construction, Test and Operation of the Large 4-T CMS Coil" in *IEEE Trans. on Appl. Superc.*, vol. 18-2, pp. 346–351. 2008.

[134] M. Fernandez *et al.*, "Experimental validation of optical simulations for microstrip detectors". http://www.eudet.org/. EUDET-memo-2008-37.

[135] **The SiD Concept Group**, "The SiD detector outline document". http://hep.uchicago.edu/~oreglia/siddod.pdf.

[136] **CMS Collaboration**, P. Sphicas, ed., *CMS: The TriDAS project. Technical design report, Vol. 2: Data acquisition and high-level trigger.* http://cdsweb.cern.ch/record/578006/files/cer-2336481.pdf. CERN-LHCC-2002-026.

[137] **ILC Project**, N. Phinney, N. Toge, and N. Walker, eds., *ILC Reference Design Report Volume 3: Accelerator.* 2007. arXiv:0712.2361 [physics.acc-ph]. ILC-REPORT-2007-001.

[138] **ATLAS Collaboration**, G. Duckeck *et al.*, eds., *ATLAS computing: Technical design report.* http://cdsweb.cern.ch/record/837738/files/lhcc-2005-022.pdf. CERN-LHCC-2005-022.

[139] **CMS Collaboration**, "CMS: The computing project. Technical design report". http://cdsweb.cern.ch/record/838359/files/lhcc-2005-023.pdf. CERN-LHCC-2005-023.

[140] "ATCA Short Form Spec.". http://www.picmg.org/pdf/PICMG_3_0_Shortform.pdf.

[141] C. Clerc, "Dimensions and weights of the ILD components". http://www.ilcild.org/documents/ild-loi-material/ILD00_dimensions-weights.pdf/at_download/file.

[142] B. Parker *et al.*, "Functional requirements on the design of the detectors and the interaction region of an e^+e^- linear collider with a push-pull arrangement of detectors". ILC-Note in preparation.

[143] T. Sanami, "IR hall dose rate estimates for a self-shielding detector". http://ilcagenda.linearcollider.org/getFile.py/access?contribId=49&sessionId=44&resId=0&materialId=0&confId=3159. Presented at the ILD workshop, Seoul, Korea.

[144] M. Warden *et al.*, "Nanometre precision interferometric stability monitoring system for key accelerator components". http://www.eurotev.org/reports_presentations/eurotev_reports/2008/e1109/EUROTeV-Report-2008-032.pdf. EUROTeV-Report-2008-032.

[145] M. Anduze, H. Videau, and M. Jore, "Note on the beam tube for ILD" (2009) . http://www.ilcild.org/documents/ild-loi-material/Beam_tube_note.pdf/at_download/file.

[146] Y. Suetsugu, "Technical note for ILD beam pipe". http://www.ilcild.org/documents/ild-loi-material/Suetsugu_beam_pipe.pdf/at_download/file.

[147] C. Clerc, "ILD work breakdown structure". http://www.ilcild.org/documents/ild-loi-material/ILD%20WBS%202009.xlsx/at_download/file.